PhD-FSTC-2015-24
The Faculty of Sciences, Technology and Communication

DISSERTATION

Presented on 15/05/2015 in Luxembourg

to obtain the degree of

DOCTEUR DE L'UNIVERSITÉ DU LUXEMBOURG

EN SCIENCES DE L'INGÉNIEUR

by

Furqan AHMED
Born on 10 October 1986 in Islamabad (Pakistan)

THE POTENTIAL OF PRECIPITABLE WATER VAPOUR MEASUREMENTS FROM GLOBAL NAVIGATION SATELLITE SYSTEMS IN LUXEMBOURG

Dissertation Defense Committee

Dr. Tonie Van Dam, Committee Chair
Professor, Université du Luxembourg

Dr. Olivier Francis, Committee Vice-Chair
Professor, Université du Luxembourg

Dr-Ing. Felix Norman Teferle, Dissertation Supervisor
Professor, Université du Luxembourg

Dr. Richard Bingley, Committee Member
Associate Professor, University of Nottingham

Dr. Guergana Gueorova, Committee Member
Associate Professor, Sofia University

Abstract

The primary objectives of this research were to investigate the potential of precipitable water vapor (PWV) estimates derived from Global Navigation Satellite Systems (GNSS) measurements, firstly, for short-term weather forecasting based on numerical weather prediction (NWP) in Luxembourg and its surroundings and, secondly, for monitoring climate on regional and global scales.

The suitability of real-time (RT) zenith total delay (ZTD) estimates obtained from three different precise point positioning (PPP) software packages was assessed by comparing them with the state-of-the-art product from the International GNSS Service (namely the IGS final troposphere product) as well as collocated radiosonde (RS) observations. It was found that the RT-PPP ZTD estimates from two of the three software packages meet the threshold requirements for NWP nowcasting. The biases between the RT-PPP ZTD and the reference ZTD were found to be stable over time for all the RT-PPP ZTD solutions. A millimetre-level impact on the RT-PPP ZTD estimates was also observed when integer ambiguities were resolved.

The impact of assimilating GNSS-derived near real-time (NRT) ZTD in the Applications of Research to Operations at Mesoscale (AROME) NWP model using a three-dimensional, variational (3D-VAR) assimilation scheme on the quality of weather forecasts for Luxembourg was studied. It was found that the assimilation of GNSS-derived ZTD systematically improves the atmospheric humidity short-range forecasts in comparison to other water vapor observing systems (radio soundings, satellite radiances, surface networks). Examination of several case studies revealed the ability of the ZTD observations to modify the intensity and location of predicted precipitation in accordance with previous studies. The addition of ZTD from the dense GNSS network in Wallonie (Belgium) was also found to be beneficial by improving the prediction of rainfall patterns in Luxembourg.

The 2D maps of IWV obtained from the hourly NRT system were compared with cloud distribution and precipitation maps from satellite and weather radar data, respectively, and a good agreement in the location of the front system was been found. A rise in IWV was recorded during a precipitation event in Luxembourg and it was shown that by observing the IWV change over the ground-based GNSS stations in Luxembourg in NRT, it is possible to determine the speed and direction of the passing fronts and hence storms can also be tracked.

A 5-year long global reprocessed GNSS data set containing over 400 ground-based GNSS stations and based on the double differencing strategy has been used to validate the ZTD estimates obtained from the climate reanalysis model of the European Centre for Medium-range Weather Forecasts (ECMWF) namely the ECMWF ReAnalysis-Interim (ERA-Interim) in different climate zones. It was found that the correlation coefficient between the GNSS-derived ZTD observations and the ZTD modeled by ERA-Interim ranges from 0.87 to 1.00. Higher correlation coefficients were found for the stations belonging to the climate zones with lower amount of water vapour. Furthermore, it was found that the mean, SDev and RMS of the differences depends on periodicity in the residuals, altitude of the stations in a particular zone as well as the topographic variation in the zone.

Monthly and seasonal means of GNSS-derived ZTD (ZTD_{gnss}) were computed using a global ZTD_{gnss} dataset consisting of 19-years of data and over 400 stations to study the climate variability in different climate zones. In terms of seasonal means, it was found that the climate zones in the northern hemisphere have ZTD maxima in Boreal Summer (June-July-August) whereas those in the southern hemisphere have ZTD maxima in Austral Summer (December-January-February). Monthly and seasonal variability in ZTD_{gnss} was also studied for the locations of 6 ground-based GNSS (SPSLux) stations in Luxembourg. It was found that all the 6 SPSLux stations experience the same monthly and seasonal variability of ZTD_{gnss}. In terms of monthly variation, it was found that the maxima in ZTD_{gnss} occurs around the month of July for all the 6 SPSLux stations whereas in terms of seasonal variation, the location of maxima was found to be in Summer (June-July-August).

The suitability of the ZTD derived using precise point positioning (PPP) strategy for climate monitoring applications was studied through its comparison with the ZTD estimates derived using double differenced positioning (DDP) using a global network of 114 stations and duration of 1 year. The mean differences between the two were found to be ranging from -3.35 to 2.37 mm over different climate zones. Furthermore, correlation coefficients ranging from 0.90 and 1.00 were found between the ZTD obtained using the two processing strategies. It was found that use of higher elevation cut-off angles and tropospheric mapping functions based on NWP improves the agreement between the PPP and DDP solutions.

Peer-reviewed Publications

- **Ahmed, F.**, Václavovic, P., Teferle, F. N., Douša, J., Bingley, R., Laurichesse, D., Comparative Analysis of Real-Time Precise Point Positioning Zenith Total Delay Estimates, GPS Solutions (2016) 20: 187, DOI: 10.1007/s10291-014-0427-z (Access online at `http://hdl.handle.net/10993/18836`)

- **Ahmed, F.**, Teferle, F. N., Bingley, R., Laurichesse, D., The Status of GNSS Data Processing Systems to Estimate Integrated Water Vapour for Use in Numerical Weather Prediction models, IAG Symposia Series, Vol. 143, DOI: 10.1007/1345_2015_178 (Access online at `http://hdl.handle.net/10993/16925`)

- Teferle F. N., Hunegnaw A., **Ahmed F.**, Sidorov D., Woodworth P. L., Foden P. R., Williams S. D. P., The King Edward Point Geodetic Observatory, South Georgia, South Atlantic Ocean: A First Evaluation and Potential Contributions to Geosciences, IAG Symposia Series, Vol. 143, DOI: 10.1007/1345_2015_175 (Access online at `http://hdl.handle.net/10993/17029`)

- Mahfouf, JF., **Ahmed F.**, Moll, P., Assimilation of zenith total delays in the AROME France convective scale model: a recent assessment, Tellus A, DOI: 10.3402/tellusa.v67.26106 (Access online at `http://hdl.handle.net/10993/19927`)

Acknowledgements

All praise belongs to Allah, Lord of all the worlds.

This Ph.D. project was funded by the Luxembourg National Research Fund (FNR, `https://www.fnr.lu/`) under the grant AFR-PhD-1090247.

I am highly grateful to my supervisor Prof. Felix Norman Teferle for his continued interest and support in my Ph.D. project all the way from the preparation of its proposal to the completion of this thesis. In addition to the guidance about the subject matter, he has always provided me with ample opportunities for my professional development. I am also thankful to the other members of my Dissertation Defense Committee (DDC) namely Prof. Tonie Van Dam (chair), Assoc. Prof. Guergana Guerova (external examiner), Assoc. Prof. Richard Bingley (external examiner), and Prof. Olivier Francis (internal examiner) for evaluating my thesis and providing valuable feedback. Furthermore, Assoc. Prof. Richard Bingley and Dr. Jean-Francois Mahfouf are thankfully acknowledged for hosting my visits to the University of Nottingham (UK) and MétéoFrance (France), respectively. Travel for conferences and collaborated activities was funded by the aforementioned AFR-PhD grant and the project COST Action ES1206 - GNSS4SWEC.

The Administration du Cadastre et de la Topographie (ACT) of Luxembourg, Service Public de Wallonie of Belgium, International GNSS Service, EUREF Permanent Network, RGP and BIGF are thankfully acknowledged for providing the GNSS observation data from their networks. Various products to support GNSS data processing were obtained from BKG, IGS, CODE, and CNES. The meteorological service unit of the Air Navigation Administration of Luxembourg (MeteoLux), the Administration des Services Techniques de l'Agriculture (ASTA) of Luxembourg, and the UK Met Office are thankfully acknowledged for providing meteorological data. The ERA-Interim products used in this study were obtained using TropDB - TropModel service of the Geodetic Observatory Pecny (GOP) of Czech Republic. Dr. Addisu Hunegnaw and the High Performance Computing (HPC) service of the University of Luxembourg are gratefully acknowledged for support in GNSS data processing.

The successful completion of my Ph.D. would have never been possible without the contributions of each of my family members towards my life. Right from my childhood, my father, my (late) mother, my elder brother, my sister and my younger brother have always helped, morally supported and encouraged me during my academic pursuits. Later, my beloved wife came to my life and added a lot through her love and emotional support. I am thankful to all of them. Even though it was painful to stay far away from all of them for the pursuit of success, I hope that my success will make them all happy and proud. I love them all.

I dedicate this achievement to my late mother, Riffat Rashda, whose prayers always stood by my side, though she could not. Blessed be her soul.

Acronyms and Abbreviations

3D-VAR	3-Dimensional Variational Assimilation
ACT	Administration du Cadastre et de la Topographie
AIRS	Atmospheric Infrared Sounder
ALADIN	Aire Limitée Adaption Dynamique et developement InterNational
ANA	Administration de la Navigation Aérienne
AR5	IPCC Annual Report 5
AROME	Application of Research to Operations at Mesoscale
ARP	Antenna Reference Point
ARPEGE	Action de Recherche Petite Echelle Grande Echelle
ASTA	Administration des Services Techniques de l'Agriculture
ATMS	Advanced Technology Microwave Sounder
BADC	British Atmospheric Data Center
BDS	BeiDou Navigation Satellite System
BIGF	British Isles continuous GNSS Facility
BKG	Bundesamt für Kartographie und Geodäsie
BNC	BKG Ntrip Client
BSW50	Bernese GPS Software v 5.0
BSW52	Bernese GNSS Software v 5.2
CNES	Centre National d'Études Spatiales
CODE	Center for Orbit Determination in Europe
COST	European Cooperation in Science and Technology
DDP	Double Differenced Positioning
DORIS	Doppler Orbitography and Radiopositioning Integrated by Satellite
DOY	Day Of Year
ECMWF	European Center for Medium-range Weather Forecasting
EGVAP	EIG EUMETNET GNSS Water Vapour Programme
EOP	Earth Orientation Parameters
EPN	EUREF Permanent Network
ERA-40	ECMWF ReAnalysis based on 40 years of data
ERA-I	ECMWF ReAnalysis - Interim
EUREF	Reference Frame Sub Commission for Europe
FTP	File Transfer Protocol

GLONASS	GLObalnaya NAvigatsionnaya Sputnikovaya Systema
GMF	Global Mapping Function
GNSS	Global Navigation Satellite System
GNSS4SWEC	Advanced Global Navigation Satellite Systems tropospheric products for monitoring severe weather events and climate
GOP	Geodetic Observatory Pecny
GPRS	General Packet Radio Service
GPS	Global Positioning System
GPT	Global Pressure and Temperature model
IERS	International Earth Rotation and Reference Systems
IGFT	International GNSS Service Final Troposphere product
IGS	International GNSS Service
IMF	Isobaric Mapping Function
IPCC	Intergovernmental Panel on Climate Change
ITRF	International Terrestrial Reference Frame
IWV	Integrated Water Vapour
LIST	Luxembourg Institute of Science and Technology
NASA	National Aeronautics and Space Administration
NCAR	National Center for Atmospheric Research
NCEP	National Centers for Environmental Prediction
NEQ	Normal Equation
NERC	Natural Environment Research Council
NMF	Niell Mapping Function
NRT	Near Real-Time
NRTK	Network Real-Time Kinematic
NTRIP	Networked Transport of RTCM via Internet Protocol
NWP	Numerical Weather Prediction
OSGB	Ordnance Survey of Great Britain
OSi	Ordnance Survey of Ireland
PCO	Phase Center Offset
PCV	Phase Center Variation
PP	Post-Processing
PPP	Precise Point Positioning
PPP-Wizard	Precise Point Positioning With Integer and Zero-difference Ambiguity Resolution Demonstrator
PWV	Precipitable Water Vapour

PWVLUX	Potential of Precipitable Water Vapour Measurements using Global Navigation Satellite Systems in Luxembourg
RGP	Réseau GNSS Permanent
RINEX	Receiver Independent Exchange format
RMS	Root Mean Square
RS	Radiosonde
RT	Real-Time
RTCM	Radio Technical Commission for Maritime Services
RTMA-HRRR	Real Time Mesoscale Analysis - High-Resolution Rapid Refresh
RTS	IGS Real-Time Service
RUC	Rapid Update Cycle
SDev	Standard Deviation
SGF	Space Geodesy Facility
SPSLux	Satellite Positioning Service Luxembourg
SPW	Service Public de Wallonie
SSR	State Space Representation
STD	Slant Total Delay
SWV	Slant Water Vapour
TEC	Total Electron Content
TPW	Total Precipitable Water
UKMO	UK Met Office
UL	University of Luxembourg
UNB	University of New Brunswick
USNO	United States Naval Observatory
UTC	Coordinated Universal Time
VLBI	Very Long Baseline Interferometry
VMF	Vienna Mapping Function
WALCORS	Wallonia Continuously Operating Reference System
WMO	World Meteorological Organization
XML	eXtensible Markup Language
ZHD	Zenith Hydrostatic Delay
ZTD	Zenith Total Delay
ZWD	Zenith Wet Delay

Contents

List of Figures

List of Tables

Chapter 1

Introduction

> *And We sent down water from the sky according to measure, and We caused it to stay in the earth - and surely it is We Who determine its taking away.*
>
> Qur'an, 23:19

This chapter provides an introduction to the research area by introducing some concepts and the state-of-the-art in GNSS meteorology and climatology. It then outlines the research objectives of this thesis and summarizes the methodology used to address these objectives. Finally, it describes the structure of this thesis by introducing the various chapters.

1.1 Overview

Water vapour, i.e. the gaseous state of water, is the most abundant and highly variable greenhouse gas in the Earth's atmosphere and is fundamental to the transfer of energy in the atmosphere and weather prediction. Various studies have shown relations between different weather events and the supply of water vapour in the atmosphere. For example, Kunkel et al. (2013) observed significant increases in atmospheric water vapour coinciding with extreme precipitation events, and suggested that this increase (in addition to other dynamic factors) could have been the cause of the intensified precipitation. About 90% of the total atmospheric water vapour is found in the lower-most layer of the atmosphere extending up to 17 km namely the troposphere where most of the weather phenomena take place. Water vapour has a high heat capacity and other than its significant role in weather formation, it also contributes to the rise in temperature of the atmosphere and the Earth's surface on longer time scales by absorbing energy from solar radiation and the radiation reflected by the surface of Earth (Taylor 2005). It has been confirmed in the past that the characteristic of water vapour to amplify the heat has the potential to increase climate warming twice in magnitude than that caused by the increase in carbon dioxide (Dessler et al. 2008).

Atmospheric water vapour is measured in terms of a quantity known as precipitable water vapour (PWV) which represents the height of a column of water in the atmosphere above a certain location on the ground. PWV is also called total precipitable water (TPW) and is measured in units of length. Integrated water vapour (IWV) is an alternative representation of the atmospheric water vapour and is defined as the total amount of water vapour present in a vertical atmospheric column with units of kg/m^2 (http://www.wmo-sat.info/oscar/variables/view/162). The terms IWV and TPW will be interchangeably used in this thesis. Currently, there are a number of ground-based and space-based instruments and techniques which are used to observe IWV and each of these has its own strengths and weaknesses. These instruments will be discussed in detail in the next chapter.

The term Global Navigation Satellite System (GNSS) refers to a system having a satellite constellation used to provide position, navigation and timing data (Hofmann-Wellenhof et al., 2007). The Global Positioning System (GPS) of the United States, the GLObal'naya NAvigatsionnaya Sputnikovaya Sistema (GLONASS) of Russia, Galileo of Europe and the BeiDou Navigation Satellite System (BDS) of China are examples of such GNSSs. The user segment of a GNSS contains the GNSS receivers which can be ground-based, airborne or space-borne depending on the desired end-user application. The working principles of GNSS, associated processing strategies and the various error sources that affect the GNSS observations will be described in the next chapter.

As the GNSS signal travels from the transmitting satellite to the ground-based receiver, it is refracted by the Earth's atmosphere and this refraction introduces a propagation delay in the signal. While the delay (ranging from 10 to 100 m) caused by the ionized portion of the atmosphere i.e. the ionosphere can be effectively removed using a linear combination of two carrier frequencies, the delay in the neutral atmosphere (mainly caused by the troposphere) cannot be removed and depends on the integral effect of the densities of dry air and water vapour along the signal path. By processing the GNSS observations, the average vertical component of the propagation delays encountered by the signals from all the satellites in view of a given ground-based station can be estimated and is called zenith total

delay (ZTD). Various data processing strategies, e.g. precise point positioning (PPP) (Zumberge et al. 1997) and double differenced positioning (DDP) (Hofmann-Wellenhof et al., 2007), allow the estimation of ZTD from ground-based GNSS observations in real-time or RT (latencies of 1 to 10 min), near real-time or NRT (latencies of up to 90 min) and post-processing or PP (latencies up to years or decades) modes (Ahmed et al. 2014a). The ZTD is divided into hydrostatic and wet parts, namely the zenith hydrostatic delay (ZHD) and the zenith wet delay (ZWD), respectively, and can be converted to IWV by using surface meteorological data (Bevis et al. 1992, 1994). Hence, over the last two decades, GNSS have emerged as a tool for monitoring the atmospheric water vapour. Figure 1.1 depicts the process of obtaining IWV from GNSS measurements. Surface pressure values at the locations of the GNSS receivers can be obtained from either observations or models. Using the pressure values, ZHD is computed and subtracted from the ZTD estimates to obtain ZWD. Finally, ZWD is converted to IWV using the temperature values, again either from observations or from models. Although IWV is of primary interest for weather forecasting and climate research, for consistency, it is only ZTD which is usually assimilated into NWP models before it is converted to IWV using homogeneous temperature values within the model (Marel 2004).

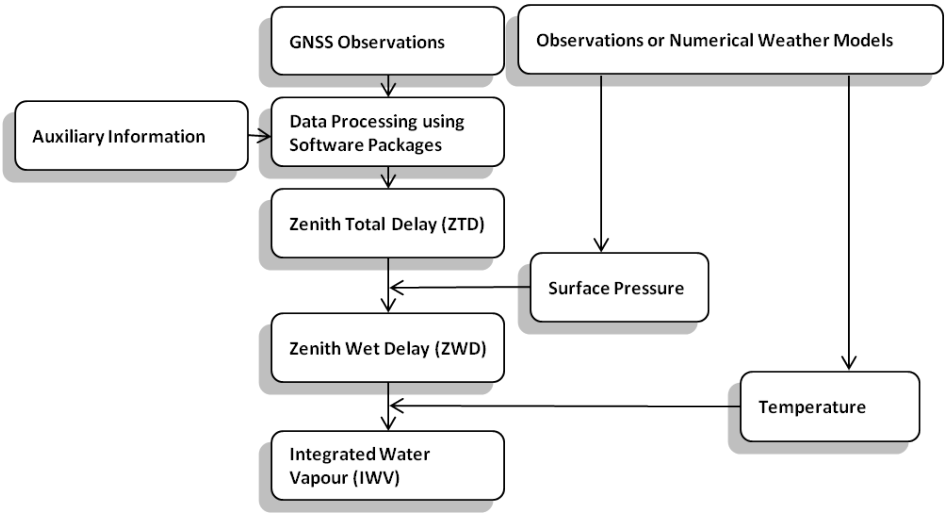

Figure 1.1: Process of obtaining IWV from GNSS measurements

Various error sources can affect the accuracy of the GNSS-derived ZTD estimates. In PPP processing, the ZTD is more sensitive to the radial component of the orbit error, whereas in DDP processing, it is more sensitive to the tangential component of the orbit error (Douša 2012). Although the first-order ionospheric delay is eliminated using the linear combination of the measurements from two different carriers, there still remains a smaller effect from the higher-order terms of the ionospheric delay especially during the times of high solar activity. There is a linear dependency between the daily mean of the Total Electron Content (TEC) unit and the estimated vertical position (Fritsche et al. 2005). If the error in ZTD is approximated as one third of the vertical position error (Hill et al. 2009), it would mean that an increase of the TEC from 25 to 175 will result in a ZTD error ranging from 0.6 to 4 mm if higher-order ionospheric corrections are not applied, however, this is not further investigated here. Furthermore, it has been shown that errors in the a-priori ZHD caused by the use of inaccurate surface pressure values could result in an error of -0.1 to -0.2 mm/hPa in vertical position estimates (Tregoning and Herring 2006) and this could also lead to an error in the ZTD. Antenna related errors, e.g. phase center offsets (PCO) and variations (PCV), and radome geometry, also lead to errors in the vertical position and the ZTD estimates. Byun and Bar-Sever (2009) and Thomas et al. (2011) have shown that differences in the estimated ZTD with and without PCV corrections may vary from 2 to 10 mm. The effect of inaccurate or unaccounted PCOs may be even larger (up to few centimeters). The tropospheric mapping functions (MF), which are used to map the tropospheric delay from line-of-sight (slant) to the zenith, also have an elevation-dependent effect on the corresponding ZTD, although the effect of the MF reduces with an increase in the elevation cut-off angle used for observations (Ning 2012).

The ZTD represents the total tropospheric delay at the zenith of a ground-based station with an assumption of an azimuthally symmetric atmosphere. Processing of GNSS observations also allows the estimation of the horizontal tropospheric gradients i.e. the rate of change of the ZTD in east-west and north-south directions and the slant total delay (STD), i.e. the line-of-sight signal propagation delay between a satellite and the ground-based station. The horizontal gradients and STD provide a higher spatial resolution and

significantly increased number of observations and hence allow an enhanced description of the state of the atmosphere. Furthermore, the STD can be converted to slant water vapor (SWV). Various studies have demonstrated the benefits of using horizontal gradients and STD for positioning (Bar-Sever et al. 1998), GNSS tomography (Bender et al. 2011), and prediction of severe weather (Ha et al. 2002). However, the use of STD is beyond the scope of this thesis.

As an observing technique, GNSS enjoy various advantages over the other observational systems in use today. In addition to being a low cost observation technique, GNSS have an all-weather operational capability and could provide observations with a temporal resolution of as high as 1 Hz. The establishment and continuous development of global and dense regional networks of ground-based GNSS stations result in a high spatial resolution of GNSS observations as compared to other types of observations. Modern telecommunication protocols also allow the rapid dissemination of GNSS observations and hence these could be obtained with very low latencies.

The term "GNSS meteorology" refers to the assimilation of GNSS-derived atmospheric information (ZTD and/or IWV) into NWP models as well as the combination of NWP model output and GNSS observations while issuing forecasts. GNSS meteorology also includes non-NWP products such as severe weather monitoring. Over the last decade, a number of international research projects and programmes in Europe (e.g. Elgered, 2001, Huang et al., 2003), North America (e.g. Smith et al., 2007) and Asia (e.g. Iwabuchi et al., 2000) have investigated the use of GNSS-derived NRT ZTD estimates in NWP models. Since 2005, the EUMETNET EIG GNSS water vapour programme (E-GVAP) (http://www.egvap.dmi.dk/) enables various analysis centres across Europe to submit their NRT ZTD estimates for assimilation into the NWP models of the partner meteorological institutions (Vedel et al., 2013). Since late 2012, another European project COST Action ES1206: Advanced Global Navigation Satellite Systems tropospheric products for monitoring severe weather events and climate (GNSS4SWEC) (Jones et al., 2014) is in progress to investigate GNSS meteorology further in the light of modern challenges and developments. As of today, NRT ZTD estimates (with 1-hourly temporal resolution) are assimilated into local, re-

gional and global scale NWP models that are run with 3-hourly to 6-hourly update cycles and produce medium-range (up to a few days) weather forecasts. The assimilation of GNSS-derived ZTD into NWP models has been found to have a positive impact on the quality of the analysis of the current state of the atmosphere and the corresponding weather forecasts (Bennit et al. 2011, De Haan 2011, Gutman et al. 2004, Mahfouf et al. 2015). With the developments of high update-rate NWP models, for example, the Rapid Update Cycle (RUC) (Benjamin et al., 2010) and the Real-Time Meso Analysis High Resolution Rapid Refresh (RTMA-HRRR) (Benjamin et al., 2013), and in order to use the ZTD estimates for NWP nowcasting and monitoring extreme short-term weather changes, it is a primary research interest nowadays, to obtain them with a minimal latency of 10 or even 5 minutes while maintaining a certain level of accuracy (Offiler 2010). Recent studies have shown that it is possible to obtain ZTD and IWV estimates with latencies as low as 1 s by processing the GNSS observations as RT-PPP (Ahmed et al. 2014b, Yuan et al. 2014). The fixing of integer phase ambiguities enhances the precision of the GNSS-derived position estimates. In the DDP strategy, common errors are removed and it becomes easier to identify and fix such integer ambiguities. However, for un-differenced observations, it was not possible to fix the integer phase ambiguities until recently (Geng et al. 2010). To date, only a few studies have been performed to study the impact of ambiguity resolution on GNSS-based ZTD estimates in RT-PPP with some of them benefitting from software and products not necessarily available to the community (Shi and Gao 2012; Geng et al. 2009). In these studies, the impact of ambiguity resolution on ZTD was observed to be around 4 to 6 mm. The recent study by Li et al. (2014), which is based on their in-house software and products, also reported on the insignificant differences between the RT-PPP float and fixed solutions after sufficiently long times of convergence. However, they demonstrated the usefulness of ambiguity fixing for the rapid re-initialization of an RT-PPP processing system (e.g. after an interruption in the RT data).

It is a widely known fact that the Earth's climate is continuously undergoing changes (Hartmann et al. 2013, Karl et al. 2009) over different time scales. These changes are clearly reflected by a rise in the frequency and intensity of extreme climate events (Groisman et al. 2005, Katz 2010)

which have caused a significant damage to human life and property to date. Therefore it is of utmost importance to investigate variations and trends in the climate by optimally utilizing the available evidence. To help with this, another atmospheric application of the GNSS observations emerges to be in climate monitoring which will be referred to as "GNSS climatology" in this thesis. Although conventional climate studies are based on datasets covering at least 30 years and GNSS observations are only available for two decades as of now, the term GNSS climatology is used by the GNSS community referring to the application of GNSS to climate monitoring. Various studies have used the long-term estimates of IWV and/or ZTD derived from GNSS to study the trends and variability in water vapour on global and regional scales (e.g. Ahmed et al. 2014c, Vey et al. 2010, Wang and Zhang 2009, Nilsson and Elgered 2008, Stende 2006, Hagemann et al. 2003). A review of state-of-the-art of the meteorological and climatological applications of GNSS can be found in [Guerova et al., 2016].

The Grand Duchy of Luxembourg (or simply Luxembourg) belongs to the West European Continental climatic region. It has a temperate climate with mild winters, cool summers and high rainfall. Because of the high rainfall, flooding is the main natural hazard and one of the major concerns in Luxembourg. The studies presented by, for example, Pfister et al., [2005], Pfister et al., [2004] and Pfister et al., [2000] discuss the trends, variability and driving factors of the hydrological extremes in Luxembourg region related to rainfall. Furthermore, climate change and a change in air temperature is also a concern for Luxembourg as evident from, for example, Junk et al., [2014], Goergen et al., [2013], and Drogue et al., [2005].

GNSS meteorology is currently not operationally in practice in Luxembourg. However, there is adequate infrastructure present in Luxembourg to locally obtain GNSS observations as well as meteorological data in this country. For example, there is a network of permanent ground-based GNSS stations inside and around the borders of Luxembourg. Furthermore, there are various meteorological sensors installed all over Luxembourg (the details about these networks will be presented in the following chapters). Therefore, it is of interest to investigate if it is possible to use the locally available meteorological data and GNSS observations for the computation of IWV

and to study the potential of GNSS meteorology in Luxembourg.

As of now, only GPS and GLONASS are fully operational GNSSs. However, as this thesis covers all the aspects of GNSS meteorology, the research presented in this thesis is based on the observations from GPS only and the analysis was not expanded to GPS+GLONASS or multi-GNSS observations. Therefore, the term GNSS implies GPS in this thesis unless stated otherwise.

1.2 Processing Terminologies Used in the Thesis

During this research, ZTD and IWV have been estimated by processing GNSS observations in several different modes and using different processing strategies. For the ease of reading, the ZTD and IWV solutions have been referred to using various abbreviations throughout the thesis that specify the exact mode and processing strategy used to obtain that solution. Table 1.1 describes these abbreviations.

Table 1.1: Abbreviations used to specify different solutions

Abbreviation	Quantity	Processing Mode	Processing Strategy
RT-PPP ZTD	ZTD	Real-time	PPP
NRT-DDP ZTD	ZTD	Near Real-time	DDP
NRT-DDP IWV	IWV	Near Real-time	DDP
PP-DDP ZTD	ZTD	Post-processing	DDP
PP-DDP IWV	IWV	Post-processing	DDP
PP-PPP ZTD	ZTD	Post-processing	PPP
PP-PPP IWV	IWV	Post-processing	PPP

1.3 Research Objectives

The primary objective of this thesis is to study the potential of GNSS meteorology and climatology for Luxembourg. It has been investigated how ground-based GNSS observations from the networks in Luxembourg and its surrounding areas in Germany, Belgium and France (collectively

known as the Greater Region) can benefit the short-term weather forecasting and climate monitoring for Luxembourg. Additionally, some research areas of a global scope, such as the validation of the European Centre for Medium-range Weather Forecasts (ECMWF)'s climate reanalysis dataset ERA-Interim, have also been addressed. Specifically, the following questions have been answered:

- Which are the best suitable software packages, tools and products to obtain GNSS-derived RT-PPP ZTD in Luxembourg?
- What is the suitability of RT-PPP ZTD estimates for use in NWP applications?
- What is the impact of using GNSS-derived NRT-DDP ZTD from Luxembourg and the surrounding areas on quality of short-term weather forecasts issued by the respective NWP model?
- What is the usefulness of GNSS-derived NRT-DDP IWV for tracking weather fronts and storms in Luxembourg?
- What is the agreement between the ZTD derived from the ERA-Interim climate reanalysis dataset with GNSS-derived PP-DDP ZTD in different climate zones?
- What is the agreement between the ZTD from climate reanalysis data and GNSS-derived ZTD in Luxembourg?
- What is the suitability of PP-PPP ZTD estimates for climate monitoring applications in Luxembourg?
- Which are the optimal sources of meteorological data for Luxembourg?

In order to address the research objectives, a number of GNSS data processing systems (RT, NRT and PP) and tools were developed. Figure 1.2 describes the scope of the research objectives addressed by the RT, NRT and PP systems.

The results from the RT, NRT and PP systems were used for the desired applications after being validated using state-of-the-art reference datasets and this was followed by the assessment of the potential of these results in

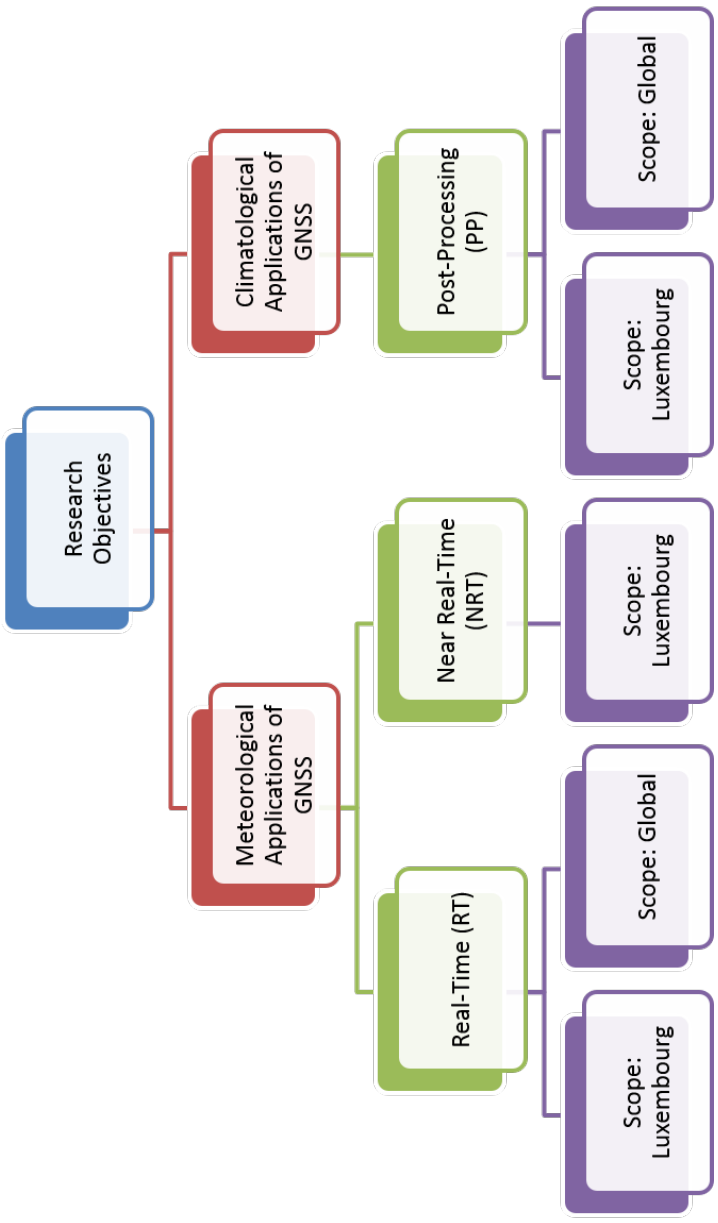

Figure 1.2: Scope of the research objectives addressed by RT, NRT and PP systems

the respective applications. The following text summarizes the methodology used to answer the above mentioned research questions.

- The weather forecasts produced by the national meteorological service of Luxembourg (MétéoLux) are based on the output of the NWP model AROME, which is run operationally at MeteoFrance. In order to improve the knowledge of the current state of atmosphere and the corresponding forecasts, the AROME model makes use of the GNSS-derived ZTD estimates from European GNSS networks but as of now, the ZTD estimates obtained from the GNSS networks in Luxembourg and the Greater Region are not operationally used for this purpose. In order to investigate the potential benefit of using the GNSS-derived ZTD observations from Luxembourg and the Greater Region in the AROME NWP model, a set of experiments was conducted in collaboration with MeteoFrance. The operational 1-hourly NRT GNSS data processing system was used to obtain ZTD estimates for a ground-based European network with a densification over Luxembourg and Wallonie (Belgium) for a period in past. With the support from MeteoFrance, this NRT-DDP ZTD data was assimilated into the AROME NWP model and various forecasts were generated. The quality of the generated forecasts of various parameters was assessed by comparing them to the observed values of the parameters.

- In order to assess the suitability of RT-PPP ZTD estimates for use in NWP applications and to identify the best suitable RT processing software and products for Luxembourg, two RT data processing systems were implemented at the University of Luxembourg (UL) to conduct a study on RT-PPP ZTD estimation. In addition, a collaboration was established with the Geodetic Observatory Pecny (GOP) and one of their RT processing systems was included in the study. The three processing systems were based on different processing engines. The precision and stability of the RT-PPP ZTD estimates obtained from each of the systems were assessed through comparisons with state-of-the-art GNSS based ZTD products and ZTD derived from a non-GNSS technique (i.e. radiosonde). Moreover, the various estimates obtained were checked for compliance with the established user requirements for NWP applications.

- Luxembourg has a ground-based GNSS network operational since late 2006 which consists of 6 stations distributed over Luxembourg. Therefore, the length of GNSS-derived ZTD records for Luxembourg is slightly over 8 years which is currently insufficient for long-term climate monitoring. However, it is still possible to use it to investigate its suitability for the climate variability on shorter time scales. A PP system was developed in order to serve this purpose. The available historic data from the stations in Luxembourg was processed along with others using state-of-the-art products and software, and time series for ZTD and IWV were obtained. The quality of GNSS-derived PP-PPP ZTD from the ground-based stations in Luxembourg was assessed by comparing it to its equivalent from the ERA-Interim dataset. Furthermore, using the GNSS-derived PP-DDP ZTD from a global network of over 400 stations, the ZTD from the ERA-Interim model was validated in different climate zones around the globe.

- The two GNSS data processing strategies, i.e. DDP and PPP, each of which has its own strengths and weaknesses, were investigated. While troposphere delay estimates from the DDP strategy are higher in accuracy than from the PPP strategy, the latter is more efficient in the computational burden and allows larger networks to be analyzed in shorter time spans. In order to assess the usefulness of the PP-PPP strategy for climate monitoring applications, a comparison of the ZTD estimates obtained using the PP-DDP and PP-PPP strategies has been performed and the variation of the differences in different climate zones has been studied.

- Pressure and temperature values from various sources of meteorological data available in Luxembourg were obtained and were used to convert the ZTD to IWV. The obtained IWV estimates were then compared to that derived from ERA-Interim model and based on the comparison results, the most accurate source of pressure and temperature data was identified.

1.4 Thesis Structure

This thesis consists of 7 chapters. Starting from an introduction to the research area and a review of the state-of-the-art, it states the objectives of the research, background and the corresponding methodology used to address these objectives. After the methodology, it introduces the data used throughout the research and the results. In the end, the interpretation of the results has been presented in form of conclusions and recommendations. A brief introduction to each of the succeeding chapters has been presented below.

Chapter 2 (Background) This chapter provides the background knowledge that is essential to understand the content of this thesis. It reviews the structure of the Earth's atmosphere, the role and importance of atmospheric water vapour in weather and climate dynamics, water vapour measurement techniques and some atmospheric physics. Furthermore, it describes the working principles of GNSS and various error sources that affect the GNSS observations. It also provides a brief introduction to NWP.

Chapter 3 (Methodology) This chapter describes the methodology that has been used to achieve the research objectives of this thesis. Firstly, it describes the RT, NRT and PP GNSS data processing systems. Secondly, it describes the experiments that have been performed using the RT, NRT and PP systems to answer the various research questions along with the configurations and experimental setup of these systems.

Chapter 4 (Data and Products) This chapter provides the details about the sources and providers of various types of data and products used for this research. Specifically, it describes the global and regional ground-based GNSS networks from which the observation data has been obtained and describes the networks of stations processed by the RT, NRT and PP processing systems. It introduces the sources of the GNSS products such as orbits and clocks that are used for processing the observations. Furthermore, it introduces the sensor networks (in Luxembourg) and models of meteorological data which have been used to obtain various meteorological parameters.

Chapter 5 (Results) This chapter presents the results of various experiments performed during this research. Along with the results, an interpretation of these results in relevance with the respective research objectives has been presented.

Chapter 6 (Potential for Luxembourg) Based on a detailed comparison the meteorological data sources in Luxembourg and the results presented in Chapter 5, this chapter discusses the current potential of GNSS meteorology and GNSS climatology for Luxembourg.

Chapter 7 (Conclusions and Suggestions for Future Work) This chapter will summarize all the results and findings of the thesis in the form of conclusions. Based on the findings of this thesis, it also makes recommendations for future work.

Chapter 2

Background

> *And We have created above you seven heavens (skies) lying one above the other.*
>
> Qur'an, 23:18

This chapter provides the background knowledge that is essential to understand the content of this thesis. It reviews the structure of the Earth's atmosphere, the role and importance of atmospheric water vapour in weather and climate dynamics and water vapour measurement techniques. Furthermore, it introduces the GNSS data processing techniques and some error sources that affect the GNSS observations. It also provides a brief introduction to NWP and climate reanalysis.

2.1 Earth's Atmosphere

The Earth's atmosphere is divided into various regions. The vertical structure of the atmosphere can be described in terms of the electromagnetic properties as well as the variation in temperature with altitude in a certain region. In terms of the temperature variation with altitude, the atmosphere is divided into regions or layers namely troposphere, stratosphere, mesosphere, thermosphere and exosphere. If described in terms of the electromagnetic properties, the atmosphere can be divided into neutral and ionized (or charged) parts. The term "ionosphere" refers to the ionized part of the atmosphere which consists of the thermosphere and a part of the exosphere. The ionosphere is further divided into the E and F layers. Figure 2.1 shows the vertical profile of the temperature as well as the electron density in these layers of the Earth's atmosphere (Taylor, 2005). The first-order effect ($\approx 99.9\%$) of the ionosphere can result in a propagation delay ranging up to a few tens of meters and can be eliminated using the linear combination of the measurements from two different carrier signals. This combination is known as the ionosphere-free linear combination. However, even after using the ionosphere-free combination, there remains a smaller effect from the

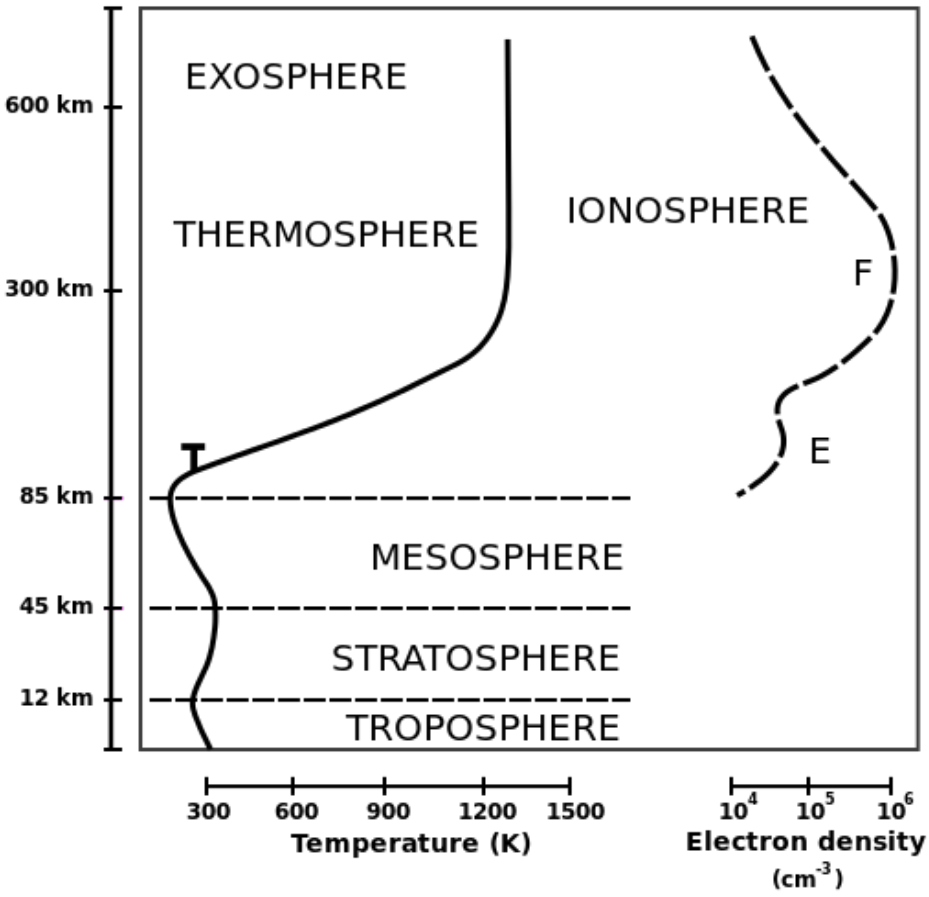

Figure 2.1: Vertical profile of temperature and electron density in various layers of the Earth's atmosphere (image source: Wikipedia)

higher-order terms ($\approx 0.1\%$) of the ionospheric delay, especially during the times of high solar activity (Hernandez-Pajares et al., 2007).

Although both the ionosphere and the troposphere have an influence on the propagation of electromagnetic signals travelling through them, for the subject of this thesis, the troposphere is of most relevance and importance. Figure 2.1 shows the troposphere as the lowest layer of the Earth's neutral atmosphere which contains approximately 80% of the total mass of the atmosphere and most of the weather phenomena take place in this layer. Furthermore, most of the atmospheric water vapour is concentrated in the troposphere. The temperature decrease rate with altitude is almost constant

($\approx 6.5\ ^{o}$C/km) in the troposphere. The thickness of the troposphere varies from 17 km at mid-latitudes to 9 km in the polar regions.

2.2 Weather and Climate

Weather is defined as the state of the atmosphere at a particular location and instant of time. It is characterized as a combination of weather elements (e.g. temperature, pressure, humidity, wind speed, wind direction) and weather phenomena (e.g. fog, thunderstorms, tornadoes and hail) over short time spans ranging from hours to days (Taylor 2005). Climate, on the other hand, is defined as the average of weather conditions for a particular location computed over long time spans ranging from months to centuries. Climate is characterized using the various atmospheric variables (Taylor 2005). Some important definitions related to climate are given in the following text.

A climate normal is a reference point which is used to compare the current climatological conditions with those from the past as well as to predict the future climate. According to the standards of the World Meteorological Organization (WMO), a climate normal is computed by averaging the atmospheric variables (e.g. temperature, precipitation, etc.) over a 30-year period. WMO requires its member countries to compute the climate normals for their geographical regions every 30 years with decadal updates. As of today, the most recent global WMO climate normal has been computed for the period of 1961-1990.

The choice of 30-year long time interval for the computation of climate normals is based on the fact that this interval is sufficiently long to filter out various short-term interannual fluctuations and anomalies in the climate (such as those caused by the El-Nino Southern Oscillation (Taylor 2005)), but on the other hand, it is also sufficiently short so that it could be used to reflect longer term (e.g. centuries) changes and trends in the climate (Arguez and Vose 2011).

The term climate change refers to the long-term (many decades) continuous change (increase or decrease) in the average of the weather conditions (i.e. climate normals) globally or for a particular location. Climate change

is a slow and gradual process and could occur as a change in magnitude of an atmospheric variable (e.g. temperature) and/or a change in the intensity and frequency of weather events like heavy precipitation, etc.

The term climate variability refers to the fluctuation of the climate around the average of the weather conditions (i.e. climate normals) globally or for a particular location. Climate variability is measured on various temporal scales including annual, seasonal, monthly and daily scales.

The Intergovernmental Panel on Climate Change (IPCC) reports on the statistical significance of the evidence of various changes in the climate available from the observations of the Earths atmosphere and surface. According to the Fifth Assessment Report (AR5) of IPCC, there is a 66-100% probability that the number of heavy precipitation events (e.g. the events above the 95th percentile of intensity) over land has increased in more regions worldwide than it has decreased since 1950. The significance of the trends in the number of extreme weather events has regional, sub-regional and/or seasonal variations. However, the level of confidence for the obtained trends for North America and Europe is the highest which reports a 66-100% probability of an increase in either the frequency or the intensity of extreme weather events in these regions (Hartmann et al. 2013).

2.3 Atmospheric Water Vapour

The gaseous form of water present in the Earth's atmosphere is known as water vapour and plays a major role in short-term weather phenomena as well as long-term climate change. For example, the intensity of the precipitation is associated with the water vapour supply and hence it is important to document and understand the distribution and dynamics of atmospheric water vapour and their relationship with precipitation extremes. Kunkel et al. (2013) observed significant increases in extreme precipitation event-related atmospheric water vapour, and suggested that this increase could have been the cause of intensified precipitation events. However, they note that dynamical factors also have a strong influence on the intensity of precipitation events, but to be more certain of the magnitude of the influences of both of these factors, the role of water vapour should be more thoroughly

explored.

As compared to the other constituents of the lower atmosphere (dry air gases), water vapour has a very high heat capacity which makes it a strong absorber of infrared radiation (directly from Sun as well as reflected from the Earth's surface) and therefore it holds a significant impact on the Earth's heat budget. In the Earth's hydrological cycle, evaporation from the land and oceans continuously forms water vapour in the atmosphere whereas precipitation continuously removes the condensed water vapor in order to maintain a global balance. Almost 90% of the total atmospheric water vapour is found in the troposphere and it has a very high temporal and spatial variability when compared to the other constituents which are almost chemically inactive.

2.3.1 Integrated Water Vapour

Atmospheric water vapour can be measured in terms of integrated water vapour (IWV) which is the total quantity of atmospheric water vapour (in units of kg/m^2) present in a vertical column of the atmosphere. Alternatively, it can also be meausered in terms of total precipitable water (TPW) which is the height (in mm) of an atmospheric column of precipitable water. Considering the density of liquid water, the IWV is equivalent to TPW i.e.

$$1\ kg/m^2\ IWV = 1\ mm\ TPW \tag{2.1}$$

2.3.2 Distribution and Variability of Atmospheric Water Vapour

Water vapour contributes up to 4% of the total volume of the atmosphere (depending on the geographical region) and its concentration varies globally with space and time. Figures 2.2 and 2.3 depict, as an example, the global distribution of the atmospheric water vapour concentration for the months of January and July, respectively, in 2003 in terms of the monthly mean of the TPW obtained from NASA's Atmospheric Infrared Sounder (AIRS) (Pidwirny 2013).

It can be seen from Figures 2.2 and 2.3 that for both months, water vapour has the highest concentrations, i.e. 50-60 mm, near the equator. The lowest

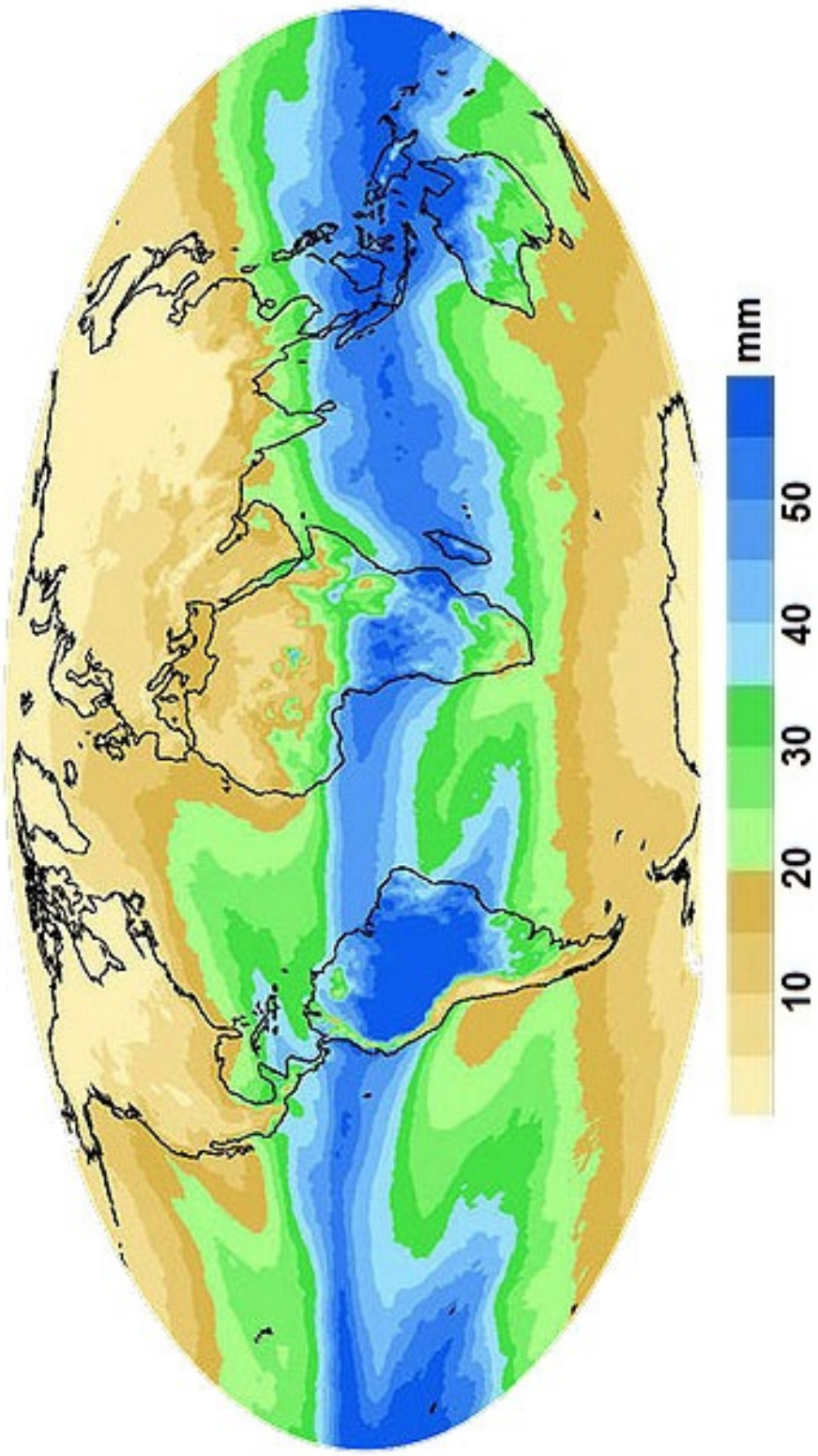

Figure 2.2: Global distribution of water vapour for January 2003 from the Earth's surface to the top of the atmosphere as measured from AIRS in millimeters of precipitable water (Pidwirny, 2013)

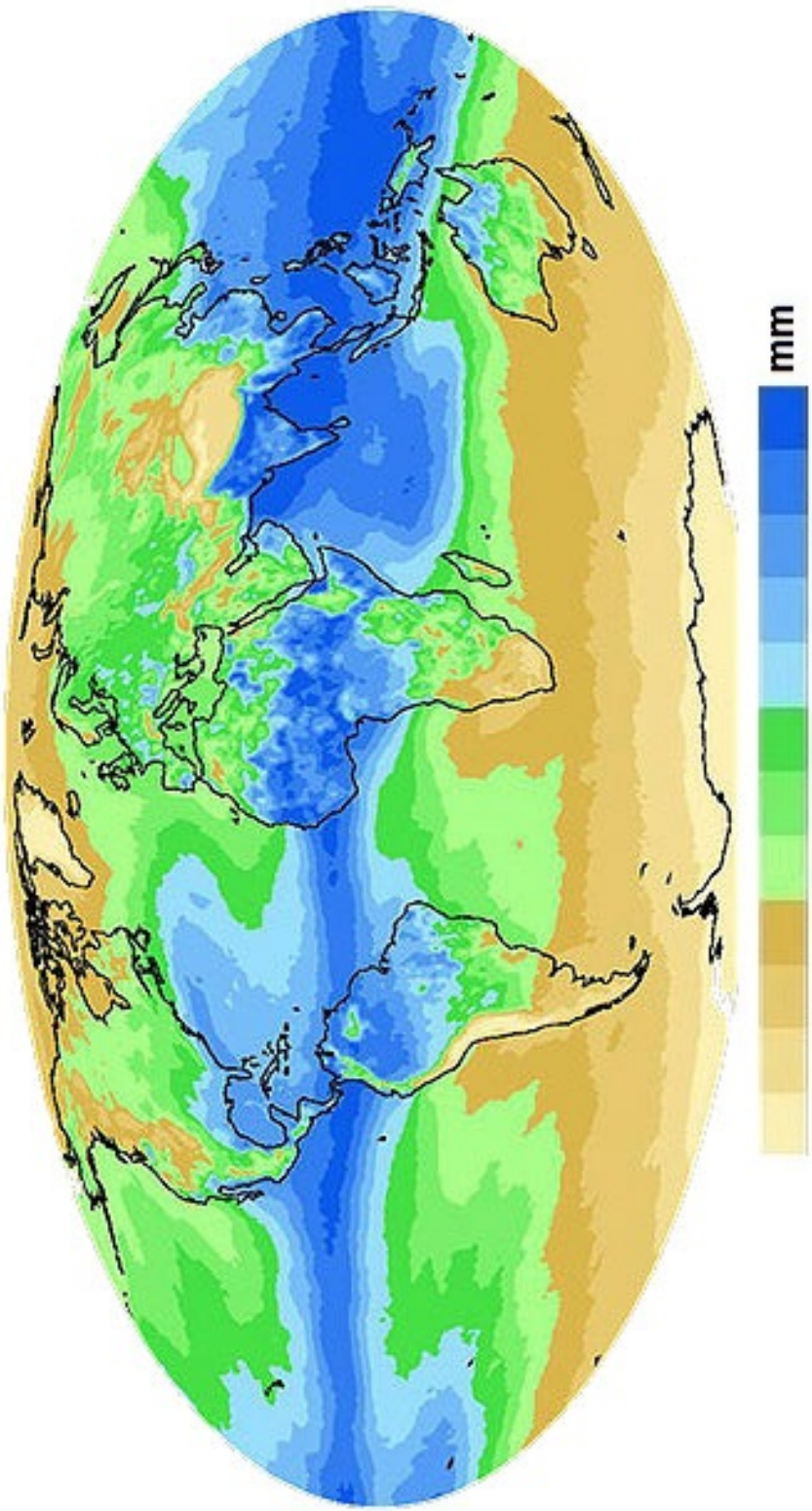

Figure 2.3: Global distribution of water vapour for July 2003 from the Earth's surface to the top of the atmosphere as measured from AIRS in millimeters of precipitable water (Pidwirny, 2013)

concentration of water vapour, i.e. 0-10 mm, on the other hand, can be seen in the polar regions.

2.3.3 Measurement Techniques and Instruments

As of today, there exist many techniques and instruments which are used to measure atmospheric water vapour. These include in situ (e.g. radiosonde), ground-based (e.g. ground-based GNSS) and satellite-based (e.g. GNSS radio occultation) techniques and instruments. Some of the measurement techniques make use of the observed absorption and re-emission of energy from water vapour in order to infer the quantity of IWV whereas some estimate the IWV using the observed propagation delay in radio signals caused by the refractivity of the atmosphere (Ning 2012). However, in this section, only those techniques and instruments have been introduced which have been used to measure the ZTD and/or IWV during this research.

Ground-based GNSS

Ground-based GNSS observations provide an opportunity to infer the amount of IWV over the location of ground-based GNSS receiver by estimating the propagation delay (ZTD) in the received signal on the way from a satellite to the ground-based receiver. The carrier signals are the primary observables for high-precision GNSS positioning and the ZTD can be estimated from the carrier phase observable (Φ). This observable can be written as

$$\Phi = \rho + c(\tau_{sat} - \tau_{rcv}) - \Delta L_{iono} + \Delta L_{tropo} + \lambda N + \varepsilon_{\Phi} \tag{2.2}$$

where ρ is the geometric distance between the satellite and the receiver antenna in meters, c is the speed of light in vacuum in m/s, $\tau_{sat,rcv}$ are the clock biases between satellite and receiver in seconds, ΔL_{iono} is the ionospheric delay in meters, ΔL_{tropo} is the tropospheric delay or the ZTD in meters, λ is the wavelength in meters, N is the integer phase ambiguity term (not to be confused with the refractivity N in Equation 2.3) and ε_{Φ} are the unmodeled phase measurement errors in meters. The carrier phase observable is the phase of the received carrier at the time of transmission with respect to the phase generated by the local oscillator in the GNSS receiver at the time of reception. The difference between the received carrier and the receiver generated carrier is called the carrier beat phase. The

problem is that the GNSS receiver cannot distinguish one cycle of a carrier from another. In practice, the receiver measures the fractional phase, and keeps track of changes to the phase. Therefore, the initial phase remains ambiguous by an integer number of cycles N.

GNSS observations from a collection of ground-based receivers, in combination with auxiliary information (satellite and receiver positions, corrections computed from models of geophysical processes) are processed using various GNSS data processing software packages to obtain the ZTD estimates. Once the ZTD is obtained, it can be converted into IWV using the relations described in Section 2.3.4. One of the salient features of ground-based GNSS as a measurement technique is its all-weather operational capability.

Radiosonde

A radiosonde is a collection of several meteorological sensors (e.g. temperature, humidity, wind sensors, etc.) attached to a weather balloon which can transmit the observed meteorological data to a ground station using a radio link. To observe the vertical profile of the atmosphere, radiosondes are launched two to four times a day. In order to estimate the IWV from radiosonde observations, the vertical profile of the absolute humidity can be integrated from the top most observation point to the ground. Radiosondes are one of the most widely used meteorological instruments and radiosonde observations are available globally for more than five decades. However, the evolution of sensor technology has lead to sensor changes in the radiosondes over the passage of time and this has compromised the long term stability of radiosonde measurements for use in climate research (Titchner et al. 2009). Furthermore, radiosonde measurements have been found to have different bias characteristics during different points in time e.g. day and night (Wang and Zhang 2009). The radiosonde data used for this research has been described in Chapter 4.

Climate Reanalysis Datasets

Climate reanalysis datasets provide a description of climate on various spatial scales in the form of long-term records of various atmospheric param-

eters. These datasets are computed using numerical forecast models while providing historical atmospheric observations as an input to the model in order to improve the model's knowledge of the initial state of the atmosphere. The word 'reanalysis' refers to the fact that these datasets are generated to describe the state of the climate for time periods in the past. The parameters provided by the climate reanalysis datasets include (but are not limited to) precipitation, temperature, soil moisture, and pressure. Examples of climate reanalysis datasets include the ECMWF ERA-Interim (Dee et al. 2011) and NCEP/NCAR Reanalysis 1 (Kalnay et al. 1996). The reanalysis dataset used for this research has been described in Chapter 4.

2.3.4 Propagation Delay in the Troposphere

As it has been mentioned in the previous section that various measurement instruments and techniques utilize the propagation delay experienced by radio signals to estimate the atmospheric water vapour, this subsection explains the relation between the propagation of the radio signal and the composition of the troposphere.

The tropospheric propagation delay in the signal is dependent on the refractivity N of the troposphere which can be expressed as (Thayer, 1974):

$$N = k_1 \frac{P_d}{T} Z_d^{-1} + k_2 \frac{P_v}{T} Z_v^{-1} + k_3 \frac{P_v}{T^2} Z_v^{-1} \tag{2.3}$$

where $P_{d,v}$ are the partial pressures of dry and wet air constituents in hPa, T is the temperature in K, $Z_{d,v}^{-1}$ are the inverse compressibility factors for dry air and water vapour and $k_{1,2,3}$ are experimentally determined coefficients in K/hPa. The path followed by the signal in the troposphere is assumed to be zenithal and therefore, the delay ΔL between a point at height h and infinity is

$$\Delta L = 10^{-6} \int_h^\infty N(h) dh \tag{2.4}$$

where ΔL is known as zenith total delay (ZTD) in mm and can be expressed as the sum of zenith hydrostatic delay (ΔL_h or ZHD) and zenith wet delay (ΔL_w or ZWD) i.e.

$$ZTD = \Delta L = \Delta L_h + \Delta L_w \tag{2.5}$$

ΔL_h can be approximated by using surface pressure and location values in the widely used Saastamoinen hydrostatic model (Saastamoinen, 1972) i.e.

$$ZHD = \Delta L_h = \frac{(2.2779 \pm 0.0024)P_S}{1 - 0.00266\cos(2\varphi) - 0.00028h} \tag{2.6}$$

where P_S is the surface pressure in hPa, φ is the latitude of the observing point in degrees and h is the height of the observing point in km above the ellipsoid.

Once the ZTD has been estimated by processing the observations, ZHD is computed using Equation 2.6, and the ZWD can be obtained from

$$ZWD = ZTD - ZHD \tag{2.7}$$

ZWD can then be combined with meteorological data i.e. pressure and temperature to convert it to IWV (Bevis et al., 1992, Bevis et al., 1994).

To convert the ZWD into IWV, the following relation can be used i.e.

$$IWV \approx \kappa \Delta L_w \tag{2.8}$$

where

$$\frac{1}{\kappa} = 10^{-6}(\frac{k_3}{T_m} + k_2')R_v \tag{2.9}$$

In Equation 2.9, R_v is the specific gas constant for water vapour and T_m is the mean temperature of the vertical column of air above the point of observation.

2.4 Tropospheric Mapping Functions

A ground-based GNSS receiver antenna can receive a signal from any elevation above the horizon and therefore, the tropospheric delay information needs to be mapped from a specific elevation into the zenith direction. For this purpose, "mapping functions" are used. A Mapping function defines the ratio of the tropospheric delay experienced at a certain elevation angle when compared to the one that would be experienced in the zenith direction. In order to take observations from satellites which are not in the zenith direction but are at a certain elevation with respect to the surface of Earth,

mapping functions are used to account for the variation in the delay in different directions. There are different mapping functions for the wet and hydrostatic parts of the atmosphere but for low elevation angles, the same mapping function can be used for both the wet and hydrostatic parts. A simple example of a mapping function is

$$m(\varepsilon) = \frac{1}{\sin \varepsilon} \tag{2.10}$$

where ε is the elevation angle. Herring (1992) proposed a continued fraction representation for mapping functions i.e.

$$m(\varepsilon) = \frac{1 + \frac{a}{1+\frac{b}{1+c}}}{\sin \varepsilon + \frac{a}{\sin \varepsilon + \frac{b}{\sin \varepsilon + c}}} \tag{2.11}$$

In the above form of a mapping function, the coefficients a, b and c depend on parameters like location of the station and the day of the year so that the seasonal variation within the troposphere is accounted for. The value of these coefficients can be derived from theoretical atmospheric models, climate reanalysis datasets or local measurements of pressure and temperature.

Niell Mapping Function

The Niell Mapping Function (NMF) (Niell 1996) was developed in 1996 with a purpose to calculate the ratios between the line of sight hydrostatic and wet atmospheric path delays to their corresponding delays in the zenith direction. This mapping function was developed to work for radio frequencies and for calculations down to an angle of 3 degrees in elevation. The hydrostatic part of NMF is represented in the continued fraction form (Equation 2.11) and the value of the coefficients is dependent on the day of year, latitude of the station and height of the station above mean sea level. The wet part of NMF depends only on the station latitude. NMF was the standard mapping function for space-geodetic techniques such as GNSS and VLBI until the advent of more advanced mapping functions such as GMF and VMF (discussed ahead).

Isobaric Mapping Function

The Isobaric Mapping Function (IMF) (Niell, 2001) is an improvement to the NMF and was proposed in 2001. This mapping function is based on numerical weather models and its data is provided on a grid. Comparisons have shown that the hydrostatic part of the IMF is an improvement on the NMF but the wet part does not have any significant improvement.

Vienna Mapping Function

The Vienna Mapping Function (VMF) (Boehm and Schuh, 2004) was developed in 2004. The VMF has the underlying principle of raytracing through the climate reanalysis dataset from the European Centre for Medium-Range Weather Forecasts (ERA-40) and is a further development of IMF. The VMF has been proved to be better than the Niell Mapping Function (NMF) e.g. its hydrostatic part is sensitive to short fluctuations unlike the NMF.

The Vienna Mapping Function 1 (VMF1) (Boehm et al., 2008) is an upgrade (in 2006) to the VMF in which, the b and c coefficients of the continued fraction hydrostatic part are recalculated using the data from the 40 years reanalysis data of the European Centre for Medium-Range Weather Forecasts (ECMWF ERA-40). Unlike the previous mapping functions, the coefficient c is dependent on the day of year in VMF1 and is not symmetric with respect to the equator. VMF and VMF1 are dependent on elevation angles but not the azimuth. An azimuth-dependent version of VMF which is called VMF-2 was determined by Boehm and Schuh (2004), however, VMF1 is the most accurate mapping function whose data is available for the whole history of GPS observations (Boehm et al 2006). The VMF forms part of the conventions of International Earth Rotation and Reference Systems Service (IERS) known as IERS 2010.

Traditionally, mapping functions are divided into a hydrostatic and a wet part. An alternate approach is the introduction of the "total Vienna mapping function" (VMF1-T) which uses the total refractivity instead of hydrostatic and wet components to map the total delays. In the total mapping function approach, the ZTD is divided into an a priori value of ZTD and a residual or correction of ZTD. In the classical approach of separat-

ing the mapping functions into hydrostatic and wet parts, the errors in the hydrostatic part cannot be compensated for completely by estimating the remaining wet part due to the significant difference between the hydrostatic and wet mapping functions. The advantage of the total mapping function approach is that the ZTD cannot be affected by a poor a priori ZHD. However, in the total mapping function approach, the ZTD is affected by bad a priori information about the wet part in the atmosphere from the numerical weather models. More details about the benefits and limitations of VMF1-T can be found in Boehm et al., (2006).

For use in real-time applications, a version of VMF1 called Forecast VMF1 (VMF1-FC) (Boehm et al., 2008) has also been developed by determining the coefficients from the forecast data from ECMWF so that data can be provided with a very short latency for use in real-time applications without significant loss of accuracy. However, the real-time software packages used in this study currently do not feature the VMF1 implementation and therefore VMF1 has not been used for the real-time processing during this study.

An alternate implementation of the VMF1 has been produced at the University of New Brunswick, Canada (UNB) and is known as UNB-VMF1 (Urquhart et al., 2014). There are only two differences between the standard VMF1 and the UNB-VMF1. The first difference is the use of a difference raytracing algorithm to compute the mapping function coefficients and the second difference is the use of a different NWP model as the source of atmospheric data. The raytracing algorithm used for UNB-VMF1 is described in Nievinski and Santos (2010) whereas the NWP model used as the data source is the Re-Analysis I dataset produced by the National Centers for Environmental Prediction (NCEP).

Global Mapping Function

The Global Mapping Function (GMF) (Boehm et al., 2006) was developed in 2006. The GMF is based on the global numerical weather model from ECMWF and its coefficients are calculated by expanding the VMF1 parameters into spherical harmonics on a global grid. The inputs to the GMF are the station coordinates and the day of year. Experiments have shown that GMF lacks short-term precision when compared to VMF1 but it sig-

nificantly reduces the height biases and annual errors of NMF. Table 2.1 summarizes the above discussion by listing the main characters of the above mentioned mapping functions.

As of today, GMF and VMF1 are widely employed. GMF follows the principles of NMF and is therefore simpler in the implementation and requires less computational time. The simplicity of implementation and requirement of less computing time make NMF and GMF very highly suitable for RT and NRT applications. VMF1, on the other hand, has a higher precision and demands high computational time and resources. Therefore, VMF1 is more suitable for post-processing applications.

Table 2.1: Summary of Mapping Functions

Models	Type	Technique	Spatial Resolution	Temporal Resolution	ϵ_{min} (°)	Input
NMF	Empirical	Derived from radiosonde launches	5 latitude bands	Annual	3	ϕ,H,DOY
GMF	Empirical	Spherical expansion to order and degree 9 of gridded VMF1 data	Degree/order 9	Annual	3	λ,ϕ,H,DOY
VMF1	Site values	Interpolated from local 0.25 x 0.25 grids derived from ECMWF data	A list of GNSS, VLBI, DORIS sites	Every 6 hours	3	λ,ϕ,H,DOY, ECMWF data
Gridded VMF1	Grid values	Derived from ECMWF data	2.5 x 2.0	Every 6 hours	3	λ,ϕ,H,DOY, ECMWF data

2.5 GNSS Data Processing

This section describes the GNSS data processing strategies used in this research.

2.5.1 Precise Point Positioning

Precise Point Positioning (PPP) is a strategy to obtain highly accurate (*cm* to *mm* level) position solutions using the observations from a single receiver (Zumberge et al., 1997). In this strategy, high precision satellite orbits and satellite clocks which are computed using a global network of ground-based GNSS stations, are used to apply the error correction to the observations in order to obtain precise coordinates and atmospheric parameters. Figure 2.4 shows the observation setup for PPP. It can be seen from Figure 2.4 that one single GNSS station is observing multiple satellites. PPP allows the sensing of the atmosphere in an 'absolute' sense as the PPP solutions refer to one single station in a global reference frame.

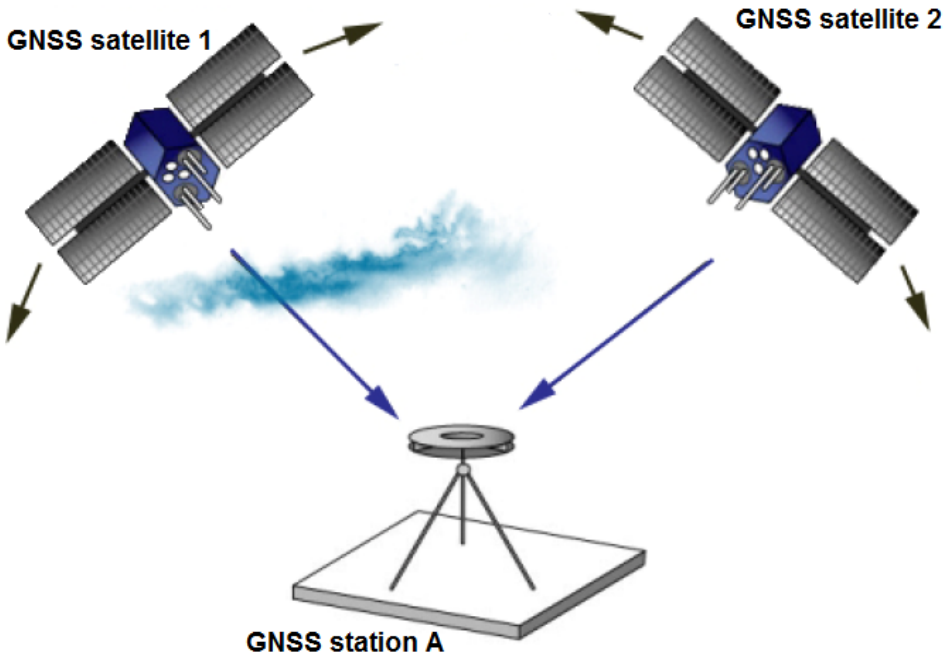

Figure 2.4: Observational setup for the PPP processing strategy

2.5.2 Double Differenced Positioning

Double Differenced Positioning (DDP) (Hofmann-Wellenhof et al., 2007) is a strategy of determination of positions by processing the differenced observations from a network of receivers. Specifically, the DDP observables are formed by differencing the observations from two GNSS receivers that are observing a similar pair of satellites. The DDP observation setup is shown in Figure 2.5. The atmospheric solutions obtained using DDP are 'relative' because of the differential observations between two stations and therefore long baselines between the stations are needed in order to sense the atmosphere in the absolute sense.

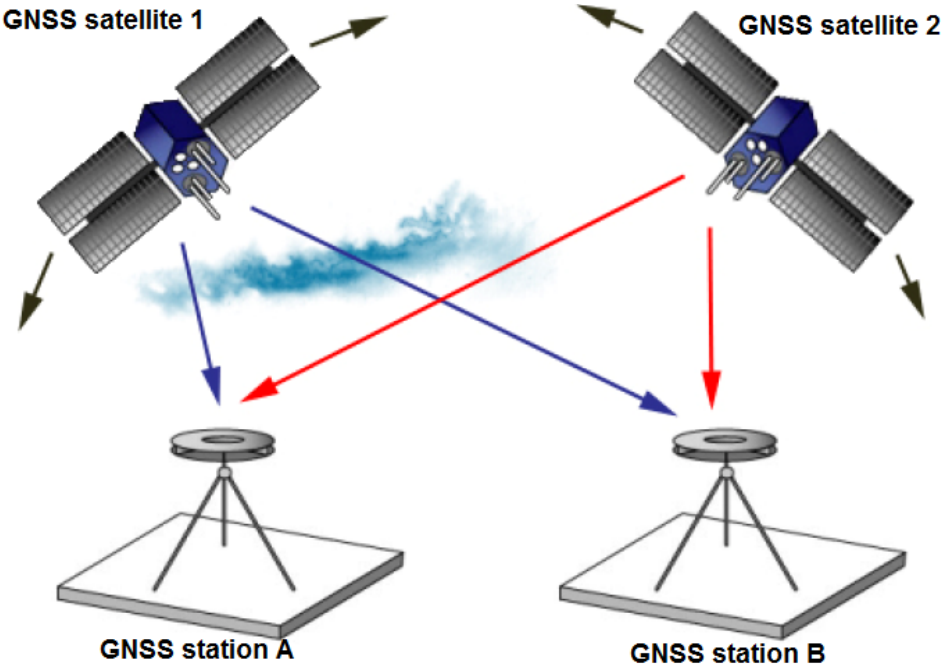

Figure 2.5: Observational setup for the DDP processing strategy

2.6 Numerical Weather Prediction

Numerical Weather Prediction (NWP) is a technique in which, a numerical model representing the physics and dynamics of the atmosphere is used to predict a latter state of the atmosphere using the initial state of the atmosphere. The initial state of the atmosphere is obtained by combining a

previous forecast ("First Guess" or "background") with the more recent atmospheric observations (e.g. GNSS-derived ZTD) obtained through various types of sensors. The process of combining the background with new observations is known as data assimilation and aims at improving the model state and bringing it closer to the observations (assuming that the observations reflect the reality). The step in which data assimilation is used to update the background is referred to as "analysis". Figure 2.6 shows a high-level flowchart of the NWP process.

The AROME 3D-VAR NWP model (Seity et al., 2011) is a limited area model derived from the global NWP model ARPEGE (Courtier et al., 1991) and is operational at Météo-France since December 2008.

The 3D-VAR data assimilation system used for AROME was developed by adapting the 6-hourly 3D-VAR data assimilation system developed for the limited area NWP model ALADIN (Bubnova et al. 1995), to the smaller scales of AROME with a 3-hourly Rapid Update Cycle (RUC)(Brousseau et al., 2011).

The AROME domain (shown in Figure 2.7) covers a significant part of Western Europe. The horizontal resolution of the model is 2.5 km on a Lambert projection with its centre at (46.4^{o}N, 2.2^{o}E) with 750 and 720 physical grid points in the eastwest and northsouth directions, respectively. The domain is vertically divided into 60 layers. The centre of the uppermost layer is located at the 1 hPa pressure level. The height of the lowest layer centre is about 10 m above the ground.

The configuration of the AROME 3D-VAR NWP model used in this research was adopted for operational applications in April 2010. More details about AROME can be found in Chapter 3.

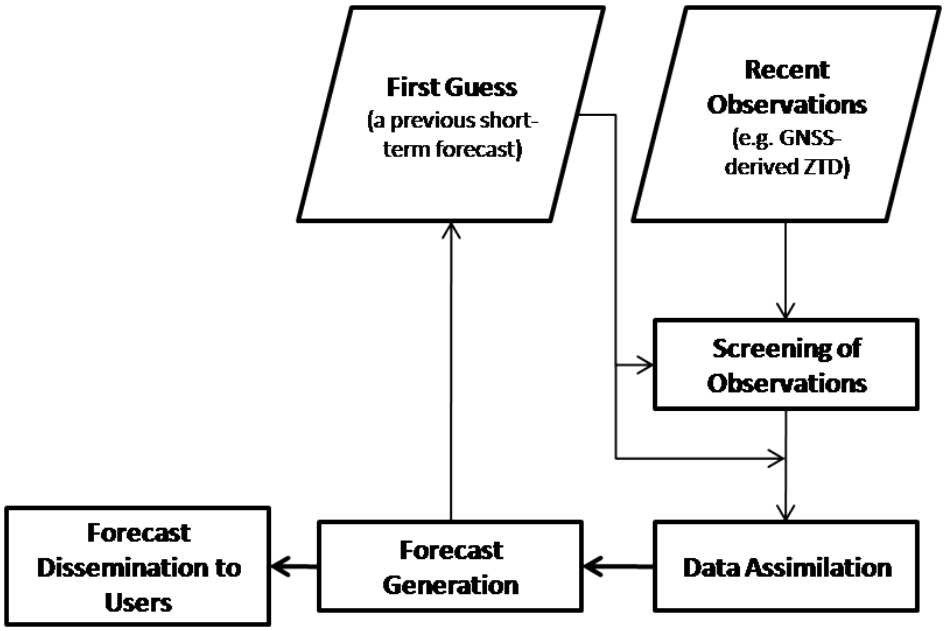

Figure 2.6: Flowchart of the NWP process

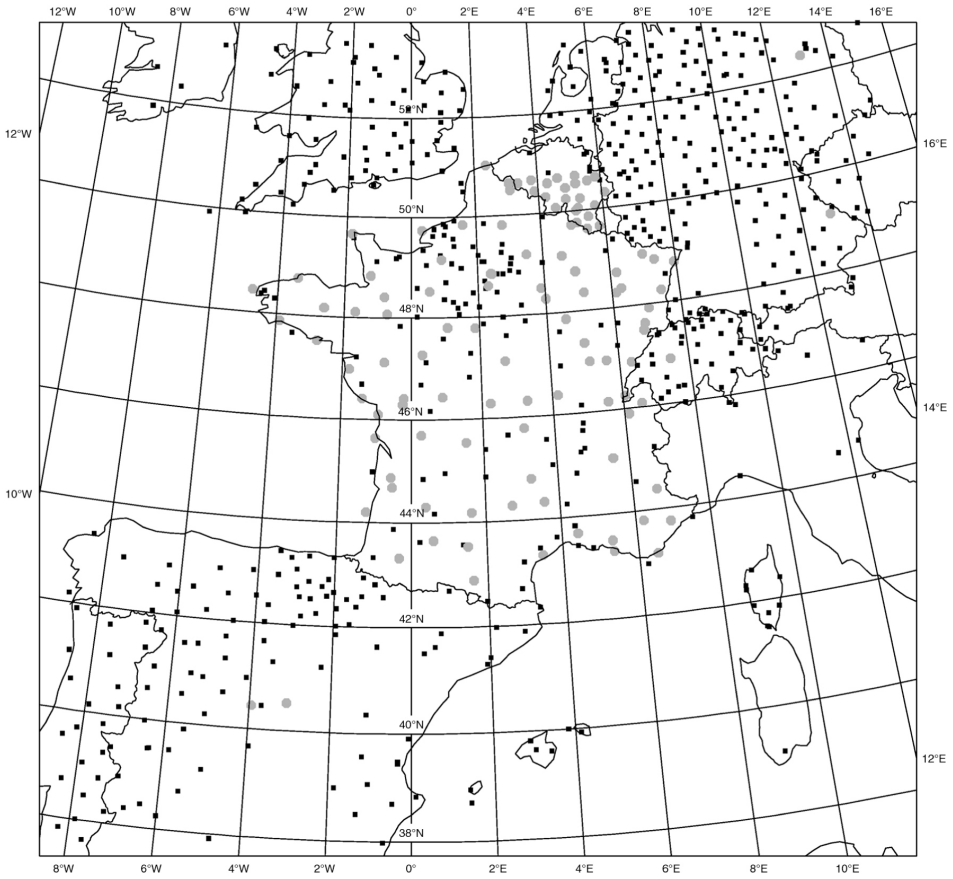

Figure 2.7: Map of the domain of the AROME model with the GPS stations selected for this study

Chapter 3

Methodology

Measure what is measurable, and make measurable what is not so.

Galileo Galilei

This chapter describes the methodology that has been used to achieve the research objectives of this thesis. Firstly, it describes the RT, NRT and PP GNSS data processing systems. Secondly, it describes the experiments that have been performed using these systems to answer the various research questions along with the configurations and experimental setup of these systems.

3.1 The GNSS Data Processing Systems

This section describes the operational structure of the various GNSS data processing systems used for this research.

3.1.1 The RT GNSS Data Processing Systems

The real-time processing for a selection of GNSS stations and time periods was simultaneously performed using the BKG Ntrip Client (BNC), the Precise Point Positioning with Integer and Zero-difference Ambiguity Resolution Demonstrator (PPP-Wizard), and the Tefnut application from the G-Nut software library.

The BNC software, developed by the Bundesamt für Kartographie und Geodäsie (BKG) (Weber and Mervart 2012), is capable of performing PPP in RT (RT-PPP). For this study, version 2.7 of the BNC software has been used to perform RT-PPP using RT streams of code plus phase observations, the broadcast ephemeris and RT correction streams for satellite orbits and clocks applied during the processing in BNC. Along with the precise position estimates, the ZTD estimates can also be obtained as one of the outputs. The component of BNC which performs PPP is called PPP Client and its operational setup (inputs and outputs) is shown in Figure 3.1. For this study, a sigma value, selected by experimenting, of $1x10^{-5}$ m/s was used to describe

the expected variation of the ZTD as estimated by BNC2.7. The recent study by Yuan et al. (2014) is also based on this software package, however, they have modified it to implement some precise bias models such as ocean tide loading, receiver antenna PCV and the computation of hydrostatic and wet mapping functions from the Global Pressure and Temperature 2 (GPT2) model (Lagler et al. 2013). The implementation of these models was beyond the scope of this thesis.

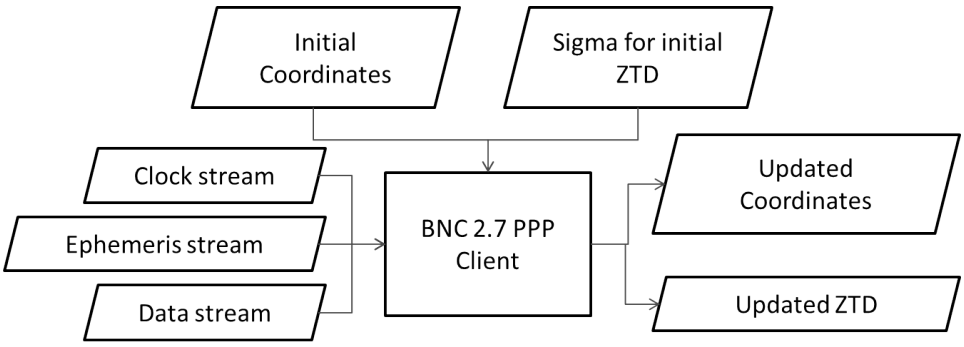

Figure 3.1: Flowchart showing ZTD estimation based on BNC 2.7 PPP Client

To promote their ambiguity fixing strategy, CNES developed the PPP-Wizard and started to produce a RT product containing further corrections for integer ambiguity resolution which can be used to fix ambiguities in RT-PPP mode (Laurichesse 2011). However, similar to BNC2.7, the PPP-Wizard was not developed with the particular application of RT GNSS meteorology in mind. Figure 3.2 shows the operational setup (inputs and outputs) of the PPP-Wizard for ZTD estimation.

Figure 3.3 shows the experimental setup of the RT processing at UL. The BKG Professional Ntrip Caster software (`http://www.alberding.eu/en/monitoringBKG.html`) was used to relay the RT data and product streams to the three processing engines i.e. BNC2.7 and the two versions of the PPP-Wizard in parallel.

The G-Nut software library (Václavovic et al. 2013) has been developed at the Geodetic Observatory Pecny (GOP) since 2011 in order to support the development of high-accuracy GNSS analysis. Several end-user applications

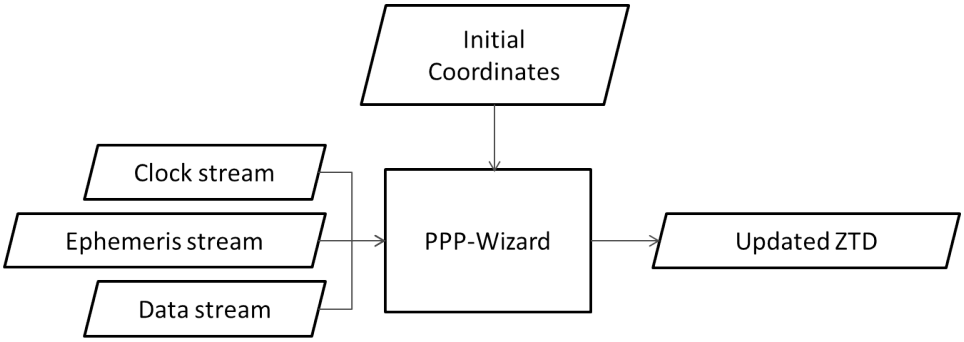

Figure 3.2: Flowchart showing ZTD estimation based on PPP-Wizard

have been derived for meteorology and climatology (Tefnut), geodesy and seismology (Geb) and GNSS quality checking (Anubis). In this study, the G-Nut/Tefnut software has been used which is capable of estimating GNSS tropospheric parameters in RT, NRT and post-processing modes (Douša and Václavovic 2014).

All the above mentioned software packages use a Kalman filter (Kalman 1960). The configuration and characteristics of the software packages used in this study are shown in Table 3.1. For the BNC2.7 and PPP-Wizard solutions, the a-priori coordinates of the stations were computed by a 20-day average of coordinates obtained using PPP with the Bernese GPS Software 5.0 (BSW50) (Dach et al. 2007). G-Nut/Tefnut does not need a-priori coordinates; however, if precise station coordinates are available, they can be introduced into the processing as a-priori values. In this campaign, G-Nut/Tefnut was used without introducing a-priori coordinates. During the RT data processing, BNC2.7 computed the receiver coordinates (unconstrained) in every epoch whereas the version of PPP-Wizard used for this study did not estimate the receiver coordinates, in order to reduce the number of unknown parameters. Hence in the PPP-Wizard solution, the coordinates were fixed to the values provided a-priori and the ZTD was estimated every 5 seconds. The G-Nut/Tefnut software applied simultaneous coordinate and ZTD estimations. The former were tightly constrained to remain stable over time while the latter were constrained loosely to optimally balance between stable and reliable tropospheric parameter estimates.

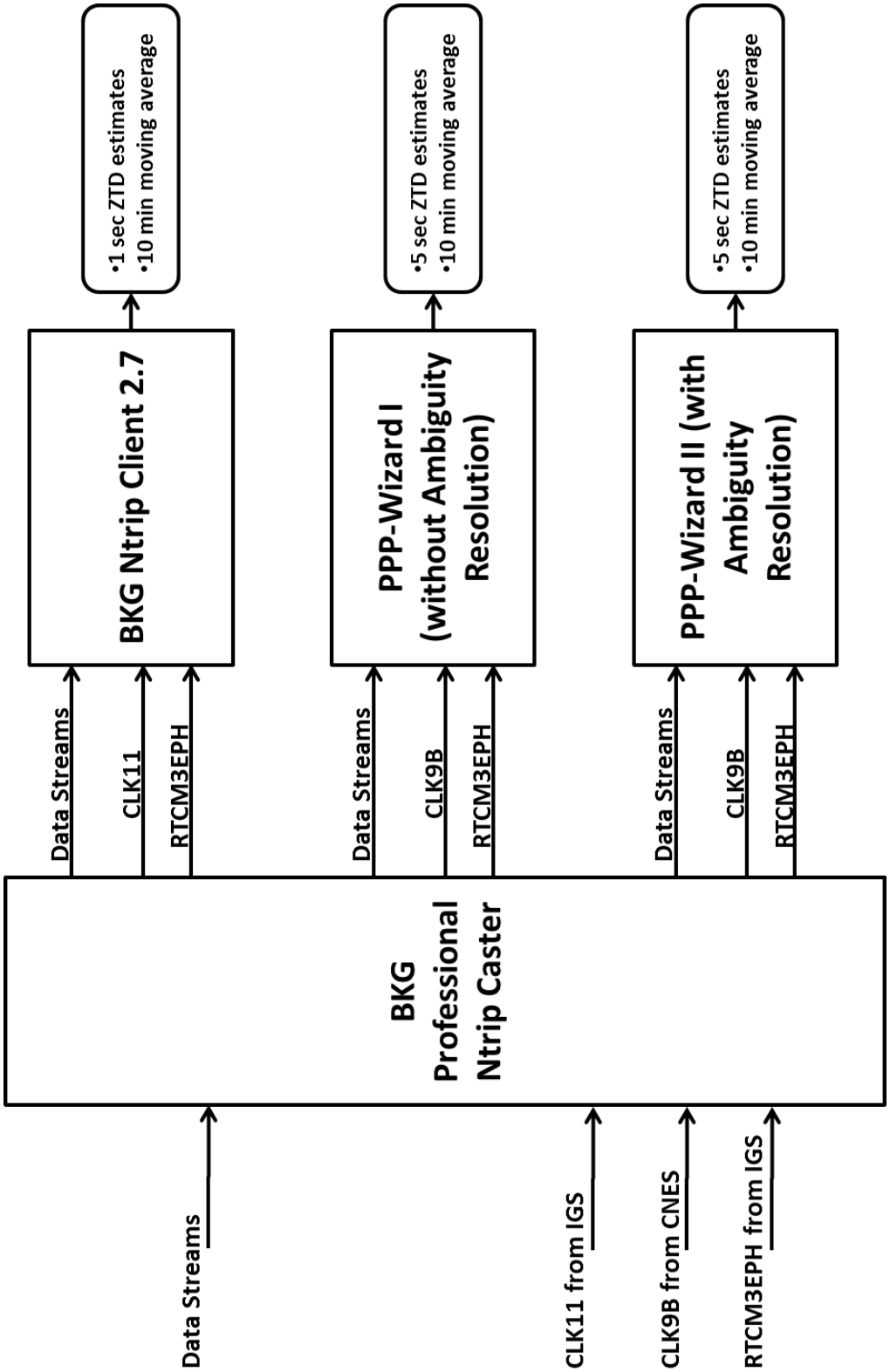

Figure 3.3: The experimental setup of the RT processing systems at UL

Table 3.1: Configuration of the software packages used in this study

Software:	BNC2.7	PPP-Wizard	G-Nut/Tefnut
Update Cycle	Real-time	Real-time	Real-time
Output Interval	1 second	5 seconds	5 seconds
GNSS Used	GPS	GPS	GPS
Strategy	PPP	PPP	PPP
A-priori ZHD Model	Saastamoinen	Constant (2.37 m)	Saastamoinen
Troposphere Mapping Function	1/cos(z)	GPS STANAG (Chaos coefficients)	GMF
Receiver PCV Correction	No	No	Elevation dependent only
Receiver PCO Correction	Yes	No	Yes
Satellite PCV Correction	No	Yes	Yes
Satellite PCO Correction	No[1]	No[1]	No[1]
Coordinates Computed	Yes	No	Yes
Ocean Tide Loading Correction	No	No	No
Input Raw Data Format	RTCM-3	RTCM-3	RTCM-3
Input Orbit/Clock Correction Format	RTCM-SSR	RTCM-SSR	RTCM-SSR
Input Broadcast Ephemeris Format	RTCM-SSR	RTCM-SSR	RTCM-SSR
Integer Ambiguity Resolution Possible?	No	Yes	No

[a]In the correction streams used, the satellites position refers to the ionosphere free phase center of its antenna and therefore the satellite antenna PCO correction is not necessary.

The convergence time of the RT-PPP solutions (coordinates and ZTD) is generally between 20 to 60 minutes depending among others on the quality of the station data and satellite constellation if no precise a-priori coordinates are provided. However, as mentioned above, for PPP-Wizard and BNC2.7, the a-priori coordinates were provided and hence the convergence time was not significant. For G-Nut/Tefnut, the results were filtered to include only the epochs after the solutions have converged.

The software packages BNC2.7 and PPP-Wizard are meant for RT and kinematic applications and therefore do not employ the most precise bias models, e.g. receiver antenna PCV corrections, ocean tide loading and higher-order ionospheric corrections. However, the G-Nut/Tefnut is meant for tropospheric applications but it is still undergoing some developments and lacks some precise bias models such as ocean tide loading.

3.1.2 The NRT GNSS Data Processing Systems

The hourly NRT GNSS data processing system has been obtained from the University of Nottingham (Orliac et al. 2005, Orliac 2009) and adapted for use in Luxembourg and the Greater Region. It is implemented as a systematic combination of various scripts and modules written using the Perl (`http://www.perl.org/`) and Python (`http://www.python.org/`) programming languages which are executed with hourly and daily intervals. Furthermore, Extensible Markup Language (XML) (`http://www.w3.org/TR/REC-xml/`) has been used to define the data structures to store the required information (station metadata and configuration parameters) for the data processing, and various databases related to the processing system are updated using MySQL (`http://www.mysql.com/`). The processing engine used in the system is the Bernese GPS Software version 5.0 (BSW5.0) (Dach et al, 2007, 2009). Using the complete setup, the hourly NRT processing system processes a network of ground-based GNSS stations every hour using the DDP processing strategy. The processed NRT network is a Europe-wide network with densification over Luxembourg and the Greater Region. The network used by the hourly NRT processing system is described in the next chapter (Section 4.2.1). In addition to the hourly NRT processing system, a sub-hourly NRT processing system with a similar operational structure and an update cycle of 15 minutes was also implemented using BSW5.0 and

was used to process 15-minute RINEX files created from RT streams. However, due to the fact that the hourly NRT results are currently sufficient for NWP applications, the sub-hourly system currently does not contribute to any meteorological activities and therefore it has not been considered for assessment in this research.

A high level flow chart depicting the operational structure of the hourly and sub-hourly NRT processing systems is shown in Figure 3.4. The overall operation of these systems is divided into four parts i.e. database management, data and products handling, processing and archiving. At the beginning of each session, the database management part is executed in which the databases containing information about available and required hourly (HD in Figure 3.4) and sub-hourly (SD in Figure 3.4) data, available and required products (OEDC, OEDCSH in Figure 3.4), and available and required meteorological data (MET in Figure 3.4) are maintained. The data and products handling part then downloads the required data and products onto the local server. After the data and products handling, the processing part is commenced which processes the downloaded raw data with BSW5.0 and converts the obtained ZTD to IWV. Finally, the archive part stores the raw data, products and processing results on the local server in addition to copying the final results to the server of E-GVAP.

The hourly NRT processing system is named as iGNSS (Orliac et al. 2005, Orliac 2009). Figure 3.5 shows the flowchart of the hourly processing cycle of iGNSS, providing the names of scripts (in the shaded region) that are executed for various tasks, whereas Table 3.2 lists the scripts and modules that are executed on a daily basis or at other time intervals. The Perl scripts in the iGNSS make use of functions defined in the various Perl modules written for iGNSS. Appendix C provides a brief description of the iGNSS scripts and modules.

As mentioned earlier, iGNSS uses the DDP processing strategy to produce hourly solutions using BSW5.0. However, to compute the a-priori coordinates of the stations in the network, PPP processing is conducted for all the stations in the network once a day and a-priori coordinates are computed as a running average of the station coordinates of the last 20

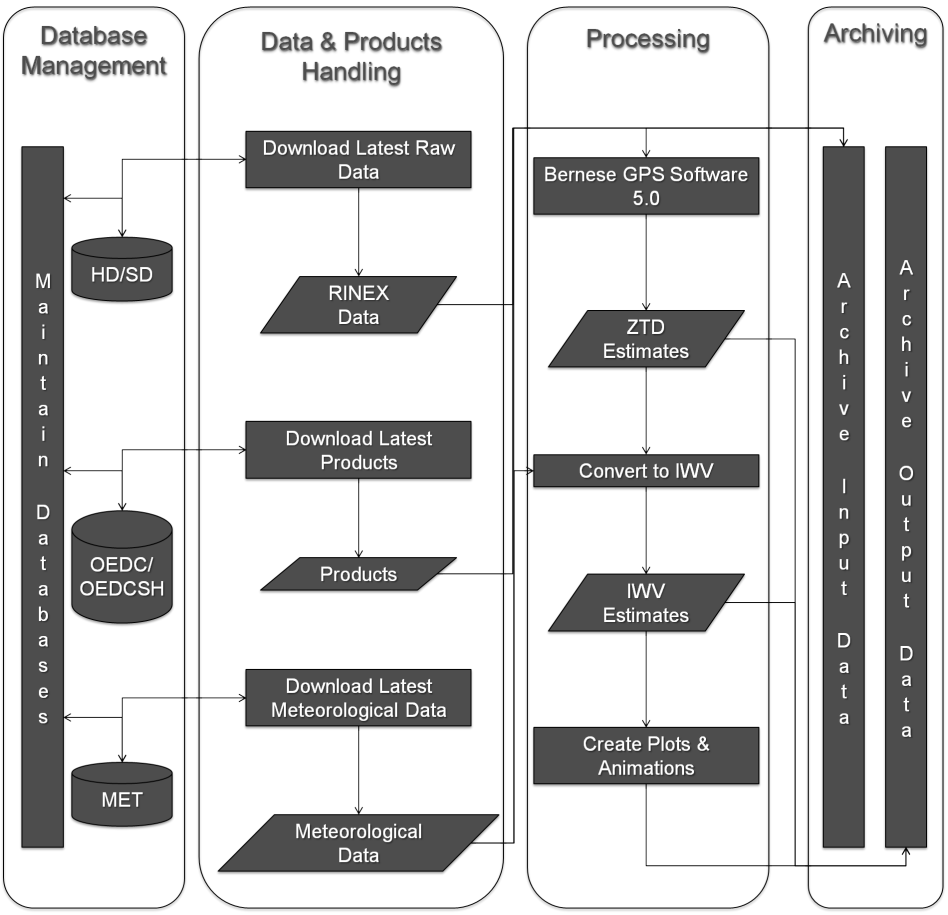

Figure 3.4: Operational structure of the NRT processing systems at UL

days. Figure 3.6 shows the flow chart of the BSW5.0 based PPP processing in iGNSS and shows the order in which the various sub-programs in BSW5.0 are executed during this processing. Similarly, Figure 3.7 shows the flow chart and BSW5.0 sub-programs execution sequence for the DDP processing which takes place in iGNSS. For the description of the BSW5.0 sub-programs mentioned in Figures 3.6 and 3.7, the reader is referred to the Bernese GPS Software 5.0 user manual (Dach et al., 2007).

The results from iGNSS are routinely provided to E-GVAP as test solution UL01. Based on the E-GVAP solution name, iGNSS will be referred to as UL01 in the following text. The processing characteristics of UL01 are shown

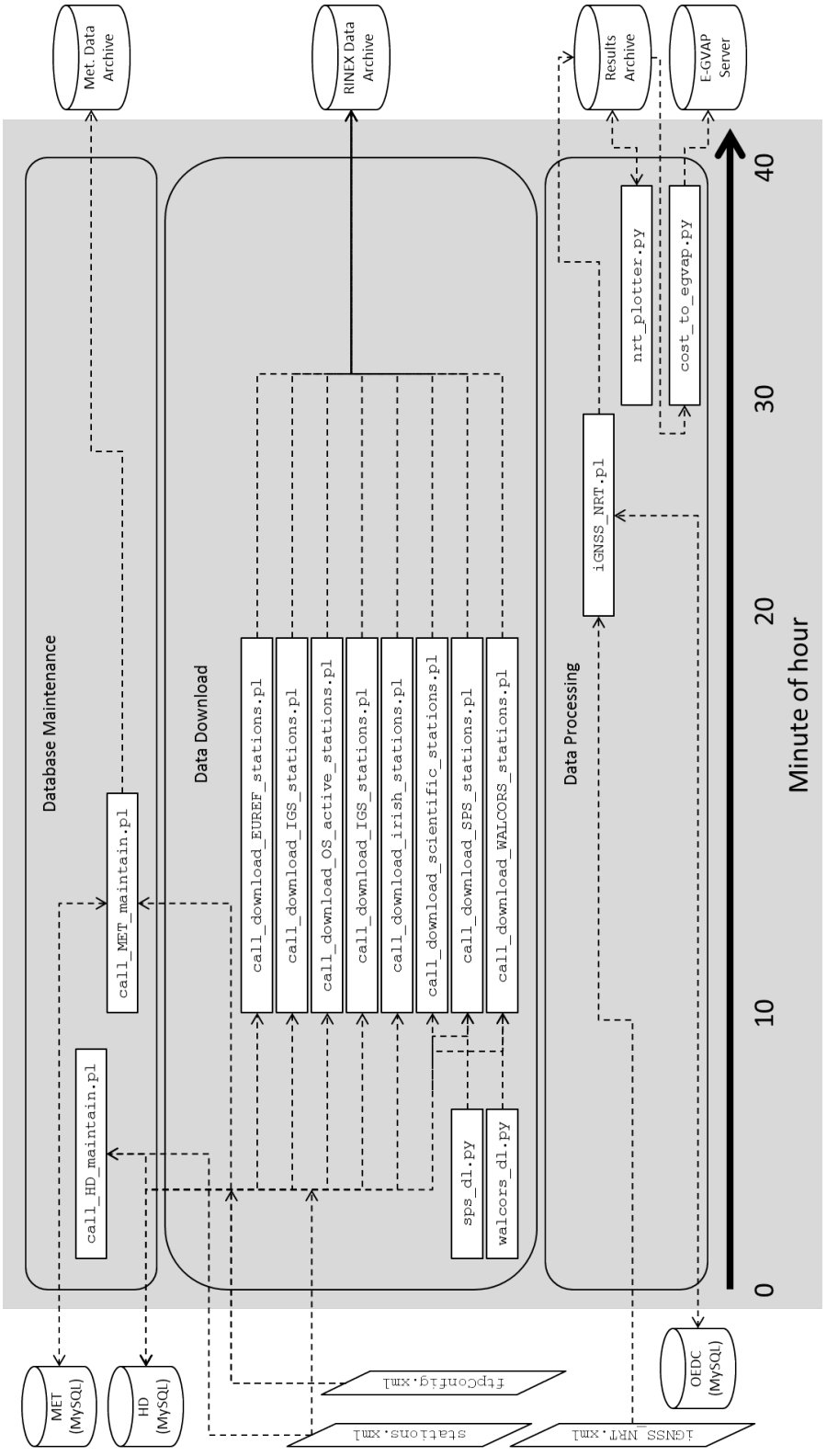

Figure 3.5: iGNSS Hourly Scripts

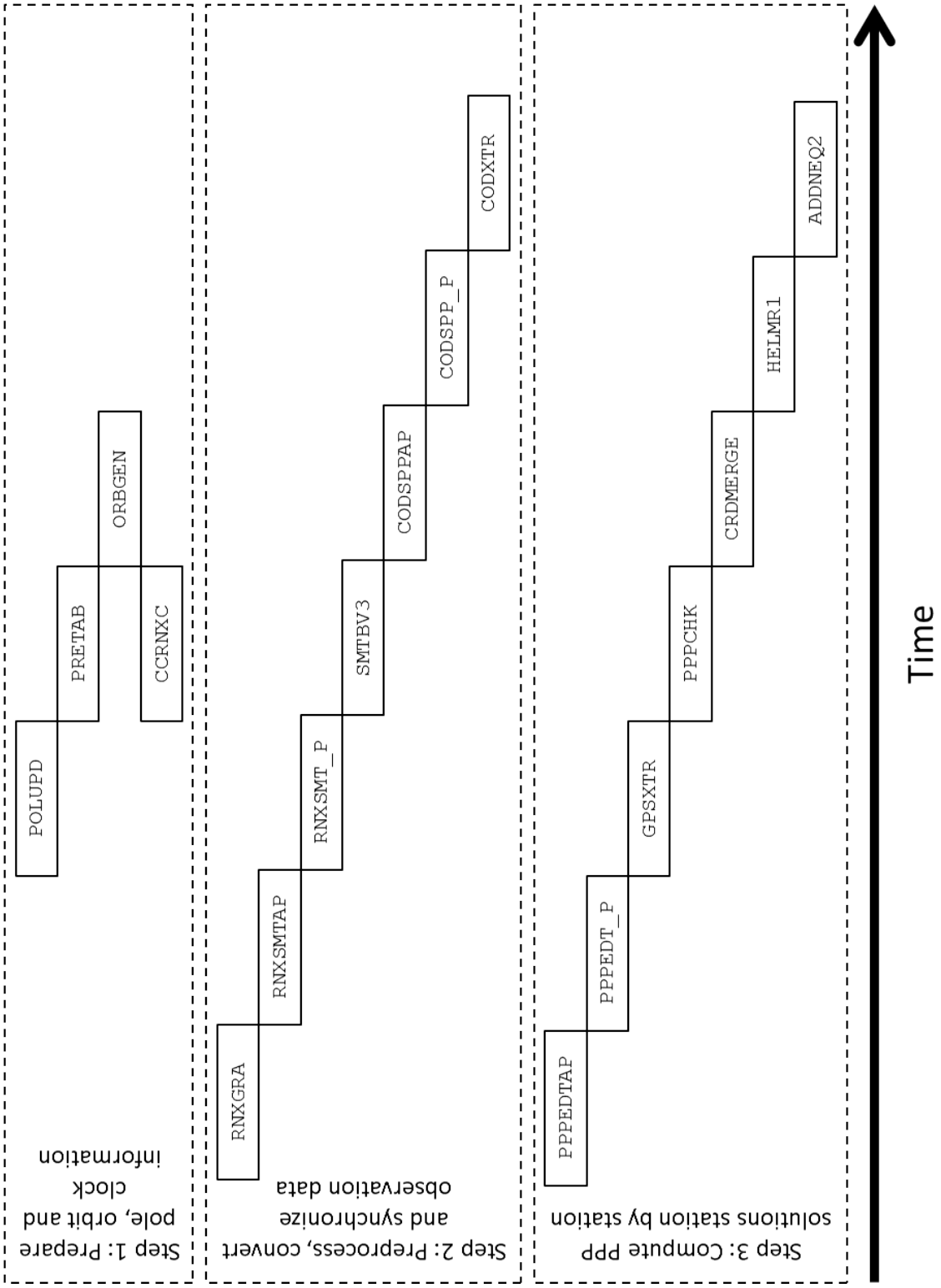

Figure 3.6: Flowchart of PPP processing in iGNSS

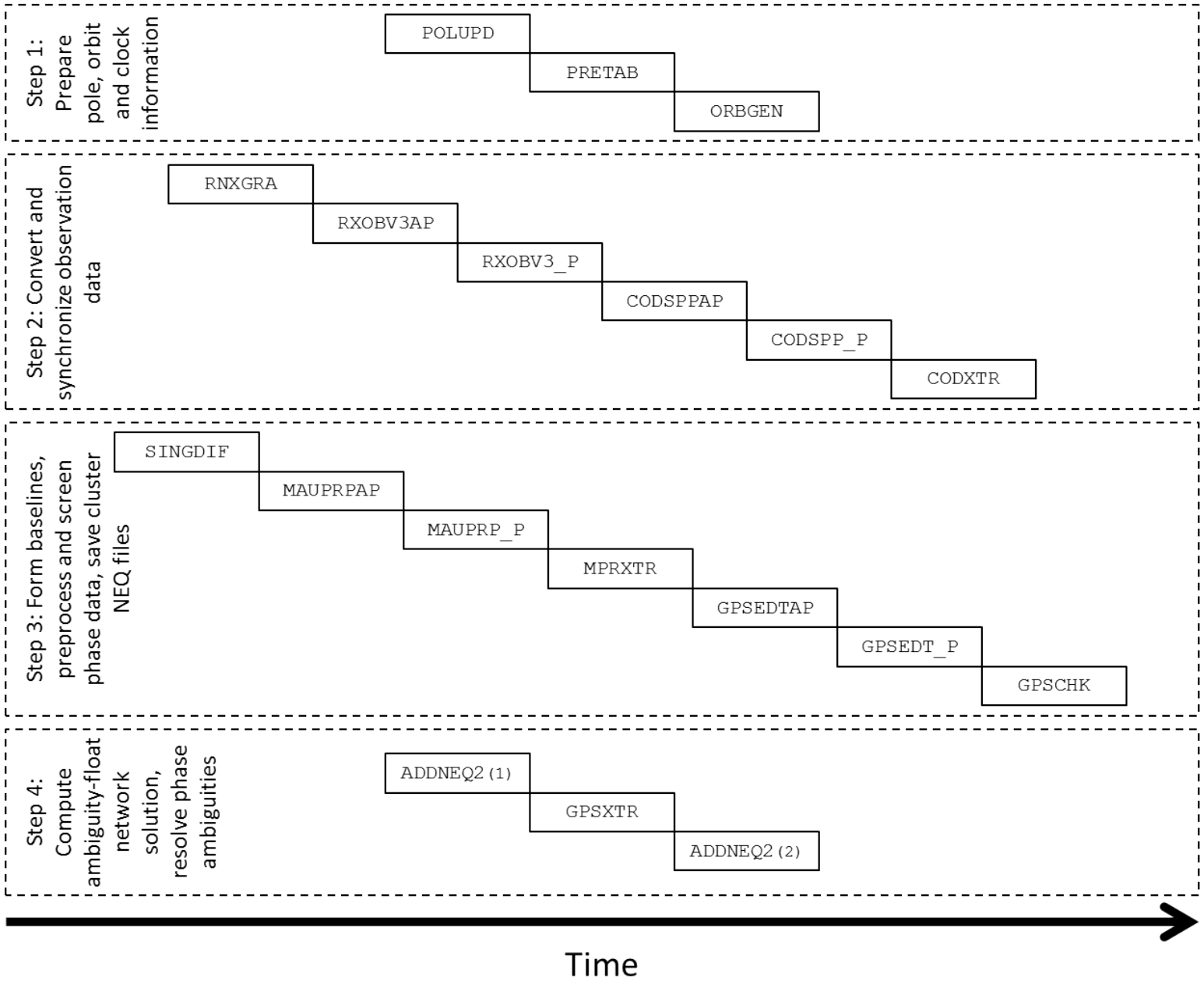

Figure 3.7: Flowchart of DDP processing in iGNSS

Table 3.2: iGNSS Daily Scripts

Script / Module Name	Time(s) of Execution (HH:MM)
genFilesDownloader.pm	05:00
	11:00
	17:00
	23:00
iGNSS_NRT_COORD_IGS08.pl	23:01
iGNSS_ANT_I08.pl	05:03
	11:03
	17:03
	23:03
get_newnrt.sta	23:20
iGNSS_PPP_EUREF_IGS08ALI.pl	20:45
iGNSS_PPP_IGS08.pl	16:45
iGNSS_PPP_IRELAND_IGS08ALI.pl	19:45
iGNSS_PPP_RGP_IGS08ALI.pl	19:45
iGNSS_PPP_SPS_IGS08ALI.pl	17:45
iGNSS_PPP_UK_IGS08ALI.pl	18:45
iGNSS_PPP_WALCORS_IGS08ALI.pl	21:45

in Table 3.3.

3.1.3 The PP GNSS Data Processing System

The PP GNSS data processing system used in this research is based on the Bernese GNSS Software v 5.2 (BSW5.2) and is capable of processing GNSS observations using both the PPP and DDP processing strategies. Furthermore, it can be adapted to use various specific processing parameters such as the orbit and clock products, and tropospheric mapping functions. Figures 3.8 and 3.9 show the BSW5.2 sub-programs execution sequence for the PPP and DDP processing, respectively, which takes place in the PP GNSS data processing system. For the description of the BSW5.2 sub-programs mentioned in Figures 3.8 and 3.9, the reader is referred to the Bernese GNSS Software 5.2 user manual (Dach et al., 2015).

During this research, the PP system was used to obtain the following ZTD datasets for the use in climate monitoring applications:

i. DDPULVMF: A 19-years long global dataset of GNSS-derived ZTD

Table 3.3: Processing characteristics of the UL01 system

Update Cycle	1 hour
Sampling Interval	15 min
Processing Engine	Bernese GPS Software 5.0
Processing Strategy	Double Differencing
GNSS Used	GPS
Input Raw Data	RINEX 2.11 (hourly)
Input Products	IGS Ultra-Rapid
A-priori Coordinates	PPP 20-day average
Satellite PCV Correction	Yes
Receiver PCV Correction	Yes
Ionosphere Correction	1st order effect accounted for using ionosphere-free linear combination
A-priori ZHD Model	Saastamoinen
Tropospheric Mapping Function	Niell Mapping Function
Ambiguity Resolution	No
Ocean Tide Loading Correction	FES2004
Input Meteorological Data (for ZTD to IWV conversion)	Hourly file of meteorological data
Reference Frame Standard	IERS Conventions (2003)
Outputs	- ZTD estimates - IWV estimates (COST-716) - 2D Plots - Animations

obtained using the DDP processing strategy and the VMF1 tropospheric mapping function

ii. PPPULVMF: A 1-year long global dataset of GNSS-derived ZTD obtained using the PPP processing strategy and the VMF1 tropospheric mapping function

Table 3.4 shows the various processing characteristics used to obtain the PP datasets.

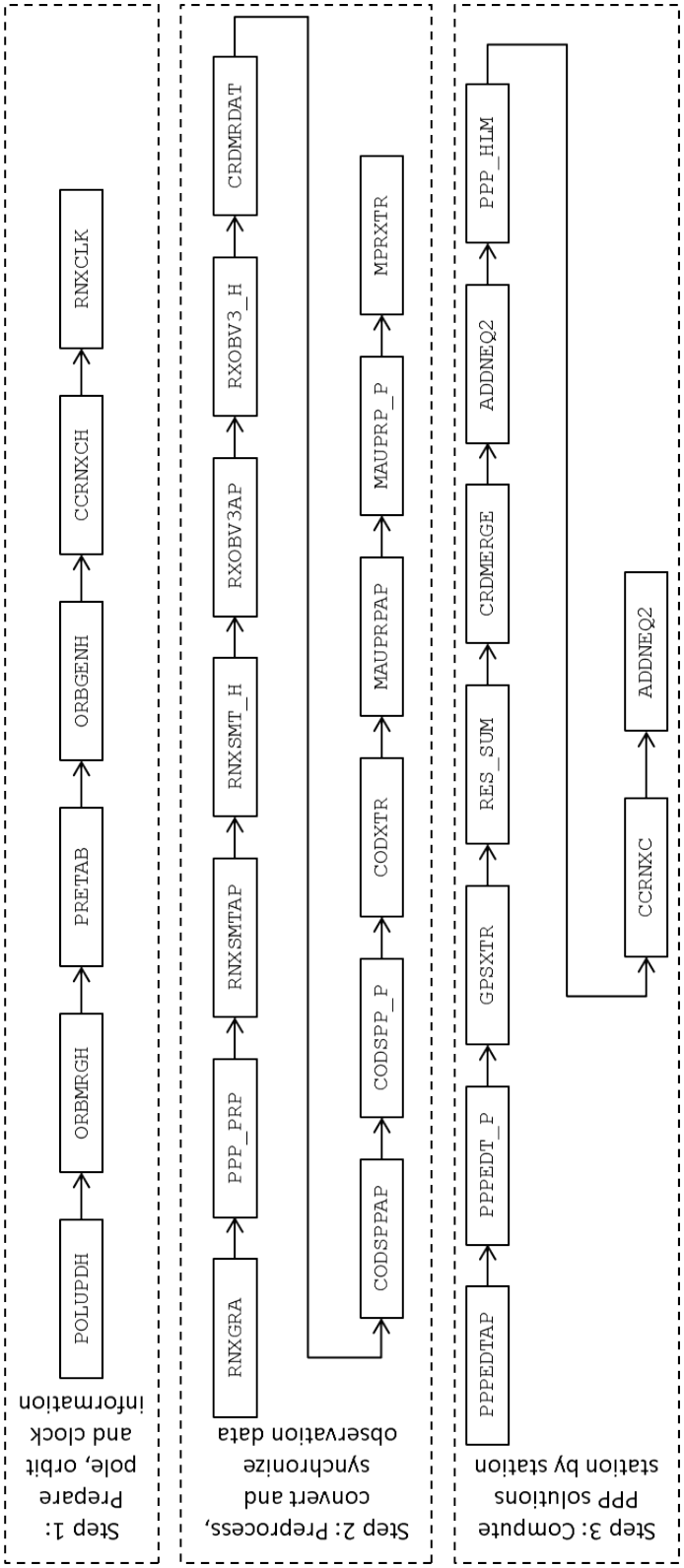

Figure 3.8: Flowchart of PPP processing in the post-processing GNSS data processing system

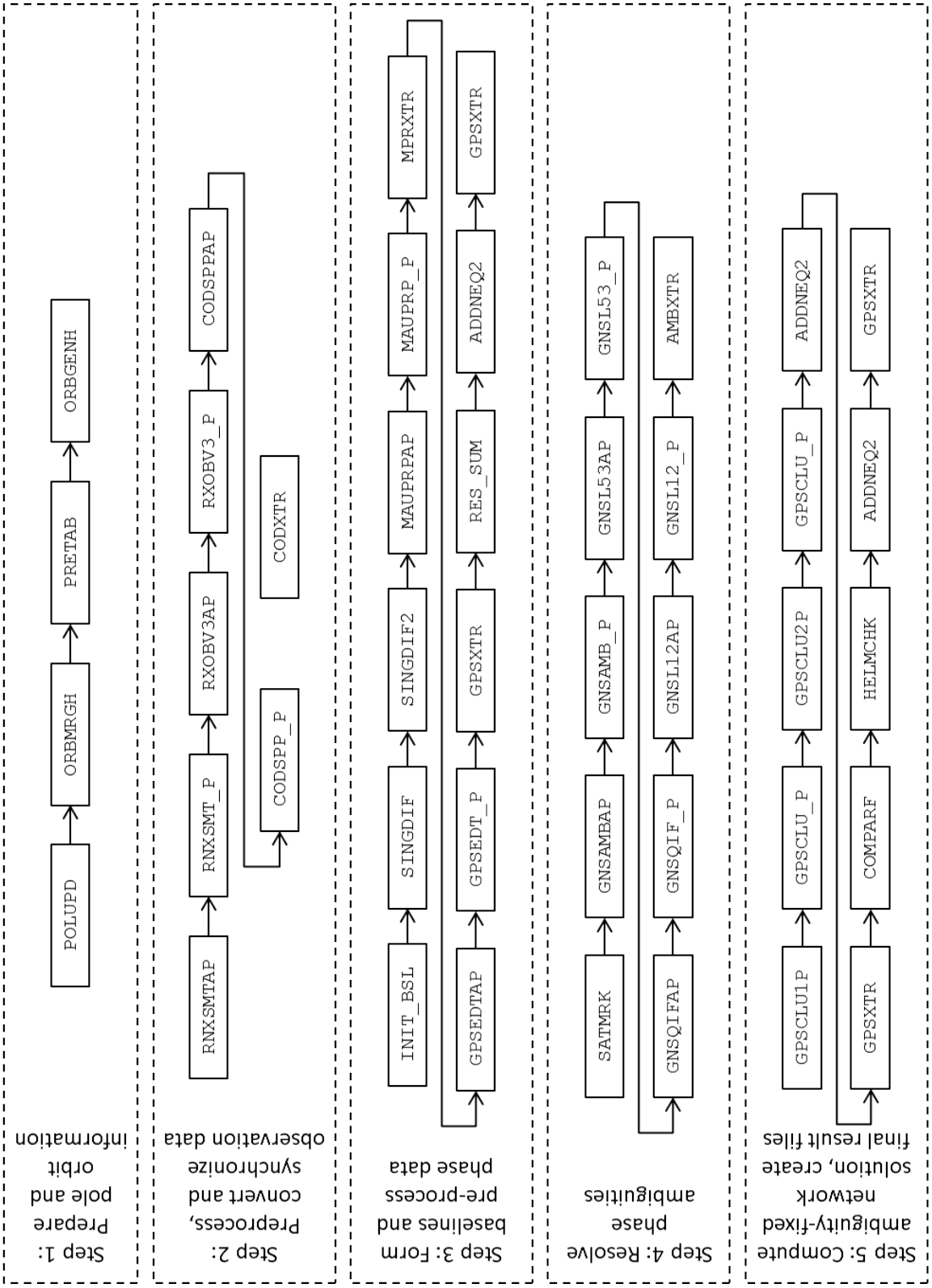

Figure 3.9: Flowchart of DDP processing in the post-processing GNSS data processing system

Table 3.4: Processing characteristics of the PP ZTD datasets

Dataset Name:	DDPULVMF	PPPULVMF
Strategy:	DDP	PPP
Processing Engine:	BSW52	BSW52
ZTD Output Interval:	2 hours	2 hours
Observation Window Used:	24 hours	24 hours
Processing Session Length:	24 hours	24 hours
GNSS Used:	GPS	GPS
A-priori Coordinates	PPP	PPP
A-Priori ZHD Model:	Dry VMF1	Dry VMF1
Troposphere Mapping Function:	Wet VMF1	Wet VMF1
Orbit Product Used:	COD Repro1	COD Repro1
Clock Product Used:	COD Repro1	COD Repro1
Antenna Models:	IGS08	IGS08
Coordinates Computed:	Yes	Yes
Elevation Cut-Off Angle:	3^o	3^o
Integer Ambiguity Resolution:	Yes	Yes
Ocean Tide Loading Correction:	FES2004	FES2004
Reference Frame Standard	IERS 2010	IERS 2010
Ionosphere Correction	1st and 2nd order	1st and 2nd order

3.2 Experiments

This section describes the various experiments conducted in order to address the research questions of this thesis. Figure 3.10 graphically lists the experiments performed using each of the RT, NRT and PP systems.

3.2.1 RT-PPP ZTD for NWP Applications

An assessment of RT-PPP ZTD estimates obtained using the three RT-PPP software packages described in Section 3.1.1 for the use in NWP applications was conducted by comparing them to two different reference datasets. Based on the results of this assessment, the best suitable RT GNSS data processing software and products for Luxembourg were identified.

The network of GNSS stations selected for this experiment comprises 22 globally distributed IGS stations, which provide RT observation data. Further details about the IGS network are provided in the next chapter (Section 4.1.1) and the relevant station information is also provided in the next chapter. A dataset containing RT-PPP ZTD estimates for these stations and a time-period of 31 days (2013-04-18 to 2013-05-18) was obtained using the software packages listed in Section 3.1.1. Only GPS observations have been used in this study. The characteristics of the RT product streams used for this study are given in the next chapter in Section 4.4.1.

The first reference dataset used to compare the RT-PPP ZTD estimates is the IGS final troposphere product (hereafter termed IGFT) generated by the U.S. Naval Observatory (USNO) (Byram et al. 2011). The IGFT is based on the final IGS orbit and clock products and contains the ZTD estimates computed by processing 27-h observation window (sum of the 24-h observations with 1.5-h observations from previous and next days) using PPP with BSW5.0 at an output sampling interval of 5 min (Section 4.1.1).

The second reference dataset consists of the ZTD estimates derived from the observations of radiosondes (RS) collocated with five selected GNSS stations. The ZHD and the zenith wet delay (ZWD) at the RS locations have been corrected for height differences (to the GNSS station height) with the height correction on ZHD applied using the method described in Teke et al.

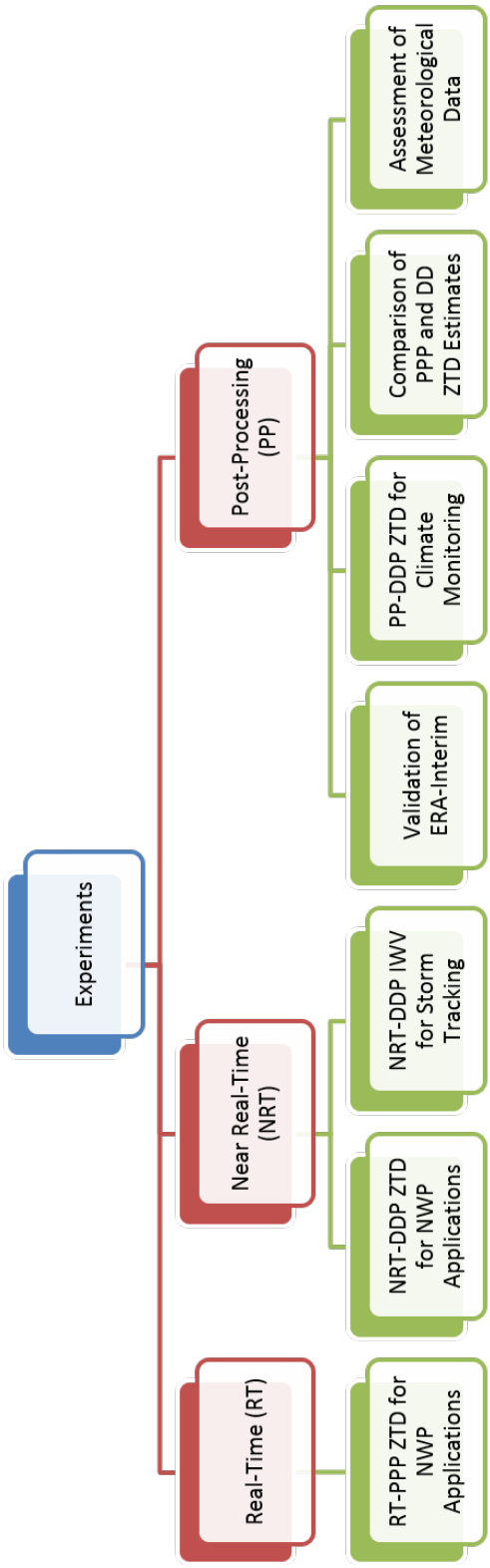

Figure 3.10: Experiments performed using the RT, NRT and PP systems

(2011), and on ZWD using the method described in Gyori and Douša (2013) (Appendix B). However, no correction has been applied for the horizontal separation between the GNSS station and the collocated RS. Details about the selection of radiosondes used for this study have been presented in the next chapter. The ZTD from GNSS observations (for five selected stations) has then been compared with the ZTD from the co-located RS.

The statistics for the comparisons have been computed using only the common epochs in the respective datasets. Considering the noise level in the RT-PPP ZTD estimates, it is argued that the statistics computed over the one month should give a good indication of the quality (precision and the stability of biases) of the estimates. However, it is also acknowledged here that the seasonality of the IWV may have a small influence on the comparison between the GNSS-derived and RS-based ZTD (Park et al. 2012), which cannot be seen using the one month period.

The results of this experiment are presented in Section 5.1 of this thesis and are also published in Ahmed et al. 2014b.

3.2.2 NRT-DDP ZTD for NWP Applications

The NRT-DDP ZTD solution from the hourly NRT processing system, i.e. the UL01 solution, is routinely submitted to E-GVAP as a test solution. However, being a test solution, it is not used for operational NWP purposes by the partner meteorological institutions of E-GVAP. Therefore, there was a need to experimentally assimilate the UL01 ZTD estimates into the AROME 3D-VAR NWP model which is used as this research's region of interest. This section describes the methodology used to assess the impact of using GNSS-derived NRT-DDP ZTD from ground-based stations in Luxembourg and the surrounding areas on the quality of short-term weather forecasts issued by the AROME 3D-VAR NWP model. It describes the AROME 3D-VAR model and the experimental setup used to conduct the assessment. The results of this experiment have been published in Mahfouf et al. 2015.

AROME 3D-VAR Data Assimilation Experiments

In order to assess the impact of assimilating the UL01 ZTD estimates in the AROME 3D-VAR NWP model, a NRT ZTD dataset was provided to

Météo-France to carry the assimilation experiments. During these experiments, the UL01 ZTD solution was assimilated in AROME in addition to the ZTD solutions from other analysis centers that are operationally assimilated through E-GVAP. Before carrying out the assimilation experiments, the ZTD datasets were quality checked. After the quality control, the assimilation was performed and a number of forecasts for past time periods were regenerated. The quality of these forecasts was then studied through comparisons with the observations. The following text describes the ZTD datasets and the approach used while carrying the experiments.

NRT-DDP ZTD Dataset

Two NRT-DDP ZTD datasets, containing the ZTD estimates for a period of approximately one month (July 17-August 20, 2013), have been used for the assimilation experiments.

The first one is the operational dataset which is routinely provided to the meteorological institutions by E-GVAP and contains the ZTD estimated by 16 different analysis centers across Europe. The ZTD sampling interval in the E-GVAP solutions varies from 5 to 60 minutes but most of the analysis centers provide the ZTD with the sampling interval of 15 minutes. Collectively, the dataset from E-GVAP provides the ZTD data from about 700 ground-based GNSS stations which are distributed all over the AROME domain. This NRT ZTD dataset will be referred to as "E-GVAP dataset" in the following text.

The second dataset used for assimilation is the UL01 ZTD dataset (described in Sections 3.1.2 and 4.2.1) which is currently being monitored by E-GVAP but not being distributed for operational purposes yet. UL01 provides ZTD estimates from about 200 stations in its hourly solutions with a ZTD sampling interval of 15 minutes. The UL01 solution contains ZTD from 29 new stations located in Belgium (WALCORS) and Luxembourg (SPSLux), and about 191 existing stations which are already processed by other analysis centers. The a priori coordinates used during the ZTD estimation in UL01 are computed by averaging the past 20-days PPP coordinates for each station. The station and antenna related information is updated on

a daily basis. This NRT ZTD dataset will be referred to as "UL01 dataset" in the following text.

It is important to note that in many cases, one GNSS station is processed by several analysis centers. Therefore, the term "station-center pair" will be used at some places in the following text which means the ZTD observations from a GNSS station provided by a certain analysis center. For example, if the GNSS station named "LIL2" is processed by the analysis centers UL01 and SGN1, then "LIL2-UL01" and "LIL2-SGN1" will be called as station-center pairs. During the pre-processing phase (which is described next), the ZTD estimates from the best station-center pair are selected for assimilation for a particular assimilation cycle i.e. the observations from the best available solution for a particular station are selected.

Pre-Processing and the White List

During the pre-processing stage, the available datasets of ZTD are checked for quality by examining the statistical behaviour of the differences between the GNSS-derived ZTD estimates and the model equivalent ZTD, namely the "background departures" or "Observed minus Background (O−B)". In AROME, the model equivalent ZTD is computed from the 3-hour AROME forecast fields of surface pressure, temperature and specific humidity using the following observation operator:

$$ZTD = 10^{-6} \int_0^{z_{top}} \left(k_1 \frac{p}{T} + k_3 \frac{e}{T^2} \right) dz \tag{3.1}$$

where p is the pressure, T the temperature, e the water vapour pressure, $k_1 = 0.776$ Pa^{-1}K, $k_3 = 3730$ Pa^{-1}K^2, and z_{top} represents the highest vertical level of the model's domain. If the contribution of the ZTD above the model top z_{top} is not accounted for in the ZTD observation operator, it could lead to a systematic underestimation of ZTD of about 2.3 mm. In this study, the contribution of the ZTD above z_{top} has been accounted for in the bias correction stage using the strategy described in Mahfouf et al (2015).

After pre-processing, the station-center pairs which have a good quality are entered into a "white list" of the station-center pairs that can potentially be assimilated. Station-center pairs with biases that are too large (larger

than 30 mm) are not selected to enter the "white list". Any station-center pair that is not present in the "white list" cannot be assimilated. However, before any station-center pair present in the "white list" can be assimilated, it has to undergo several further quality controls. Further information about the AROME "white lists" can be found in Poli et al. (2007) and Yan et al. (2009a, 2009b).

The ZTD estimates from both the datasets were monitored for quality by the pre-processing stage described above and a "white list" was created.

Bias Correction and Final Selection

After the creation of the "white list", a spatial thinning is done to ensure that the distance between two stations is no less than 10 km. The observation error is set to 12 mm for all E-GVAP stations. For UL01, this error has been assigned for each station based on the standard deviation of background departures and assuming a model background error of 6 mm, leading to actual values for individual stations ranging between 10 and 15 mm. The mean value of background departure statistics is used to provide a constant bias correction (accounting mostly for the difference in altitude between the model and the station and for the atmospheric contribution to ZTD above z_{top}) that is applied to each station-center pair before assimilation. The time series of background departures have been computed over the 1-month assimilation period performed in this study for the UL01 ZTD observations whereas the statistics for E-GVAP ZTD observations correspond to the period of April 2013. It has been checked that the biases computed over the two different periods are very similar (not shown). During the assimilation, for a given station, the processing centre is chosen on the basis of its availability and by comparing the background departure statistics, instead of being selected a-priori in the white list. For each 3-hourly analysis, when several observations are available for a given station-centre pair, the GPS observation closest to the analysis time and within $\pm$ 1.5 hours around the analysis time is selected. Like other observations assimilated in the AROME 3D-VAR, ZTD data are subject to a First-Guess Quality Control check that rejects data too far from the model background. This check is based on background and observation errors with a threshold value of 3.5. In practice, it means that ZTD values leading to background departures (O$-$B)

larger than 40 mm are systematically rejected, accounting for too-large mismatches between model and station altitudes.

Data Assimilation

Three AROME assimilation experiments have been conducted in order to investigate the impact of the assimilation of GPS ZTD observations with the most recent version of the 3D-VAR system and also to evaluate the impact of additional ZTD data provided by the UL01 dataset. Each of the three experiments are described below:

i. NOGPS: In this experiment, all the observations from the operational AROME 3D-VAR since July 2, 2013 were assimilated but all the GNSS-derived ZTD observations were excluded from assimilation.

ii. EGVAP: In this experiment, the GNSS-derived ZTD observations from the EGVAP dataset were assimilated in addition to those assimilated in the NOGPS experiment.

iii. UL01: In this experiment, the GNSS-derived ZTD observations from both the EGVAP and UL01 datasets were assimilated in addition to those assimilated in the NOGPS experiment.

The three assimilation experiments started at 0300 UTC on July 18, 2013 from the AROME operational analysis and ended at 2100 UTC on August 20, 2013. Short-range forecasts were run every 3 hours to provide the background of the next analysis and once a day at 0300 UTC a 30 hours forecast run was launched. The experimental setup is summarized in Table 3.5.

Table 3.5: AROME 3D-VAR data assimilation experiments

Experiment Name:	NOGPS	EGVAP	UL01
GNSS ZTD Assimilated	No	Yes	Yes
GNSS Networks Used for ZTD Assimilation	-	E-GVAP Operational Solutions only	E-GVAP Operational Solutions UL01 Test Solution

The experiment without the assimilation of GNSS-derived ZTD observations was performed with the intention that its output can be compared to the experiments in which GNSS-derived ZTD assimilation was used and an impact assessment of this assimilation on the AROME model can be performed. The two experiments with the GNSS-derived ZTD assimilation were performed for studying the impact of assimilating the ZTD estimates from the UL01 solution in addition to the operational EGVAP ZTD solutions. From the output of these three experiments, various parameters were extracted and statistics for the comparisons between those were calculated. The impact assessment was carried out in two parts, i.e. studying the impact on the model analysis and studying the impact on model forecasts.

The results of this experiment are presented in Section 5.2 of this thesis and are also published in Mahfouf et al. (2015).

3.2.3 NRT-DDP IWV for Storm Tracking

This section describes a comparison of the two-dimensional (2D) NRT-DDP IWV fields obtained from the UL01 system with the images of clouds and precipitation obtained from satellite and weather radar respectively for a precipitation event that occurred in Luxembourg.

To generate these 2D NRT-DDP IWV maps in the UL01 system, IWV is first estimated over all the individual stations and then using Generic Mapping Tools (GMT) (Wessel et al. 1998), a grid with a resolution of 15 minutes is computed by block averaging followed by an adjustable tension continuous curvature surface gridding algorithm (Smith et al., 1990). Therefore the density of the network of GNSS stations has an influence on the quality of these maps. It must be noted that the systems do not automatically detect and remove outlying IWV estimates.

During 22-23 February 2012, a warm front (i.e. a warm air-mass moving towards a cold air-mass) moved over northern France, Belgium and Germany. This front was associated with a low-pressure system situated over southern Scandinavia. Cloud formation and stratiform precipitation was caused by riding of warm air-mass over the cold air-mass and a light rainfall at 0400UTC was observed in Luxembourg. For this event, the 2D NRT-DDP

IWV fields obtained by the UL01 system were compared to the precipitation and cloud images obtained from the weather radar (www.meteox.de) and satellite.

The output of the UL01 system has a sampling interval of 15 minutes and hence the 2D NRT-DDP IWV maps are generated for every 15th minute. This makes it possible to graphically observe the changes in the amount of IWV and compare these changes with the weather processes. Such an example has been presented by showing the 2D NRT-DDP IWV maps obtained by UL01 for a time period of 15 hours with intervals of 3 hours during the passage of the above mentioned warm front over Luxembourg and the Greater Region. Furthermore, the time series of IWV over the six GNSS stations in Luxembourg for the same event has been presented and the changes in the IWV associated with the passage of the front has been studied.

The results of this experiment are presented in Section 5.3 of this thesis and are also published in Ahmed et al. 2012.

3.2.4 Validation of ERA-Interim Climate Reanalysis Dataset

This section describes the experiment performed to conduct a validation of the ZTD estimates derived from the ERA-Interim climate reanalysis model (Dee et al. 2011) using GNSS-derived ZTD estimates from the DDPULVMF PP-DDP solution.

ERA-Interim reanalysis does not make use of ground-based GNSS-derived ZTD observations for data assimilation. The objective of this experiment is to investigate the agreement between the ZTD estimates derived using ground-based GNSS and ERA-Interim in different geographical areas classified by their climate types. The classification of climate types used here is the one given by Peel et al. (2007) as an updated version of the Köppen-Geiger climate classification that consists of 30 climate types. The 30 climate types are further grouped into 5 groups i.e. tropical, arid, temperate, cold, and polar. The symbols denoting these climate types, their description and their association to the climate group are shown in Table 3.6. In the following text, the term "climate zone" will refer to a geographical area associated with a certain climate type.

Table 3.6: Climate Type Classification

Climate Type Symbol	Description	Group
Af	Tropical - Rainforest	Tropical
Am	Tropical - Monsoon	
As	Tropical - Dry Summer	
Aw	Tropical - Savannah	
BSh	Arid - Steppe - Hot	Arid
BSk	Arid - Steppe - Cold	
BWh	Arid - Desert - Hot	
BWk	Arid - Desert - Cold	
Cfa	Temperate - Without dry season - Hot Summer	Temperate
Cfb	Temperate - Without dry season - Warm Summer	
Cfc	Temperate - Without dry season - Cold Summer	
Csa	Temperate - Dry Summer - Hot Summer	
Csb	Temperate - Dry Summer - Warm Summer	
Csc	Temperate - Dry Summer - Cold Summer	
Cwa	Temperate - Dry Winter - Hot Summer	
Cwb	Temperate - Dry Winter - Warm Summer	
Cwc	Temperate - Dry Winter - Cold Summer	
Dfa	Cold - Without dry season - Hot Summer	Cold
Dfb	Cold - Without dry season - Warm Summer	
Dfc	Cold - Without dry season - Cold Summer	
Dfd	Cold - Without dry season - Very Cold Winter	
Dsa	Cold - Dry Summer - Hot Summer	
Dsb	Cold - Dry Summer - Warm Summer	
Dsc	Cold - Dry Summer - Cold Summer	
Dwa	Cold - Dry Winter - Hot Summer	
Dwb	Cold - Dry Winter - Warm Summer	
Dwc	Cold - Dry Winter - Cold Summer	
Dwd	Cold - Dry Winter - Very Cold Winter	
EF	Polar - Frost	Polar
ET	Polar - Tundra	

The global ground-based GNSS network processed to obtain the DDPULVMF solution contains over 400 stations and these stations are situated in 25 of the 30 climate zones listed in Table 3.6. The distribution of GNSS stations included in this experiment is shown in the next chapter (Section 4.2.2). along with the classification of GNSS stations with respect to the various climate zones. The ERA-Interim ZTD at the locations of the ground-based GNSS stations for a 5-year period (2010 to 2014 inclusive) has been obtained using the online service of the Geodetic Observatory Pecny (GOP), called "GOP - TropDB - TropModel" (`http://www.pecny.cz/gop/index.php/gop-tropdb/tropo-model-service`). The GNSS-derived ZTD has been used as reference and the difference between the GNSS and ERA-Interim ZTD has been computed with the resolution of 6-hours for the 5-year period mentioned above.

The results of this experiment are presented in Section 5.4 in form of statistics and plots.

3.2.5 PP-DDP ZTD for Climate Monitoring

This section describes the methodology used to study the variability in the climate for the various climate zones showed in Table 3.6 for different timescales using the PP-DDP GNSS-derived ZTD dataset (DDPULVMF).

The network of ground-based GNSS stations processed to obtain the PP datasets has been described in the next chapter in Section 4.2.2. From the global network, stations have been divided into the geographical areas associated with various climate types listed in Table 3.6 in order to conduct the studies for each type of climate.

Variability in the ZTD

In order to study the annual and seasonal variability in ZTD in different climate zones, the fully available ZTD estimates from the DDULVMF dataset for the GNSS stations in every climate zone have been used. Station-wise monthly and seasonal means were computed for all the available GNSS stations and then the means for the stations in each climate zone were averaged.

Luxembourg has a network of 6 ground-based GNSS stations namely the SPSLux network (described in next chapter in Section 4.1.5) which is in operation since late 2006. Therefore, at the time of this research, observation data from SPSLux was available for a timespan slightly above 8 years. Even though the timespan of 8 years is not yet sufficient for climate monitoring applications, climate variability analysis has been performed for SPSLux also in order to assess its potential for regional climate studies in the future.

The results of this experiment are presented in Section 5.5 of this thesis.

3.2.6 Comparison of PP-PPP and PP-DDP ZTD Estimates

The DDP processing strategy is generally considered more accurate than the PPP strategy. However, PPP is computationally more efficient than DDP network solutions and requires less resources for processing large amounts of data and it is of interest to study the suitability of the PPP strategy for climate monitoring applications.

To study the suitability of the PP-PPP strategy for climate monitoring applications, a comparison of the ZTD estimates derived using the PP-DDP and PP-PPP strategies has been conducted for 114 globally distributed stations and the year 2001. It has been studied that how the difference between DDP and PPP ZTD estimates vary in different climate zones listed in Table 3.6. Correlation and other statistics have been computed for these differences.

The results of this experiment are presented in Section 5.6 of this thesis.

3.2.7 Assessment of Meteorological Data

As discussed in the previous chapter, surface pressure and temperature are needed in order to obtain IWV or TPW from GNSS-derived ZTD. Therefore, it is of interest to assess the quality of the available sources of temperature and pressure values.

For the location of the ground-based GNSS stations in Luxembourg, there are various sources for obtaining the pressure and temperature values which

are described in the next chapter in Section 4.5. The quality of each of these sources have been assessed by:

i. Comparing the pressure and temperature values from each of the sources to those obtained from the ERA-Interim climate reanalysis dataset

ii. Converting the GNSS-derived ZTD to IWV using the pressure and temperature values from each of the sources and then comparing this IWV to that obtained from the ERA-Interim climate reanalysis dataset

The results of this experiment are not combined with Chapter 5 but are presented separately in Chapter 6 while discussing the potential of GNSS meteorology for Luxembourg.

Chapter 4

Data and Products

Data is a precious thing and will last longer than the systems themselves.

Tim Berners-Lee

This chapter provides details about the sources and providers of various types of data and products used for this research. Specifically, it describes the global and regional ground-based GNSS networks from which the observation data have been obtained and processed by the RT, NRT and PP processing systems. It introduces the sources of the GNSS products such as orbits and clocks that are used for processing the observations. Furthermore, it introduces the sensor networks and models of meteorological data which have been used to obtain various meteorological parameters.

4.1 Sources of Ground-based GNSS Observations

In order to obtain the ground-based GNSS observations, stations from various networks (global, regional and national) have been used. Each of these networks are introduced below.

4.1.1 International GNSS Service

The International GNSS Service (IGS) (Dow et al., 2009) is a non-profit consortium that has established, through the collaboration of its members, a global network of over 400 permanent and continuously operating grounbased GNSS stations with the goal of freely providing high quality GNSS data and products for various research areas. Figure 4.1 shows the complete IGS network of ground-based GNSS stations at the time of writing this thesis. The IGS network contains stations that provide data on RT, hourly as well as daily time scales. With the first available observations from 1994, the IGS network continues to expand and densify to date.

A subset of the complete IGS network is used for defining a reference frame to be used as a basis for the products computed by the IGS. To define

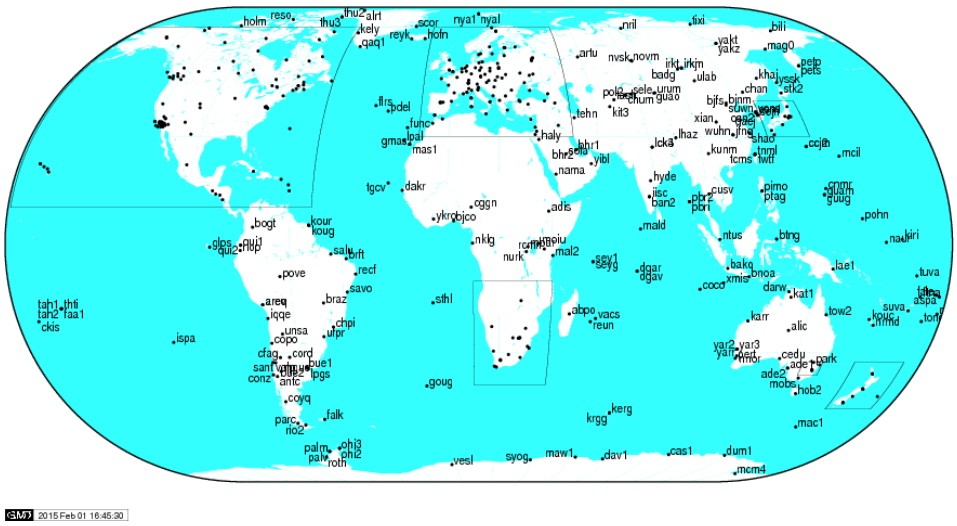

Figure 4.1: The IGS ground-based GNSS network [image source: http://www.igs.org, accessed February 1, 2015]

such a reference frame, the IGS uses its realization of the latest version of the International Terrestrial Reference Frame (ITRF) (Altamimi et al., 2012). IGb08 (Rebischung et al., 2012) is the current reference frame used by the IGS to compute its products and is derived from the ITRF2008 reference frame. The network used to define the IGb08 reference frame consists of over 230 IGS stations. Considering the heterogeneous distribution of stations in the IGb08 network, a subset of the IGb08 network namely the IGb08 core network with a uniform global distribution of IGS stations is selected for use in aligning global reference frames. More information about the IGS network can be obtained at `http://www.igs.org/`.

The RT transfer of GNSS data is carried out in the formats specified by the Special Committee 104 (SC104) of the Radio Technical Commission for Maritime Services (RTCM) (http://www.rtcm.org/) using the Network Transport of RTCM via Internet Protocol (NTRIP) (Weber et al. 2006). Since December 2012, the Real-Time Service (RTS) of the IGS (Dow et al. 2009; Caissy et al. 2012) is making ground-based GNSS observations from the RT stations in its network officially available to the GNSS community. The IGS together with RTCM-SC104 have defined a format for the dissemination of observation data in RT which is called RTCM-3.

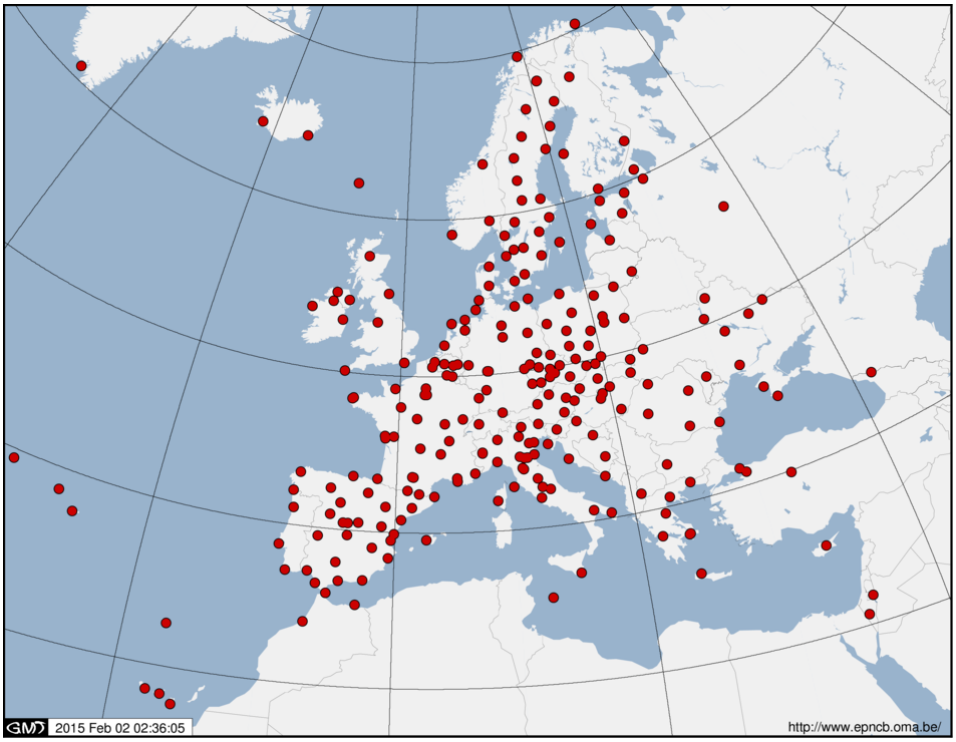

Figure 4.2: The EPN ground-based GNSS network [image source: http://www.epncb.oma.be]

4.1.2 EUREF Permanent Network

The Reference Frame Sub Commission for Europe (EUREF) (Bruyninx et al., 2008) has established a permanent network of ground-based GNSS stations in Europe which is known as EUREF Permanent Network (EPN). Figure 4.2 shows the station distribution of the ground-based GNSS stations in the EPN. The EPN contains stations that provide data on RT, hourly as well as daily time scales. Some of the stations in EPN also belong to the IGS network. More information about the EPN network can be obtained at `http://www.epncb.oma.be/`.

4.1.3 Réseau GNSS Permanent

The Institut National de L'information Géographique et Forestire (IGN) [English: National Institute of Geographic and Forestry Information] of France has established a permanent network of ground-based GNSS stations

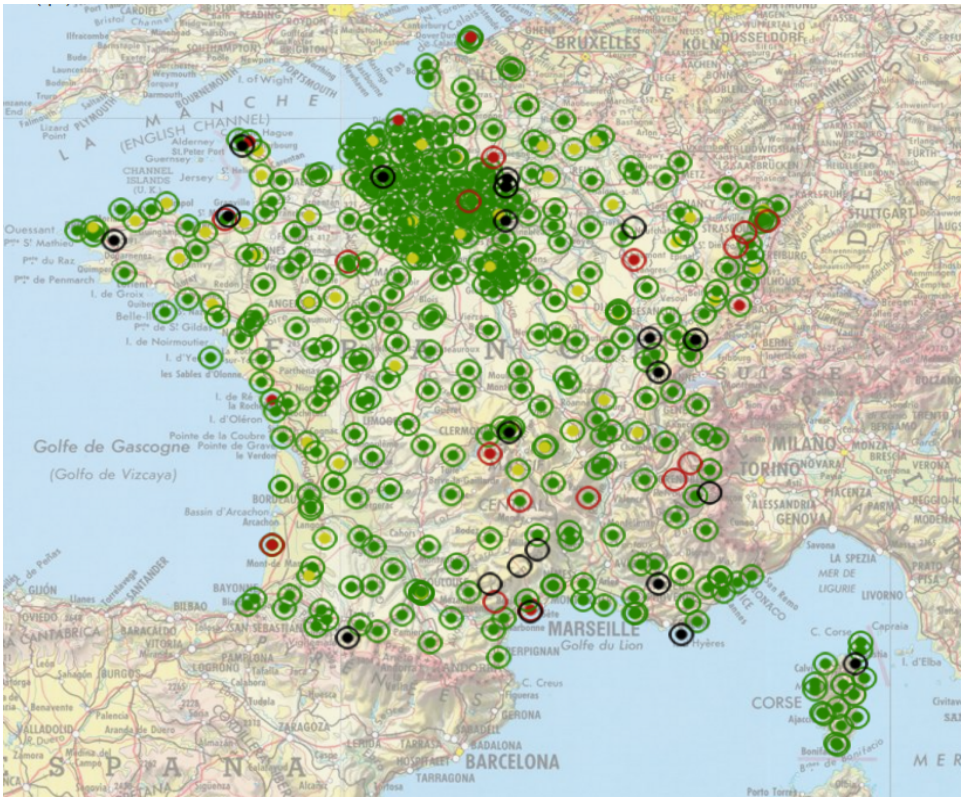

Figure 4.3: The RGP ground-based GNSS network [image source: http://rgp.ign.fr/]

in France which is known as Réseau GNSS Permanent (RGP) [English: Permanent GNSS Network]. The RGP network contains stations that provide data on RT, hourly as well as daily time scales. Some of the stations in RGP also belong to the IGS and EPN networks. A map of RGP stations is shown in Figure 4.3. More information about the RGP network can be obtained at `http://rgp.ign.fr/`.

4.1.4 British Isles continuous GNSS Facility

The British Isles continuous GNSS Facility (BIGF) (`http://www.bigf.ac.uk`) is a facility funded by the Natural Environment Research Council (NERC), United Kingdom to support the research community by providing quality controlled archived observation data from various ground-based GNSS networks in the United Kingdom and Ireland. In this research, the

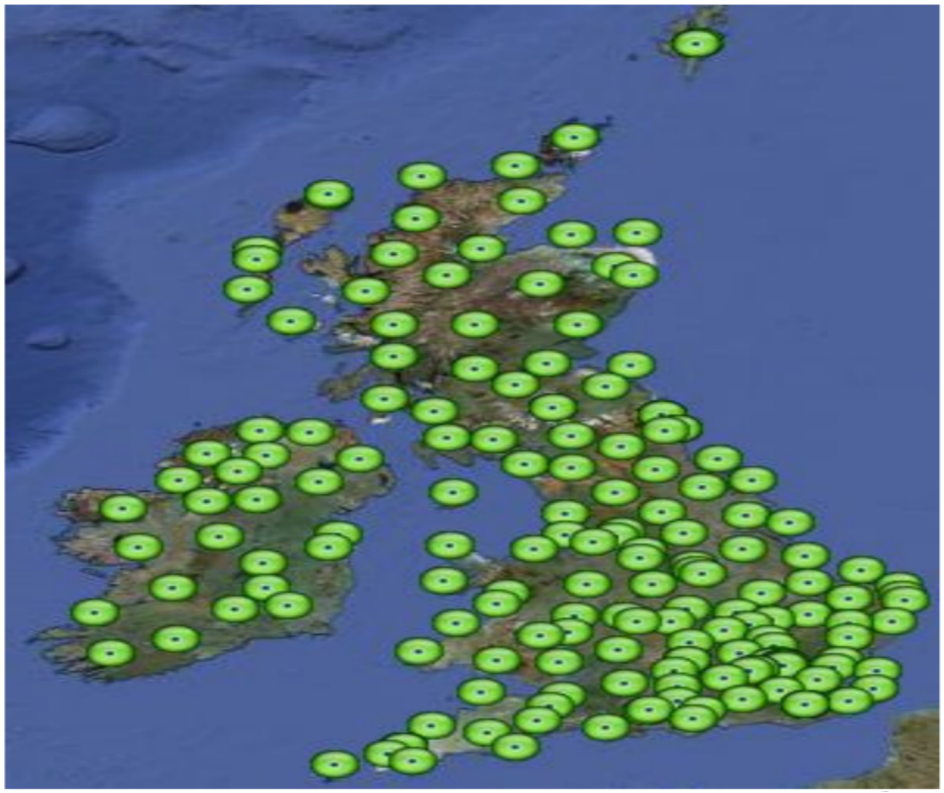

Figure 4.4: The BIGF ground-based GNSS network [image source: http://bigf.ac.uk/]

BIGF data archive has been used to obtain the observation data from the GNSS networks of Ordnance Survey of the Great Britain (OSGB), Ordnance Survey of Ireland (OSi) and the NERC Space Geodesy Facility (NERC SGF). In total, the BIGF archive holds data for about 160 stations and few of these are also a part of the EUREF and IGS networks. A map of RGP stations is shown in Figure 4.4. More information about the BIGF network can be obtained at `http://www.bigf.ac.uk/`.

4.1.5 Satellite Positioning Service Luxembourg

The Administration du Cadastre et de la Topographie (ACT) [English: The Administration of Cadastre and Topography] of Luxembourg has established a network of six ground-based GNSS stations in Luxembourg in order to commercially provide Network Real-Time Kinematic (NRTK) po-

sitioning services. This NRTK service is known as Satellite Positioning Service Luxembourg (SPSLux) and the GNSS network is referred to as the SPSLux network (`http://www.act.public.lu/fr/gps-reseaux/spslux/index.html`). All the SPSLux stations are capable to provide observation data on RT, hourly and daily time scales. Figure 4.5 shows the SPSLux network of ground-based GNSS stations and Table 4.1 provides the locations and heights of these stations. Unlike some EPN and RGP stations, none of the SPSLux stations belongs to any other network. The observation data from SPSLux is available since late 2006.

In addition to pointing the locations of the six GNSS stations (shown as gray pillars with red hats), Figure 4.5 also describes the infrastructure of the SPSLux network. It can be seen that five of the six stations are maintained by CREOS Luxembourg S.A. (`http://www.creos-net.lu/`) which is a company that owns and operates electricity and natural gas networks. One of the six stations (Walferdange) is maintained by European Center for Geodynamics and Seismology (ECGS), Luxembourg (`http://www.ecgs.lu/`). The data from these six stations is transmitted to the Centre des technologies de l'information de l'Etat (CTIE) [English: Centre for Information Technology of the State], Luxembourg (`http://www.ctie.public.lu`) which further transfers it to ACT. ACT disseminates the observation and correction data to the NRTK users through a General Packet Radio Service (GPRS) link and to other types of users through the File Transfer Protocol (FTP) and NTRIP. More information about the SPSLux network can be obtained at `http://www.act.public.lu/fr/gps-reseaux/spslux/index.html`.

4.1.6 Wallonian network of Continuously Operating Reference Stations

The Service Public de Wallonie (SPW) [English: Public Service of Wallonie] of Belgium has established a network of 23 ground-based GNSS continuously operating reference stations (CORS) in the Wallonian region of Belgium. This network is called WALCORS (`http://gnss.wallonie.be`) and is used to commercially provide NRTK positioning services. All the WALCORS stations are capable to provide observation data on RT, hourly and daily time scales. Figure 4.6 shows the station distribution of the WALCORS network and Table 4.2 provides the locations and heights of the

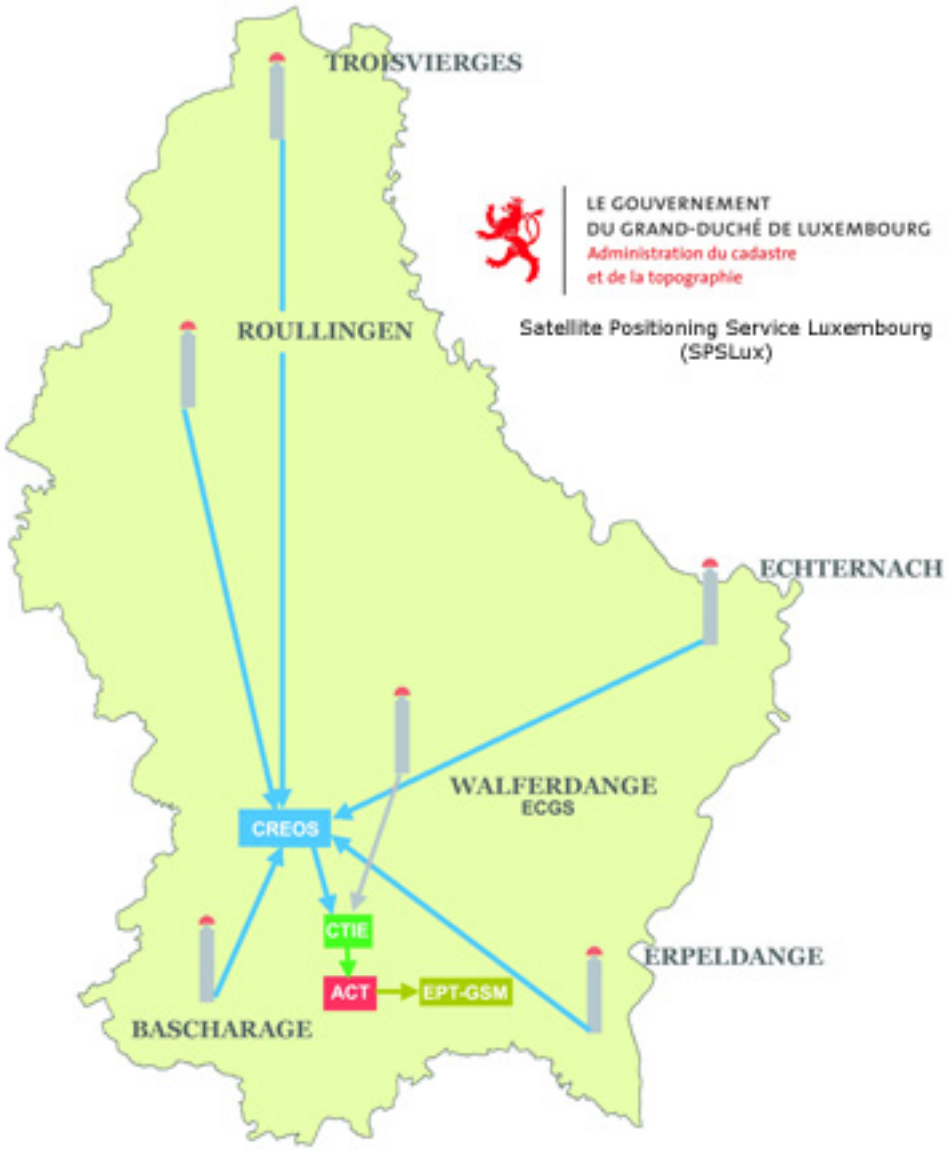

Figure 4.5: The SPSLux ground-based GNSS network [image source: http://www.act.public.lu/fr/gps-reseaux/spslux/index.html]

Table 4.1: Location and data availability of SPSLux ground-based GNSS stations

Geographical Information						Data Availability			
Station ID	Location	Country	Latitude [^{o}]	Longitude [^{o}]	Ellipsoidal Height [m]	Real-Time	Hourly	Daily	Since
BASC	Bascharage	Luxembourg	49.57	5.94	375.76	✓	✓	✓	2006
ECHT	Echternach	Luxembourg	49.80	6.44	304.53	✓	✓	✓	2006
ERPE	Erpeldange	Luxembourg	49.55	6.32	217.39	✓	✓	✓	2006
ROUL	Roullingen	Luxembourg	49.95	5.92	542.38	✓	✓	✓	2006
TROI	Troisvierges	Luxembourg	50.13	6.01	537.82	✓	✓	✓	2006
WALF	Walferdange	Luxembourg	49.66	6.13	292.40	✓	✓	✓	2006

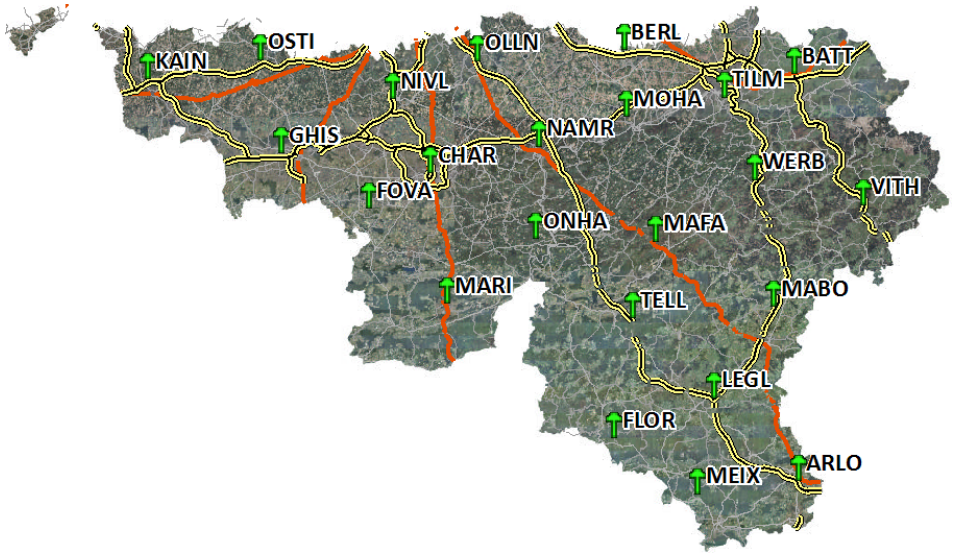

Figure 4.6: The WALCORS ground-based GNSS network [image source: http://gnss.wallonie.be]

WALCORS stations. Unlike some EPN and RGP stations, none of the WALCORS stations belongs to any other network. More information about the WALCORS network can be obtained at `http://gnss.wallonie.be/`.

Table 4.2: Location and data availability of WALCORS ground-based GNSS stations

Geographical Information						Data Availability		
Station ID	Location	Country	Latitude [^{o}]	Longitude [^{o}]	Ellipsoidal Height [m]	Real-Time	Hourly	Daily
ARLO	Arlon	Belgium	49.65	5.82	428.68	√	√	√
BATT	Battice	Belgium	50.64	5.83	322.83	√	√	√
BERL	Berloz	Belgium	50.70	5.19	185.60	√	√	√
CHAR	Charleroi	Belgium	50.41	4.45	164.72	√	√	√
FLOR	Florenville	Belgium	49.76	5.14	448.00	√	√	√
FOVA	Fontaine-Valmont	Belgium	50.32	4.22	172.18	√	√	√
GHIS	Saint-Ghislain	Belgium	50.45	3.88	79.79	√	√	√
KAIN	Kain	Belgium	50.63	3.37	66.37	√	√	√
LEGL	Leglise	Belgium	49.86	5.51	544.52	√	√	√
MABO	Maboupre	Belgium	50.07	5.74	493.86	√	√	√
MAFA	Marche-en-Famenne	Belgium	50.24	5.3	287.22	√	√	√
MARI	Mariembourg	Belgium	50.09	4.51	210.31	√	√	√
MEIX	Meix-devant-Virton	Belgium	49.62	5.44	369.50	√	√	√
MOHA	Moha	Belgium	50.54	5.19	180.91	√	√	√
NAMR	Namur	Belgium	50.47	4.86	159.37	√	√	√
NIVL	Nivelles	Belgium	50.59	4.3	186.24	√	√	√
OLLN	Louvain-la-Neuve	Belgium	50.68	4.63	189.24	√	√	√
ONHA	Onhaye	Belgium	50.25	4.85	293.05	√	√	√
OSTI	Ostiches	Belgium	50.68	3.8	90.30	√	√	√
TELL	Tellin	Belgium	50.05	5.21	451.67	√	√	√
TILM	Sart-Tilman	Belgium	50.58	5.57	302.43	√	√	√
VITH	St-Vith	Belgium	50.32	6.09	607.30	√	√	√
WERB	Werbomont	Belgium	50.38	5.68	490.04	√	√	√

4.2 Selected GNSS Networks

This section describes the selection of ground-based GNSS stations on various spatial scales that was used by the different processing systems in this research.

4.2.1 RT and NRT Networks

The operational RT and NRT processing systems process the observations from ground-based GNSS stations inside Europe. The network of GNSS stations (Figure 4.7) used for these systems has been selected with the aim of achieving good spatial coverage of Europe with a focus on Luxembourg and the Greater Region. Out of the networks introduced in the previous section, the complete networks of SPSLux and WALCORS were used whereas selected stations were used from the remaining networks. In Figure 4.7, the triangles represent the GNSS stations providing hourly data and circles represent those providing the data as RT streams. The hourly NRT processing system processes data from the stations that either provide RT streams or hourly data. On the other hand, the sub-hourly NRT and the RT processing systems only process data from RT stations. Table 4.3 shows the list of the GNSS networks used for various regions (Figure 4.7). A list of all the stations in the RT and NRT networks has been provided in Appendix A.

Table 4.3: GNSS data providers

Network	Region
SPSLux (red)	Luxembourg
WALCORS (orange)	Wallonie (Belgium)
RGP (gray)	France
OSGB+OSi+NERC-SGF (yellow)	UK
EPN (blue)	Europe
IGS (black)	Global

Although the operational RT processing system process data from a European network, a global network of 22 RT stations from the IGS RTS was used in order to assess the suitability of RT-PPP ZTD estimates for NWP applications. Figure 4.8 shows this network and Table 4.4 provides antenna related characteristics of the stations in this network.

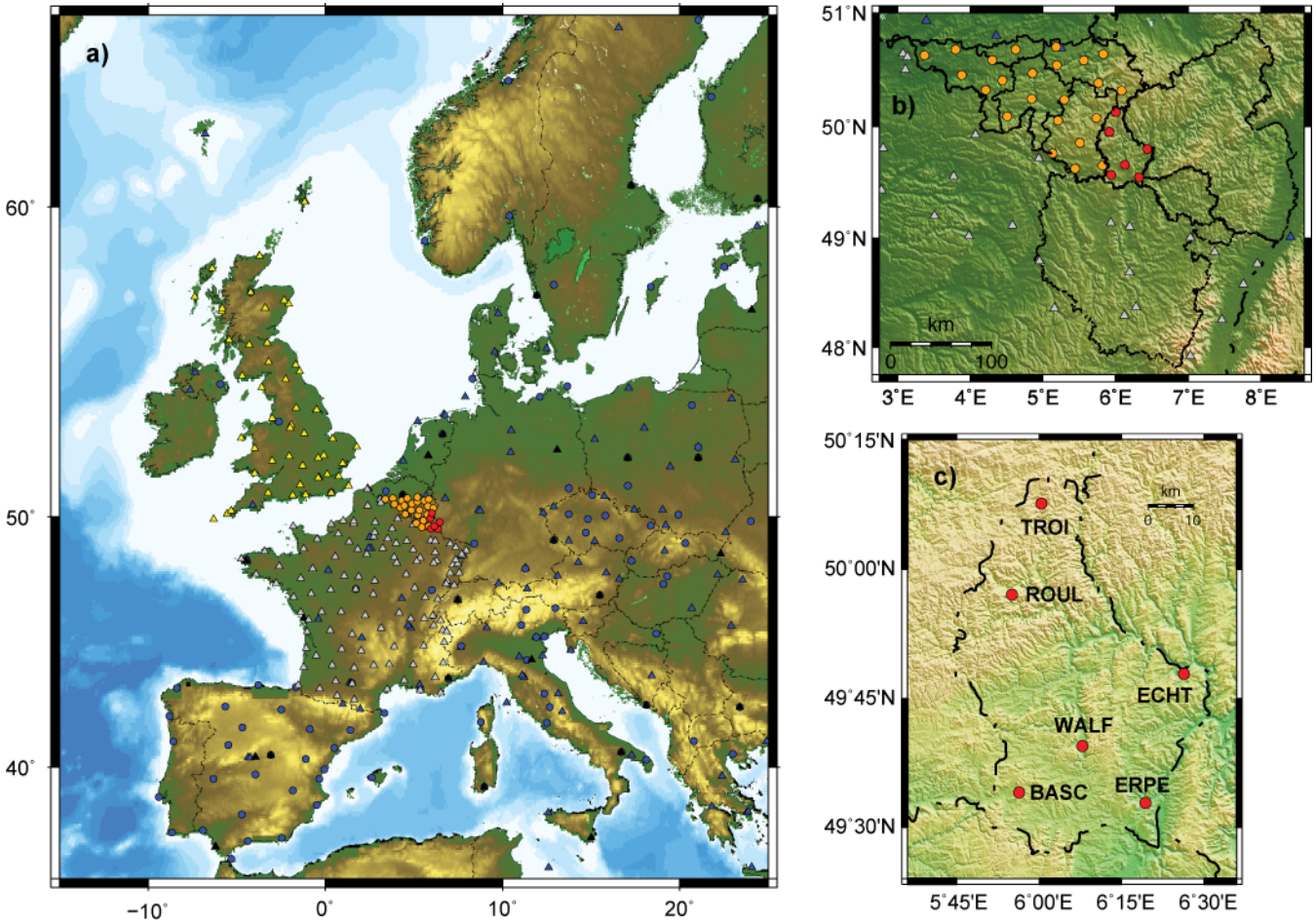

Figure 4.7: Ground-based GNSS networks used for RT and NRT processing systems on scales of a) Europe, b) the Greater Region and c) Luxembourg. The triangles represent the GNSS stations providing hourly data and circles represent those providing the data as RT streams. Table 4.3 shows the color coding w.r.t providers.

Table 4.4: Receiver and antenna information for IGS real-time stations used in this study

Station	IERS DOMES Number	Receiver Type	A ntenna and Radome		ARP Eccentricity (Up) [m]
ADIS	31502M001	JPS LEGACY	TRM29659.00	NONE	0.001
ALBH	40129M003	AOA BENCHMARK ACT	AOAD/M_T	SCIS	0.1
AUCK	50209M001	TRIMBLE NETR9	TRM55971.00	NONE	0.055
BOR1	12205M002	TRIMBLE NETRS	AOAD/M_T	NONE	0.0624
BRST	10004M004	TRIMBLE NETR9	TRM57971.00	NONE	2.0431
BUCU	11401M001	LEICA GRX1200GGPRO	LEIAT504GG	LEIS	0.097
COCO	50127M001	TRIMBLE NETR8	AOAD/M_T	NONE	0.004
DAEJ	23902M002	TRIMBLE NETRS	TRM59800.00	SCIS	0
DUBO	40137M001	TPS NETG3	AOAD/M_T	NONE	0.1
GOPE	11502M002	TPS NETG3	TPSCR.G3	TPSH	0.1114
HERT	13212M010	LEICA GRX1200GGPRO	LEIAT504GG	NONE	0
HOFN	10204M002	LEICA GR25	LEIAR25.R4	LEIT	0.0319
KIR0	10422M001	JPS EGGDT	AOAD/M_T	OSOD	0.071
MATE	12734M008	LEICA GRX1200GGPRO	LEIAT504GG	NONE	0.101
NKLG	32809M002	TRIMBLE NETR9	TRM59800.00	SCIS	3.043
NTUS	22601M001	LEICA GRX1200GGPRO	LEIAT504GG	NONE	0.0776
ONSA	10402M004	JPS E_GGD	AOAD/M_B	OSOD	0.995
POTS	14106M003	JAVAD TRE_G3TH DELTA	JAV_RINGANT_G3T	NONE	0.1206
REYK	10202M001	LEICA GR25	LEIAR25.R4	LEIT	0.057
THTI	92201M009	TRIMBLE NETR8	ASH701945E_M	NONE	1.047
VIS0	10423M001	JPS EGGDT	AOAD/M_T	OSOD	0.071
WTZR	14201M010	LEICA GRX1200+GNSS	LEIAR25.R3	LEIT	0.071

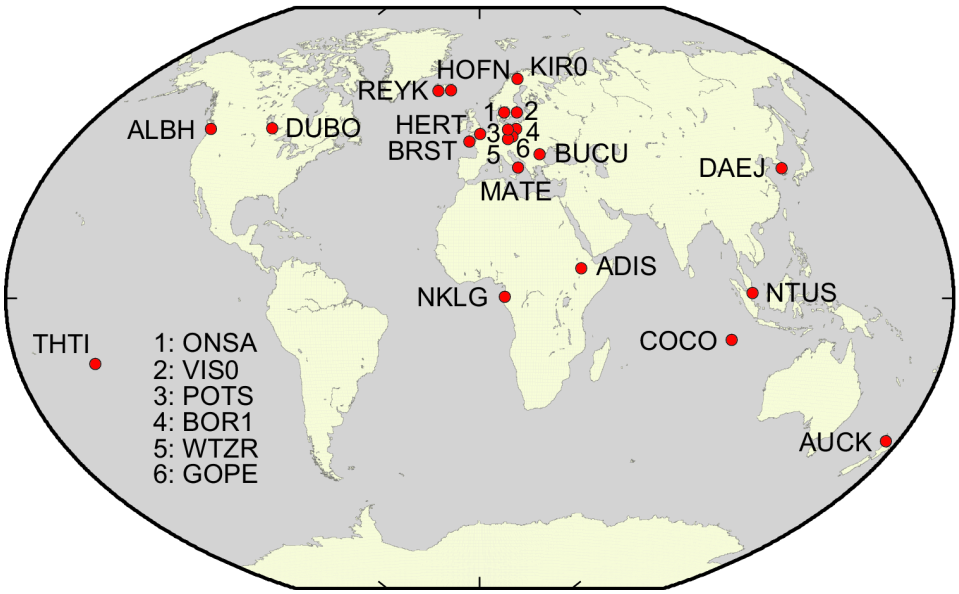

Figure 4.8: The global ground-based GNSS networks used for the assessment of RT-PPP ZTD estimates for NWP applications

4.2.2 PP Network

The ground-based GNSS network used for the PP processing system comprises of over 400 globally distributed stations (Figure 4.9) from all the above mentioned providers except WALCORS. The WALCORS network was not included in the PP network due to the very short availability of its observation data i.e. starting from 2012. Figure 4.9 also shows the divisions of the stations (in different colours) according to the climate types described in the previous chapter (Table 3.6) used to study the regional climate variability in the regions of different climate types. Furthermore, symbols in Figure 4.9 represent groups of climate zones i.e. tropical (triangles), arid (circles), temperate (squares), cold (stars) and polar (diamonds). The evolution of the number of stations processed by the PP processing system with time is shown in Figure 4.10 whereas Figure 4.11 shows a histogram of the lengths of available ZTD time series.A list of all the stations in the PP network has been provided in Appendix A.

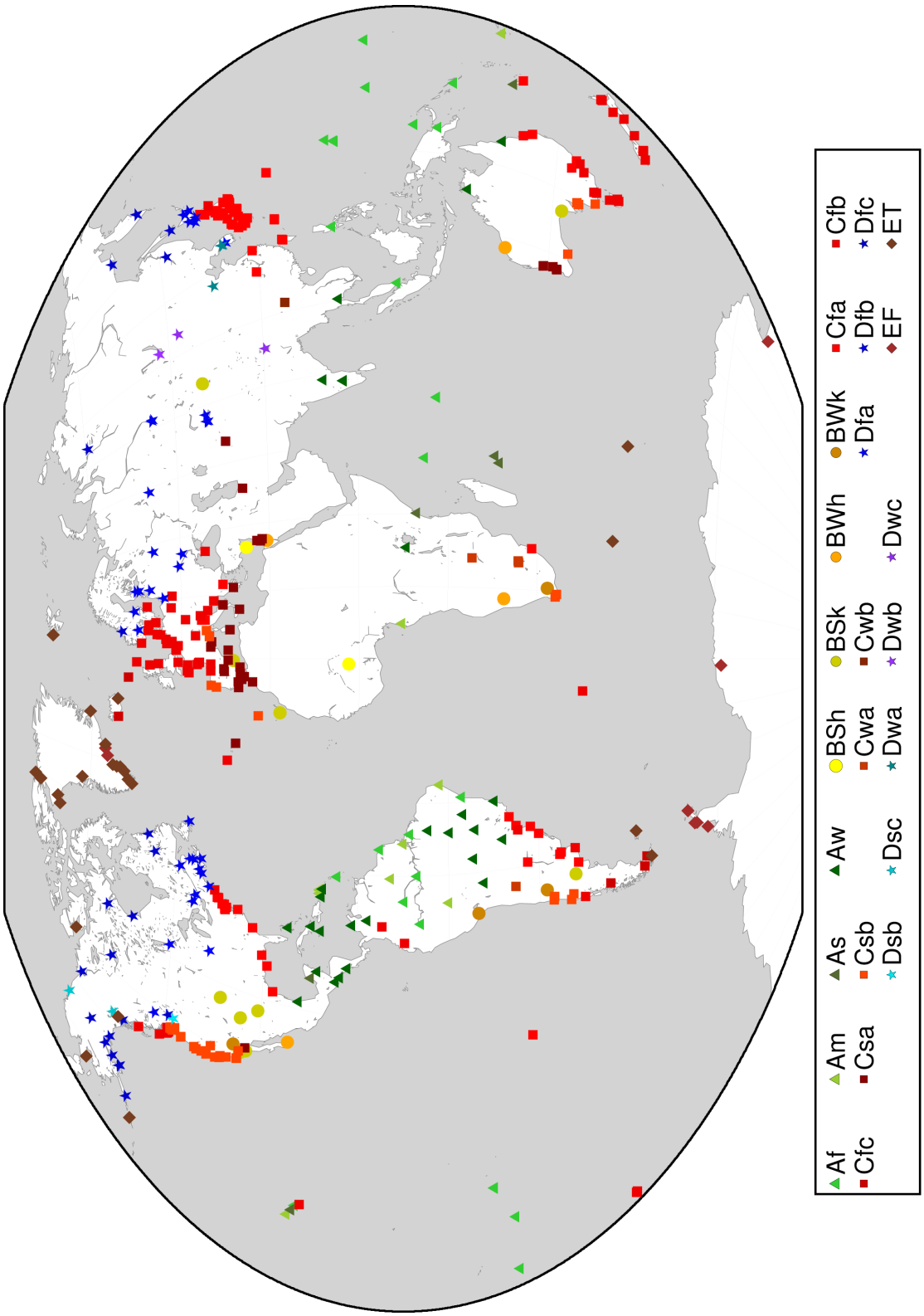

Figure 4.9: The network of stations processed by the PP processing system

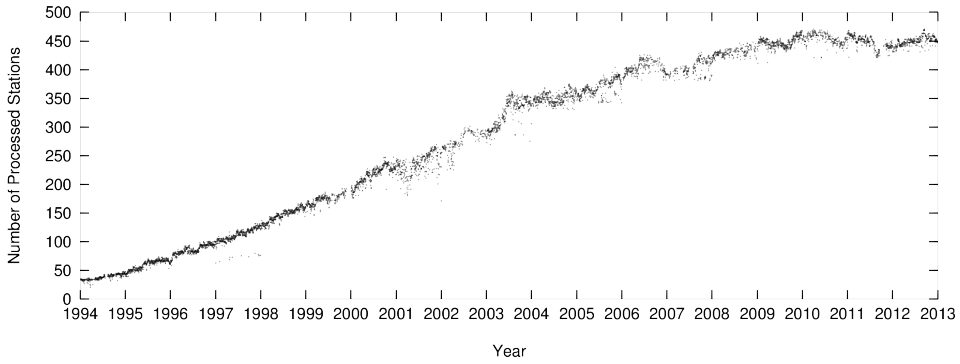

Figure 4.10: The number of processed stations by the PP processing system

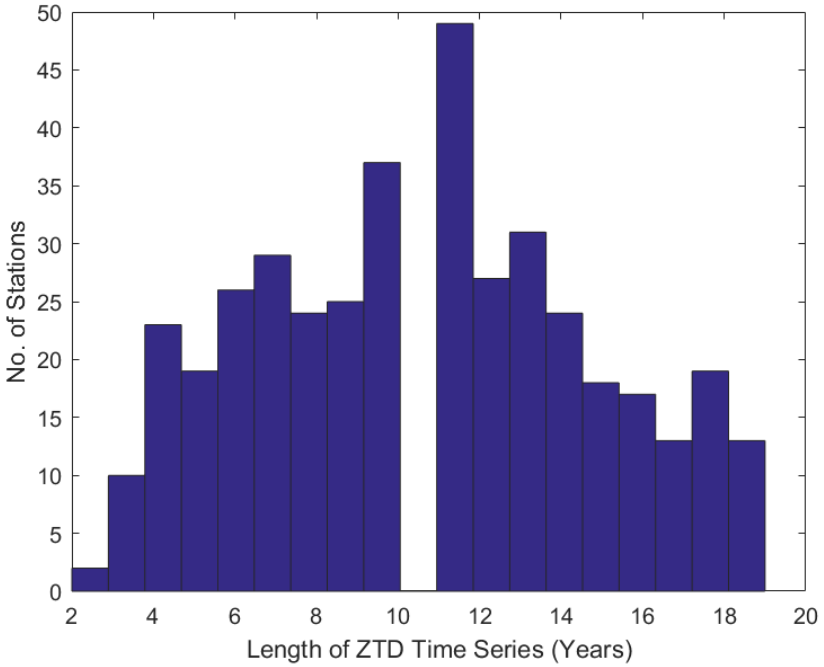

Figure 4.11: Histogram of the length of available ZTD time series

4.3 Sources of GNSS Products

In order to process the ground-based GNSS observations for different applications in this research, the required GNSS products such as orbits and clocks have been obtained from various providers. The following subsections will introduce these providers.

4.3.1 International GNSS Service

Other than providing the observation data, the IGS uses its network to compute various products that are required for processing the GNSS observations. These products include orbits, clocks and atmospheric products and are computed with various accuracy levels and latencies. After their computation, these products are disseminated to the research community. Table 4.5 lists some of the available GNSS products from the IGS along with their latencies and accuracies.

The IGS RTS also disseminates GNSS products in RT using NTRIP. These products include the broadcast ephemeris and the orbit and clock corrections. The transmission of GNSS products is carried out in a format specified by the SC104 of RTCM which is called the RTCM-SSR format where SSR stands for State Space Representation (Wübbena 2005). The RTCM-SSR RT streams are composed of various types of messages. Some of the RTCM-SSR message types are listed in Table 4.6 along with their description.

The IGS also provides tropospheric and ionospheric products with different latencies and accuracy levels. The characteristics of the IGS troposphere products are shown in Table 4.7.

4.3.2 Center for Orbit Determination in Europe

The Center for Orbit Determination in Europe (CODE) is a consortium of various institutions in Switzerland and Germany, managed by the Astronomical Institute of the University of Bern (AIUB), Switzerland which collectively acts as an analysis center for the IGS and along with other products, provides the orbit and clock products. More information about CODE can be found at `http://www.aiub.unibe.ch/`.

Table 4.5: Characteristics of various GPS orbit and clock products provided by the IGS [http://www.igs.org/products]

Type		**Accuracy**	**Latency**	**Updates**	**Sample Interval**
Broadcast	orbits	100 cm	real time	–	daily
	Sat. clocks	5 ns RMS 2.5 ns SDev			
Ultra-Rapid (predicted half)	orbits	5 cm	real time	at 03, 09, 15, 21 UTC	15 min
	Sat. clocks	3 ns RMS 1.5 ns SDev			
Ultra-Rapid (observed half)	orbits	3 cm	3 - 9 hours	at 03, 09, 15, 21 UTC	15 min
	Sat. clocks	150 ps RMS 50 ps SDev			
Final	orbits	2.5 cm	12 - 18 days	every Thursday	15 min
	Sat. & Stn. clocks	75 ps RMS 20 ps SDev			Sat.: 30s Stn.: 5 min

Table 4.6: Description of various RTCM v3 message types (http://igs.bkg.bund.de/ntrip/orbits)

RTCM-SSR message type	Content
1019	GPS Broadcast Ephemeris
1020	GLONASS Broadcast Ephemeris
1045	Galileo Broadcast Ephemeris
1057	GPS Orbit corrections to Broadcast Ephemeris
1058	GPS Clock corrections to Broadcast Ephemeris
1059	GPS Code biases
1060	Combined Orbit and Clock corrections to GPS Broadcast Ephemeris
1061	GPS User Range Accuracy
1062	High-rate GPS clock corrections to Broadcast Ephemeris
1063	GLONASS orbit corrections to Broadcast Ephemeris
1064	GLONASS clock corrections to Broadcast Ephemeris
1065	GLONASS code biases
1066	Combined orbit and clock corrections to GLONASS Broadcast Ephemeris
1067	GLONASS User Range Accuracy
1068	High-rate GLONASS clock corrections to Broadcast Ephemeris

Table 4.7: The IGS Final Troposphere Product

Type	Accuracy	Latency	Updates	Sample Interval
Final tropospheric zenith path delay	4 mm	< 4 weeks	weekly	2 hours

4.3.3 Centre National d'Etudes Spatiales

The Centre National d'Etudes Spatiales (CNES) [English: National Centre for Space Studies] is the national space research agency of France. CNES produces a RT product containing further corrections for integer ambiguity resolution which can be used to fix ambiguities in RT-PPP mode (Laurichesse 2011). This product is called CLK9B and is disseminated using NTRIP. More information about CNES can be found at `http://www.cnes.fr/`.

4.4 Selected GNSS Products

This section describes the selection of GNSS products used by the different processing systems in this research.

4.4.1 RT Products

The RT processing conducted in this research has made use of the RT orbit and clock product streams from the IGS RTS and CNES. Table 4.8 shows the names and characteristics of these product streams.

Table 4.8: Description of RT product streams

Stream	Content	Message Types	Provider
RTCM3EPH	Broadcast Ephemeris	1019, 1020, 1045	BKG
IGS01	Orbit/Clock Correction (single epoch solution)	1059, 1060	ESA
IGS02	Orbit/Clock Correction (Kalman filter combination)	1057, 1058, 1059	BKG
IGS03	Orbit/Clock Correction (Kalman filter combination)	1057, 1058, 1059, 1063, 1064, 1065	BKG
CLK9B	Orbit/Clock Correction + Corrections for Integer Ambiguity Resolution	1059, 1060, 1065, 1066	CNES

4.4.2 NRT Products

Out of the products listed in Table 4.5, the NRT processing systems use the IGS Ultra-Rapid (IGU) products for the hourly processing and IGS Final products for the computation of a priori coordinates using PPP.

4.4.3 PP Products

The PP processing system used in this research makes use of the reprocessed orbit and clock products generated by CODE (referred to as CODE Repro2 products). The reason for the selection of the CODE Repro2 products is the consistency of these products during the whole processing period.

4.4.4 Atmospheric Products

The IGS Final zenith total delay product (Table 4.7) has been used in this research as one of the reference products to conduct the assessment of RT-PPP ZTD estimates. In the text of this thesis, this product is referred to as the IGS Final Troposphere product (IGFT).

4.5 Sources of Meteorological Data

This section introduces the sources of meteorological data which have been used in this research. The sources consist of meteorological sensors, reanalysis datasets based on numerical weather models and gridded data files.

4.5.1 MeteoLux Weather Station

MeteoLux is the meteorological service unit of the Air Navigation Administration (ANA) of Luxembourg and provides the aeronautical and general meteorological services for Luxembourg. MeteoLux (`http://www.meteolux.lu/`) operates a weather station at Luxembourg Airport which has a World Meteorological Organization (WMO) identifier 06590. As the airport is located in the Findel area of Luxembourg, this weather station will be referred to as Findel in this thesis. Findel provides meteorological data with a temporal resolution of 1-minute which is updated at hourly intervals. It has been used to obtain precipitation and temperature data for this research. Table 4.9 shows the coordinates of the Findel sensor whereas Table 4.10

shows the distances and height differences between the six SPSLux GNSS stations and Findel. The height differences in Table 4.10 are computed by subtracting the Findel sensor height from the SPSLux station heights.

Table 4.9: Coordinates of the MeteoLux Findel meteorological sensor

Latitude [^{o}]	Longitude [^{o}]	Height [m]
49.62	6.22	369

Table 4.10: Distance and height difference between various SPSLux stations and the Findel sensor

SPSLux Station	Findel	
	Distance [km]	Height Difference [m]
BASC	21.05	6.76
ECHT	25.34	-64.47
ERPE	10.95	-151.61
ROUL	42.78	173.38
TROI	58.39	168.82
WALF	7.65	-76.60

4.5.2 The ASTA Network of Meteorological Sensors

The Administration des Services Techniques de l'Agriculture (ASTA) [English: Administration of Technical Services for Agriculture] of Luxembourg has established a network of over 50 meteorological sensors in Luxembourg (`http://www.agrimeteo.lu/`) to provide meteorological information to the agricultural community of the country. All the sensors in this network measure temperature whereas only 3 of the sensors measure the surface pressure in addition to temperature. The temporal resolution of the meteorological data from the ASTA network is 1-hour and is available for download at (`http://www.agrimeteo.lu/`). The pressure is reported at mean sea level (MSL) and temperature is reported 2 m above surface. ASTA files are provided in comma separated values (CSV) format and the order of columns in the station-specific files depend on the number of parameters available in a particular station data. Due to the dense distribution of the sensors all over the country, all of the 6 SPSLux GNSS stations have an ASTA meteorological sensor located nearby. Table 4.11 lists the nearby pressure and

temperature sensors to each of the SPSLux station along with the distance and height differences. The height differences in Table 4.11 are computed by subtracting the ASTA sensor heights from the SPSLux station heights.

The ASTA data amongst others form the basis for the Atlas Hydro-Climatique du Grand-Duch de Luxembourg (English: Hydroclimatic Atlas of the Grand Duchy of Luxembourg) prepared by the Luxembourg Institute of Science and Technology (LIST) (`https://www.list.lu/`). LIST therefore performs a quality control of the ASTA data. However, as LIST currently does not provide these quality controlled data in a timely manner required for NRT and RT applications, it is inevitable to use the raw ASTA data (i.e. the data which is not quality controlled) for this thesis. Nevertheless, ASTA data has been screened for outliers during this research.

4.5.3 UK Met Office

To support GNSS meteorology applications, the UK Met Office routinely provides an hourly file of meteorological data from the network of globally distributed WMO weather stations. The hourly NRT system used in this research uses this file to convert the ZTD at the ground-based GNSS station locations to IWV by choosing and correcting the pressure and temperature values from the nearest available WMO station. This is important to mention that data from the MeteoLux Weather Station (Findel) is also included in this hourly file and is thus the first choice for the ZTD to IWV conversion for the SPSLux GNSS stations. The format of the hourly file provided by the UK Met Office is shown in Table 4.12. As an example, Table 4.13 shows an extract from the hourly file provided by the UK Met Office at 2015-03-28 0000UTC. The data record from the Findel sensor has been emphasized in Table 4.13 for visibility purposes.

4.5.4 Radiosonde Observations

For validation and evaluation of RT-PPP GNSS-derived ZTD, the ZTD estimates derived from the observations of RS have been used as a non-GNSS reference product. The observations from radiosondes collocated with five selected GNSS stations have been obtained from British Atmospheric

Table 4.11: SPSLux GNSS stations and their nearest ASTA meteorological stations

SPSLux Station	Closest Pressure Sensor			Closest Temperature Sensor		
	Name (ID)	Distance [km]	Height Difference [m]	Name (ID)	Distance [km]	Height Difference [m]
BASC	Oberkorn	7.27	-49.99	Reckange	5.17	35.01
ECHT	Merl	32.87	-50.89	Echternach	0.10	13.78
ERPE	Merl	17.88	-138.03	Remich	2.16	-37.36
ROUL	Reuler	14.94	2.63	Dahl	5.13	20.63
TROI	Reuler	8.08	-1.93	Holler	3.06	33.07
WALF	Merl	6.26	-63.02	Merl	6.26	-63.02

Table 4.12: Format of the hourly meteorological file provided by the UK Met Office

Column	Content
1	First two characters of station ID
2	3rd to 5th characters of station ID
3	Station latitude
4	Station longitude
5	Station height
6	Year of the observation
7	Month of the observation
8	Day of the observation
9	Hour of the observation
10	Minute of the observation
11	Dry temperature [K]
12	Wet temperature [K]
13	Pressure (Mean Sea Level) [Pa]

Data Centre (NCAS/BADC) (NCAS-BADC 2006). Table 4.14 shows the selection of the RS sites along with their horizontal and vertical distances to the respective GNSS stations.

4.5.5 ERA-Interim

The climate reanalysis dataset from the European Centre for Medium-range Weather Forecasts (ECMWF) namely the ECMWF Reanalysis-Interim (ERA-Interim) (Dee et al., 2011) is a global dataset with a grid resolution of 0.75^o x 0.75^o, temporal resolution of 6 hours, and temporal coverage of 1976 to present (with real-time updates). Figure 4.12 shows the grid points of ERA-Interim model over Europe. In this research, the pressure and temperature values from the ERA-Interim have been assessed for their use in ZTD to IWV conversion for Luxembourg and the ZTD from the ERA-Interim has been used to validate the GNSS-derived ZTD for climate monitoring applications. All the data from ERA-Interim (pressure, temperature, ZWD, ZTD) used in this thesis have been obtained using the GOP - TropDB - TropModel online service (`http://www.pecny.cz/gop/index.php/gop-tropdb/tropo-model-service`) by specifying the coordinates of the desired locations. This service performs a bilinear interpolation of the ERA-Interim values to the requested coordinates.

Table 4.13: An extract from the hourly meteorological file provided by the UK Met Office at 2015-03-27 2300UTC

6.00	484.00	49.62	5.58	324.00	2015.00	3.00	27.00	15.00	0.00	281.50	272.5	102190.0
6.00	490.00	50.48	5.92	477.00	2015.00	3.00	27.00	23.00	0.00	277.00	272.5	102450.0
6.00	494.00	50.52	6.07	673.00	2015.00	3.00	27.00	23.00	0.00	274.10	271.6	102440.0
6.00	496.00	50.48	6.18	567.00	2015.00	3.00	27.00	23.00	0.00	273.40	272.0	102530.0
6.00	*590.00*	*49.62*	*6.22*	*379.00*	*2015.00*	*3.00*	*27.00*	*23.00*	*0.00*	*276.50*	*272.5*	*102520.0*
6.00	601.00	47.55	7.58	316.00	2015.00	3.00	27.00	23.00	0.00	276.40	272.3	102660.0
6.00	602.00	47.35	7.35	439.00	2015.00	3.00	27.00	23.00	0.00	273.80	272.4	102790.0
6.00	604.00	47.00	6.95	487.00	2015.00	3.00	27.00	23.00	0.00	278.00	271.3	102640.0
6.00	605.00	47.13	7.07	1599.00	2015.00	3.00	27.00	23.00	0.00	270.00	267.6	********
6.00	606.00	47.05	7.07	*******	2015.00	3.00	27.00	23.00	0.00	277.40	272.0	102680.0
6.00	608.00	47.05	6.98	1136.00	2015.00	3.00	27.00	23.00	0.00	273.60	268.8	********
6.00	609.00	46.55	7.02	1973.00	2015.00	3.00	27.00	23.00	0.00	268.50	267.0	********
6.00	610.00	46.82	6.95	491.00	2015.00	3.00	27.00	23.00	0.00	274.90	272.1	102710.0
6.00	612.00	47.08	6.80	1018.00	2015.00	3.00	27.00	23.00	0.00	270.90	269.6	********
6.00	616.00	47.43	6.95	597.00	2015.00	3.00	27.00	23.00	0.00	276.40	271.3	102680.0
6.00	617.00	46.98	6.62	1050.00	2015.00	3.00	27.00	23.00	0.00	269.00	268.3	********
6.00	618.00	46.73	6.57	438.00	2015.00	3.00	27.00	23.00	0.00	274.20	271.0	102750.0
6.00	621.00	47.60	9.28	*******	2015.00	3.0	27.00	23.00	0.00	278.50	273.0	102600.0

Table 4.14: The selected radiosondes used for comparison

GNSS Station ID	RS ID (WMO)	Vertical Separation (GNSS-RS) [m]	Horizontal Separation [km]
BUCU (Bucuresti, Romania)	15420	53	4
COCO (Cocos, Australia)	96996	-37	1.8
HERT (Hailsham, United Kingdom)	3882	32	4
THTI (Papeete, French Polynesia)	91938	97	3.4
VIS0 (Visby, Sweden)	2591	33	2

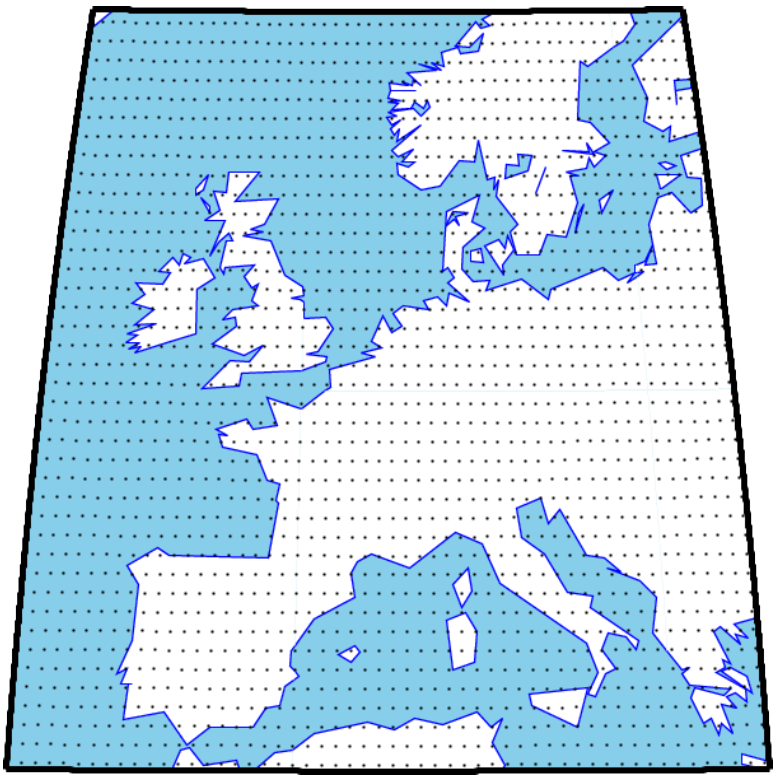

Figure 4.12: Grid of the ERA-Interim model over Europe

4.6 Data Available in Luxembourg

Figure 4.13 shows all the different types of data along with the location of the respective sensors inside the territory of Luxembourg. The red circles show the SPSLux ground-based GNSS stations, the triangles show the ASTA meteorological stations with the classification of those which provide both the temperature and pressure (purple) and those which provide only temperature (orange), and the blue square shows the location of the Findel sensor of MeteoLux. The green star shows the location of the ERA-Interim gridpoint which lies inside Luxembourg.

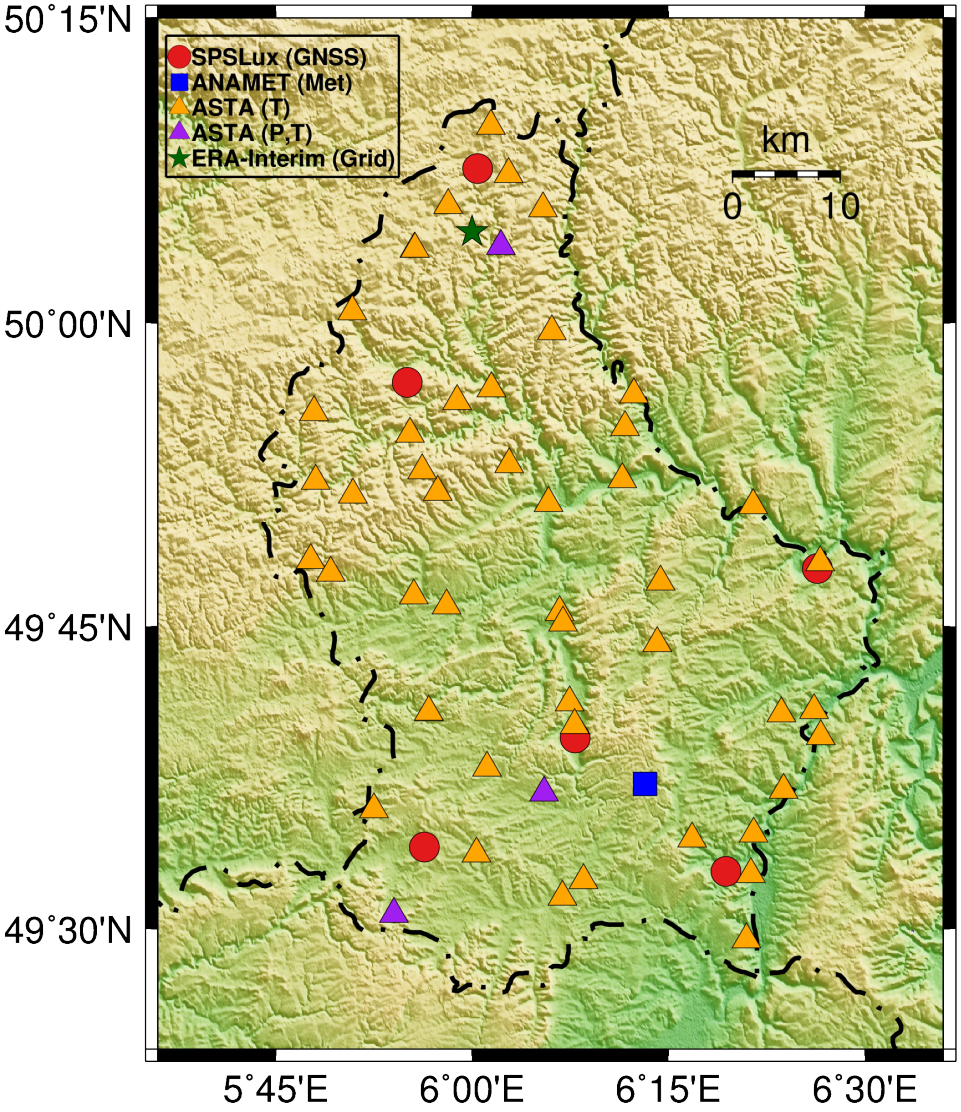

Figure 4.13: Ground-based GNSS and meteorological data sources available inside Luxembourg

Chapter 5

Results

> *In the creation of the heavens and the earth and in the alternation of the night and the day there are indeed Signs for men of understanding.*
>
> Qur'an, 3:191

This chapter presents the results of the various experiments described in Chapter 3. Along with the results, an interpretation of these results with relevance to the respective research objectives has been presented.

5.1 RT-PPP ZTD for NWP Applications

This section provides the results of the comparisons of the RT-PPP ZTD estimates obtained using various software packages as well as the results of the assessment of the suitability of RT-PPP ZTD for NWP applications. This experiment is described in Section 3.2.1.

For brevity, the BNC2.7 solutions using the IGS01 products will below be referred to as BN01, the BNC2.7 solutions using the IGS02 products as BN02, the PPP-Wizard (ambiguity float) solutions as PWFL, the G-Nut/Tefnut solutions using IGS01 products as GN01, and the G-Nut/Tefnut solutions using IGS02 products as GN02. Table 5.1 gives an overview of the product streams and software used in each of the solutions. IGS01 and IGS02 (tested with BNC2.7 and G-Nut/Tefnut) streams contain single-epoch and Kalman filter combined solutions, respectively and could help studying any impact of the product combination approaches on the RT-PPP ZTD estimates. Although the PPP-Wizard is also able to ingest the IGS01 and IGS02 product streams in non ambiguity-fixing mode, it was tested only with the CLK9B stream in order to examine the impact of ambiguity fixing by keeping all other parameters in the fixed and float solutions consistent. Various technical problems, often related to data communication, compromise the transfer of real-time data and lead to gaps in the observation data and hence 100% of the data is not available in real-time, which results in

Table 5.1: Combinations of software package and product streams used in RT-PPP ZTD solutions

Solution	Software Used	Ephemeris Stream Used	Orbit/Clock Product Used
BN01	BNC2.7	RTCM3EPH	IGS01
BN02	BNC2.7	RTCM3EPH	IGS02
PWFL	PPP-Wizard	RTCM3EPH	CLK9B
GN01	G-Nut/Tefnut	RTCM3EPH	IGS01
GN02	G-Nut/Tefnut	RTCM3EPH	IGS02

gaps in the RT-PPP ZTD time series. In addition, some software packages provide more ZTD estimates than others based on the same input data. Table 5.2 shows the percentage of ZTD estimates obtained from each of the RT solutions for each station.

On average, the RT-PPP ZTD estimates were available for 78% of the selected time period from BNC27, 65% from PPP-Wizard, and 92% from G-Nut/Tefnut. The lower amount of available RT-PPP ZTD estimates from PPP-Wizard is due to missing data and product streams caused by a temporary network related issue at UL from 2013-05-10 to 2013-05-18. Apart from the missing data, another reason for missing estimates for some epochs is that during the PPP convergence period after a data gap, ZTD estimates with large formal sigma are rejected.

5.1.1 Internal Evaluation

For each station used in this study, the various RT-PPP ZTD time series obtained from all the solutions follow the same pattern. As an example, the RT-PPP ZTD time series from four stations is shown in Figure 5.1. Figure 5.2 shows the time series of the difference between the RT-PPP ZTD estimates and the IGFT for these stations. The difference time series of PWFL solution in Figure 5.2 has been plotted after removing the mean bias (considering the fact that the bias in the ZTD is removed before NWP assimilation, however, it is important that the bias is stable over time). The gap in the PWFL difference time series around day 11 for all 4 stations is due to a temporary interruption in the CLK9B product stream. For the station BOR1 (top right), the gap in the difference time series for all the RT solutions around day 3 is due to an interruption in the data stream from

Table 5.2: Percentage of available RT-PPP ZTD epochs in different solutions

Station	BN01	BN02	PWFL	GN01	GN02
ADIS	75	67	64	94	94
ALBH	97	95	55	95	95
AUCK	91	86	68	97	96
BOR1	87	87	63	92	91
BRST	88	86	68	98	98
BUCU	98	98	68	85	84
COCO	60	86	65	95	95
DAEJ	96	96	67	96	96
DUBO	98	97	64	98	98
GOPE	92	92	64	93	93
HERT	93	91	68	98	98
HOFN	93	90	67	97	97
KIR0	90	89	66	98	98
MATE	61	52	65	83	82
NKLG	52	53	69	99	99
NTUS	53	74	68	99	98
ONSA	88	86	66	99	98
POTS	56	52	68	98	98
REYK	73	77	61	91	91
THTI	61	47	68	99	99
VIS0	94	95	68	84	84
WTZR	81	81	61	89	89

that station for this period. The gap in the GN01 and GN02 solution for the station BUCU (bottom left) around day 14 is also due to an interruption in the data stream at that time at GOP.

The overall biases between the RT-PPP ZTD estimates from the individual RT solutions and the IGFT are shown in Table 5.3. It can be seen that the G-Nut/Tefnut solutions (GN01 and GN02) have a better stability (i.e. lower standard deviation of the mean bias) as compared to the BNC2.7 solutions (BN01 and BN02). It should be noted that the two G-Nut/Tefnut solutions used the same strategy, software and data access, so any difference in results reflects stability and reliability issues related to the applied products. Similarly, for the two BNC2.7 solutions, the same processing strategy was used and the only difference was in the applied products. However, unlike the G-Nut/Tefnut solutions, the mutual difference (in terms of mean

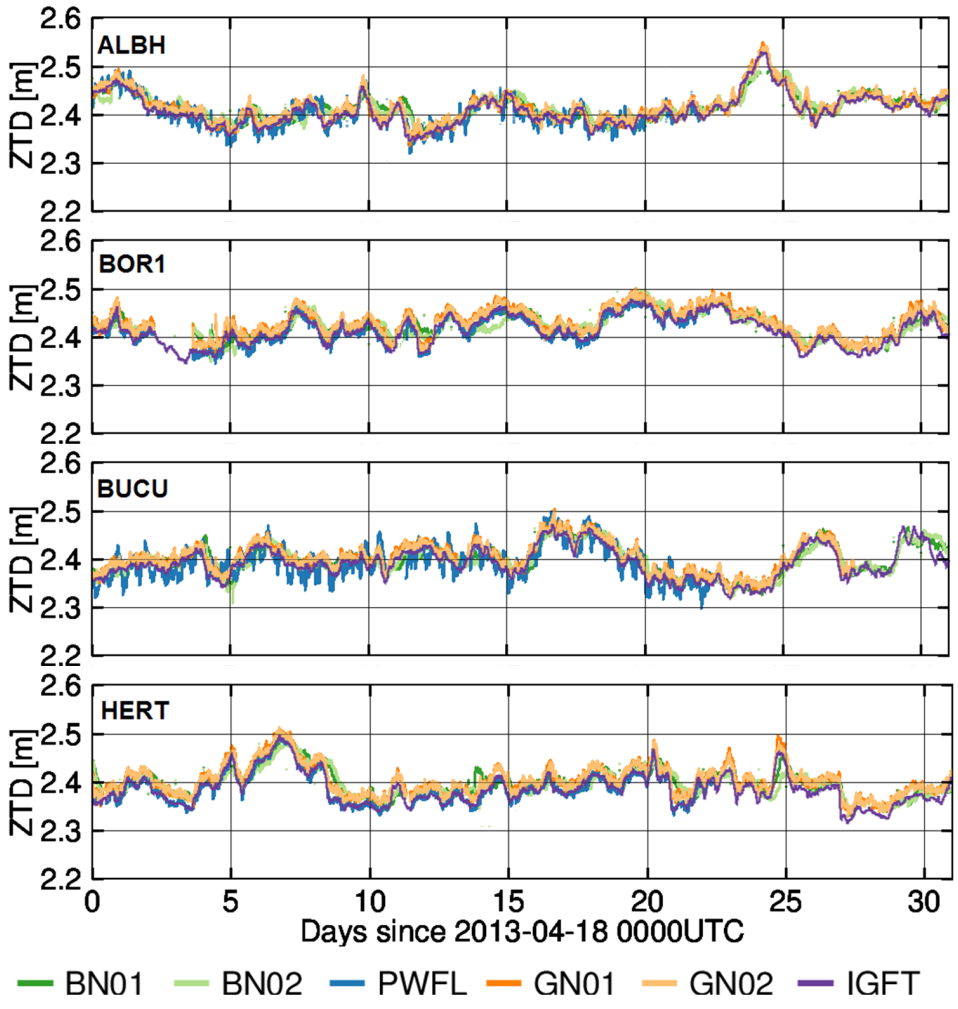

Figure 5.1: Time series of RT-PPP ZTD for the stations ALBH, BOR1, BUCU and HERT in days since 2013-04-18 18:00:00 UTC

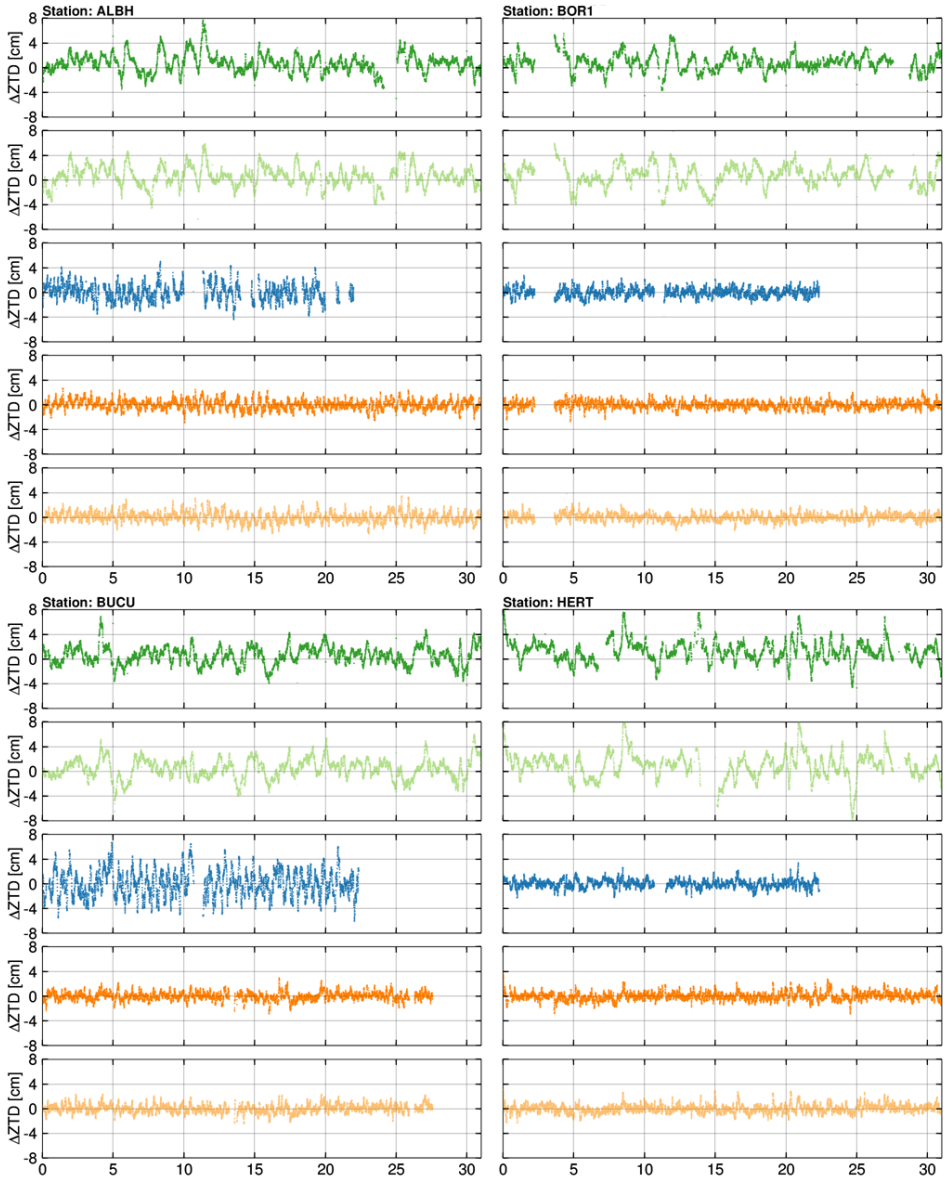

Figure 5.2: Difference of RT-PPP ZTD estimates and IGFT for the stations ALBH, BOR1, BUCU and HERT in days since 2013-04-18 18:00:00 UTC. Panels from the top: BN01, BN02, PWFL, GN01, GN02

Table 5.3: Biases in RT-PPP ZTD solutions to IGFT

Solution	Mean [cm]	SDev [cm]	RMS [cm]
BN01	3.17	4.61	6.04
BN02	0.21	2.72	2.92
PWFL	6.81	2.42	14.96
GN01	1.16	0.82	1.43
GN02	1.09	0.80	1.38

bias and RMS bias) between the two BNC2.7 solutions is relatively larger. One possible reason for the lower mean bias and RMS bias in BN02 as compared to BN01 could be the use of a Kalman Filter combination orbit/clock correction stream (IGS02) rather than a correction stream with single epoch solution (IGS01) as in BN01. The RMS of the mean bias between the RT-PPP ZTD from the BNC software and that from the IGFT as shown by Yuan et al. (2014) is lower than that found in this study and this is because of the fact that they have implemented ocean tide loading corrections, an improved mapping function and receiver antenna PCV corrections in their version of BNC. The PPP-Wizard's ambiguity float solution (PWFL) has the largest mean bias and RMS bias which is a consequence of the fact that the PPP-Wizard currently does not allow the application of antenna reference point (ARP) up eccentricity (height from the survey marker to the ARP) and receiver antenna phase center PCO and PCV corrections, hence resulting in a mismatch between the constrained coordinates of the survey marker and the ZTD estimation at the antenna phase center. Table 5.4 shows the station-wise biases in PWFL with respect to the ARP up eccentricities. However, for the assimilation into NWP models, it can be argued that the standard deviation of the mean bias is of more importance than the mean bias, because any station-specific biases are corrected for during the screening process before the assimilation. Also, aforementioned mean biases of the RT-PPP ZTD solutions (calculated over all stations) have less significance than that of the standard deviations because the biases vary with location and characteristics of the station.

As mentioned earlier, the PPP-Wizard is capable of resolving integer ambiguities in RT-PPP. In order to study the effect of integer ambiguity resolution on the RT-PPP ZTD estimates, another RT solution for the same

Table 5.4: Station-wise mean bias in PWFL and the ARP UP eccentricity

Station	ARP Up Eccentricity [cm]	PWFL Bias [cm]
ADIS	0.10	3.14
ALBH	10.0	2.2
AUCK	5.50	-3.29
BOR1	6.24	4.66
BRST	204.31	54.58
BUCU	9.70	9.09
COCO	0.40	-4.78
DAEJ	0.00	-0.77
DUBO	10.00	2.15
GOPE	11.14	5.73
HERT	0.00	2.53
HOFN	3.19	4.92
KIR0	7.10	12.45
MATE	10.10	5.85
NKLG	304.30	64.74
NTUS	7.76	-75.81
ONSA	99.50	26.03
POTS	12.06	6.11
REYK	5.70	4.78
THTI	104.70	13.67
VIS0	7.10	5.05
WTZR	7.10	6.73

stations and time period as above was obtained using PPP-Wizard with the integer ambiguity resolution feature. We term this solution as PWFX. Keeping in view the time needed for ambiguity convergence, only those epochs ($\approx$ 40% of the total) from PWFX have been included in the evaluation for which the number of fixed ambiguities is greater than or equal to 4. The mean bias between the RT-PPP ZTD of PWFL and PWFX solutions was found to be 0.61 $\pm$ 4.66 cm with an RMS bias of 4.93 cm. The observed impact of ambiguity resolution on ZTD is approximately 6 mm which compares well to, e.g. the 20% (4 to 5 mm) impact observed by Geng et al. (2009). The recent study by Li et al. (2014), which is based on their in-house software and products, also reported on insignificant differences between the RT-PPP float and fixed solutions after sufficiently long times of convergence. However, they demonstrated the usefulness of ambiguity fixing for the rapid re-initialization of an RT-PPP processing system (e.g.

after an interruption in the data stream).

To verify the claimed reason for the large mean bias and RMS bias in the PPP-Wizard solutions, i.e. the lack of ARP up eccentricity, PCO and PCV corrections, another processing experiment for a different 1-week long period using the PPP-Wizard was conducted in which the coordinates were corrected for the ARP up eccentricities and the PCO prior to processing, where the L1 and L2 PCOs have been combined by using the ionosphere-free linear combination, i.e.

$$PCO_{L1+L2} = \frac{f_1^2 PCO_{L1} - f_2^2 PCO_{L2}}{f_1^2 - f_2^2} \tag{5.1}$$

where $f_1 = 1575.42MHz$, $f_2 = 1227.60MHz$ and PCO values are in millimeters.

Integer ambiguity resolution was also applied during this experiment. We name the PPP-Wizard solution from this new experiment as PWFX2. The RT-PPP ZTD estimates from PWFX2 were then compared to the corresponding IGFT estimates. The mean bias between IGFT and PWFX2 was found to be 2.33 ± 2.76 cm (in contrast to 6.81 ± 2.42 cm for IGFT-PWFL) with an RMS bias of 4.60 cm (in contrast to 14.96 cm for IGFT-PWFL). This implies that after applying the ARP up eccentricity and PCO corrections to the a-priori coordinates, the mean bias between the ZTD estimates from PPP-Wizard and IGFT was reduced by approximately 66% and the RMS reduced by approximately 70%.

5.1.2 External Evaluation

The statistics from the comparison of GNSS-derived ZTD and RS-based ZTD are summarized in Table 5.5. In terms of standard deviation, the G-Nut/Tefnut solutions (GN01 and GN02) show the best agreement with the RS-based ZTD whereas, in terms of the mean bias, BNC2.7 solutions (BN01 and BN02) show the best agreement with the RS-based ZTD. The BNC2.7 solutions show mean biases between 1 to 2 cm, whereas G-Nut/Tefnut and PPP-Wizard solutions show mean biases between 2 to 3 cm with the RS-based ZTD. In contrast to the comparison with IGFT (Table 5.3), the mean bias of the BN01 solution is lower than that of the G-Nut/Tefnut solutions

Table 5.5: Statistics of comparison between GNSS-derived and RS-based ZTD

RT-PPP Solution	Mean (ZTD_{GNSS}-ZTD_{RS}) [cm]	SDev (ZTD_{GNSS}-ZTD_{RS}) [cm]	RMS (ZTD_{GNSS}-ZTD_{RS}) [cm]
BN01	1.40	3.44	4.41
BN02	1.71	3.19	4.30
PWFX2*	2.76	3.12	5.23
GN01	2.17	1.32	3.04
GN02	2.12	1.29	3.01

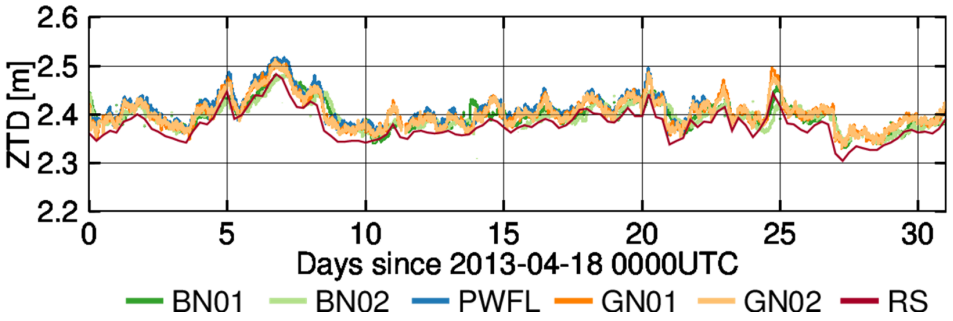

Figure 5.3: RT-PPP ZTD estimates and RS-based ZTD for station HERT

which is because of the fact that the statistics of the radiosonde comparisons are based on the 5 selected stations (unlike 22 stations in the case of IGFT comparisons) and the biases are station specific. However, the RS-based ZTD also has an uncertainty and it is possible that it has a bias due to inaccurate height corrections. Figure 5.3 shows the time series of GNSS-derived and RS-based ZTD estimates for the station HERT as an example. It can be seen that all the time series follow the same pattern and both the GNSS-derived and RS-based ZTD are sensitive to the variations in a similar fashion. This is also the case for the other 4 stations not shown in Figure 3. The time series of the difference between the RT-PPP ZTD solutions and the RS-based ZTD for the station HERT are shown in Figure 5.4.

5.1.3 Comparison with User Requirements for NWP Nowcasting

The COST Action 716: Exploitation of Ground-Based GPS for Climate and Numerical Weather Prediction Analysis, which was a demonstration project

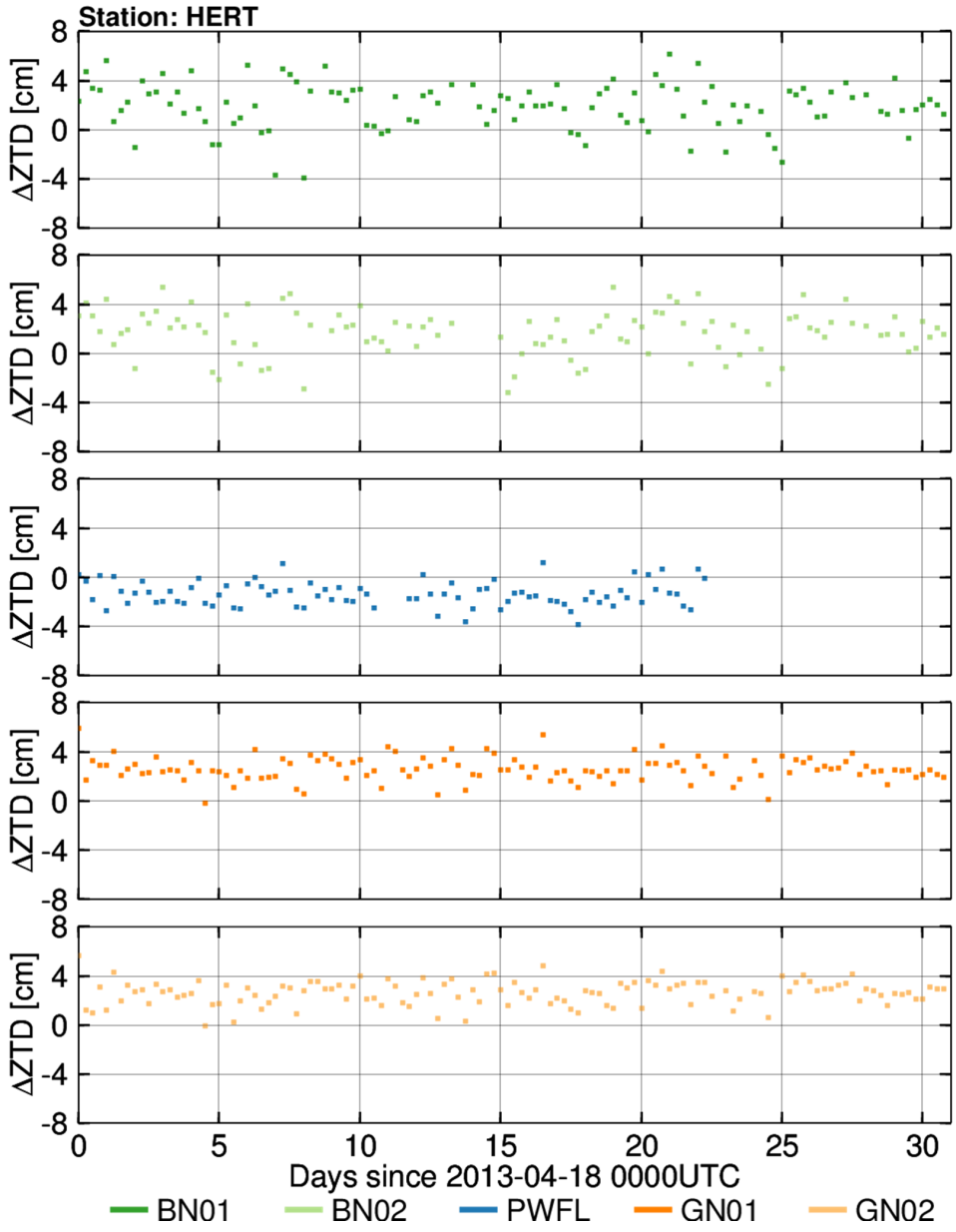

Figure 5.4: Difference of RT-PPP ZTD and RS-based ZTD estimates for station HERT

Table 5.6: User requirements for GNSS meteorology (NWP nowcasting)

Integrated Water Vapour (IWV)		
Parameter	Target	Threshold
Horizontal Domain	Europe to National	
Repetition Cycle	5 min	1 hour
Integration Time	MIN(5 min, rep cycle)	
Relative Accuracy	1 kg/m^2 (6 mm in ZTD)	5 kg/m^2 (30 mm in ZTD)
Timeliness	5 min	30 min

to study the potential of ZTD products from ground-based GPS networks for NWP and climate monitoring, specified various user requirements (Offiler, 2010) for GNSS meteorology which define threshold and target values on resolution, accuracy and timeliness of ZTD and IWV estimates for use in NWP nowcasting and climate monitoring. These requirements are widely accepted for quality control during operational use. Table 5.6 summarizes the current user requirements for NWP nowcasting however, during the new COST Action ES1206 (GNSS4SWEC), these requirements will be revised. The typical value of the dimensionless conversion factor Q (Askne and Nordius, 1987) used for the conversion of ZWD to IWV is approximately 6 and therefore 1 kg/m^2 of IWV is equivalent to about 6 mm of ZTD (Glowacki et al. 2006). Using this equivalence, the accuracy requirements for IWV can be translated to their equivalent for ZTD which are 6 mm (0.6 cm) target and 30 mm (3 cm) threshold values. Considering the IGFT as the truth and the RMS bias of each solution from IGFT as a measure of its relative accuracy, the obtained RT-PPP ZTD solutions can be compared to these requirements. Table 5.7 shows this comparison for each RT solution generated in this study.

It can be seen from Table 5.7 that BN02, GN01 and GN02 meet the threshold requirement for relative accuracy whereas BN01, PWFL and PWFX2 exceed the threshold. Noting that although the application of the ARP up eccentricity and PCO corrections on the coordinates prior to processing has improved the relative accuracy of the PPP-Wizard solution (PWFX2), it still currently exceeds the threshold requirements for NWP nowcasting.

A similar comparison to these user requirements conducted by considering the RMS of the difference between GNSS-derived ZTD and RS-based ZTD

Table 5.7: Comparison of RT systems to the user requirements for GNSS Meteorology as outlined by COST Action 716

RT-PPP Solution	ZTD relative accuracy [cm]	Difference from required target [cm]	Difference from required threshold [cm]	Remarks
BN01	6.04	5.44	3.04	Exceeds the threshold
BN02	2.92	2.32	-0.08	Meets the threshold
PWFL	14.96	14.36	11.96	Exceeds the threshold
GN01	1.43	0.83	-1.58	Meets the threshold
GN02	1.38	0.78	-1.62	Meets the threshold
PWFX2	4.60	4.00	1.60	Exceeds the threshold

as a measure of relative accuracy yields that only the two G-Nut/Tefnut solutions (GN01 and GN02) meet the threshold requirements whereas the others exceed the threshold. However, the RS-based ZTD also has an uncertainty and it is possible that it has a bias due to inaccurate height corrections.

5.2 NRT-DDP ZTD for NWP Applications

This section provides the results of the various stages of the experiment conducted to assess the impact of the assimilation of GNSS-derived NRT-DDP ZTD into the AROME 3D-VAR NWP model. This experiment is described in Section 3.2.2.

5.2.1 Pre-Processing and the White List

At the time of this research, the operational "white list" for AROME contained 806 station-center pairs from the E-GVAP dataset. This list was extended by adding 155 stations from UL01 dataset.

The statistics from the comparison of the NRT-DDP ZTD estimates from the UL01 solution to those obtained by the 3-hour short range forecast of the AROME model are shown in Figures 5.5 and 5.6. Figure 5.5 shows the station-wise mean of the bias in ZTD (UL01−AROME) computed over the period of July 17−August 20, 2013 whereas Figure 5.6 shows the station-wise standard deviation of this bias computed over the same period. This monitoring was performed in order to select the stations that could enter a white list prior to data assimilation. Even though stations present in the white list could be rejected a-posteriori in the assimilation process through various quality controls, the stations absent from the white list are rejected a-priori.

Figure 5.7 displays the number of observations assimilated in the AROME operational system, that went operational on the 2nd of July 2013, for a particular day (26 January 2014) with significant rainfall events over the domain. Four main observation types dominate: radiances from the two IASI instruments (with more than 100 channels each) (27%), radial winds and pseudo-humidity profiles from radars (22%), data from surface weather stations (16%), and aircraft reports (15%). Then, satellite data (dominated

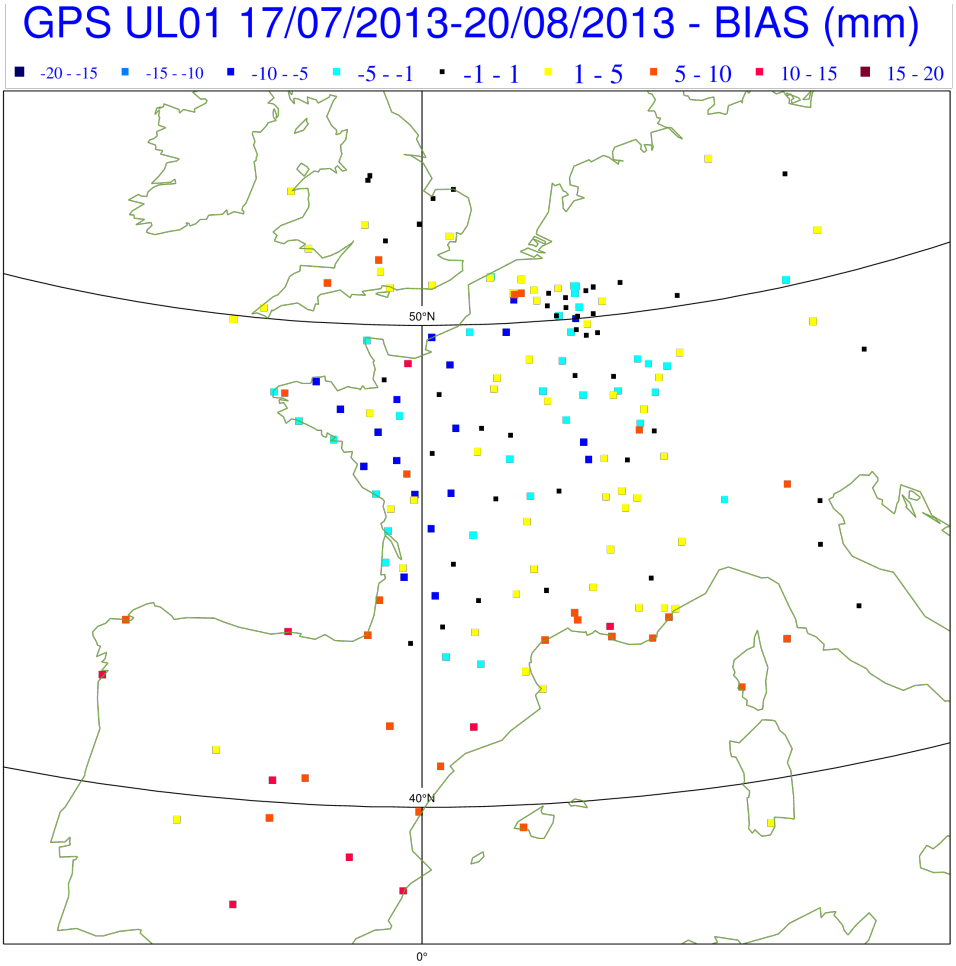

Figure 5.5: Station-wise mean bias in NRT-DDP ZTD (UL01-AROME)

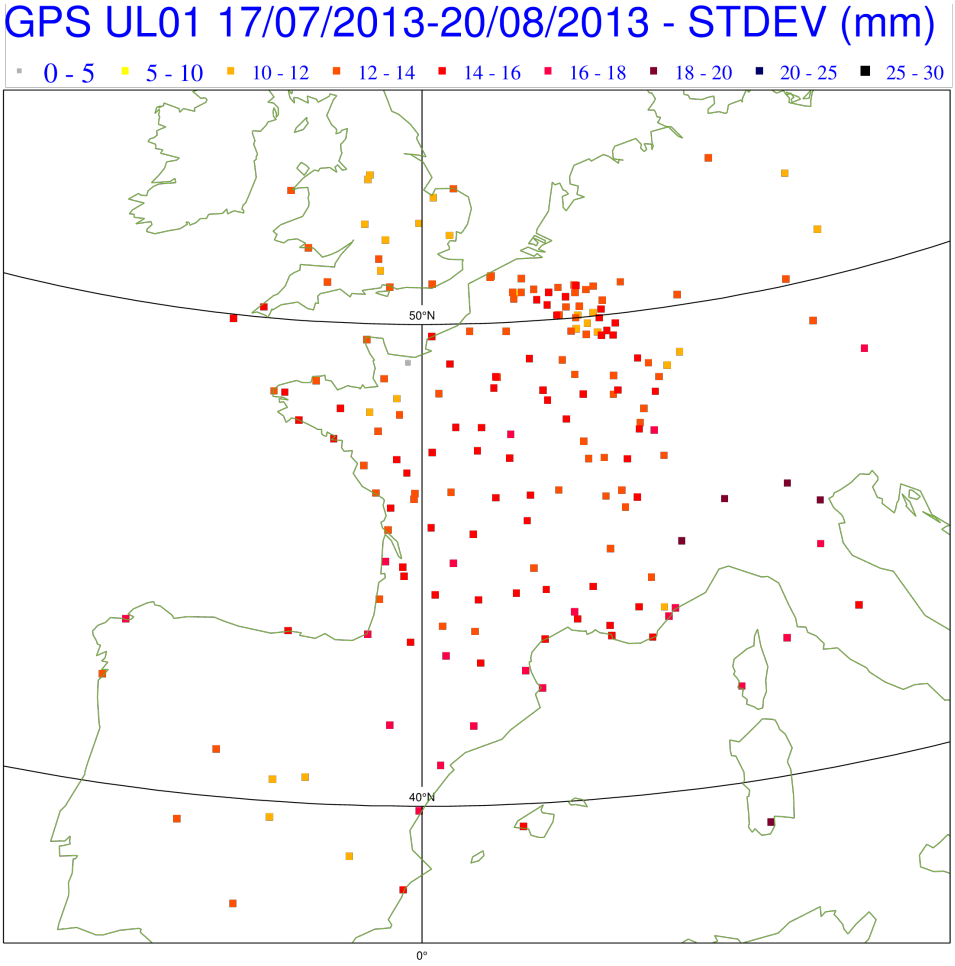

Figure 5.6: Station-wise standard deviation of the mean bias in NRT-DDP ZTD (UL01-AROME)

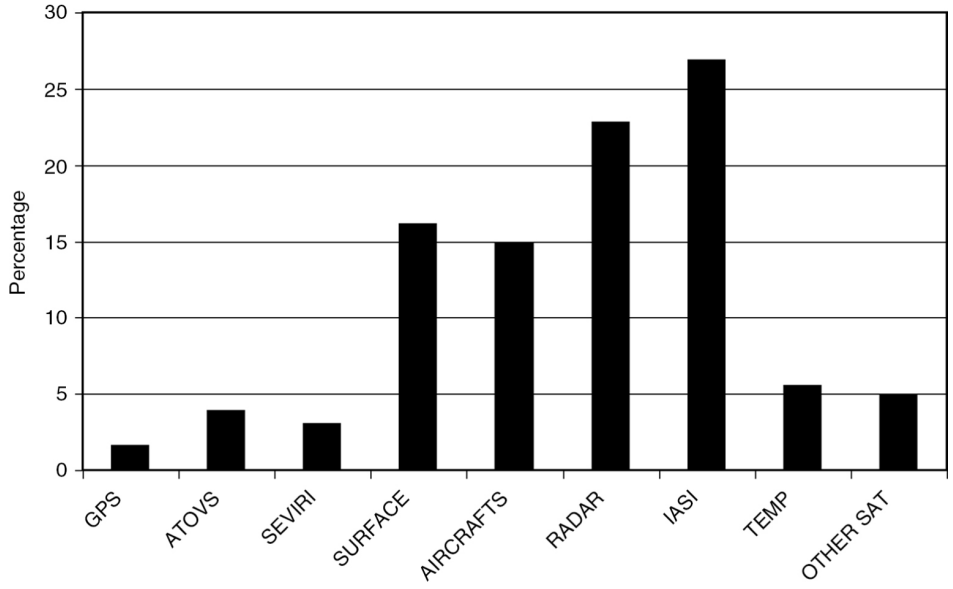

Figure 5.7: Number of observation types (expressed in percentage) assimilated in the operational 3D-Var AROME system on 26 January 2014. The total number of observations is 309 393

by SEVIRI and ATOVS radiances) and radiosoundings represent about 17% of the observations, whereas GPS ZTD are only 1.6% of the total data. This percentage still only reaches 6% when considering only observations sensitive to atmospheric moisture; however, this small amount is partly compensated by the fact that these measurements are available every 3 hours in the AROME 3D-Var RUC in all weather conditions with a relatively good accuracy.

5.2.2 Bias Correction and Final Selection

From the initial list of GPS stations from UL01 (about 200), only 155 were retained for assimilation based on the selection criteria. In particular the set of six stations in Luxembourg were excluded since they presented too large mean biases (around 30 mm). Here it is worth mentioning that this was the first time that the 6 stations from SPSLux were compared to a non-GPS technique for the estimation of ZTD and therefore the existence of this large bias was one of the important findings of this study. Upon investigation, it was found that the reason for this behaviour was the double application of

Table 5.8: Statistics of bias with AROME equivalent ZTD for SPSLux and WALCORS networks

Network	No. of stations	Bias [mm]	SDev [mm]
SPSLux (Luxembourg)	6	-30.58	15.38
WALCORS (Wallonie)	22	0.63	12.87

PCO corrections on the SPSLux observation data i.e. once on RT streams (and in the resulting RINEX files) and once during the processing. This problem was fixed after the completion of this study and if such a study is conducted in the future, it is assured that the 6 SPSLux stations will meet the requirements to enter the "white list". On the other hand, a set of 22 stations in Belgium was retained since the mean bias was only 0.63 mm. Figure 5.5 reveals this increased density of stations over the Eastern part of Belgium (Wallonie).

The mean bias between the NRT-DDP ZTD estimates from UL01 and those from AROME (for the complete UL01 network) was found to be 0.18 $\pm$ 13.92 mm with an RMS of 15.29 mm. As mentioned earlier, the added value of the UL01 stations as compared to the existing E-GVAP solutions was the dense GNSS network over Luxembourg and Wallonie (Belgium) regions and hence it was of great interest to look at the quality of NRT-DDP ZTD estimates from the stations in that network. The statistics for this network are explicitly shown in Table 5.8.

It can be seen from Table 5.8 that the NRT-DDP ZTD estimates from the 6 GNSS stations located in Luxembourg (SPSLux) have a large mean bias of -30.58 mm and hence were rejected after the initial screening whereas the stations belonging to the WALCORS network show a sub-millimeter bias and passed the criteria of the initial screening. After the initial screening, various processes are applied on the ZTD observations (e.g. spatial thinning, bias removal) and a final list of stations to be used for assimilation is prepared. Figure 5.8 shows the number of stations from the UL01 solution finally selected for assimilation during the whole period of the experiment. It can be seen from Figure 5.8 that the number of selected UL01 stations has a diurnal cycle. Similar diurnal cycles (or those with a phase difference) were also found for various other analysis centers. The reason for

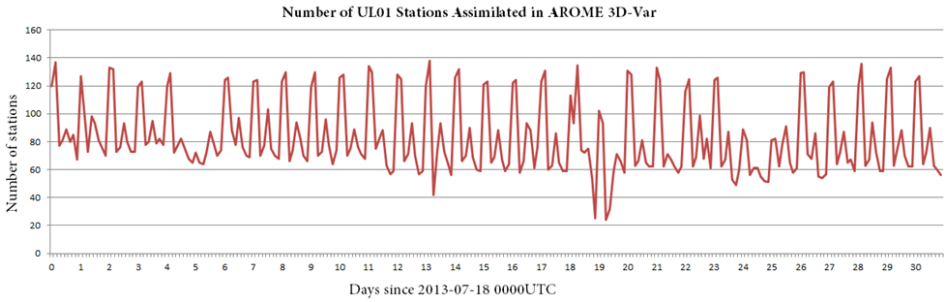

Figure 5.8: Number of UL01 stations selected for assimilation

this diurnal cycle is the variation of the agreement between the GNSS ZTD and the model equivalent ZTD at different times of the day which is caused by, for example, the day-night bias in the radiosonde observations used in the NWP model. The map of the domain of AROME model and the stations selected finally for assimilation are shown in Figure 5.9. In Figure 5.9, the black squares show the stations provided through the E-GVAP network (EGVAP), while the grey circles show the new stations processed by the UL01 solution. It should be noted that except for stations located in Belgium, the UL01 stations are also processed by other E-GVAP analysis centres.

Quality Assessment of ZTD Observations

This section summarizes the findings about the quality and suitability of the UL01 ZTD observations for data assimilation. Figure 5.10 shows the distributions of the analysis departure (the difference between the NRT-DDP ZTD observations from the equivalent from analysis) and the first-guess departure (the difference between the observed NRT-DDP ZTD and the model equivalent ZTD computed from the 3-hour AROME forecast) for the whole period of the experiment. One of the criteria that the NRT-DDP ZTD observations from a given station need to pass in order to be assimilated is that its first-guess departures should follow a Gaussian distribution. If there are more than one analysis center processing a same station, the observations are selected from the one which has the smallest standard deviation of the first-guess departures and the closest distribution of the first-guess departures to Gaussian distribution. Figures 5.10 (a) and 5.10 (b) show the distribu-

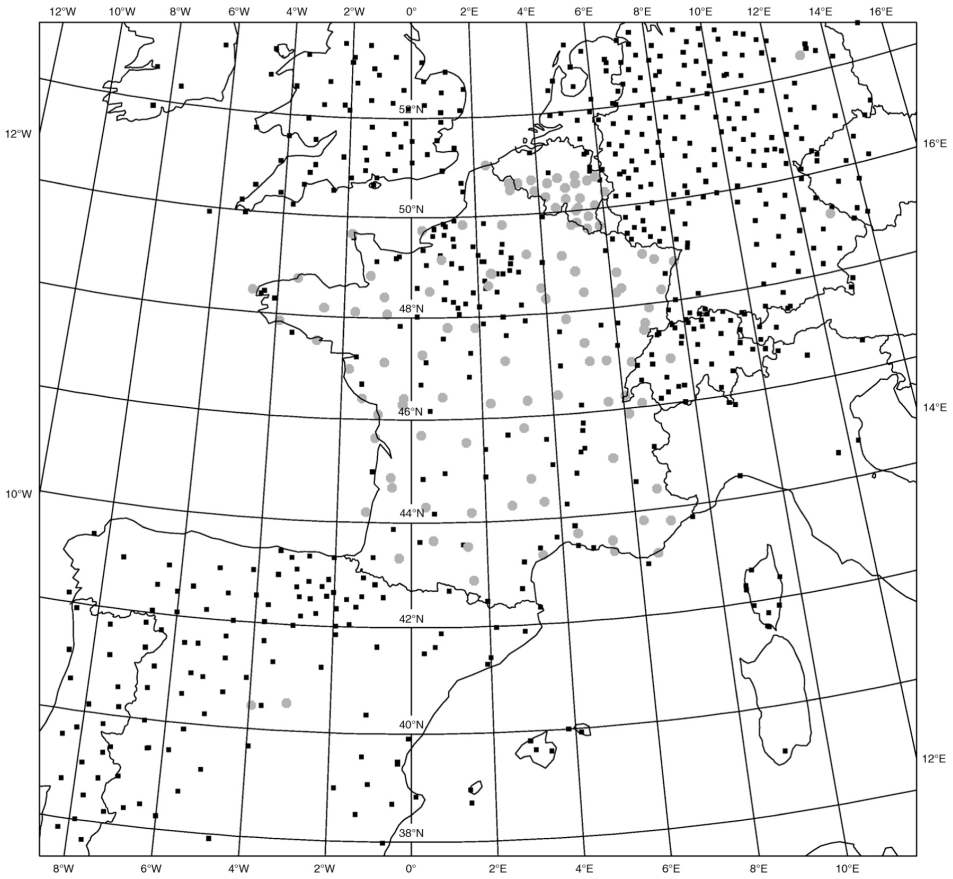

Figure 5.9: Map of the domain of the AROME model with the GPS stations selected from assimilation on the 18 July 2013 at 03 UTC

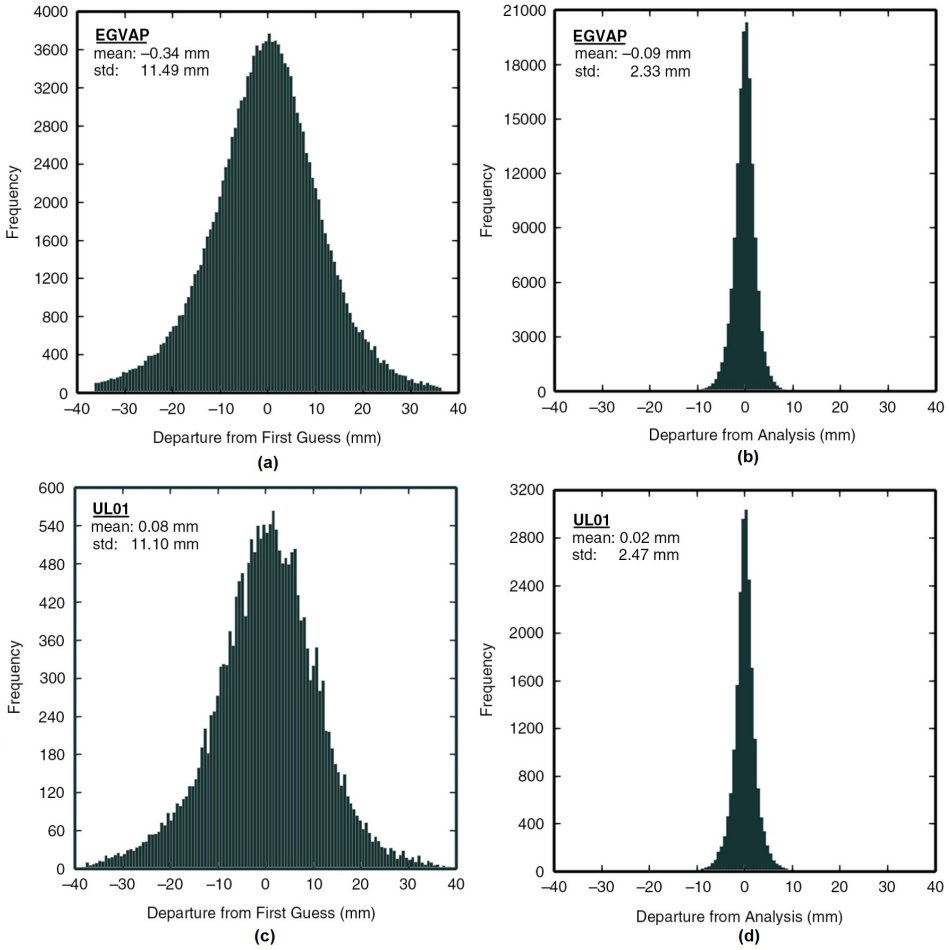

Figure 5.10: Histograms of first guess (left) departures and analysis (right) departures for GNSS-derived ZTD from experiments EGVAP and UL01

tion of analysis departure and first-guess departure, respectively, of all the ZTD observations from the operational EGVAP solutions whereas Figures 5.10 (c) and 5.10 (d) show the distribution of analysis departure and first-guess departure, respectively, of NRT-DDP ZTD observations from only the UL01 solution. First-guess and analysis departure statistics have been computed between 18 July 2013 and 21 August 2013. The upper row in Figure 5.10 corresponds to EGVAP stations (sample size: 147591) and the lower row corresponds to UL01 stations (sample size: 20572). It can be clearly seen that the UL01 observations analysis and first-guess departures follow a Gaussian distribution and hence are suitable for assimilation.

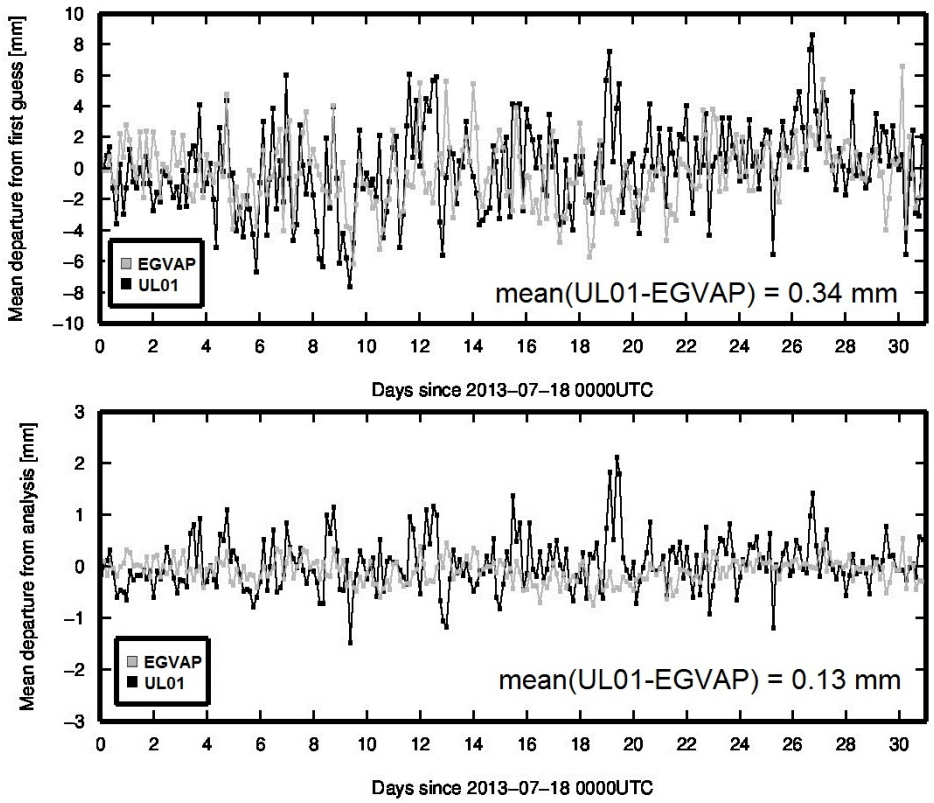

Figure 5.11: Mean of analysis departures and first guess departures for EGVAP and UL01 solutions

Figure 5.11 compares the time series of the mean of the analysis departures and first guess departures for EGVAP and UL01 solutions. It can be seen that the UL01 solution has analysis and first guess departures that are on average higher than those of the EGVAP solution. Also, the high and low values in time series of the mean analysis departure correspond to the time series in Figure 5.8 (number of stations selected for assimilation) i.e. the mean analysis departure has a higher value when the number of assimilated stations is low and vice versa. It can also be seen that the UL01 solution has a first-guess departure that is on average higher than that of the EGVAP solution but a standard deviation (Figure 5.12) that is on average lower than EGVAP.

5.2.3 Impact on Analysis

As can be seen in Figure 5.10, the narrower distribution of analysis departures, or "Observed minus Analysis" (O−A) with respect to first guess departures, or "Observed minus Background" (O−B), and a reduction of the standard deviation from 11.49 to 2.33 mm, indicates that the assimilation has brought the model state, mostly in terms of humidity field, closer to GNSS-derived ZTD observations. Considering only the GNSS-derived ZTD values processed by the UL01, the histograms also have a Gaussian shape for both (O−B) and (O−A), but they are less smooth than EGVAP due to the smaller size of the data sample (20572 vs. 147591). The mean and standard deviation of the (O−B) and (O−A) distributions compare well to those obtained with the whole set of selected EGVAP stations. This agreement reveals that the selected stations processed by UL01 have the same quality as the EGVAP stations and that the 3D-Var AROME system can assimilate them efficiently. This is also a very good check that the bias correction and the observation error specifications for UL01 are fully consistent with values imposed for the EGVAP stations. Another useful aspect of the (O−B) and (O−A) statistics to examine is their temporal evolution during the period of interest. Time series of standard deviations for (O−B) and (O−A) are compared for the two datasets EGVAP and UL01 in Figure 5.12. There is a good level of agreement between these two datasets both in terms of daily and synoptic variations. Despite a much smaller number of stations coming from UL01, their geographical distribution covers a large part of the AROME domain, allowing them to capture almost the same variability as the full EGVAP network. A diurnal cycle of the departures is also present on both time series. This is a feature present for all analysis centres: maximum values take place at 21 UTC whereas minimum values are noticed at 06 UTC, and is likely a signature of the diurnal cycle of water vapour in the boundary layer. A dependency of the bias correction with the diurnal cycle could be envisaged in future developments. Synoptic events show up on time series: the anticyclonic situations are characterized by lower values of (O−B) and (O−A), around day 14 and day 24, whereas perturbed situations exhibit higher values, around days 6, 10 and 16.

The previous analysis of (O−A) and (O−B) distributions and time series allows to check that the 3D-VAR AROME behaves as expected regarding

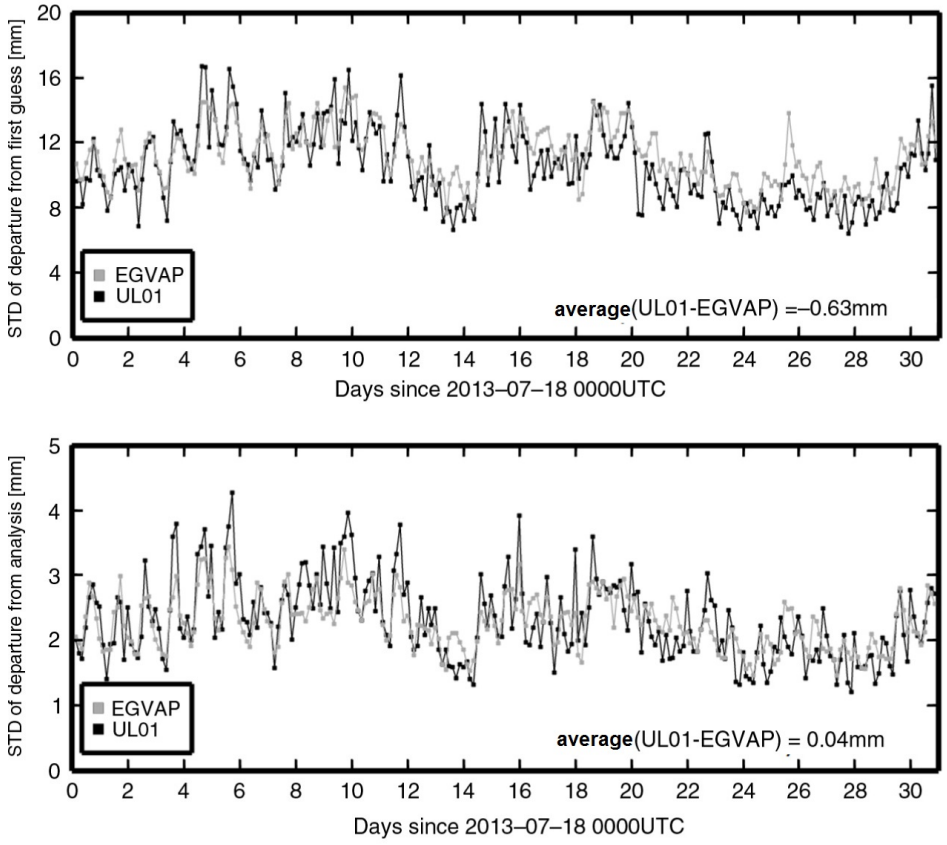

Figure 5.12: Standard deviation of analysis departures and first guess departures for EGVAP and UL01 solutions

the use of GNSS-derived ZTD observations. This is a necessary condition, but not sufficient to demonstrate that the analysis is improved by the GNSS-derived ZTD observations. Since they modify mostly the humidity field, by examining the fit of the model short-range forecasts (3-hour) to independent observations (i.e. that have not been assimilated yet), it is possible to check if the analysis from the previous cycle has been able to bring the model predicted state closer to the truth.

Figures 5.13, 5.14 and 5.15 show the fit of the AROME 3-hour forecasts to other observations sensitive to humidity (radiosoundings and moisture sensitive channels from satellite radiometers). The assimilation of GNSS-derived ZTD reduces the standard deviation of (O−B) for specific humidity from radiosoundings below 500 hPa (Figure 5.13). The UL01 observations enhance this reduction at 1000 hPa but are slightly detrimental at 700 hPa with respect to EGVAP. Regarding the window channels of the SSMI/S instrument (Figure 5.13), non-negligible improvements are noticed by the use of EGVAP for the weak water vapour absorption band at 22 GHz and also for the 85 GHz channel in vertical polarization (that has the largest errors). The influence of UL01 is either neutral or slightly negative with respect to EGVAP, but always positive with respect to NOGPS. Since SSMI/S is only available over ocean surfaces, it indicates that the corrections brought by the GNSS-derived ZTD data over land have propagated over the ocean through error correlations and model dynamics (AROME has 40% of ocean surfaces). The (O−B) of the sounding channels from the ATMS microwave instrument in the water vapour absorption band at 183 GHz are displayed in Figure 5.15. The largest impact shows up for the high peaking channels (that are closer to the centre of the absorption line at 183 GHz). It means that ZTD observations have the potential to also modify the mid-tropospheric humidity (between 500 and 300 hPa), probably through the vertical correlations imposed in the background error covariance matrix of the 3D-VAR system. This signal is more pronounced when the model state is projected onto the brightness temperature space of ATMS than on radiosonde data. The impact of UL01 is either neutral or slightly detrimental with respect to EGVAP, but still positive when compared to NOGPS. However, the signal coming from radiosoundings is certainly more robust given the fact that in the mid-troposphere the number of data from that observ-

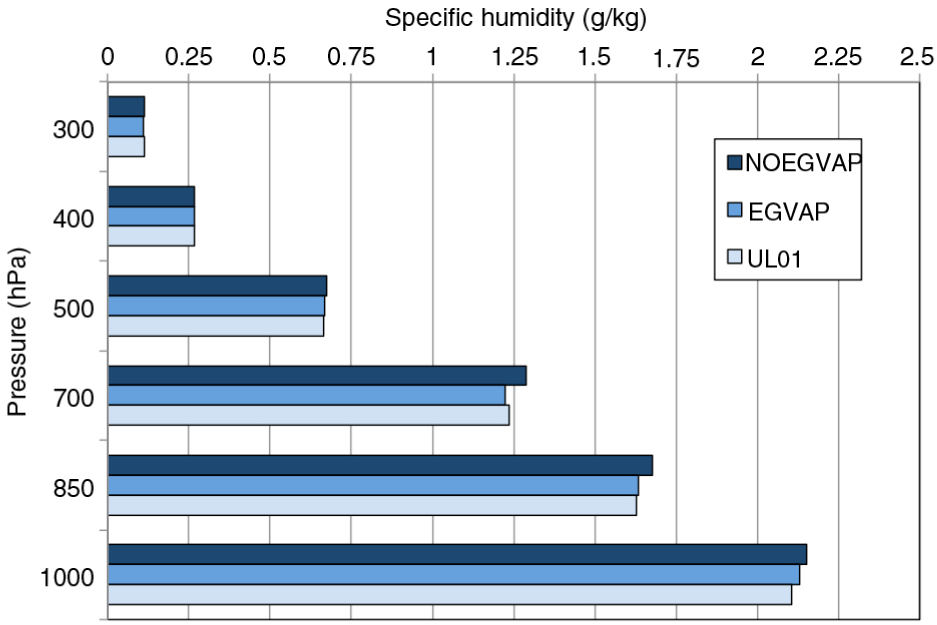

Figure 5.13: Statistics of first guess departures for specific humidity from radiosoundings (SDev errors in g/kg) computed from 18 July to 20 August 2013

ing system is about three times larger than ATMS radiances. Regarding the (O−B) biases for specific humidity from radiosoundings, negative values are noticed in the boundary layer (i.e. the model is too moist) for the experiment NOGPS (around 0.2 g/kg) are slightly reduced by about 10% through the assimilation of GNSS-derived ZTD observations.

In order to examine the impact of the background error covariance matrix on the assimilation of ZTD observations for a given analysis, the analyses produced after the first cycle of the three 3D-Var experiments were compared. Indeed, since each experiment starts from the same background field, the differences in analysis indicate the contribution of the GNSS-derived ZTD from EGVAP to modifications of the humidity field when compared to the experiment NOGPS, and also the contribution of UL01 on top of EGVAP (through differences between UL01 and EGVAP). The differences in IWV between EGVAP and NOGPS and UL01 and EGVAP are shown in Figure 5.16, and can be interpreted as analysis increments produced in the 3D-VAR by the EGVAP and UL01 ZTD networks, respectively. The

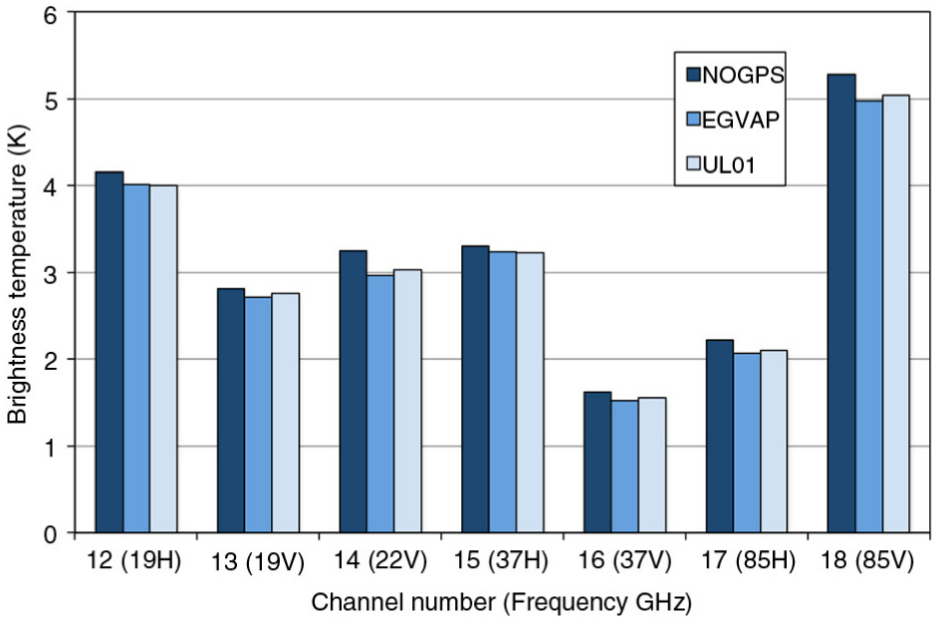

Figure 5.14: Statistics of first guess departures for the brightness temperature of the microwave radiometer SSMI/S on board DMSP F18 (SDev errors in K) computed from 18 July to 20 August 2013

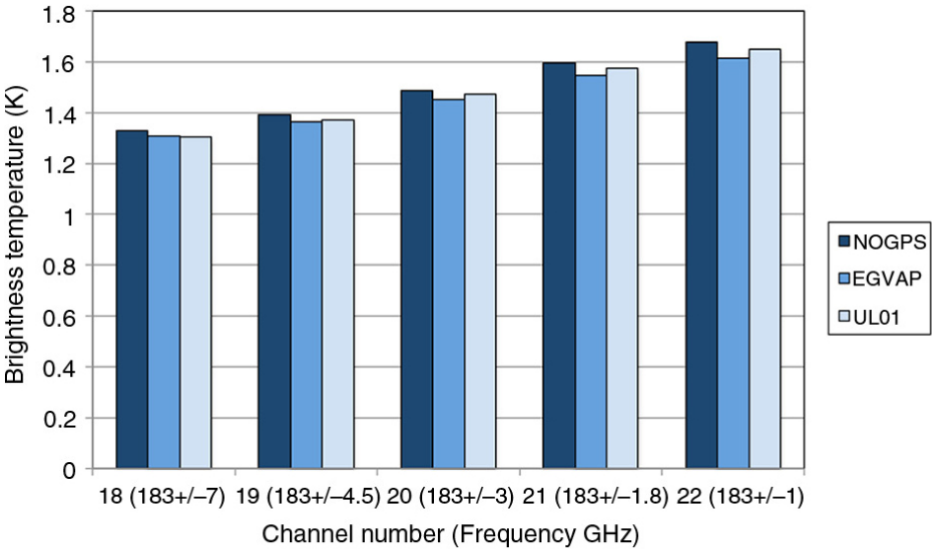

Figure 5.15: Statistics of first guess departures for the brightness temperature of the microwave sounder ATMS on board Suomi-NPP (SDev errors in K) computed from 18 July to 20 August 2013

geographical distribution of the increments follows the density of each network. The standard deviation of IWV increments for EGVAP is 0.87 mm that can be compared to the mean IWV value of 23 mm over the whole domain. The corresponding value for UL01 is 0.38 mm. Therefore the mean corrections are small. Even though mean corrections are very close to zero for EGVAP and UL01, the distribution of increments for UL01 is skewed towards positive corrections. This is specific to this date: through the whole period there is no tendency for the UL01 dataset to systematically moisten or dry the model. Maximum corrections are about 45 mm, whereas with EGVAP over the western part of Switzerland there is a local drying of 7 mm. With UL01, large corrections are taking place over the Wallonie region due to the density of the network. In the northeastern part of France (Alsace and Lorraine regions) UL01 brings corrections around 3 mm whereas almost no corrections were provided by EGVAP. This stems from the fact that the UL01 solutions have been chosen instead of the SGN (name of analysis centres from the French National Geographical Institute) ones, on the basis of a better statistical behaviour.

5.2.4 Impact on Forecasts

The impact on screen-level relative humidity RH_{2m} forecasts is presented in Figure 5.17. The AROME forecasts are examined in terms of mean and standard deviation errors with respect to a reference assumed to be close to the truth. The reference is given by screen-level analyses based on the optimum interpolation CANARI (Mahfouf et al 2015). Screen-level analyses are done independently from the atmospheric 3D-VAR analyses and are used for diagnostic purposes and to correct soil temperatures and moisture contents. Around 1600 observations are used to perform the screen-level analyses, with rather dense surface networks except over Italy and Spain. The RH_{2m} mean errors have a strong diurnal cycle with values close to zero during daytime and negative ones during night-time. The nocturnal surface boundary layer is too moist but it is also too warm as revealed by T_{2m} biases (not shown), contributing to reduce the RH_{2m} bias. The standard deviation increases with the forecast range up to 15 hours (18 UTC) and then remains around 9% error until the end of the forecast (after 30 hours). The assimilation of GNSS-derived ZTD has a small positive impact on the bias by reducing it after 15 hours of forecasts. The impact on the standard

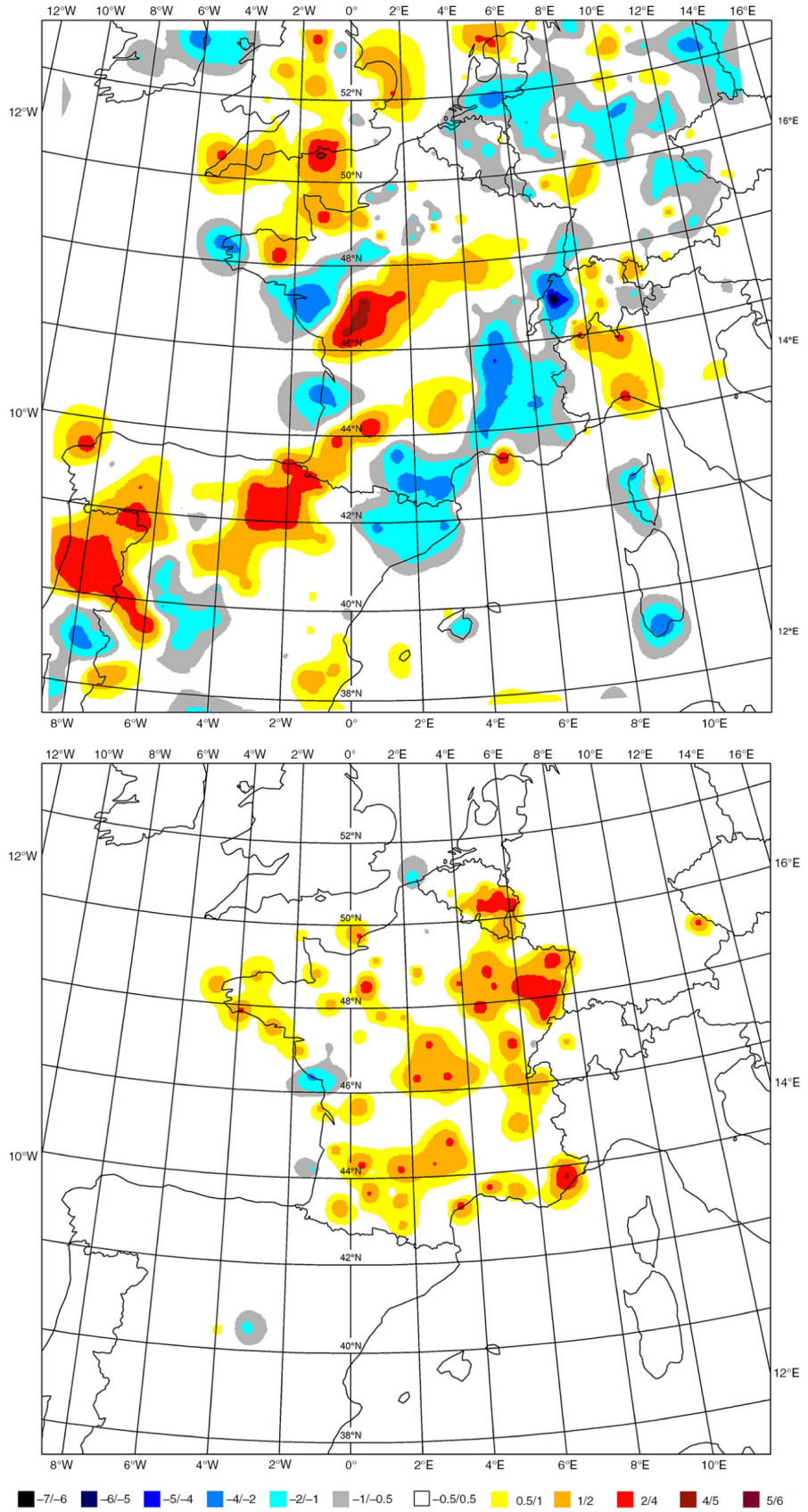

Figure 5.16: Differences in IWV analyses between experiments EGVAP and NOGPS (top panel) and UL01 and EGVAP (bottom panel) on the 18 July 2013 at 0300 UTC (unit is mm)

deviation error is also rather small, with non-negligible values only at 15 UTC (12-hour forecast).

The spatial distribution of these errors is examined more precisely at 15 UTC where the largest differences are noticed between the baseline NOGPS and the experiments. This can be more easily performed on gridded analyses than with actual observations at irregular locations. The mean and standard deviation 12-hour forecast errors for RH_{2m} at 15 UTC are shown in Figure 5.18. Firstly, the reference simulation NOGPS is examined. The most striking pattern of the mean errors is a positive bias (model too moist) over areas with significant orography (mostly the Alps but also the Pyrenes and the Massif Central). Values are above 10% over the western part of Switzerland. The eastern part of France and Germany are characterized by moist positive biases around 5%. On the other hand, Spain and Italy exhibit a slight negative bias (model too dry) whereas over Sardinia values are around -10%. Regarding the standard deviation errors, there are only few areas with values below 5% (Southern Spain), most of the errors being between 10 and 15%. Regions with the largest errors around 20% appear over Western Germany, eastern France and around the Pyrenes. Over oceans the biases and the standard deviations are small since the surface boundary layer is constrained by a saturated surface for which the temperature is imposed from a dedicated surface analysis.

The assimilation of GNSS-derived ZTD data has a tendency to reduce the positive biases noticed over Germany and eastern France (for this last region it has been replaced by a small negative bias). The maxima over western Switzerland is also decreased. No noticeable differences exist between EGVAP and UL01 experiments. The areas of lower biases are also regions where the standard deviation errors are significantly decreased. The band of large values (above 20%) oriented SouthWest/NorthEast from the Massif Central to Western Germany in the NOGPS experiment is not present in the experiments when ZTD data are assimilated (both EGVAP and UL01). A number of rainfall events have passed through the domain during the chosen period, most of them having an orientation SouthWest/NorthEast (discussed later), that can explain why significant moisture errors can be found in the boundary layer at these locations.

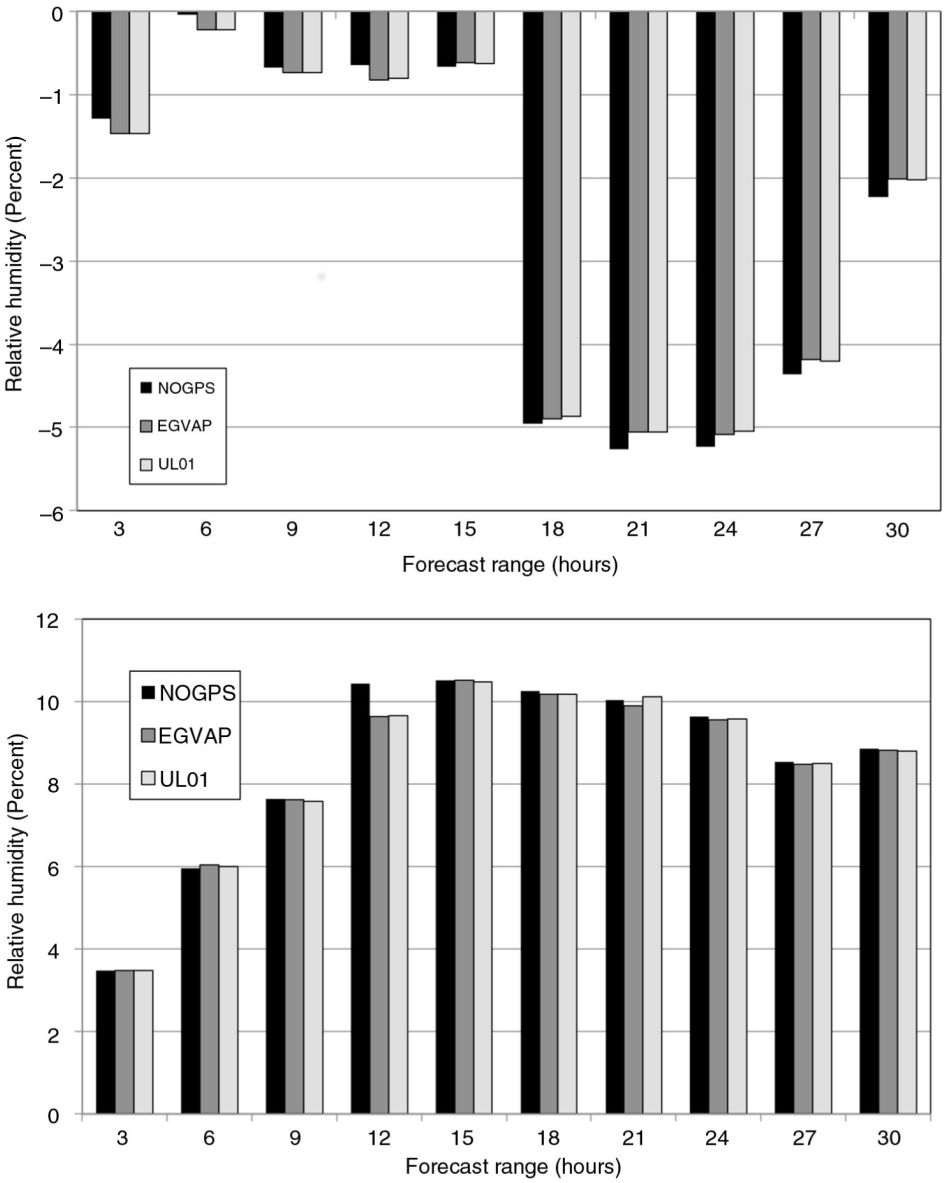

Figure 5.17: Mean (top panel) and standard deviation (bottom panel) forecast errors of screen-level relative humidity (%) according to forecast range (hours) for the three experiments NOGPS, EGVAP and UL01. The scores are averaged from 20 July to 20 August 2013 and are computed against screen-level relative humidity analyses

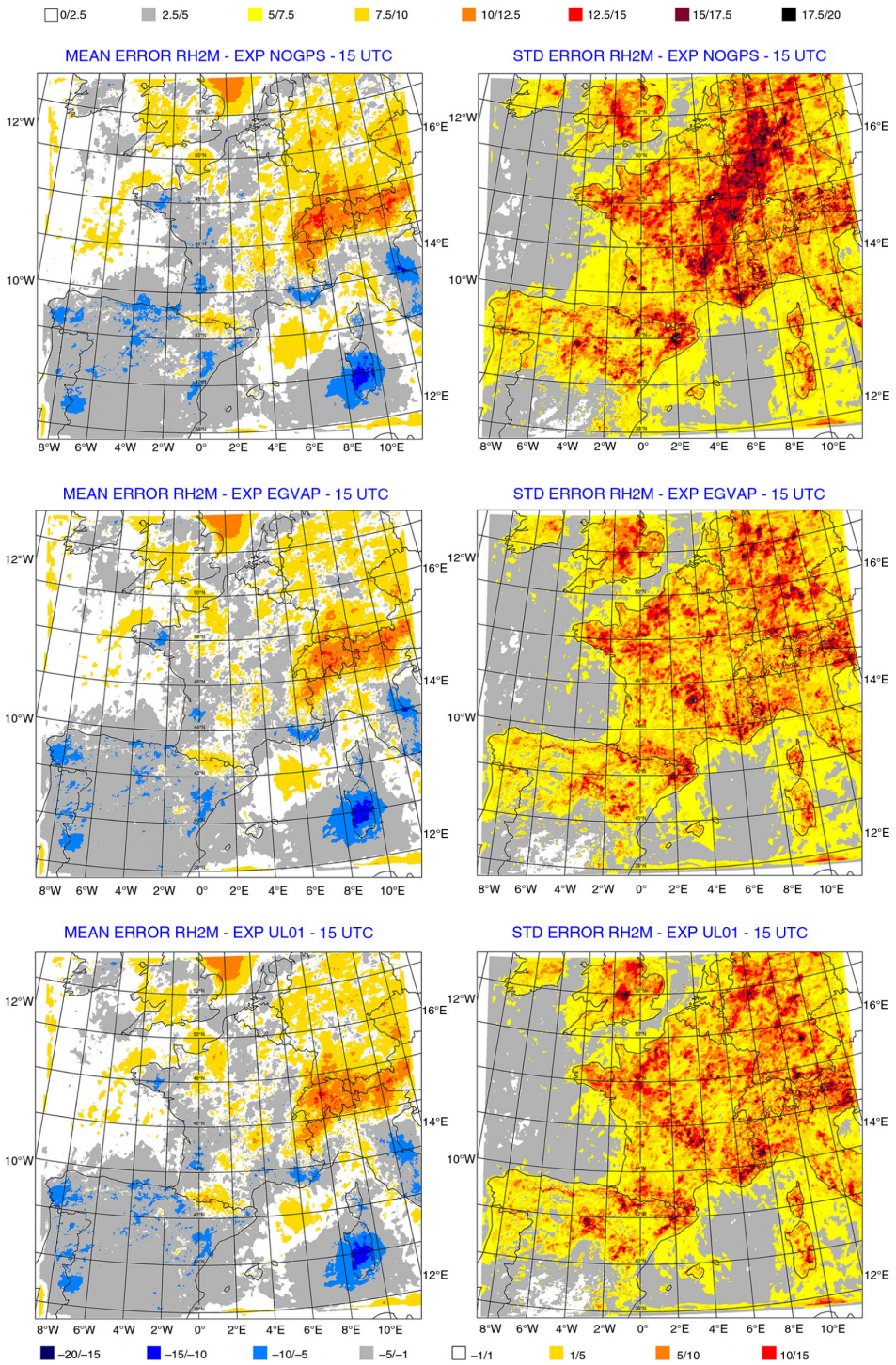

Figure 5.18: Mean and standard deviation of screen-level relative humidity 12-hour forecast errors (15 UTC) in percentages for experiments NOGPS (top panels), EGVAP (middle panels) and UL01 (lower panels) averaged from 20 July to 20 August 2013

The precipitation forecasts are compared over France against precipitation analyses developed at Météo-France at 0.012^o resolution at hourly time scales from a blend between radar derived rain rates for small scale precipitation (convective events) and rain gauges that describe accurately the large-scale precipitation events and that can be spatially interpolated using a classical Kriging technique. This analysis called ANTILOPE can be considered as the closest representation of the truth over France. In the following, only 24-hour accumulations from 06 UTC on day 1 to 06 UTC on day 2 from AROME are evaluated against ANTILOPE. First an objective comparison with classical categorical scores derived from contingency tables is performed and summarized in Figure 5.19 for the Frequency Bias Index (FBI), the Probability of Detection (POD), the False Alarm Ratio (FAR) and the Equitable Threat Score (ETS) for the following thresholds: 0.2, 1, 2, 5, 10 and 20 mm. The actual definition of these scores can be found at: `http://www.cawcr.gov.au/projects/verification`. The NOGPS experiment exhibits a slight positive bias up to 15% for large precipitation amounts (above 5 mm). Both ZTD assimilation experiments reduce this bias. The bias has the smallest value with UL01 for all rates. When examining the POD, the three experiments produce very similar values; however, EGVAP appears to slightly degrade the POD above 5 mm, whereas the quality of UL01 is always as good as or better than NOGPS. The assimilation of ZTD reduces the FAR for all thresholds, but UL01 is better above 1 mm. Finally the ETS, that accounts within a single measure for the POD and FAR skills, reveals higher values with the assimilation of ZTD, but the UL01 is clearly better since the improvement with EGVAP is only noticeable below 5 mm. The small detrimental effect of ZTD assimilation for the lowest threshold (0.2 mm) on the POD is also present on the ETS. These results are consistent with previous feasibility studies and also reveal that increasing the density of the GNSS network even by a small percentage can be beneficial to the quality of precipitation forecasts from NWP models, despite an almost neutral impact on other predicted quantities.

A number of case studies were examined that took place during the period of interest in order to highlight the sensitivity of the assimilation of GNSS-derived ZTD data on the prediction of severe convective events.

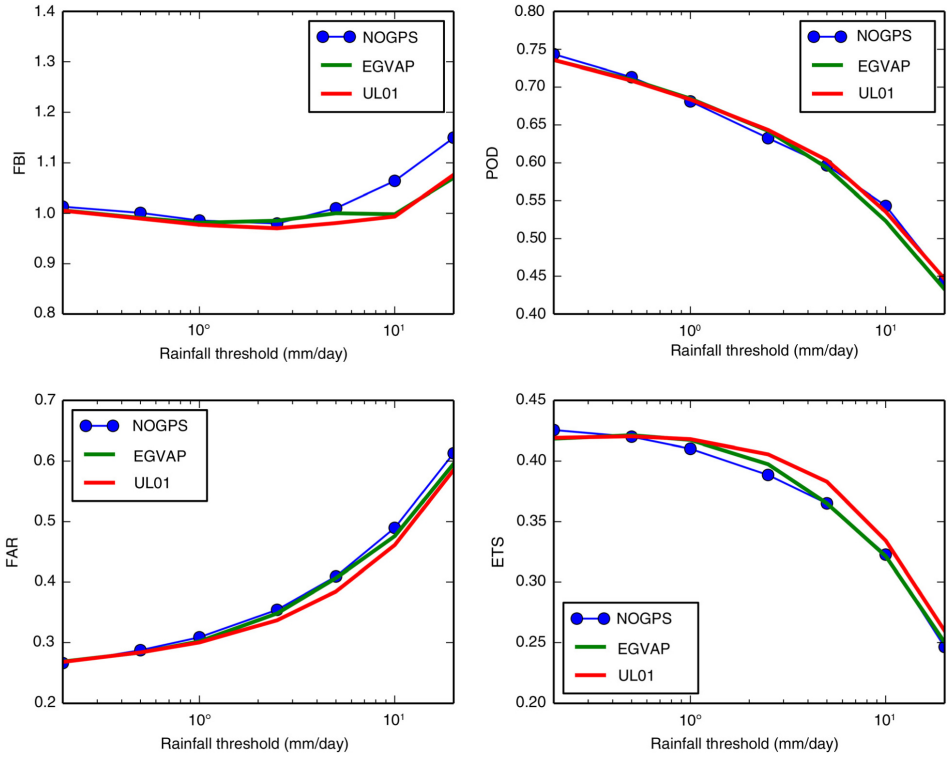

Figure 5.19: Categorical scores (FBI: Frequency Bias Index; POD: Probability of Detection; FAR: False Alarm Ratio; ETS: Equitable Threat Score) for daily accumulated precipitation AROME forecasts from the three experiments: NOGPS, EGVAP, UL01 compared with ANTILOPE precipitation analyses over France (period of interest: 18 July to 21 August 2013)

On 25 July 2013, two intense rainy bands are present in the ANTILOPE analysis that are embedded in a frontal system crossing France in a synoptic southwesterly flow (Figure 5.20). A first rain band is located south of Paris crossing the 48^o latitude and located to the East of the Greenwich meridian, and a second one is located in southwestern part of France (Bordeaux region) with also a small band of precipitation above (Charentes region). Precipitation maxima are above 50 mm. In the NOGPS experiment, AROME has the capacity to simulate these two rainy systems, but the northern one is located too far west from its actual position with an excessive southerly orientation, and the intensity of the system is underestimated. The system over the Bordeaux region is better described, but in terms of orientation and precipitation maxima, it extends too far east. The EGVAP experiment intensifies the northern precipitation band but with the wrong orientation and the extension too far west is amplified, while the intensity of the southern precipitation band is globally reduced. This can be seen as an improvement for the spurious cell located on the east, but as a degradation for the intense cell located near the coast of the Atlantic Ocean. In the UL01 experiment, the northern system is displaced northwards and eastwards, therefore improving significantly its location with respect to the truth, while keeping the larger amounts already produced by the EGVAP experiment. Similarly, the southern system is closer to the observed location, being less elongated to the east.

On 26 July 2013, the frontal system described above has only moved slightly northwards (Figure 5.21). The northern precipitating area is located above Paris (Picardie and Nord regions) with three narrow bands: two with a WestEast orientation and another one above them with a SouthWest/NorthEast orientation. The southern precipitating area has a NorthSouth orientation. In the NOGPS experiment, there is a hint of the three bands observed in the northern part of France, but the third one to the East is too wide and too intense particularly over Luxembourg, while the southern precipitating system has a correct orientation but is situated too far west over the Atlantic Ocean. The EGVAP experiment reduces the intensity of the rainy cell over Luxembourg but is displaced to the South where it is not observed, while for the southern precipitating system, there is a reduction of the rainy band over the ocean and an intensification of the band over the

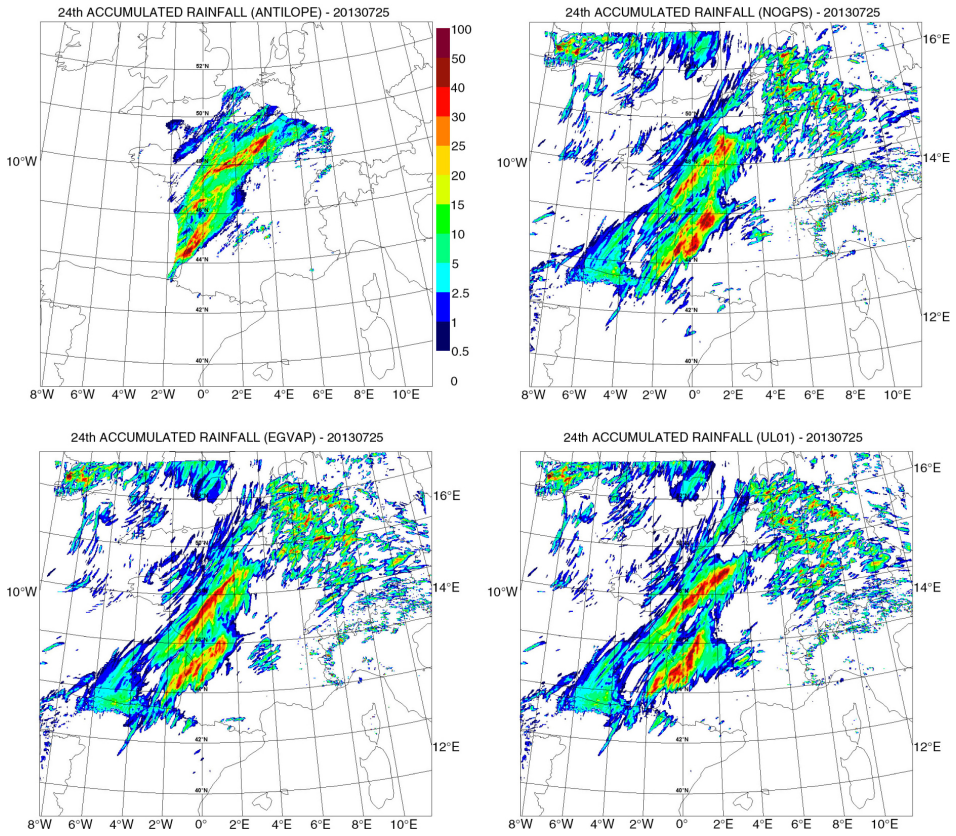

Figure 5.20: Daily accumulated precipitation in mm as analyzed by ANTILOPE and simulated by the AROME model starting from different atmospheric analyses on 25 July 2013: analysis (upper left), experiment NOGPS (upper right), experiment EGVAP (lower left), experiment UL01 (lower right)

continent parallel to this one. When considering UL01, in the northern part of the domain, the too-wide precipitating area southwest of Luxembourg is not simulated anymore, and it has been replaced by narrower rainy bands that, even though not exactly at the proper location, resemble the actual precipitation patterns in this area, while in the southwestern part of France, the northern branch of the precipitating system is improved but not the southern one.

On 02 August 2013, a rainy system moved over France in a southwesterly large-scale flow leading to precipitation around 15 mm over the Lorraine

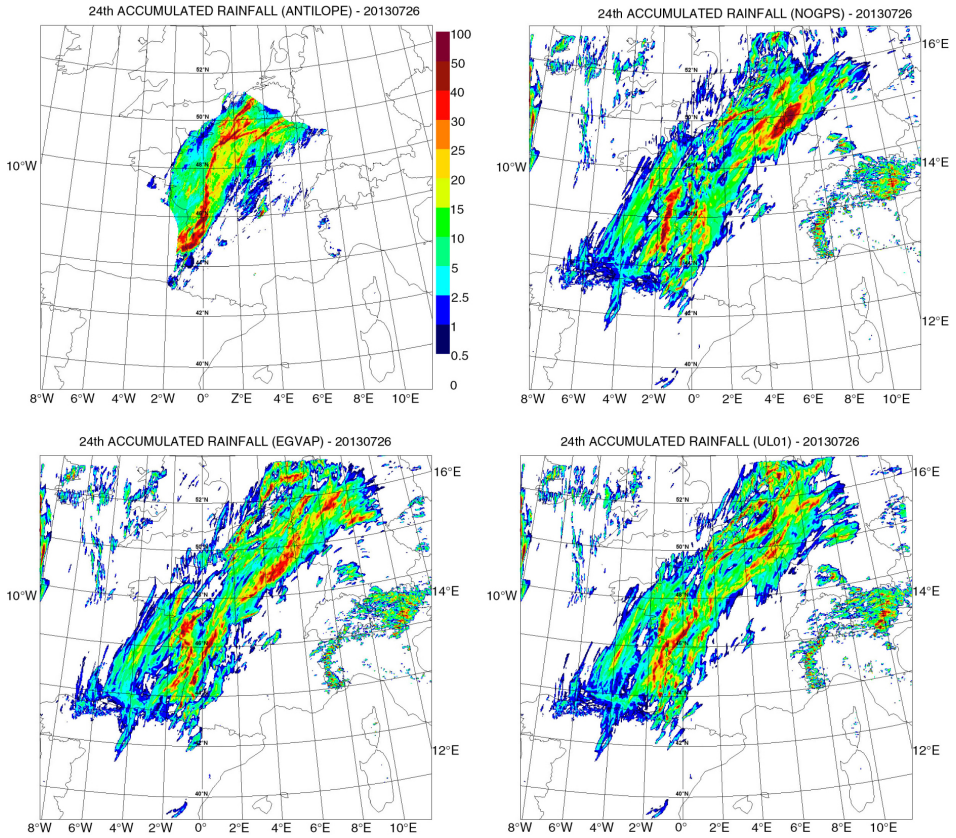

Figure 5.21: Daily accumulated precipitation in mm as analyzed by ANTILOPE and simulated by the AROME model starting from different atmospheric analyses on 26 July 2013: analysis (upper left), experiment NOGPS (upper right), experiment EGVAP (lower left), experiment UL01 (lower right)

region (northeastern part of France) and in the Centre region (Figure 5.22). A band of more intense precipitation with values above 30 mm and a more westerly orientation is noticed over the Aquitaine region. Several narrow precipitation bands are captured by the ANTILOPE analysis. In experiment NOGPS, even though the model simulates a rainy system with the correct orientation and maxima located in the southwestern part of the domain, their intensity is underestimated by a factor of 2 (around 25 mm) and the precipitation band does not extend enough westwards near the Atlantic Ocean coast. In experiment EGVAP, the area of precipitation maxima located over the Aquitaine region is strongly enhanced with maximum values

close to the observed ones (40 mm), while the assimilation of ZTD data from UL01 leads to an even wider precipitating area in the southwestern part of France. However, none of the simulations can describe the small-scale patterns of the precipitation displayed in the analysis, although in experiment UL01, the underestimation of observed precipitation located east of Paris, already present in experiment EGVAP, is somewhat amplified with respect to experiment NOGPS.

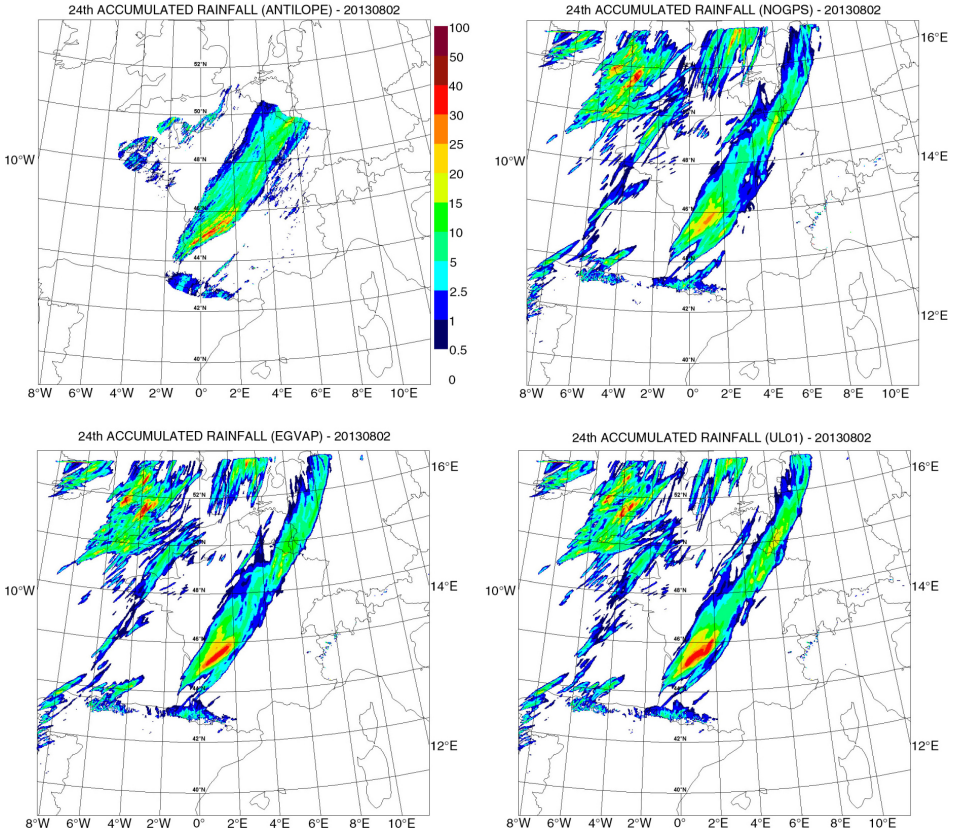

Figure 5.22: Daily accumulated precipitation in mm as analyzed by ANTILOPE and simulated by the AROME model starting from different atmospheric analyses on 2 August 2013: analysis (upper left), experiment NOGPS (upper right), experiment EGVAP (lower left), experiment UL01 (lower right)

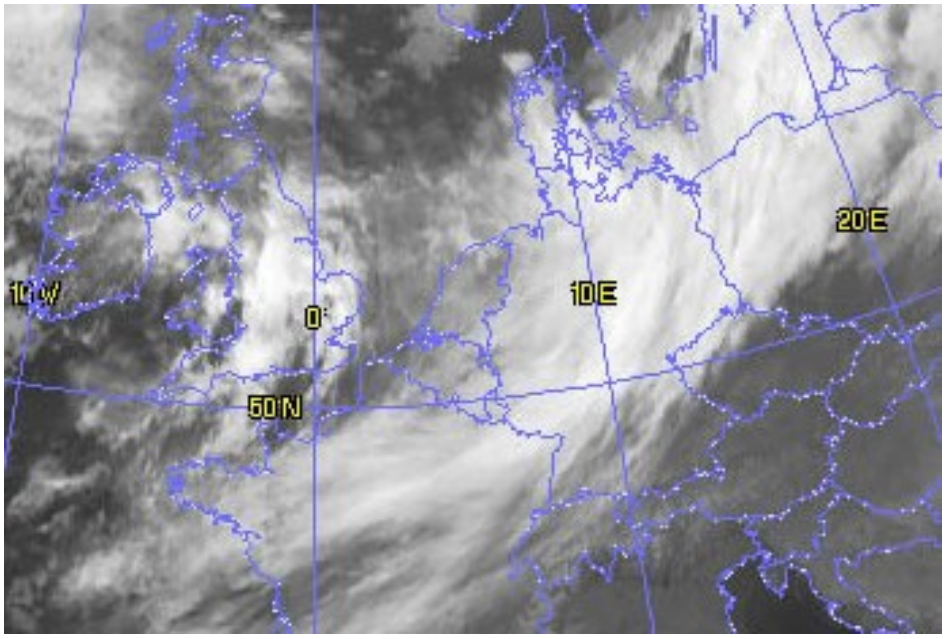

Figure 5.23: Satellite picture of cloud distribution at 23 February 2012 0000 UTC

5.3 NRT-DDP IWV for Storm Tracking

This section provides the results of the experiment described in Section 3.2.3. During 22-23 February 2012, a warm front (i.e. a warm air-mass moving towards a cold air-mass) moved over northern France, Belgium and Germany. This front was associated with a low-pressure system situated over southern Scandinavia. Cloud formation and stratiform precipitation was caused by riding of warm air-mass over the cold air-mass and a light rainfall at 0400 UTC was observed in Luxembourg. A satellite picture of the cloud distribution, as taken by Meteosat second generation (`http://www.esa.int/SPECIALS/MSG/`), associated with this front at 23 February 0000 UTC is shown in Figure 5.23.

Figure 5.24 (a) shows the precipitation in millimetres at 23 February 0000 UTC over Europe as captured by weather radar (`http://www.meteox.de`) whereas Figure 5.24 (b) is a 2D map of the NRT-DDP IWV distribution over the same region at the same time. The black dots in Figure 5.24 (b) represent the ground-based GNSS stations which are included for processing in UL01.

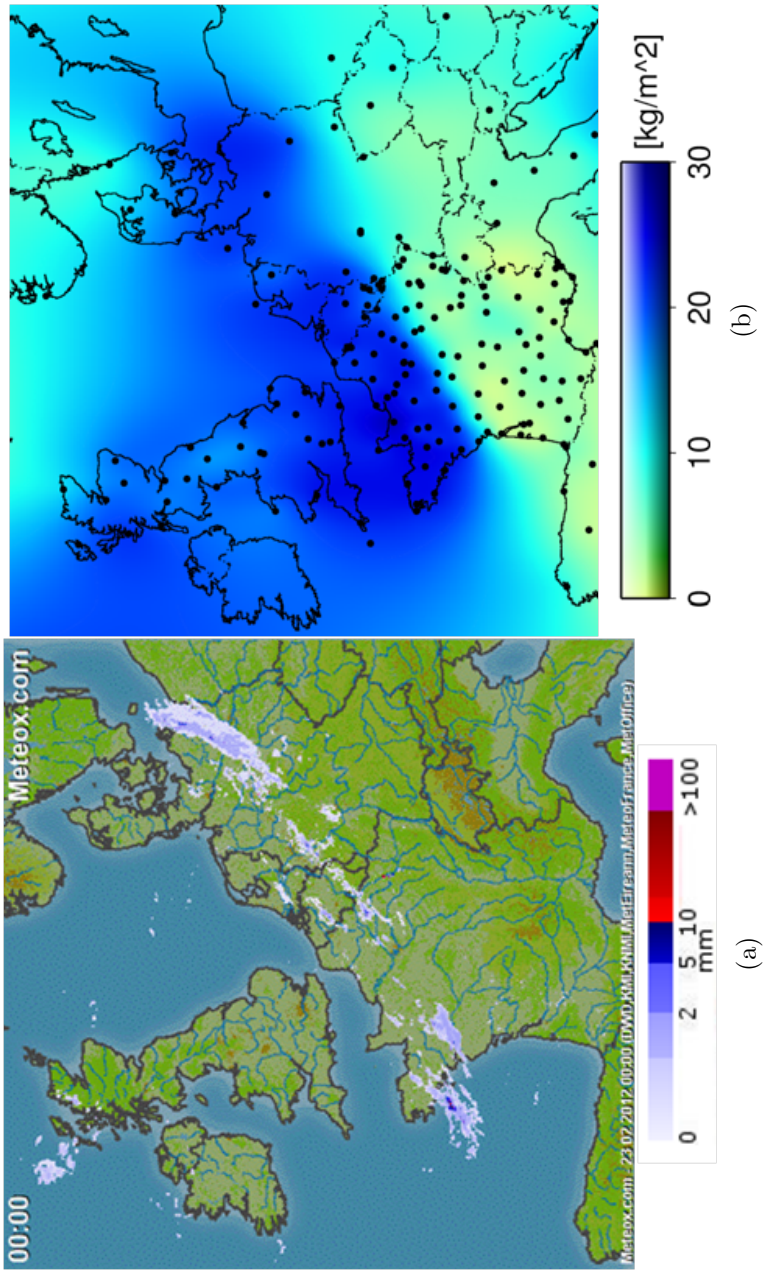

Figure 5.24: Comparison of weather radar (a) and NRT-DDP IWV (b) at 2012-02-23 0000 UTC

To generate the IWV maps like that in Figure 5.24 (b) in the UL01 system, IWV is first estimated over all the individual stations and then a grid with a resolution of 15 minutes is computed by block averaging followed by an adjustable tension continuous curvature surface gridding algorithm (Smith et al., 1990). Therefore the density of the network of GNSS stations has an influence on the quality of these maps. It must be noted that at this point the systems do not automatically detect and remove outlying ZTD or IWV estimates. It can be seen that the zones with the largest gradients in IWV overlap with the fore-front of the precipitation events caused by the warm front as identified by the weather radar.

The output of the NRT processing systems has a sampling interval of 15 minutes and hence the NRT-DDP IWV maps are generated for every 15th minute. This makes it possible to graphically observe the changes in the amount of IWV and compare these changes with the weather processes. Such an example is presented in Figure 5.25 which shows the IWV maps obtained by UL01 for a) 20120222-1500 UTC, b) 20120222-1800 UTC, c) 20120222-2100 UTC, d) 20120223-0000 UTC, e) 20120223-0300 UTC and f) 20120223-0600 UTC. The sequence of NRT-DDP IWV maps in Figure 5.25 shows the evolution of the distribution of IWV corresponding to the passage of the warm front shown in Figure 5.24 over Luxembourg and the Greater Region.

Figure 5.26 presents the time series of NRT-DDP IWV over the six GNSS stations in Luxembourg for the same time-period as that in Figure 5.25. It can be seen that the amount of IWV increases by approximately 15 kg/m^2 as the warm front passes over Luxembourg. The station Troisvierges (TROI) is the first to observe this change and as the front proceeds in a south-easterly direction, the other stations observe this change too. Over TROI, IWV reaches a value of 15.2 kg/m^2 at 20120222-2245 UTC whereas over Erpeldange (ERPE), the same value is reached at 20120223-0015 UTC which indicates that the warm front has taken about 90 minutes to travel from Troisvierges to Erpeldange (approximately 28 km/h). This demonstrates the possibility of calculating the speed and direction (not explicitly shown) of a moving weather front using GNSS and hence storms can be tracked.

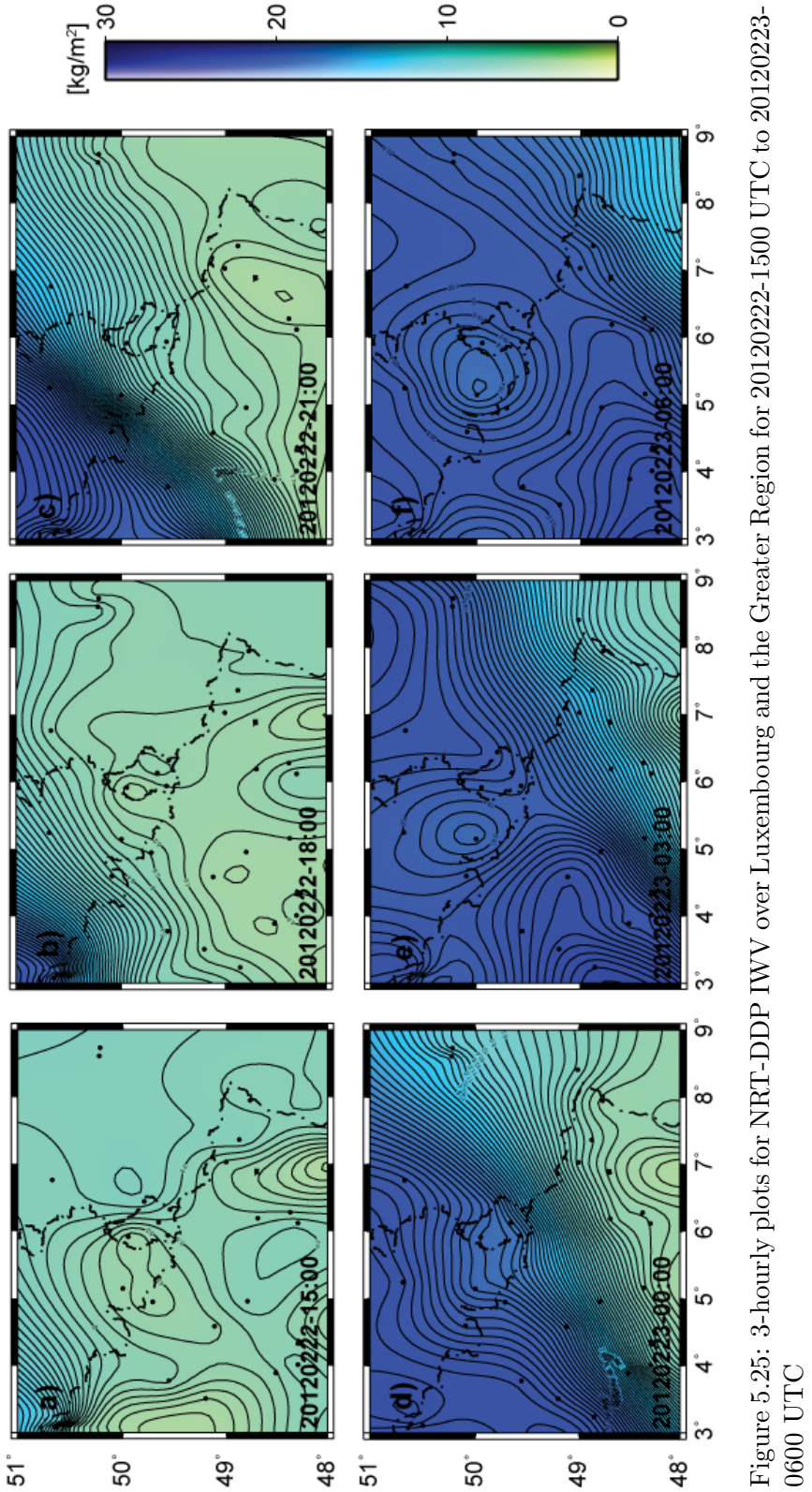

Figure 5.25: 3-hourly plots for NRT-DDP IWV over Luxembourg and the Greater Region for 20120222-1500 UTC to 20120223-0600 UTC

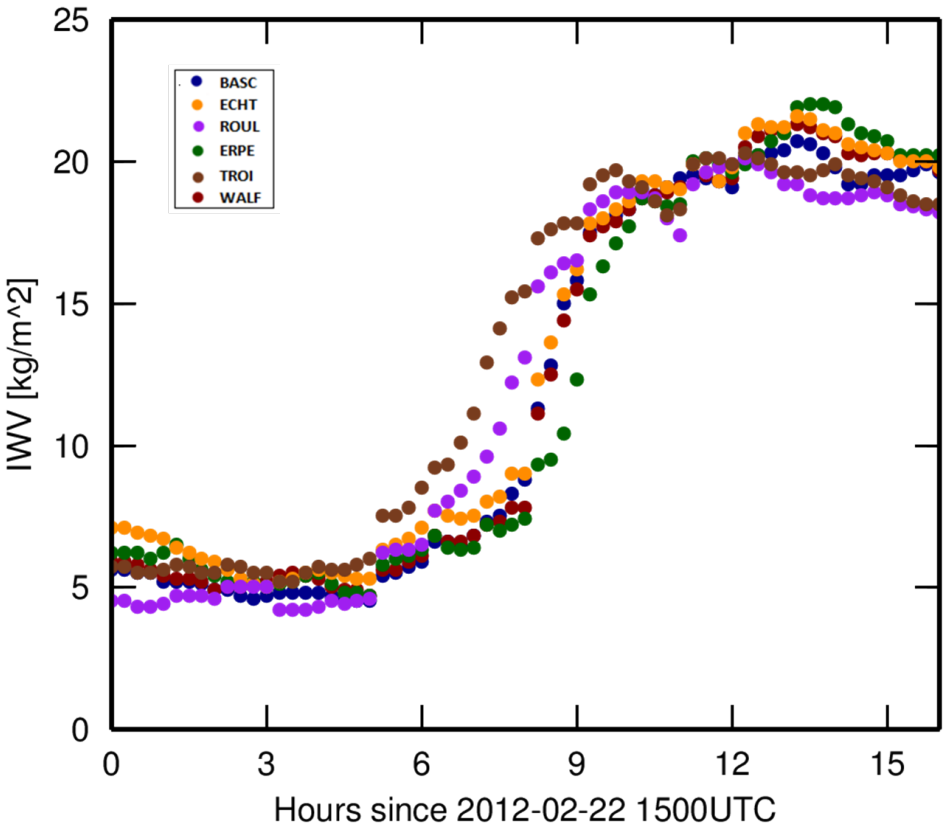

Figure 5.26: NRT-DDP IWV Time series for the 6 GNSS stations in Luxembourg for the period 20120222-1500 UTC to 20120223-0600 UTC

5.4 Validation of ERA-Interim Climate Reanalysis Dataset

This section provides the results of validation of the ZTD derived from the ERA-Interim climate reanalysis dataset (referred to as ZTD_{erai} in the following text) using GNSS-derived ZTD (referred to as ZTD_{gnss} in the following text) from a global network of stations. This experiment is described in Section 3.2.4.

The total number of ground-based GNSS stations from the network of DDULVMF solution included in the analysis for each climate zone (depending on the data availability for the comparison period) is shown in Figure 5.27. It could be seen that there is no data available for the Csc, Cwc, Dfd, Dsa, and Dwd climate zones. Therefore, this analysis is based on 25 out of the 30 climate zones.

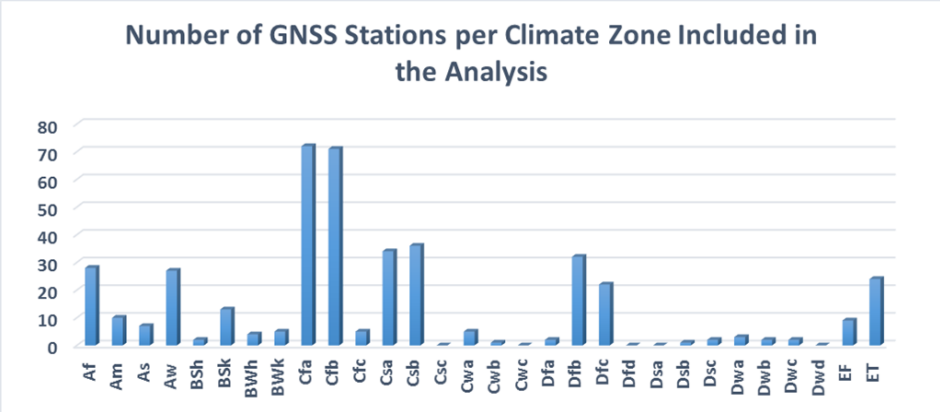

Figure 5.27: Number of ground-based GNSS stations included in the analysis for each climate zone

Studies in the past have shown that the climate reanalysis models are not always able to accurately account for the topographic differences within the model domain. It is due to the fact that these models are gridded and assume the same value of pressure for a complete grid cell. However, in the regions with high topographical variability, the actual pressure values can vary rapidly and on spatial scales smaller as compared to the size of the

Table 5.9: Ellipsoidal heights of GNSS stations in different climate zones

Zone	Average [m]	Minimum [m]	Maximum [m]	No. of Stations
Af	185.87	-64.93	3062.10	28
Am	156.98	-30.39	1167.35	10
As	298.79	-20.92	1558.38	7
Aw	314.37	-25.48	1337.54	27
BSh	260.53	190.00	331.05	2
BSk	831.10	-22.54	2347.73	13
BWh	678.93	-14.85	1734.64	4
BWk	1555.11	702.55	2488.91	5
Cfa	53.71	-27.96	397.35	72
Cfb	277.46	-3.88	3754.70	71
Cfc	146.76	22.30	476.17	5
Csa	289.27	-27.25	1842.57	34
Csb	159.70	-26.34	1319.32	36
Cwa	1394.26	1257.81	1558.08	5
Cwb	1986.20	1986.20	1986.20	1
Dfa	161.93	116.82	207.03	2
Dfb	244.94	-15.99	1714.20	32
Dfc	163.20	-19.45	541.86	22
Dsb	238.60	238.60	238.60	1
Dsc	722.24	17.13	1427.36	2
Dwa	72.83	48.81	87.43	3
Dwb	502.20	502.07	502.34	2
Dwc	2600.05	1575.51	3624.58	2
EF	354.74	20.99	1720.83	9
ET	315.55	0.42	2134.57	24

model grid cells. This fact can lead to the different behaviour of the models in different geographical areas or in the areas of different altitudes. For example, van Dam et el. (2010) have shown the existence of topographically induced errors in climate reanalysis models. Therefore, for this analysis, it is important to consider the topography and altitude of the stations located in the different climate zones. Table 5.9 lists the minimum, maximum and average ellipsoidal heights of the ground-based GNSS stations (included in this analysis) located in the different climate zones.

The ZTD time series, difference time series, ZTD correlation plots and ZTD difference histograms for the comparison between ZTD_{erai} and ZTD_{gnss}

for all the stations included in this analysis are provided in Appendix D. To show the example of these comparison plots, one of these (for station WTZR) is shown in Figure 5.28. For each of the 25 analyzed climate zones, the histograms of the difference between ZTD_{erai} and ZTD_{gnss} plotted by combining the differences from all the stations in each zone, are shown in Figure 5.29.

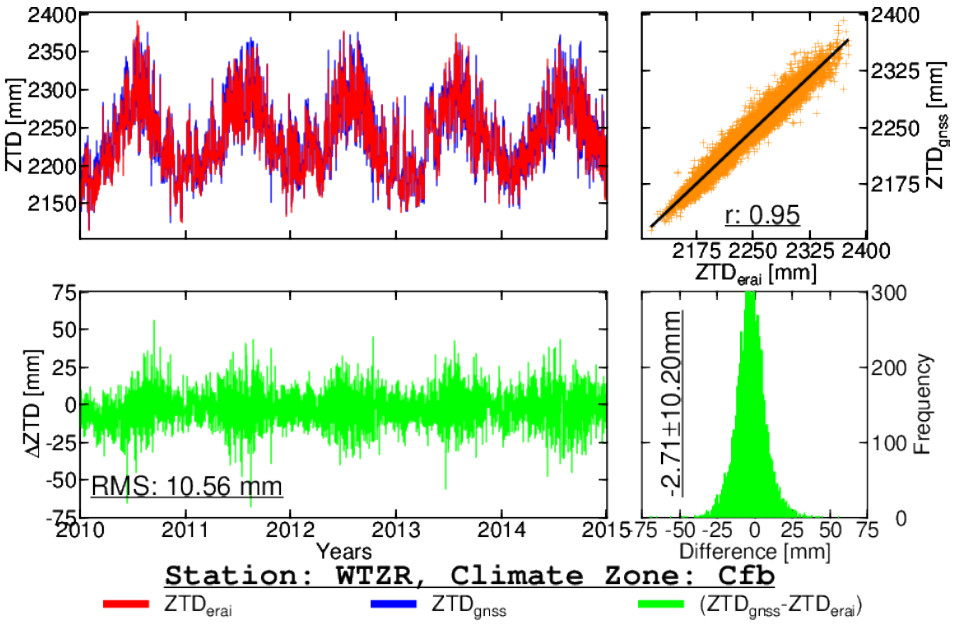

Figure 5.28: Comparison between ZTD_{erai} and ZTD_{gnss} for station WTZR (Bad Koetzting, Germany)

Table 5.10 shows the statistics of the comparison between ZTD_{erai} and ZTD_{gnss} for all the climate zones computed using all the available stations in each zone. r_{eg} in Table 5.10 is the correlation coefficient between ZTD_{erai} and ZTD_{gnss} averaged over all the stations in each zone. In order to study the periodic behaviour of the ZTD difference in the various climate zones, one station has been selected from each zone and the Lomb-Scargle periodogram (not shown) has been computed for the ZTD difference time series of each station. Table 5.11 shows the normalized power of annual (1 cpy), semi-annual (2 cpy), seasonal (4 cpy), monthly (12 cpy) and diurnal (365 cpy, 366 cpy) frequencies in the ZTD difference time series for stations in all the climate zones.

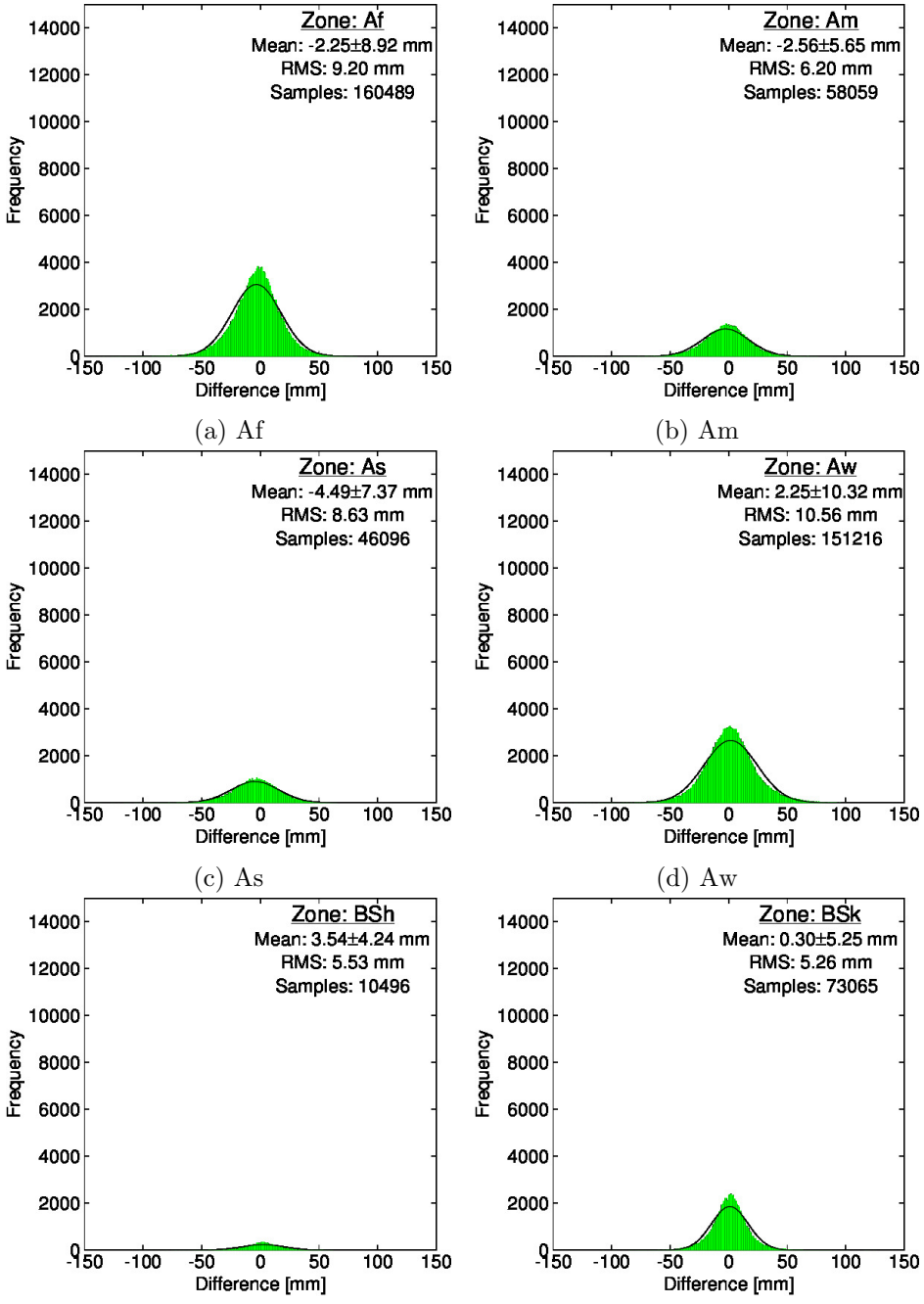

(a) Af (b) Am

(c) As (d) Aw

(e) BSh (f) BSk

Figure 5.29: Histogram (green) with a normal distribution fit (black) of the differences between ZTD_{erai} and ZTD_{gnss} for various climate zones

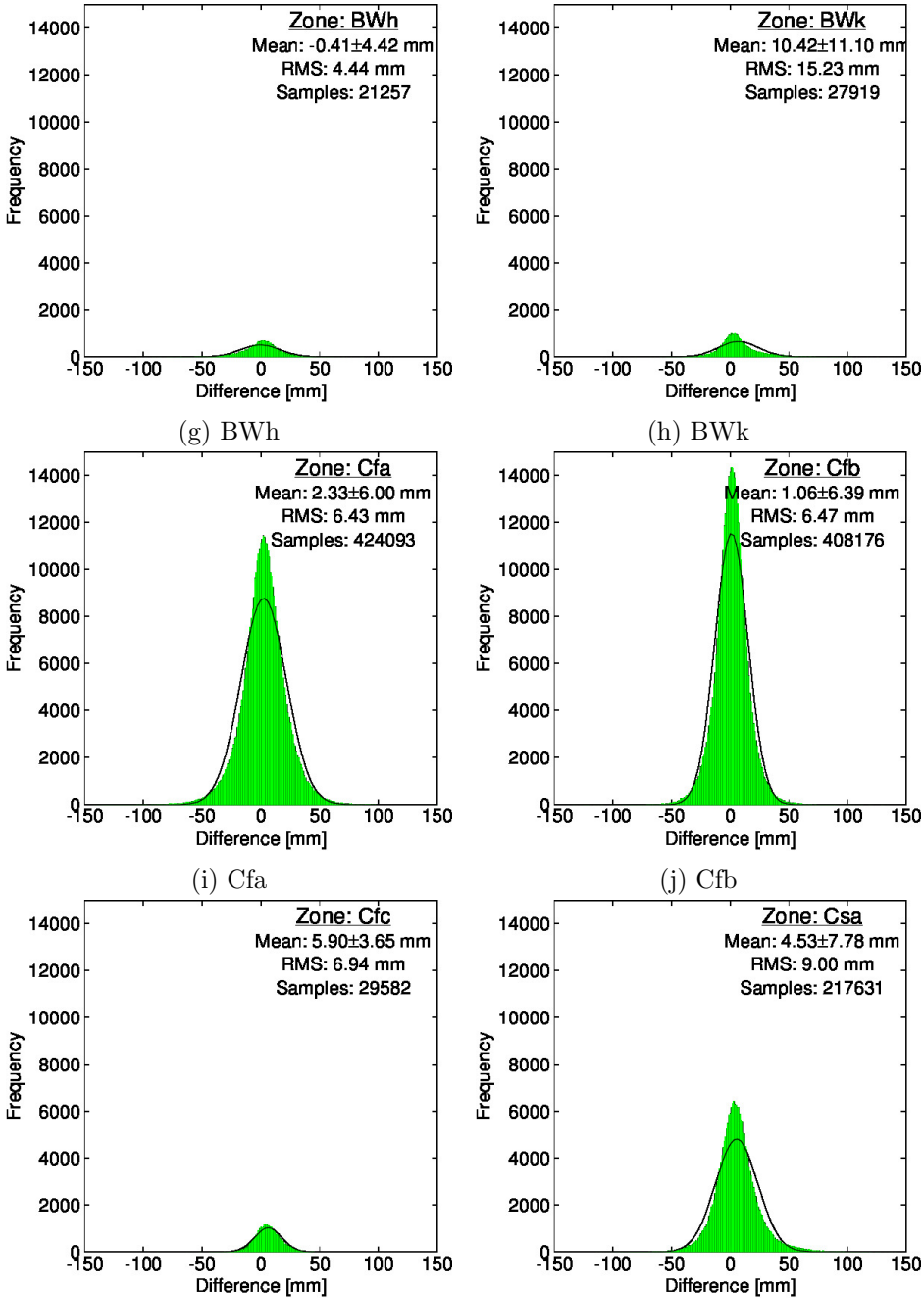

(g) BWh (h) BWk

(i) Cfa (j) Cfb

(k) Cfc (l) Csa

Figure 5.29: (continued from previous page) Histogram (green) with a normal distribution fit (black) of the differences between ZTD_{erai} and ZTD_{gnss} for various climate zones

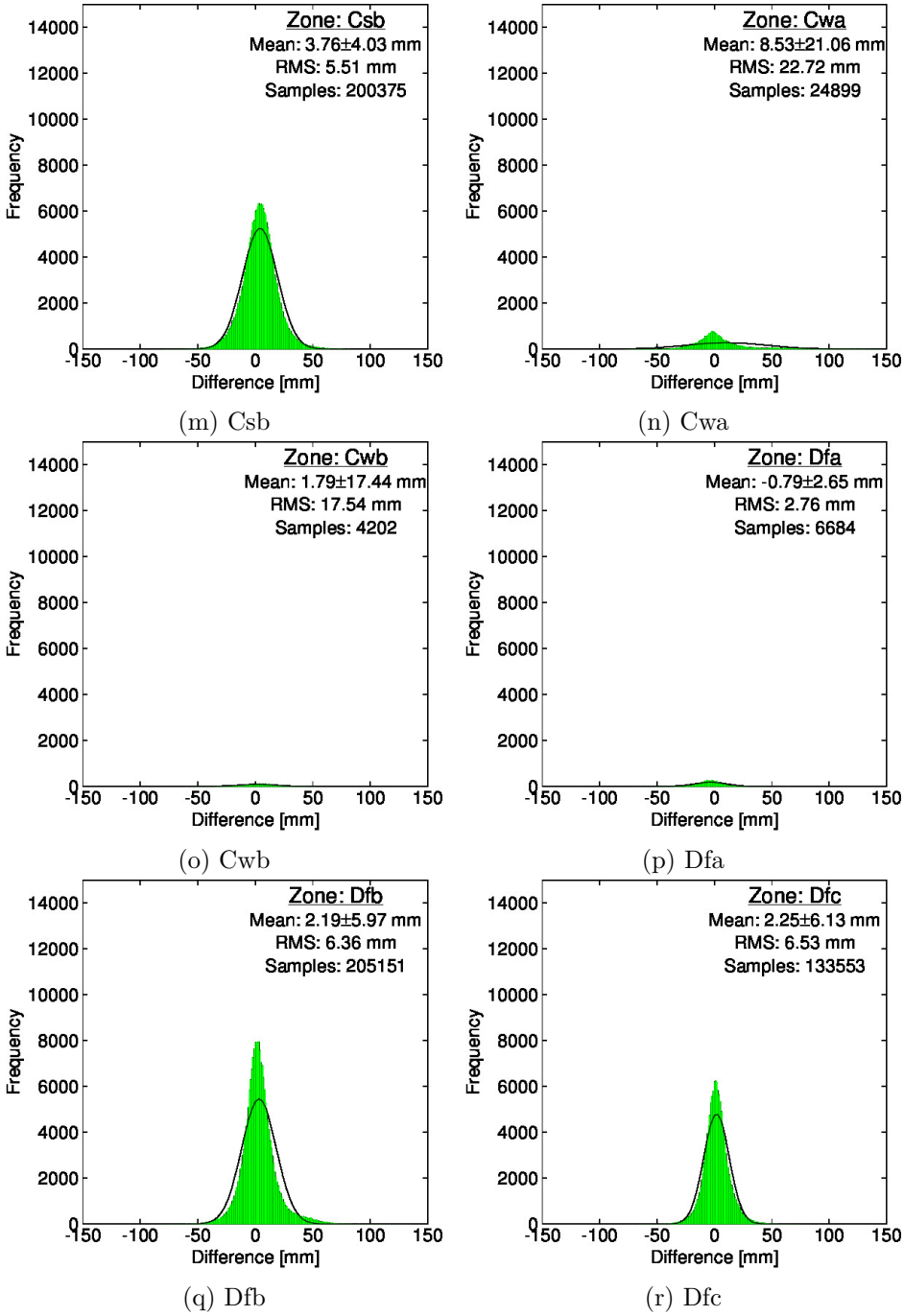

(m) Csb (n) Cwa

(o) Cwb (p) Dfa

(q) Dfb (r) Dfc

Figure 5.29: (continued from previous page) Histogram (green) with a normal distribution fit (black) of the differences between ZTD_{erai} and ZTD_{gnss} for various climate zones

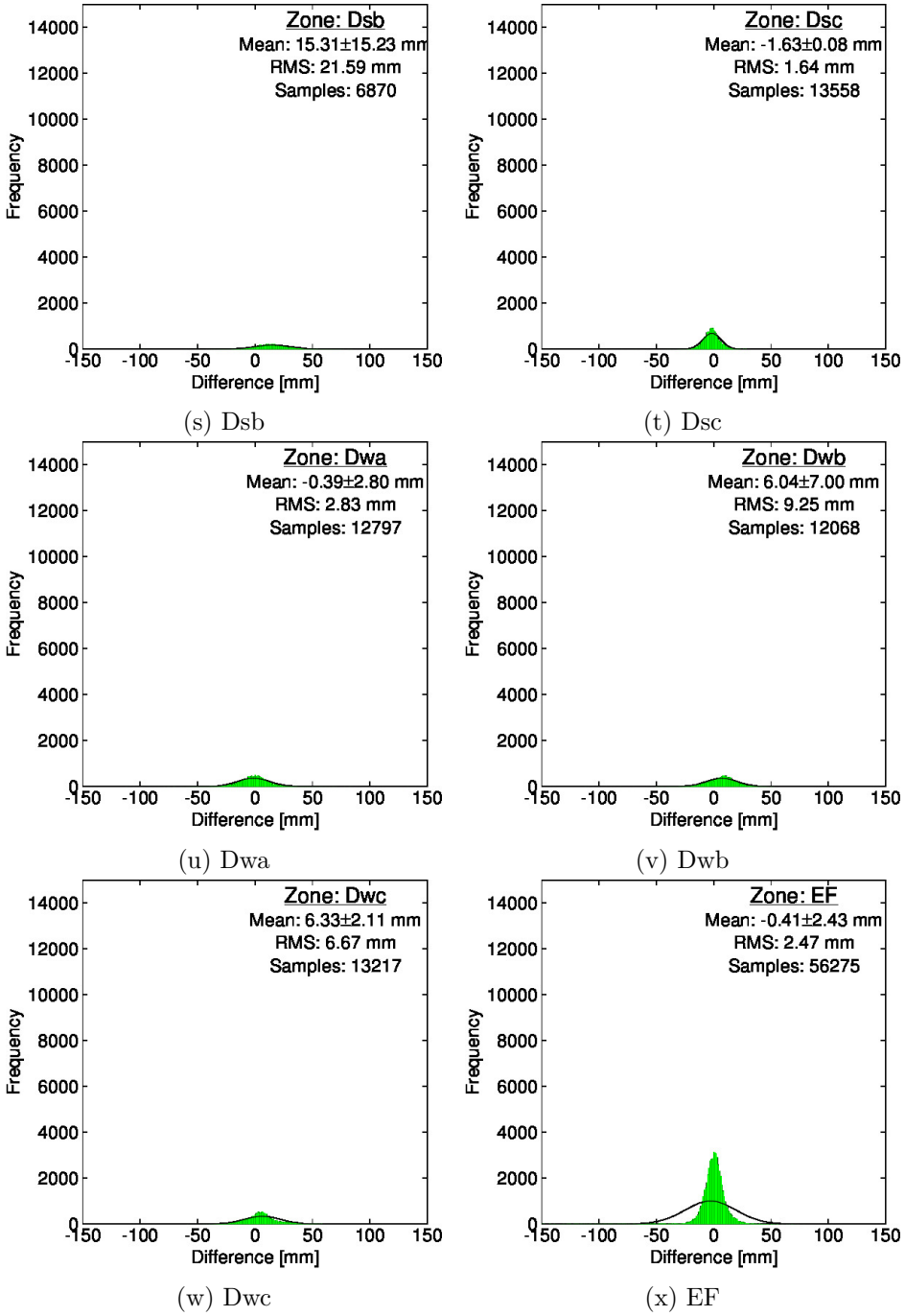

(s) Dsb (t) Dsc

(u) Dwa (v) Dwb

(w) Dwc (x) EF

Figure 5.29: (continued from previous page) Histogram (green) with a normal distribution fit (black) of the differences between ZTD_{erai} and ZTD_{gnss} for various climate zones

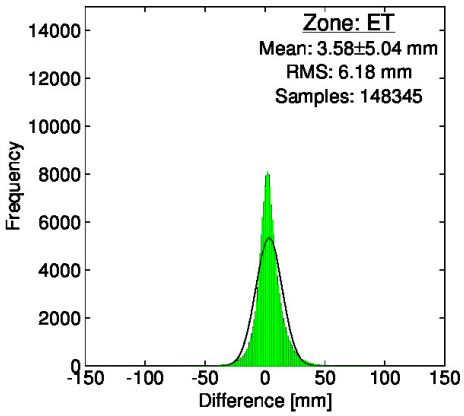

(y) ET

Figure 5.29: (continued from previous page) Histogram (green) with a normal distribution fit (black) of the differences between ZTD_{erai} and ZTD_{gnss} for various climate zones

The correlation coefficient (r_{eg}) between ZTD_{erai} and ZTD_{gnss}, as can be seen from Table 5.10, has been found to be between 0.87 and 1.00 for the various climate zones. The highest value of r_{eg} (1.00) has been found for the three climate zones of the climate group "Cold (D)" i.e. Dsc (cold - dry summer - cold summer), Dwa (cold - dry winter - hot summer) and Dwc (cold- dry winter - cold summer), and the second-highest value (0.99) of r_{eg} has also been found for a zone of Cold climate type (Dwc or cold-dry winter - cold summer). The lowest value of r_{eg} (0.87) has been found for the Tropical climate zone Af (tropical - rainforest) whereas the second-lowest value (r_{eg} = 0.88) has been found for the Tropical climate zones As (tropical - dry summer) and Aw (tropical - savannah). These statistics suggest that the correlation between ZTD_{erai} and ZTD_{gnss} is high in the regions with low amount of atmospheric water vapor and is low in the regions with high amount of atmospheric water vapour. It can also be seen from Table 5.10 that the mean of the ZTD differences varies from -4.49 mm to 15.31 mm over different climate zones whereas the standard deviation of the ZTD differences varies from 0.08 mm to 21.06 mm and the RMS varies from 1.64 mm to 22.72 mm. The highest RMS difference of 22.72 mm has been found for the climate zone Cwa (Temperate - Dry Winter - Hot Summer) which has data available from 5 GNSS stations with ellipsoidal heights ranging from 1257.81 m to 1558.08 m, and mean ZTD difference of

8.53±21.06 mm. The standard deviation for Cwa (21.06 mm) has also been found to be the highest which indicates that the ZTD differences in this zone have the highest variability among all the analyzed climate zones. By examining Table 5.11, it can be seen that among all the analyzed zones, the Cwa zone has the highest power of periodic signals with the power of semi-annual (2 cpy) frequency being the highest and annual (1 cpy) being the second-highest. The high standard deviation and RMS arise from the high periodicity in the ZTD differences. Furthermore, the range of ellipsoidal heights of GNSS stations in the Cwa zone indicate that this zone contains high altitude regions and a high topographic variation may lead to large differences between ZTD_{erai} and ZTD_{gnss} in this zone. The second-highest RMS difference of 21.59 mm has been found for the climate zone Dsb (Cold - Dry Summer - Warm Summer) which has data available from 1 GNSS station with ellipsoidal height of 238.60 m, and mean ZTD difference of 15.31±15.23 mm. The standard deviation for this zone has been found to be the second-highest among all the analyzed zones. Table 5.11 reveals that the ZTD difference for the station in this zone has the second-highest powers of annual (1 cpy), semi-annual (2 cpy) and monthly (12 cpy), and fifth-highest power of seasonal (4 cpy) signals. The third-highest RMS difference of 17.54 mm has been found for the climate zone Cwb (Temperate - Dry Winter - Warm Summer) which has data available from 1 GNSS station with ellipsoidal height of 1986.20 m, and mean ZTD difference of 1.79±17.44 mm. For this zone, the powers of all the periodic signals lie within the five lowest powers among all the analyzed zones. The lowest RMS difference of 1.64 mm has been found for the climate zone Dsc (Cold - Dry Summer - Cold Summer) which has data available from 2 GNSS stations with ellipsoidal heights of 17.13 m and 1427.36 m, and mean ZTD difference of -1.63±0.08 mm. The standard deviation for this zone has been found to be the lowest among all the analyzed zones. Table 5.11 reveals that for this zone, the powers of all the periodic signals lie within the three lowest powers among all the analyzed zones.

Figures 5.30, 5.31 and 5.32 show the global distribution of the mean, standard deviation and RMS, respectively, of the differences between ZTD_{erai} and ZTD_{gnss}. Furthermore, the global distribution of r_{eg} is shown in Figure 5.33. In terms of latitude, these figures show relatively better agreement

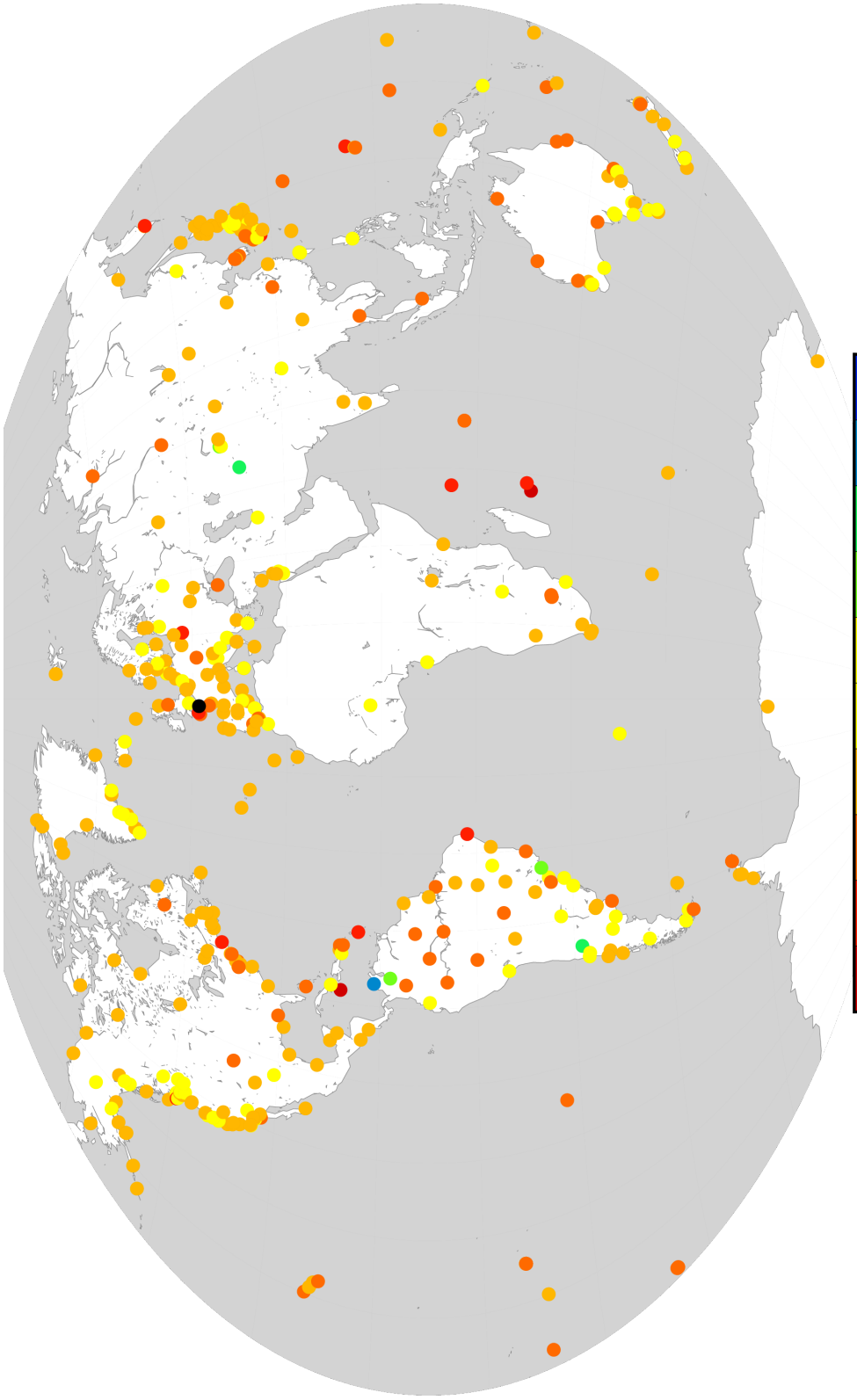

Figure 5.30: Global distribution of mean of the difference between ZTD_{erai} and ZTD_{gnss}

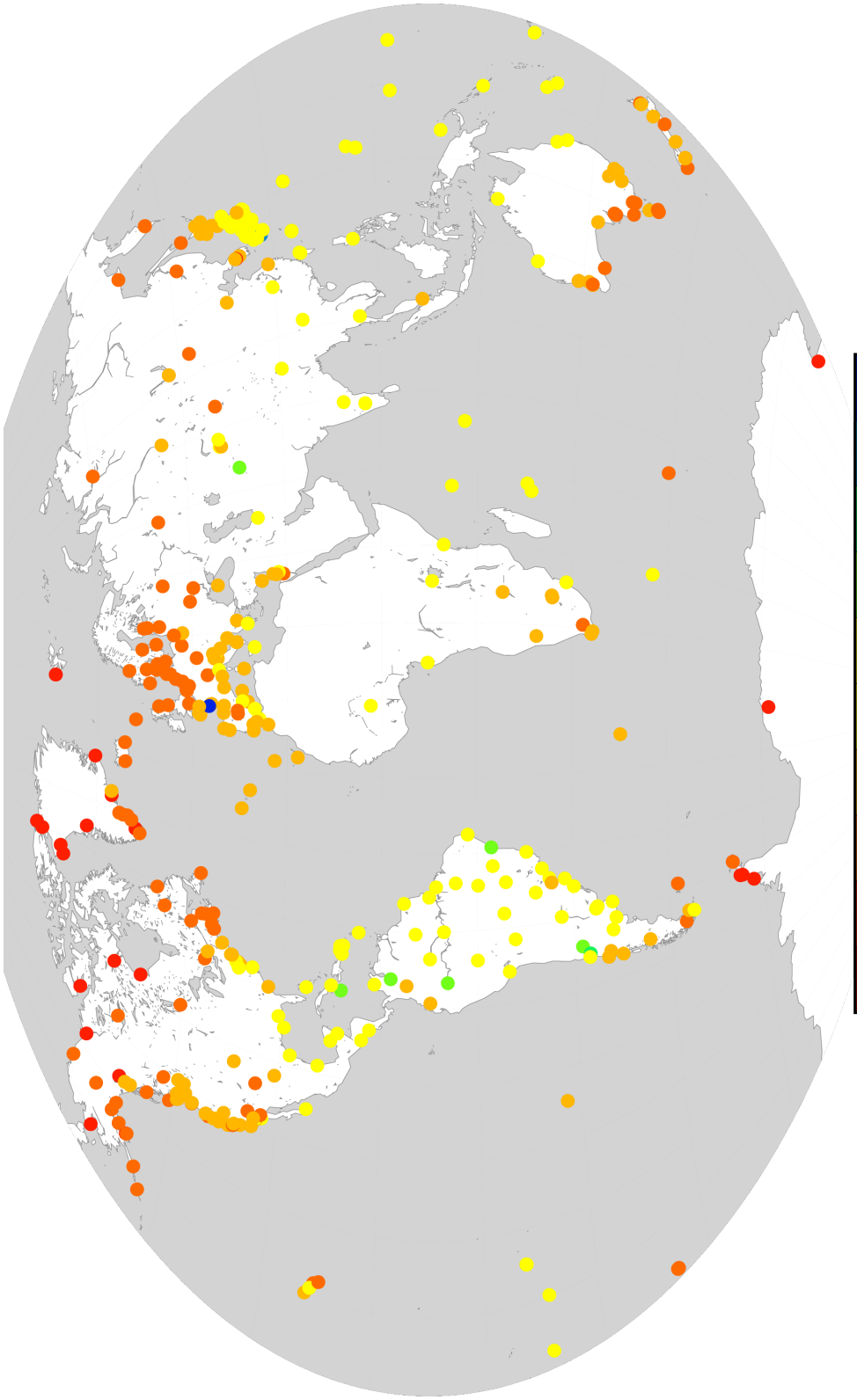

Figure 5.31: Global distribution of the standard deviation of the difference between ZTD_{erai} and ZTD_{gnss}

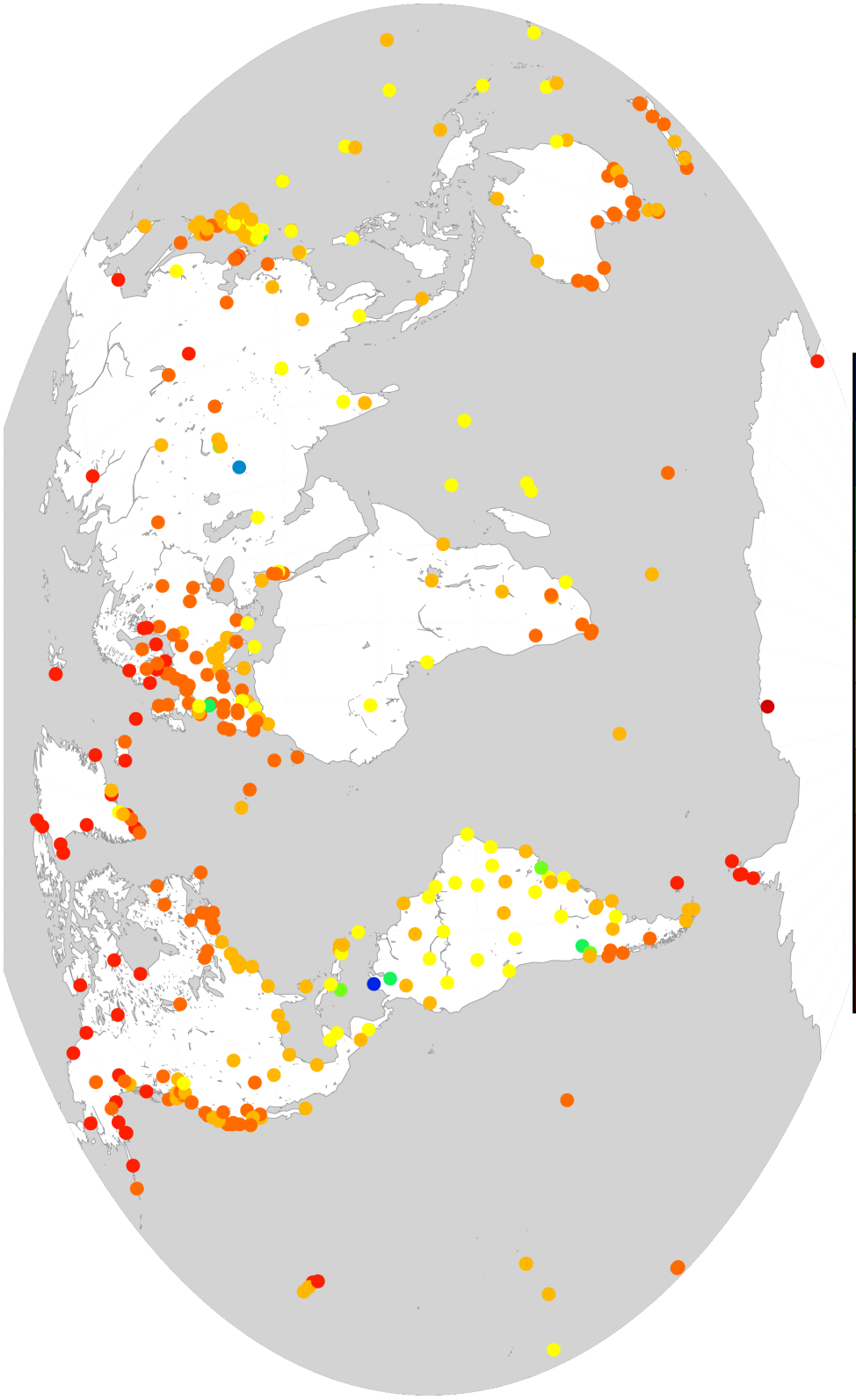

Figure 5.32: Global distribution of the RMS of the difference between ZTD_{erai} and ZTD_{gnss}

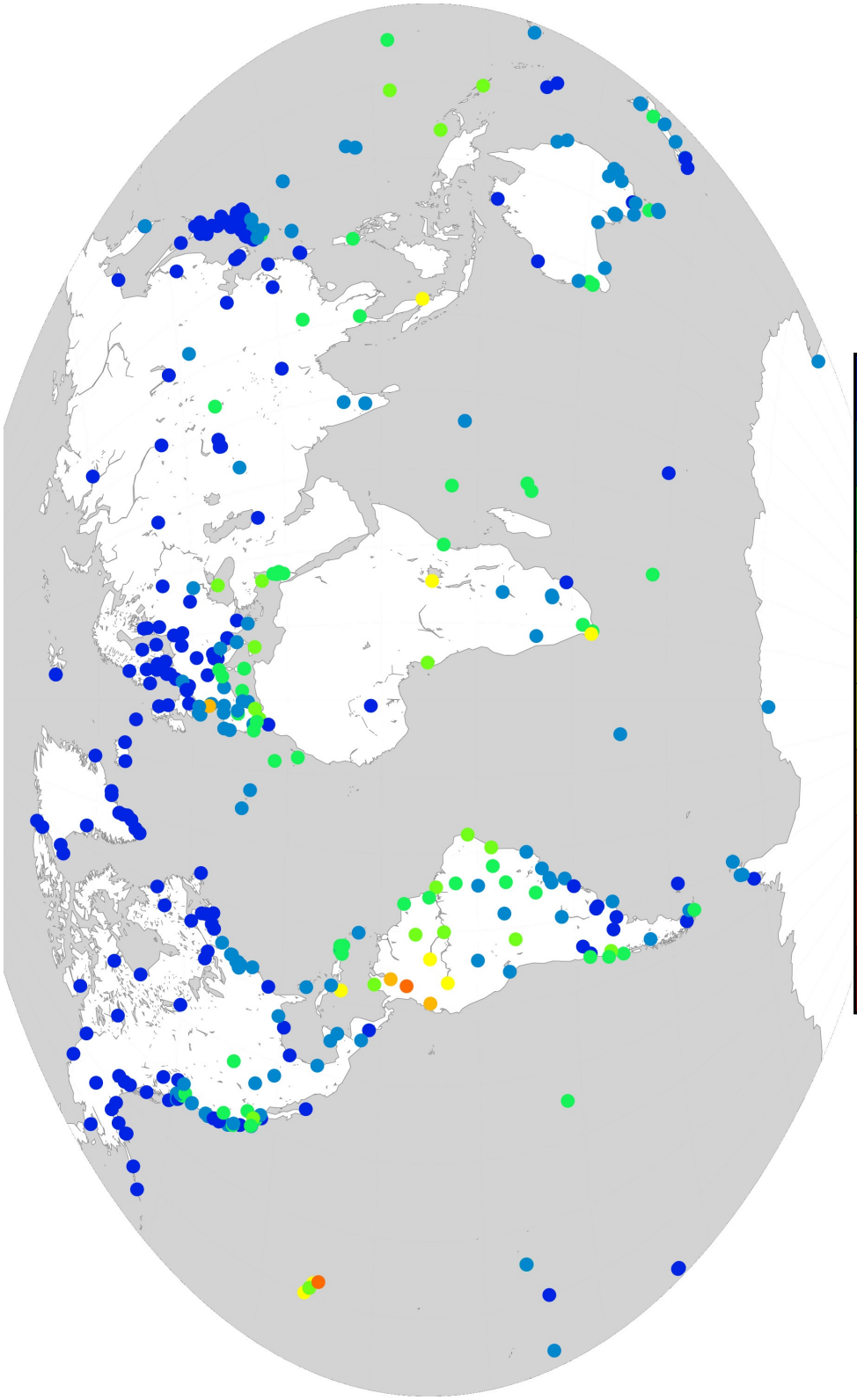

Figure 5.33: Global distribution of the correlation coefficient (r_{eg}) of the difference between ZTD_{erai} and ZTD_{gnss}

Figure 5.34: Variation of RMS, SDev. mean and correlation coefficient (r_{eg}) of differences between ZTD_{erai} and ZTD_{gnss} with latitude

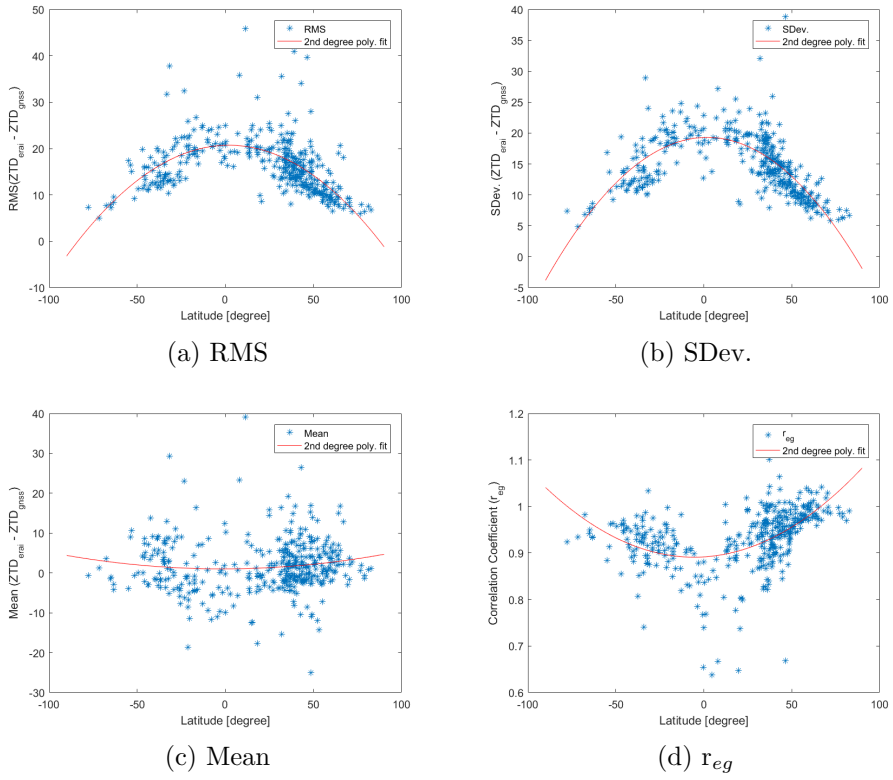

(a) RMS (b) SDev.

(c) Mean (d) r_{eg}

between ZTD_{erai} and ZTD_{gnss} towards the polar regions as compared to the regions around the equator. The variation in the RMS, SDev., mean and correlation coefficient (r_{eg}) with latitude can be seen in Figure 5.34.

Table 5.10: Difference between ZTD_{erai} and ZTD_{gnss} in different climate zones

Zone	Mean [mm]	SDev [mm]	RMS [mm]	Min. [mm]	25th Percentile [mm]	75th Percentile [mm]	Max. [mm]	r_{eg}
Af	-2.25	8.92	9.20	-12.50	-5.67	-0.60	36.23	0.87
Am	-2.56	5.65	6.20	-11.74	-4.80	-0.43	10.30	0.87
As	-4.49	7.37	8.63	-18.64	-8.17	-0.12	4.46	0.88
Aw	2.25	10.32	10.56	-17.66	-2.53	4.45	39.13	0.88
BSh	3.54	4.24	5.53	-0.70	1.42	5.67	7.79	0.92
BSk	0.30	5.25	5.26	-7.24	-3.86	4.54	9.15	0.91
BWh	-0.41	4.42	4.44	-6.81	-2.40	1.80	5.59	0.94
BWk	10.42	11.10	15.23	-1.50	2.83	16.32	29.25	0.92
Cfa	2.33	6.00	6.43	-15.37	-2.00	5.98	23.06	0.96
Cfb	1.06	6.39	6.47	-25.00	-2.26	5.76	13.83	0.93
Cfc	5.90	3.65	6.94	0.21	4.54	8.98	10.63	0.96
Csa	4.53	7.78	9.00	-4.51	-0.65	7.39	31.64	0.90
Csb	3.76	4.03	5.51	-2.03	0.09	7.19	13.00	0.91
Cwa	8.53	21.06	22.72	-5.82	-4.32	7.00	49.64	0.97
Cwb	1.79	17.44	17.54	-206.9	-8.5	12.3	100.4	0.89
Dfa	-0.79	2.65	2.76	-3.43	-2.11	0.54	1.86	0.95
Dfb	2.19	5.97	6.36	-10.41	-0.93	3.86	26.46	0.98
Dfc	2.25	6.13	6.53	-14.33	-0.41	4.69	16.96	0.99
Dsb	15.31	15.23	21.59	-97.40	5.40	24.10	98.70	0.95
Dsc	-1.63	0.08	1.64	-1.72	-1.68	-1.59	-1.55	1.00
Dwa	-0.39	2.80	2.83	-4.34	-1.46	1.59	1.76	1.00
Dwb	6.04	7.00	9.25	-0.96	2.54	9.54	13.04	0.99
Dwc	6.33	2.11	6.67	4.23	5.28	7.38	8.44	1.00
EF	-0.41	2.43	2.47	-4.22	-1.86	1.47	3.52	0.95
ET	3.58	5.04	6.18	-3.96	0.42	5.18	16.82	0.98

Table 5.11: Normalized spectral power of the periodic signals in ZTD differences in different climate zones

Zone	Station	Annual (1 cpy)	Semi-annual (2 cpy)	Seasonal (4 cpy)	Monthly (12 cpy)	Diurnal (365 cpy, 366 cpy)
Af	PIMO	0.0171	0.0254	0.0012	0.0019	0.0005, 0.0004
Am	KOKB	0.0021	0.0029	0.0019	0.0022	0.0001, 0.0000
As	ICAM	0.0017	0.0017	0.0023	0.0017	0.0001, 0.0003
Aw	DARW	0.0378	0.0055	0.0054	0.0017	0.0003, 0.0002
BSh	NICO	0.0004	0.0002	0.0000	0.0001	0.0000, 0.0001
BSk	CEDU	0.0179	0.0015	0.0015	0.0004	0.0001, 0.0002
BWh	KARR	0.0150	0.0158	0.0058	0.0036	0.0002, 0.0002
BWk	GOLD	0.0151	0.0063	0.0001	0.0006	0.0000, 0.0003
Cfa	USNO	0.0075	0.0173	0.0013	0.0053	0.0001, 0.0000
Cfb	DUND	0.0021	0.0021	0.0009	0.0001	0.0002, 0.0002
Cfc	REYK	0.0121	0.0047	0.0005	0.0001	0.0000, 0.0001
Csa	MATE	0.0006	0.0026	0.0004	0.0008	0.0000, 0.0004
Csb	JPLM	0.0183	0.0023	0.0065	0.0046	0.0006, 0.0001
Cwa	UNSA	0.8081	1.0000	0.0281	0.0606	0.0047, 0.0034
Cwb	KUNM	0.0016	0.0030	0.0004	0.0009	0.0001, 0.0000
Dfa	DAEJ	0.0004	0.0077	0.0002	0.0023	0.0001, 0.0003
Dfb	LAMA	0.0088	0.0019	0.0017	0.0007	0.0000, 0.0004
Dfc	CHUR	0.0004	0.0006	0.0012	0.0010	0.0000, 0.0001
Dsb	BREW	0.0989	0.0364	0.0045	0.0145	0.0004, 0.0006
Dsc	WHIT	0.0014	0.0008	0.0001	0.0000	0.0000, 0.0000
Dwa	SUWN	0.0005	0.0038	0.0022	0.0024	0.0000, 0.0001
Dwb	IRKT	0.0057	0.0045	0.0034	0.0068	0.0001, 0.0002
Dwc	ULAB	0.0188	0.0026	0.0036	0.0044	0.0000, 0.0001
EF	OHI2	0.0027	0.0046	0.0008	0.0018	0.0004, 0.0003
ET	HOFN	0.0201	0.0206	0.0001	0.0006	0.0001, 0.0000

5.5 PP-DDP ZTD for Climate Variability Analysis

This section provides the results of the studies used to apply the PP-DDP ZTD for climate variability analysis. This experiment is described in Section 3.2.5.

5.5.1 Monthly Variability in the ZTD

In order to study the monthly variability in the ZTD for the 25 climate zones analyzed in the previous section, monthly ZTD means for all the stations in each zone were averaged. Figure 5.35 presents the zone-wise time series of monthly ZTD means. The left panel in Figure 5.35 shows the monthly mean time series with the actual magnitude of the ZTD (to differentiate between ZTD magnitudes in different zones) whereas the right panel shows the monthly mean time series after subtracting the mean of each time series from it (to magnify the pattern of variability).

A close inspection of Figure 5.35 reveals the scatter of ZTD in different types of climates as well as the months where the maxima and minima of the ZTD occur. For tropical climate zones (climate group A), the scatter of ZTD values lies within 40 mm. The ZTD in all the four zones of this type (Af, Am, As and Aw) has one maximum around the month of May whereas that in the zones Am and Aw has a second maximum around the month of October. The ZTD in the arid climate zones (climate group B) has a scatter of 70 mm with one maximum in July for the zones BSh and BSk, two maxima for the zone BWh in January and September, and two maxima for the zone BWk in January and December. The minima of ZTD in this climate group occur in May for the zone BWh and in June for BWk. For the climate zones in the temperate climate group, the scatter of the ZTD lies within 160 mm. The climate zone Cwa has one ZTD minimum in July (during Austral Winter) whereas all the other zones in climate group C have a maximum of ZTD in the month of July (during Boreal Summer). The scatter of ZTD in the cold climate zones (climate group D) lies within 200 mm and all the climate zones in this group experience one ZTD maximum in the month of July. In the polar climate zones (climate group E), the scatter of ZTD lies within 60 mm. In the climate zone ET (Polar - Tundra), one maximum of the

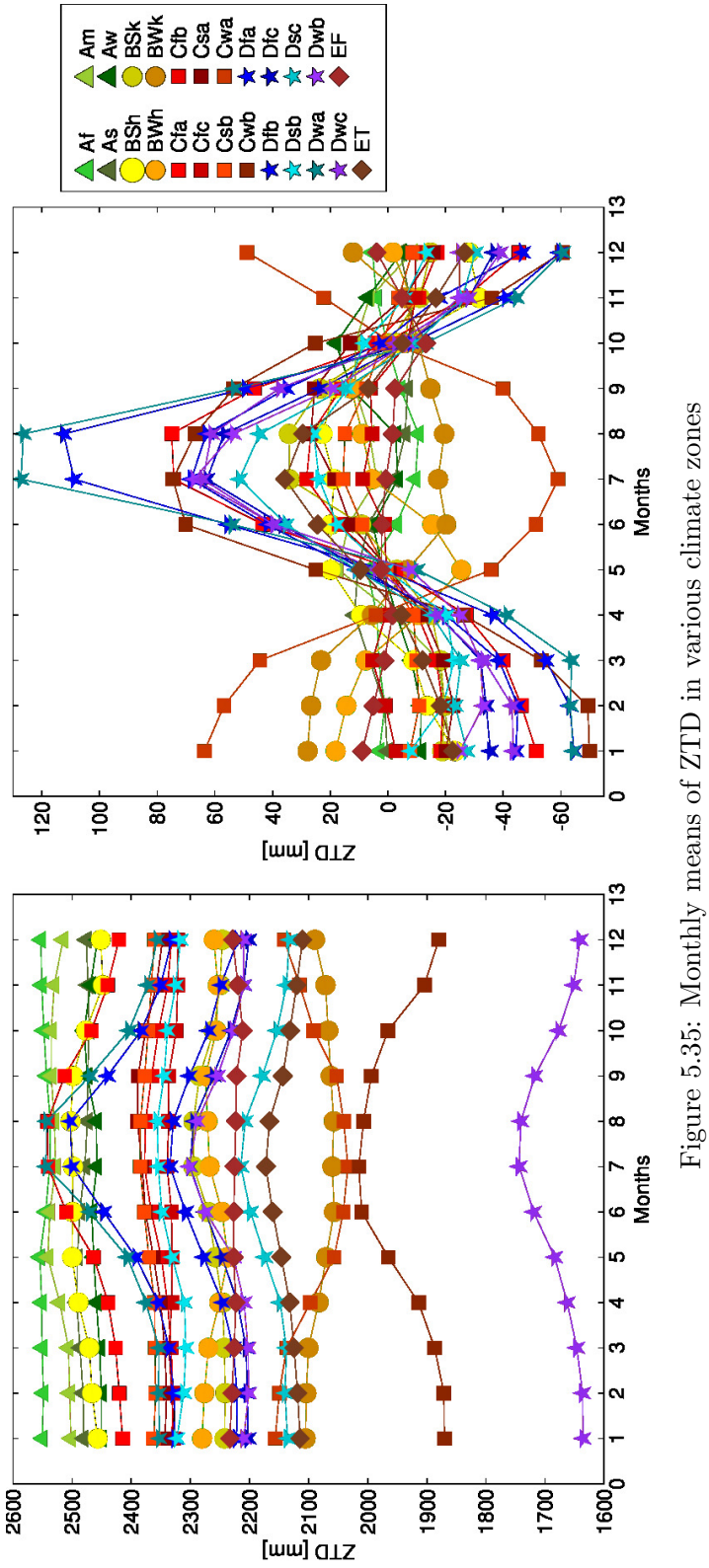

Figure 5.35: Monthly means of ZTD in various climate zones

ZTD has been found in July whereas for the zone EF (Polar - Frost), one minimum in October and two maxima in January and December have been found.

Furthermore, in order to study the inter-annual variability in the ZTD in Luxembourg, monthly averages of ZTD were calculated for all the 6 SPSLux stations for the period 2007-2014. Figure 5.36 shows, for each of the 6 SPSLux stations, the time series of monthly ZTD averages for the years 2007 to 2014 along with their mean. It can be seen that all the 6 SPSLux stations experience the same monthly variation of the ZTD and the maximum occurs around July. However, the magnitude of the ZTD averages for the stations vary because the stations are located at different heights.

5.5.2 Seasonal Variability in the ZTD

In order to study the seasonal variability in the ZTD for the 25 climate zones analyzed in the previous section, 3-monthly ZTD means for all the stations in each zone were averaged. The months have been combined in the groups of December-January-February (DJF), March-April-May (MAM), June-July-August (JJA), and September-October-November (SON), to represent a total of four seasons in a year. Figure 5.37 presents the zone-wise time series of seasonal ZTD means. The left panel in Figure 5.37 shows the seasonal mean time series with the actual magnitude of the ZTD (to differentiate between ZTD magnitudes in different zones) whereas the right panel shows the seasonal mean time series after subtracting the mean of each time series from it (to magnify the pattern of variability).

Similar to the case of monthly means, a close inspection of Figure 5.37 reveals the scatter of ZTD in different types of climates as well as the seasons where the maxima and minima of ZTD occur. Figure 5.37 confirms the values of the scatter of ZTD for all climate groups found in the analysis of the monthly variability (Figure 5.35). In terms of seasonal averages, the climate zones in the northern hemisphere have been found to have ZTD maxima in Boreal Summer (JJA) whereas those in the southern hemisphere have been found to have ZTD maxima in Austral Summer. In the polar climate zones, the ET (Polar - Tundra) has been found to have maxima in DJF and JJA seasons, and minima at MAM and SON seasons.

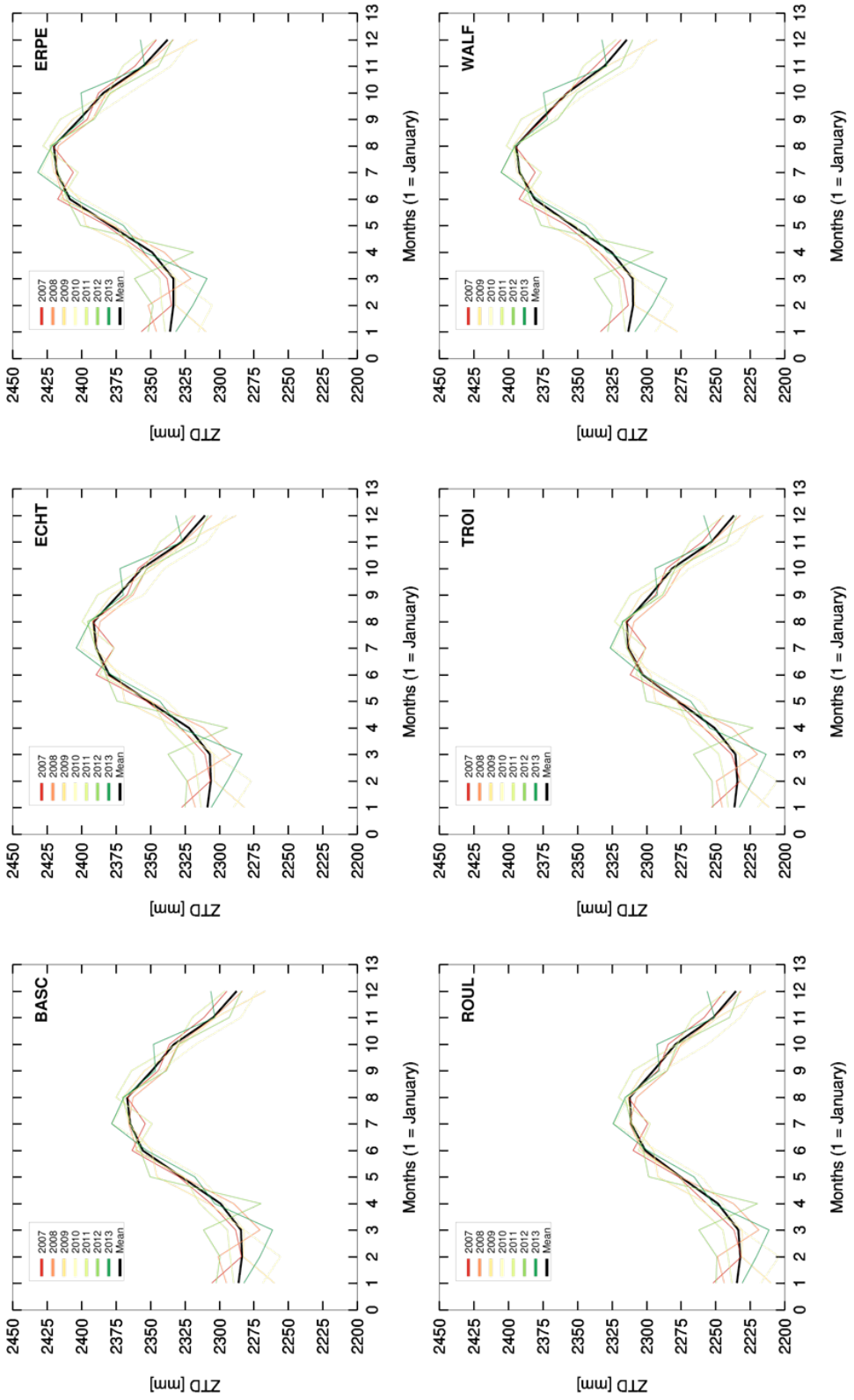

Figure 5.36: Monthly ZTD averages for the SPSLux stations

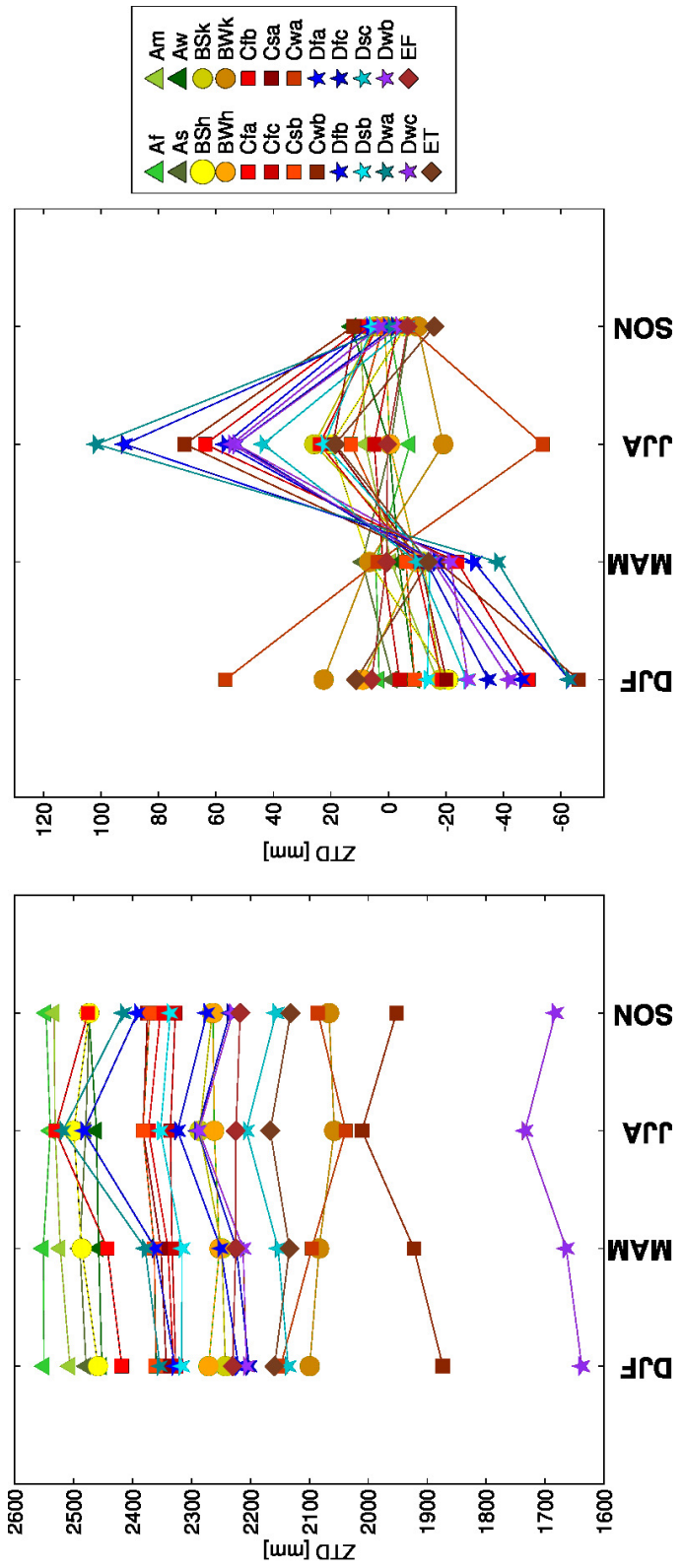

Figure 5.37: Seasonal means of ZTD in various climate zones

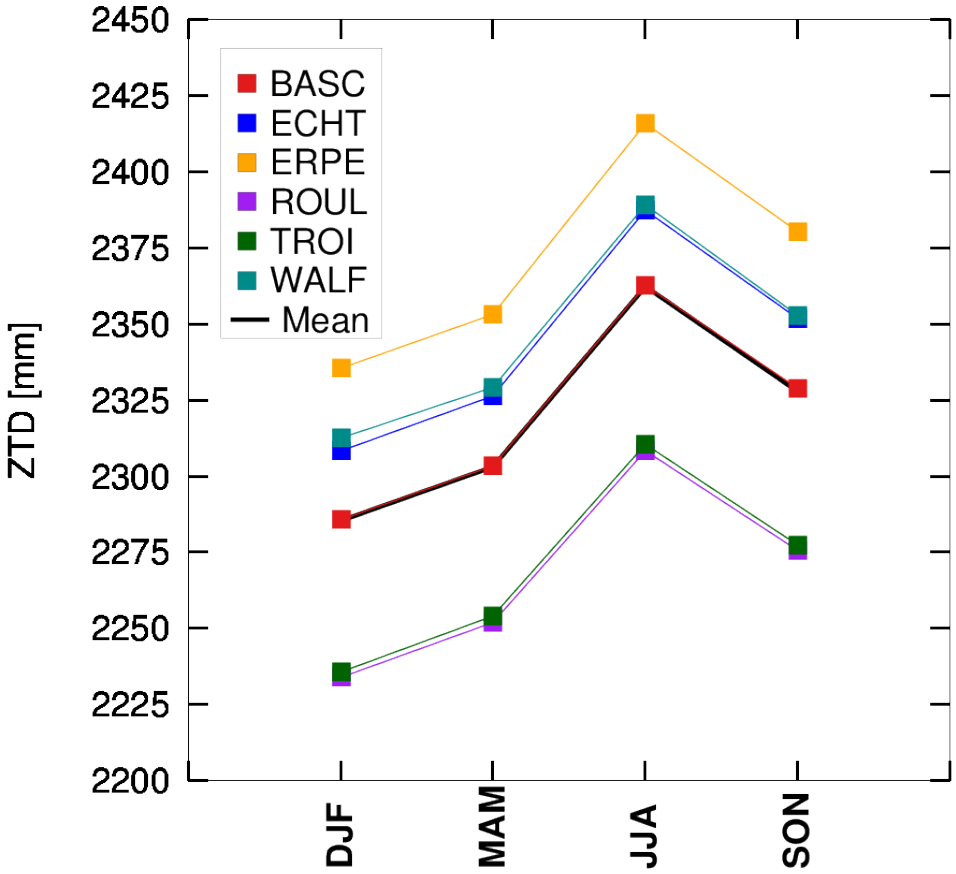

Figure 5.38: Seasonal ZTD averages for the SPSLux stations

Furthermore, in order to study the seasonal variability in the ZTD in Luxembourg, seasonal averages of ZTD were calculated for all the 6 SPSLux stations for the period 2007-2014. Figure 5.38 shows, for each of the 6 SPSLux stations, the time series of seasonal ZTD averages for the years 2007 to 2014 along with their mean. It can be seen that all the 6 SPSLux stations experience the same seasonal variation of the ZTD and the maximum occurs in Summer. However, the magnitude of the ZTD averages for the stations vary because the stations are located at different heights.

5.6 Comparison of PP-PPP and PP-DDP ZTD Estimates

The DDP processing strategy is generally considered more accurate than the PPP strategy. However, PPP is computationally more efficient than DDP network solutions and requires less resources for processing large amounts of data. Therefore, it is of interest to study the suitability of the PPP strategy for climate monitoring applications. To serve this purpose, a comparison of the ZTD estimates from PP-DDP and PP-PPP solutions has been conducted for 114 globally distributed stations and the year 2001. This experiment is described in Section 3.2.6. The statistics of the differences between the PP-PPP and PP-DDP ZTD solutions are summarized in Table 5.12. For brevity, the PP-PPP ZTD is referred to as ZTD_{ppp} and the PP-DDP ZTD is referred to as ZTD_{ddp} in the following text.

It can be seen from Table 5.12 that the mean difference between the ZTD_{ppp} and ZTD_{ddp} ranges from -3.35 to 2.37 mm over all the 25 analyzed climate zones. Furthermore, a strong correlation (ranging from 0.90 to 1.00) has been found between ZTD_{ppp} and ZTD_{ddp} for all climate zones. The highest RMS of the ZTD difference (5.55 mm) has been found for the climate zone Cwb (Temperate - Dry Winter - Warm Summer) which has data available from 1 GNSS station with ellipsoidal height of 1986.20 m. This implies that for a station at very high altitude, the difference between ZTD_{ppp} and ZTD_{ddp} has very high instability (leading to a large standard deviation) whereas the lowest RMS of the difference (1.19 mm) has been found for the climate zone Am (Tropical - Monsoon). In terms of IWV, these RMS differences range from 0.19 to 0.93 kg m^{-2}.

In addition to the results shown above, two additional experiments (not shown in this thesis) have showed that 1) for the Antarctic region, the RMS of the difference between ZTD_{ppp} and ZTD_{ddp} reduces and the correlation coefficient increases when a higher cutoff angle of 7^o is used, and 2) the agreement between ZTD_{ppp} and ZTD_{ddp} is degraded when the Global Mapping Function (GMF) is used during the processing (due to the fact that GMF is not based on NWP raytracing and does not properly account for the changes in atmospheric water vapour).

Table 5.12: Comparison of PP-PPP and PP-DDP ZTD Estimates. r_{pd} is the correlation coefficient between ZTD_{ppp} and ZTD_{ddp}.

Zone	Mean [mm]	SDev [mm]	RMS [mm]	Min. [mm]	25th Percentile [mm]	75th Percentile [mm]	Max. [mm]	r_{pd}
Af	0.92	0.96	1.33	-0.42	0.16	1.62	2.35	0.92
Am	2.37	0.27	2.39	2.10	2.24	2.51	2.64	0.91
As	0.63	1.01	1.19	-0.38	0.13	1.13	1.64	0.95
Aw	-0.92	1.97	2.17	-3.34	-2.38	0.01	2.61	0.94
BSh	-0.78	5.13	5.19	-9.35	-4.91	3.00	9.88	0.92
BSk	0.43	2.66	2.69	-3.23	-1.53	2.82	3.23	0.96
BWh	-2.18	1.75	2.80	-3.93	-3.06	-1.30	-0.43	0.91
BWk	-0.77	0.95	1.22	-1.72	-1.24	-0.29	0.18	0.95
Cfa	0.10	4.34	4.34	-6.66	-2.72	0.84	9.91	0.98
Cfb	-1.29	3.26	3.51	-9.02	-3.02	0.93	3.05	0.97
Cfc	-0.95	4.93	5.02	-5.37	-4.84	2.50	7.95	0.96
Csa	1.92	4.74	5.12	-2.11	0.14	1.49	15.69	0.97
Csb	1.86	3.62	4.07	-3.41	-1.15	4.06	8.21	0.92
Cwa	-1.04	3.20	3.37	-6.27	-1.77	0.59	2.43	0.96
Cwb	0.76	5.53	5.55	-9.97	-3.61	5.51	9.89	0.92
Dfa	-1.17	1.48	1.89	-2.65	-1.91	-0.43	0.31	0.98
Dfb	-1.06	2.05	2.31	-5.42	-2.10	-0.36	2.48	0.98
Dfc	-0.54	1.35	1.45	-1.59	-1.35	-0.58	2.69	0.98
Dsb	-0.42	4.99	5.01	-15.60	-3.20	1.80	17.30	0.91
Dsc	1.36	4.50	4.69	-8.34	-1.71	4.62	6.11	0.95
Dwa	-0.44	1.60	1.66	-2.71	-1.04	0.69	0.75	0.99
Dwb	-0.02	5.12	5.14	-9.91	-3.98	4.10	9.17	0.96
Dwc	1.00	4.41	4.52	-9.99	-1.90	4.20	7.85	1.00
EF	-3.35	3.77	5.05	-8.68	-4.82	-0.69	-0.42	0.90
ET	-2.61	3.19	4.13	-6.72	-4.45	-0.56	1.07	0.97

Chapter 6

Potential for Luxembourg

Ideas do not always come in a flash but by diligent trial-and-error experiments that take time and thought.

Charles K. Kao

This chapter provides an assessment of GNSS and meteorological data available in Luxembourg from various sources. It also presents the results of a comparison of various IWV datasets derived using different sources of meteorological data. Furthermore, based on the overall results of this thesis, it presents the current potential of GNSS meteorology and GNSS climatology for Luxembourg by discussing the applications of RT, NRT and PP ZTD as well as the available meteorological data.

6.1 Assessment of GNSS-derived ZTD

The historical observation data from the six GNSS stations in Luxembourg (SPSLux) is available since late 2006 and at the time of this thesis, the SPSLux data availability is slightly over 8 years. Although for long term climate research, this length of available data is not yet sufficient, however, the available historic data from SPSLux have been processed using the PP processing system during this research in order to examine their quality and suitability for climate monitoring applications. For validation of the PP-PPP ZTD estimates from the SPSLux stations, these have been compared to the ZTD obtained from the ERA-Interim dataset at the SPSLux station heights for a 3-year period (2011 - 2014). The ZTD values from ERA-Interim, interpolated to the six SPSLux GNSS stations, were obtained directly using the GOP - TropDB - TropModel service (`http://www.pecny.cz/gop/index.php/gop-tropdb/tropo-model-service`) by specifying the SPSLux station coordinates. Table 6.1 shows the statistics for this comparison. Figure 6.1 shows the comparison of ZTD time series from the six SPSLux GNSS stations and the corresponding ERA-Interim equivalent ZTD using ZTD time series, ZTD difference time series, correlation plots and histograms of the ZTD difference.

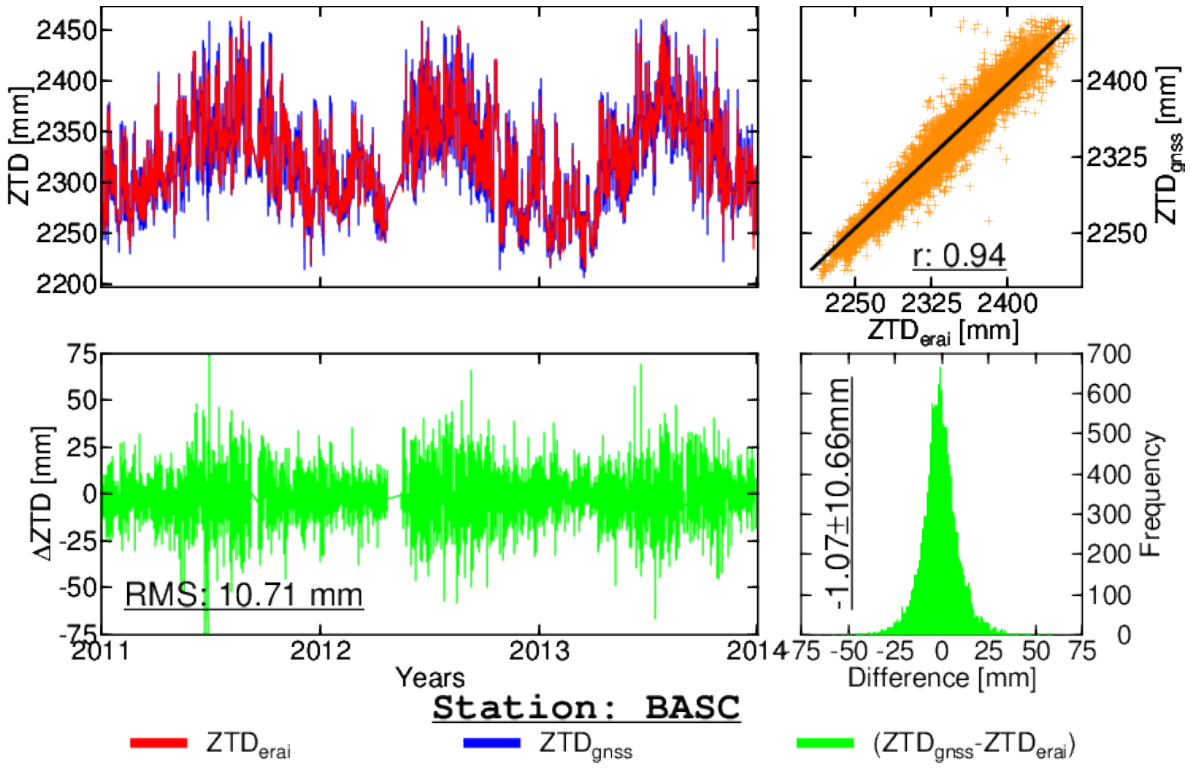

(a) BASC

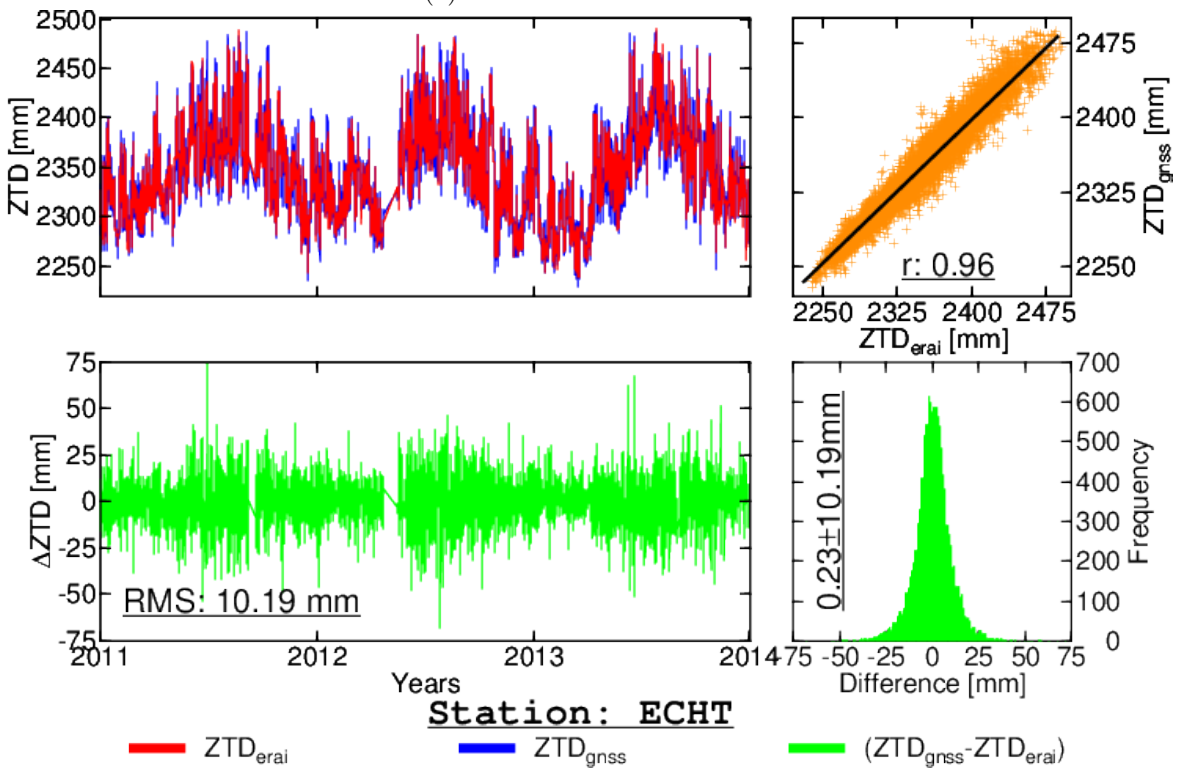

(b) ECHT

Figure 6.1: Comparison of GNSS and ERA-Interim ZTD for SPSLux (Stations: BASC, ECHT)

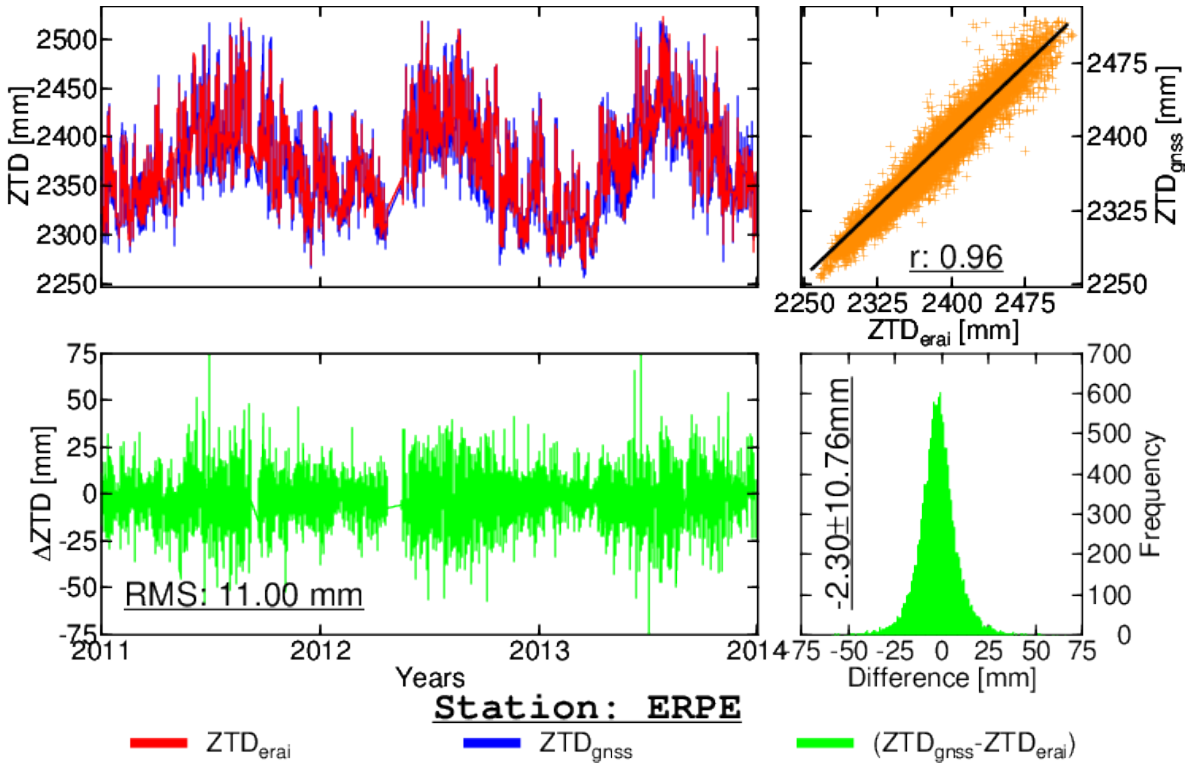

(c) ERPE

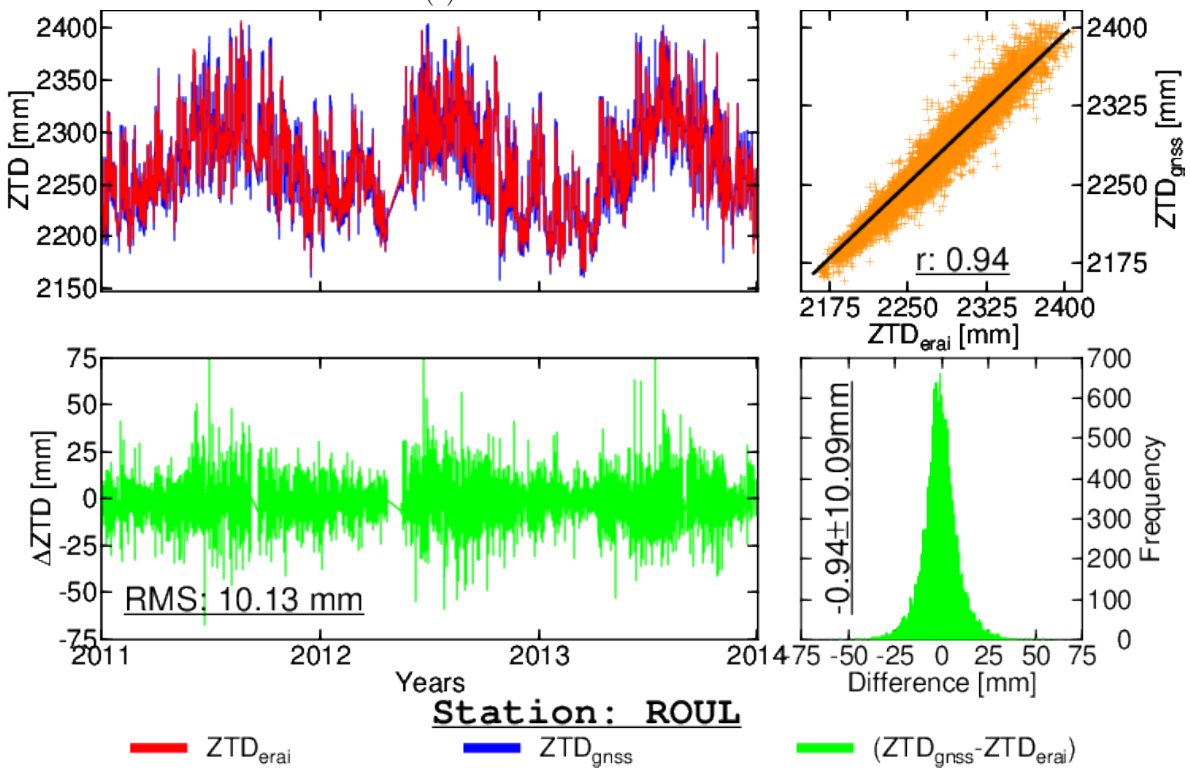

(d) ROUL

Figure 6.1: Comparison of GNSS and ERA-Interim ZTD for SPSLux (Stations: ERPE, ROUL)

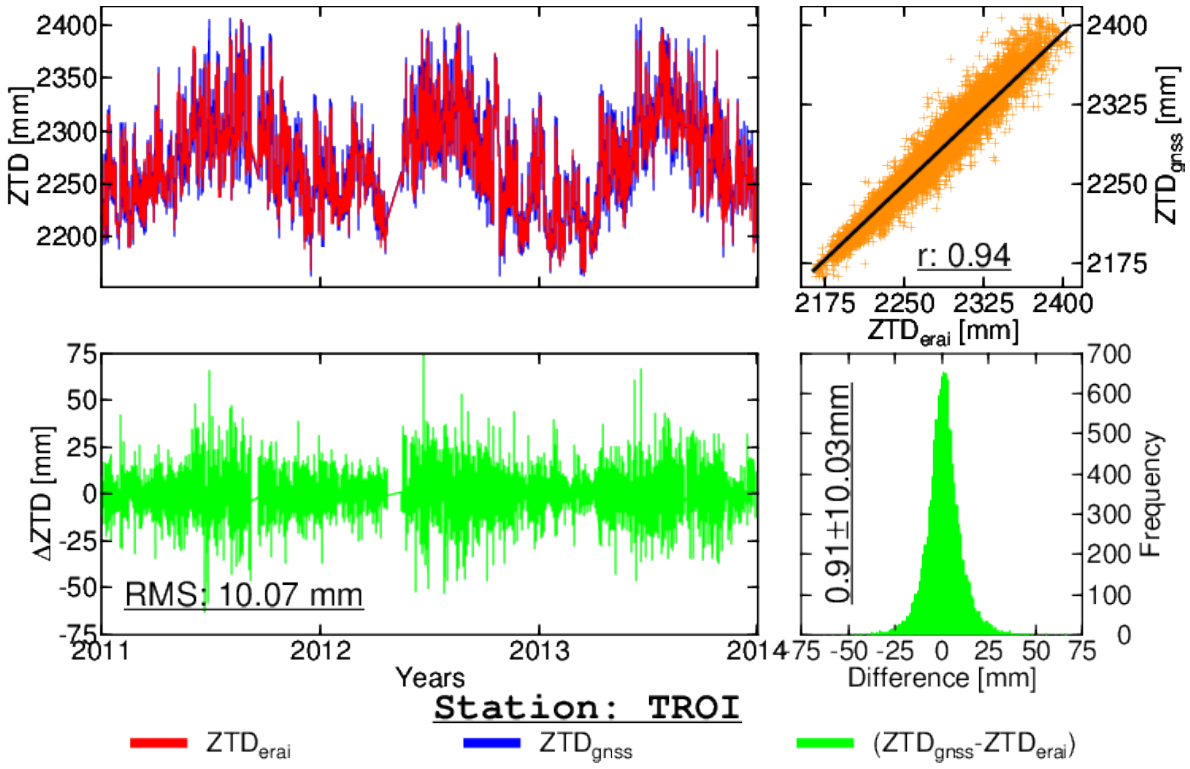

(e) TROI

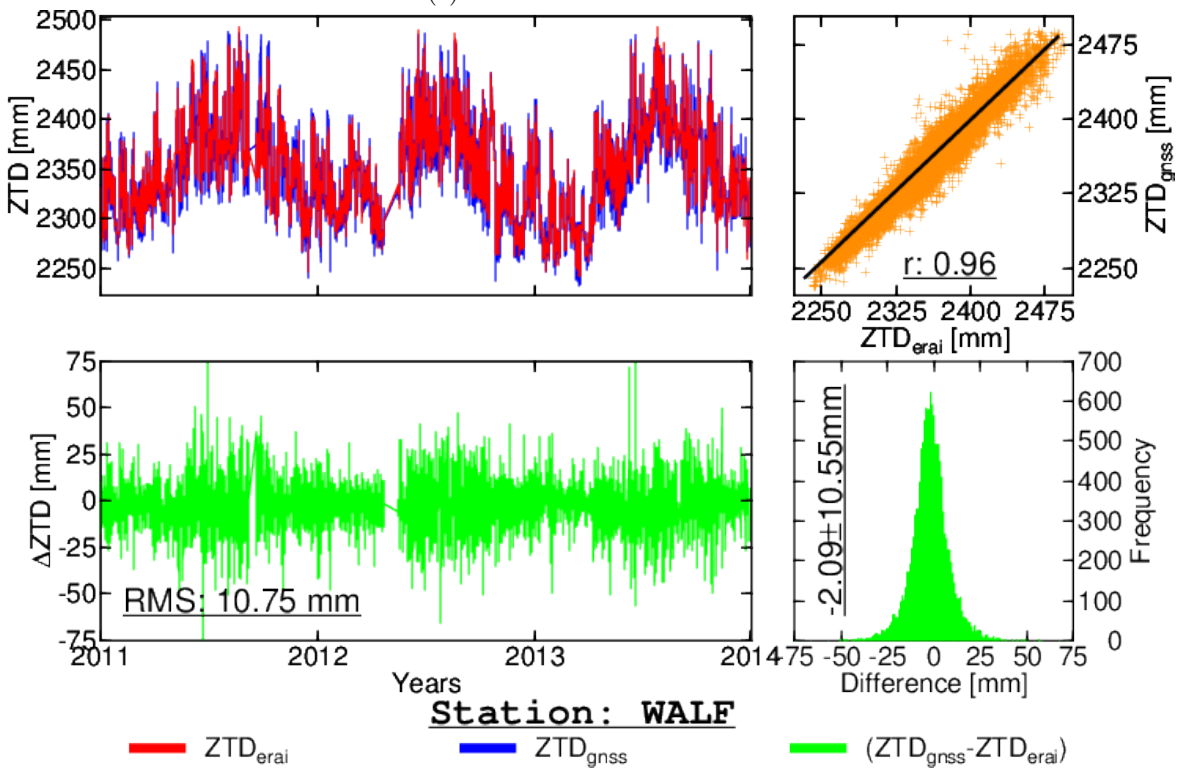

(f) WALF

Figure 6.1: Comparison of GNSS and ERA-Interim ZTD for SPSLux (Stations: TROI, WALF)

Table 6.1: Comparison of GNSS and ERA-I ZTD for SPSLux stations

Station	Mean [mm]	SDev. [mm]	RMS [mm]
BASC	-1.07	10.66	10.71
ECHT	0.23	10.19	10.19
ERPE	-2.30	10.76	11.00
ROUL	-0.94	10.09	10.13
TROI	0.91	10.03	10.07
WALF	-2.10	10.54	10.75
Average	-0.88	10.38	10.48

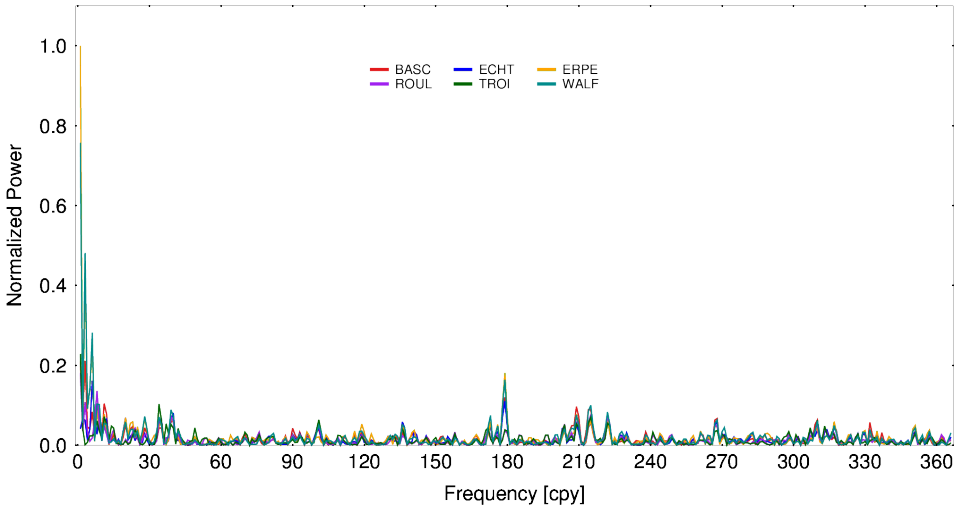

Figure 6.2: Lomb-Scargle Periodogram of difference between ZTD_{gnss} and ZTD_{erai} for SPSLux stations

It can be seen from Table 6.1 and Figure 6.1 that the SPSLux and ERA-Interim ZTD time series follow the same pattern, however, they have mean biases ranging -2.30 to 0.91 millimeter (which, as per the results presented in Chapter 5, is also the case for GNSS stations located in other parts of the world). The standard deviation and RMS of the differences are consistent around 10 mm. The correlation coefficient (r) between GNSS-derived ZTD and ERA-Interim ZTD for all the six SPSLux stations has been found to be 0.94 to 0.96. To investigate about the presence of any periodic behaviour in the differences between SPSLux (GNSS) and the equivalent ERA-Interim ZTD, Figure 6.2 shows the Lomb-Scargle periodogram of the ZTD differences for the six SPSLux stations for the frequencies ranging from 1 to 366 cycles per year (cpy). The spectral power (normalized using the highest power i.e. annual for ERPE) of the annual, semi-annual, seasonal (3-monthly), monthly and diurnal signal for each of the six stations are also listed in Table 6.2. It could be seen from Table 6.2 that except for the station ECHT, the annual signal (1 cpy) has the highest power.

Table 6.2: Normalized spectral power of the periodic signals in ZTD differences for SPSLux stations

Station	Annual (1 cpy)	Semi-annual (2 cpy)	Seasonal (4 cpy)	Monthly (12 cpy)	Diurnal (365 cpy, 366 cpy)
BASC	0.21	0.07	0.05	0.08	0.01, 0.01
ECHT	0.04	0.07	0.01	0.07	0.01, 0.02
ERPE	1.00	0.04	0.09	0.03	0.01, 0.01
ROUL	0.18	0.03	0.03	0.03	0.01, 0.01
TROI	0.23	0.04	0.01	0.05	0.00, 0.01
WALF	0.76	0.06	0.09	0.05	0.02, 0.03

6.2 Assessment of Meteorological Data

Surface pressure (referred to as "pressure" in the following text) and surface temperature (referred to as "temperature" in the following text) are needed to convert the ZTD into IWV (Figure 1.1, Section 2.3.4). This assessment has been carried out by comparing the pressure and temperature values obtained from various sources to their equivalent values derived from the ERA-Interim dataset. The pressure and temperature values from ERA-Interim, interpolated to the six SPSLux GNSS stations, were obtained directly using the GOP - TropDB - TropModel service (`http://www.pecny.cz/gop/index.php/gop-tropdb/tropo-model-service`) by specifying the SPSLux station coordinates.

6.2.1 Assessment of Pressure Data

The surface pressure values at the SPSLux station locations were obtained from the sources mentioned in Section 4.5 i.e. UKMO, ANAMET (MétéoLux), ASTA and ERA-Interim datasets and using the ERA-Interim dataset as a reference, a comparison of these values was performed using the common epochs available in all datasets for a period of 2011-2014. The UKMO and ASTA pressure values are only reported at the mean seal level (MSL) and were therefore corrected (using the formulas given in Appendix B) to the SPSLux station heights (Table 4.1). The ANAMET pressure values are available at both the sensor height and MSL, but for consistency, the MSL values have been used and are corrected for SPSLux station heights (using the formulas given in Appendix B). It is important to mention here that the ASTA data obtained is not quality controlled and therefore contains various outliers that have been removed (by rejecting the values with a difference greater than 10 hPa with the reference) prior to computing the statistics. The ASTA data amongst others form the basis for the Atlas Hydro-Climatique du Grand-Duch de Luxembourg (English: Hydroclimatic Atlas of the Grand Duchy of Luxembourg) prepared by the Luxembourg Institute of Science and Technology (LIST) (`https://www.list.lu/`) and therefore these are quality controlled by LIST. However, as LIST currently does not provide these quality controlled data in a timely manner required for NRT and RT applications, it is inevitable to use the raw ASTA data (i.e. which is not quality controlled) for this thesis. The ERA-Interim pres-

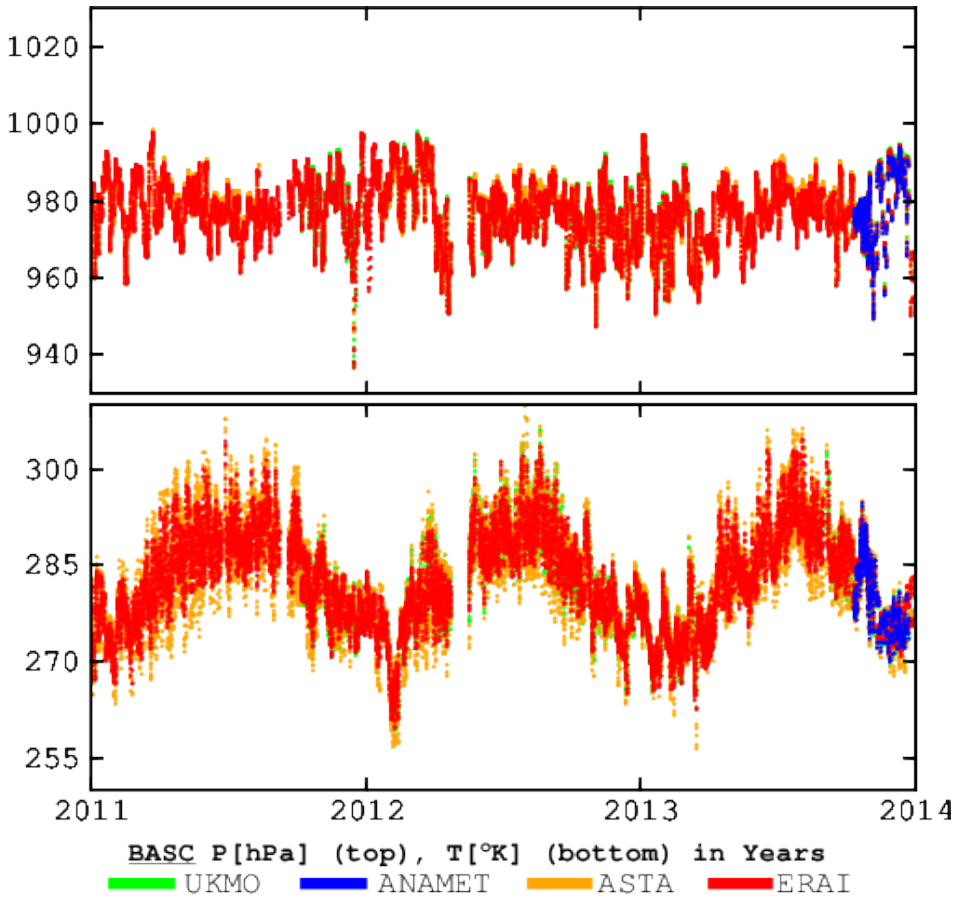

Figure 6.3: Pressure (top) and Temperature (bottom) time series from various sources for SPSLux station BASC

sure values correspond directly to the SPSLux station locations as these were interpolated from the grid (linear spatial and temporal interpolations). Furthermore, the temporal resolution of pressure values used for this comparison is 1 hour. The top panel in Figure 6.3 shows the time series (after removal of outliers) of the available pressure values [hPa] in all datasets for SPSLux station BASC and the period 2011-2014. For the other five SPSLux stations, the pressure time series can be seen in Appendix E.

Table 6.3 provides the statistics of the comparison of the pressure values. In terms of the average of mean differences for all the 6 SPSLux stations, it can be seen that the ANAMET pressure values are in the best agree-

ment with the ERA-Interim pressure values with the average difference of -0.21 hPa whereas the highest average difference of 1.17 hPa has been found in the pressure values from ASTA.

For some cases, Table 6.3 also shows a relation between the pressure difference and the distance between the GNSS station and the pressure observing sensor (the reader is referred to Table 4.11 in Chapter 4 for the distances between GNSS stations and corresponding meteorological sensors). For example, for $(P_{ukmo} - P_{erai})$, the highest mean and RMS difference (0.85 hPa and 1.22 hPa) are found for the most distant station TROI. The second highest mean and RMS difference (0.65 hPa and 1.02 hPa) are found for the second-most distant station ROUL. This is the case for four out of the six SPSLux stations. The lowest mean and RMS difference (0.19 hPa and 0.63 hPa) are found for the station ERPE which has the second-lowest distance to the pressure sensor. In the cases of $(P_{anamet} - P_{erai})$ and $(P_{asta} - P_{erai})$, however, a clear relation between station-sensor distance and the value of the difference has not been found. The UKMO and ANAMET datasets represent the observations from the same (Findel) sensor but it was found that the MSL pressure values in these two datasets have a mean difference of $-0.27 \pm 1.01\ hPa$ with minimum and maximum differences of $-3.92\ hPa$ and $2.74\ hPa$, respectively. This difference is believed to be due to the quality control of the observations by the WMO. In the case of ASTA, it has been found that the pressure difference is small (less than $0.5\ hPa$) when the observations from the ASTA sensors Oberkorn and Roullingen are used.

6.2.2 Assessment of Temperature Data

The surface temperature values at the SPSLux station locations were obtained from the UKMO, ANAMET (MétéoLux), ASTA and ERA-Interim datasets and using the ERA-Interim dataset as a reference, a comparison of these values was performed using the common epochs available in all datasets for a period of 2011-2014. Considering the very small lapse rate of temperature (-0.0065 K/m), no height corrections have been applied to either of the temperature values. Furthermore, the temporal resolution of temperature values used for this comparison is 1 hour. Table 6.4 provides the statistics of this comparison. It can be seen that temperature values from all the sources

Table 6.3: Comparison of pressure data available in Luxembourg at SPSLux stations

GNSS Station	P_{ukmo}−P_{erai}			P_{anamet}−P_{erai}			P_{asta}−P_{erai}		
	Mean [hPa]	SDev [hPa]	RMS [hPa]	Mean [hPa]	SDev [hPa]	RMS [hPa]	Mean [hPa]	SDev [hPa]	RMS [hPa]
BASC	0.39	0.67	0.76	-0.36	0.99	1.05	0.38	1.37	1.42
ECHT	0.46	0.61	0.77	-0.26	1.00	1.03	2.31	2.67	3.54
ERPE	0.19	0.60	0.63	-0.62	0.91	1.10	2.12	2.63	3.38
ROUL	0.65	0.78	1.02	0.05	1.23	1.23	-0.15	1.66	1.66
TROI	0.85	0.89	1.22	0.32	1.34	1.38	0.07	1.68	1.68
WALF	0.37	0.64	0.74	-0.37	0.99	1.06	2.28	2.66	3.50
Average	0.49	0.70	0.86	-0.21	1.08	1.14	1.17	2.11	2.53

show a sub-Kelvin agreement to those from the ERA-Interim dataset. The behaviour of the differences ($T_{anamet} - T_{erai}$) and ($T_{ukmo} - T_{erai}$) is very consistent except for the presence of a constant bias between the two. The smallest mean bias has been found for ($T_{anamet} - T_{erai}$). Furthermore, the effect of station-sensor distances on temperature difference was found to be marginal unlike some cases in the pressure comparison.

Table 6.4: Comparison of temperature data available in Luxembourg at SPSLux stations

GNSS Station	$T_{ukmo}-T_{erai}$			$T_{anamet}-T_{erai}$			$T_{asta}-T_{erai}$		
	Mean [K]	SDev [K]	RMS [K]	Mean [K]	SDev [K]	RMS [K]	Mean [K]	SDev [K]	RMS [K]
BASC	-0.10	1.26	1.26	-0.32	1.00	1.05	-0.63	1.85	1.96
ECHT	-0.27	1.43	1.45	-0.50	1.09	1.20	-0.41	1.53	1.58
ERPE	-0.57	1.45	1.56	-0.80	1.07	1.34	-0.59	1.20	1.33
ROUL	-0.50	1.72	1.79	-0.73	2.13	2.25	-0.58	1.97	2.05
TROI	-0.55	1.74	1.82	-0.78	2.14	2.28	-0.84	2.91	3.03
WALF	-0.24	1.48	1.50	-0.47	1.10	1.19	-0.34	1.23	1.28
Average	-0.37	1.51	1.56	-0.60	1.42	1.55	-0.57	1.78	1.87

6.3 Comparison of IWV Datasets

In order to investigate the suitability of meteorological data available in Luxembourg for conversion of GNSS-derived ZTD into IWV, IWV has been obtained using ZTD from SPSLux GNSS stations using various meteorological data sources and compared to its equivalent from the climate reanalysis model ERA-Interim. For this comparison, a total of four IWV datasets have been computed for each of the six SPSLux GNSS stations. These datasets are briefly described below whereas the formulas and procedures used to obtain these datasets are presented in Appendix F.

ERA-Interim IWV ($\mathbf{IWV}_{erai}$) This IWV dataset, which is used as a reference, has been derived using the ZWD and mean atmospheric temperature (T_m) values extracted from the ERA-Interim dataset (interpolated to the SPSLux station positions).

ASTA IWV ($\mathbf{IWV}_{asta}$) This IWV dataset has been derived by first computing the ZHD using surface pressure from ASTA sensors and then converting the resulting ZWD to IWV using the surface temperature from ASTA sensors.

ANAMET IWV ($\mathbf{IWV}_{anamet}$) This IWV dataset has been derived by first computing the ZHD using the surface pressure which is obtained using the meteorological data directly provided by ANAMET (the WMO Findel sensor).The resulting ZWD has been converted to IWV using the surface temperature from the ANAMET meteorological data.

UKMO IWV ($\mathbf{IWV}_{ukmo}$) This IWV dataset has been derived using the meteorological data for the WMO Findel sensor provided in the UKMO hourly meteorological data file. First, the ZHD has been computed using the surface pressure and then the resulting ZWD has been converted to IWV using the surface temperature.

Figures 6.4 and 6.5 show the comparison of the time series of ERA-Interim and other three IWV datasets for the SPSLux GNSS stations. It could be seen that all the IWV time series follow the same pattern. The statistics of the comparison between ERA-Interim and the other IWV datasets are shown

Table 6.5: Comparison of different IWV datasets for Luxembourg

GNSS Station	$IWV_{ukmo}-IWV_{erai}$			$IWV_{anamet}-IWV_{erai}$			$IWV_{asta}-IWV_{erai}$		
	Mean [kg/m^2]	SDev [kg/m^2]	RMS [kg/m^2]	Mean [kg/m^2]	SDev [kg/m^2]	RMS [kg/m^2]	Mean [kg/m^2]	SDev [kg/m^2]	RMS [kg/m^2]
BASC	-1.42	1.65	2.18	-1.90	1.59	2.48	-1.49	1.76	2.30
ECHT	-1.25	1.57	2.00	-1.72	1.62	2.36	-2.01	1.86	2.74
ERPE	-1.59	1.65	2.30	-2.00	1.67	2.61	-2.36	1.95	3.06
ROUL	-1.49	1.58	2.17	-1.84	1.54	2.40	-1.28	1.67	2.11
TROI	-1.29	1.57	2.03	-1.66	1.54	2.27	-1.07	1.66	1.97
WALF	-1.57	1.61	2.25	-2.04	1.63	2.61	-2.35	1.91	3.02
Average:	-1.44	1.61	2.16	-1.56	1.60	2.46	-1.79	1.80	2.53

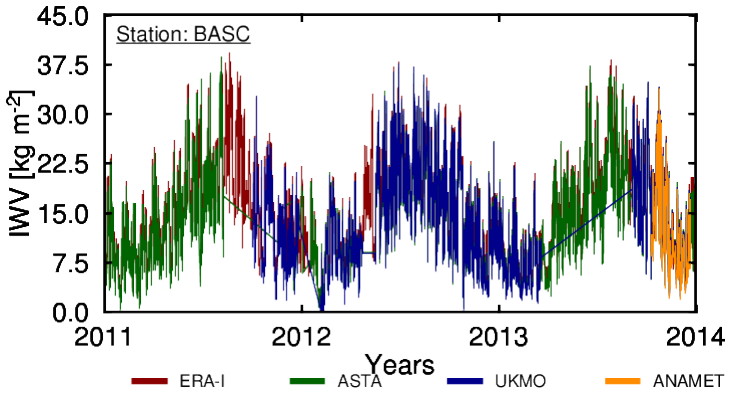

(a) BASC

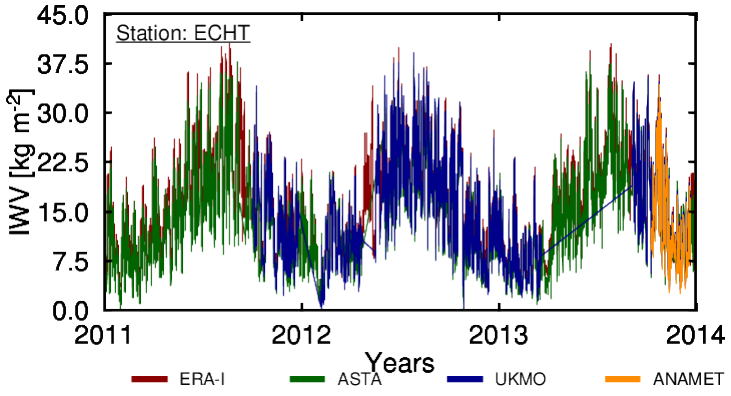

(b) ECHT

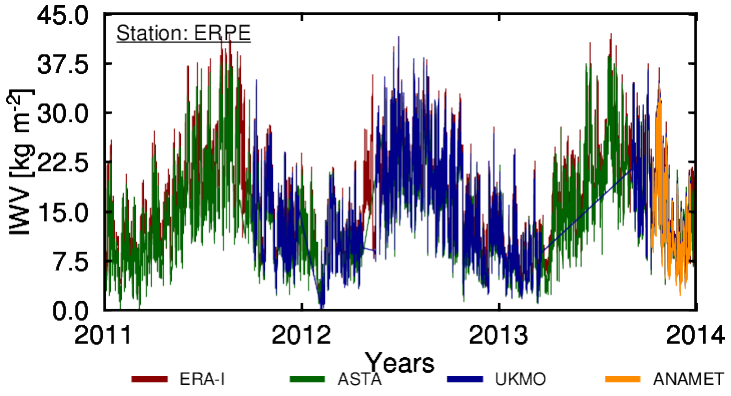

(c) ERPE

Figure 6.4: Time series of IWV derived from ERA-Interim and SPSLux GNSS (Stations: BASC, ECHT, ERPE)

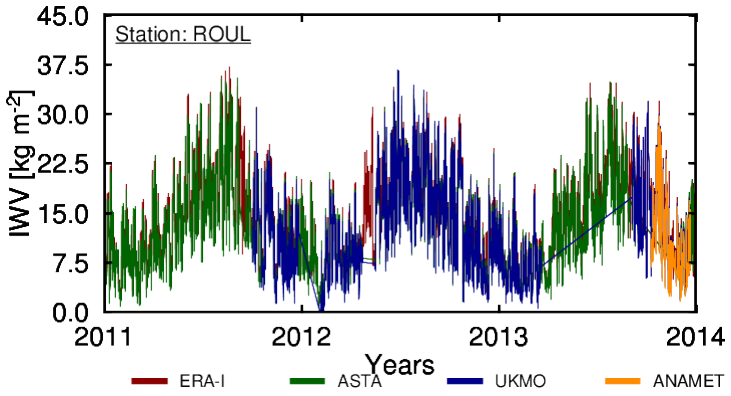

(a) ROUL

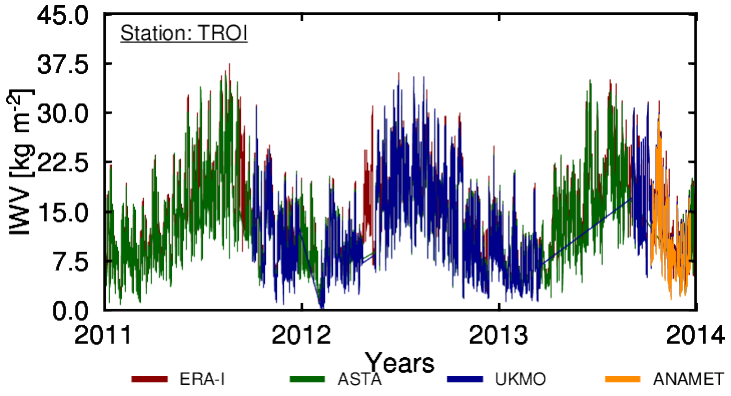

(b) TROI

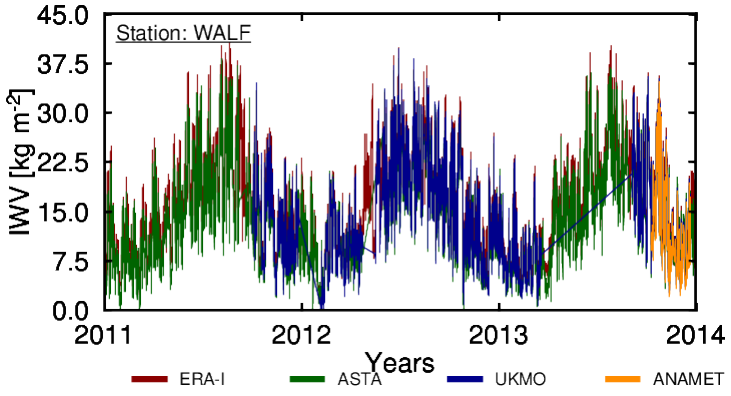

(c) WALF

Figure 6.5: Time series of IWV derived from ERA-Interim and SPSLux GNSS (Stations: ROUL, TROI, WALF)

Table 6.6: RMS of differences in Pressure, Temperature and IWV for various solutions

Solution	RMS(ΔP) [hPa]	RMS(ΔT) [^oK]	RMS(ΔIWV) [$kg\ m^{-2}$]
UKMO	0.86	1.56	2.16
ANAMET	1.14	1.55	2.46
ASTA	2.53	1.87	2.53

in Table 6.5. It can be seen from Table 6.5 that the mean difference between IWV of the three solutions and the reference ranges from $-1.79\ kg\ m^{-2}$ to $-1.44\ kg\ m^{-2}$ with the lowest mean difference being for IWV_{asta}. However, the differences of IWV_{ukmo} and IWV_{anamet} are more stable (lower standard deviation than IWV_{asta}).

In order to study the impact of using the pressure and temperature values from different sources on the differences between the obtained and reference IWV, the RMS differences of pressure, temperature and IWV from each of the three datasets are shown in Table 6.6. It can be seen from Table 6.6 that using the pressure and temperature values from UKMO leads to the lowest RMS difference ($2.16\ kg\ m^{-2}$) in the obtained IWV. Using the pressure and temperature values from ANAMET leads to an IWV difference of $2.46\ kg\ m^{-2}$ whereas using those from ASTA leads to an IWV difference of $2.53\ kg\ m^{-2}$. However, the difference between the obtained and reference IWV (for all three cases) agrees within $0.37\ kg\ m^{-2}$.

6.4 Application of RT ZTD

As mentioned in Chapter 4, Luxembourg has a network of six GNSS stations which all belong to the Administration du Cadastre et de la Topographie (ACT) [English: The Administration of Cadastre and Topography] of Luxembourg. While the primary application of these stations is in the NRTK Satellite Positioning Service (SPSLux) of ACT, the GNSS data can also be obtained in RT. Using the SPSLux RT observation streams and an appropriate RT GNSS processing software, e.g. BNC or G-Nut/Tefnut (Section 3.1.1), RT-PPP ZTD estimates for these six stations can be obtained with an update rate as high as 1 second. Furthermore, using the 1 second ZTD estimates, moving averages (e.g. 5 minutes or 10 minutes) can be computed

and hence the ZTD can be provided to the meteorological community with a latency of as low as 5 minutes which is adequate for data assimilation into NWP models.

Using the high-rate pressure and temperature data from the meteorological sensors present in Luxembourg (Sections 4.5 and 6.2), it is possible to convert the ZTD into IWV with latencies of as low as 5 minutes and this low latency IWV can be used to monitor the movement of weather fronts or storms as discussed in Section 5.3.

6.5 Application of NRT ZTD

The weather forecasts issued for Luxembourg are based on the output of the AROME NWP model operational at MétéoFrance. It has been shown in Section 5.2 that the NRT ZTD solution produced during this research has a positive influence on the quality of weather forecasts (specially precipitation forecasts) for Luxembourg. The NRT ZTD solution produced during this research (UL01) is routinely submitted to EGVAP as a test solution for monitoring purposes (which means that it is not currently assimilated in any NWP model). The results presented in Section 5.2 show that if the UL01 solution is made an operational solution, i.e. it is operationally assimilated in the AROME NWP model, it will improve the quality of forecasts of precipitation and other parameters for Luxembourg and the Greater Region (Mahfouf et al., 2015).

The results presented in Section 5.3 show that it is possible to use the 2D IWV fields obtained from the hourly NRT system developed during this research can be used to monitor the rapid changes in IWV over Luxembourg which can in turn lead to the monitoring of weather fronts and storms in the region.

6.6 Application of PP ZTD

The results presented in Section 5.4 show that the SPSLux historic data can be used to produce a good quality ZTD time series for the whole period since the stations are in operation. During this research, the available

ZTD time series from SPSLux has been used to study the variability and trends in the climate over Luxembourg and provided that the SPSLux stations are kept operational and maintained properly over the years to come, the SPSLux observations can provide good means of studying the climate of the region. Furthermore, it is of utmost importance to document and report any hardware changes occurring at the SPSLux GNSS stations so that the effects of such changes can be accounted for during the data processing and inconsistencies in the ZTD time series can be avoided. The findings in Sections 6.2 and 6.3 also suggest that using the meteorological data available in Luxembourg, historical (and long-term when more data is available) IWV time series for Luxembourg can be obtained for climate monitoring applications.

6.7 Application of Meteorological Sensors

Luxembourg has a large amount of meteorological sensors (including 1 WMO sensor (Findel) and 52 sensors from ASTA) located all around the country's territory (shown in Figure 6.6 and Section 4.6). The Luxembourg Institute of Science and Technology (LIST) (`https://www.list.lu/`) carries out quality control of the data available from these sensors but these quality controlled data are not readily available for NRT and RT applications. Some of these meteorological sensors are located nearby each of the six SPSLux ground-based GNSS stations. Therefore, the suitability of the pressure and temperature values from these sensors for the conversion of the ZTD obtained at the SPSLux station locations has been investigated in Section 6.2. Furthermore, these sensors have a fairly uniform distribution across the country and this fact leads to the possibility of defining a high resolution grid of meteorological data over Luxembourg which could be used for many research, industrial and agricultural applications.

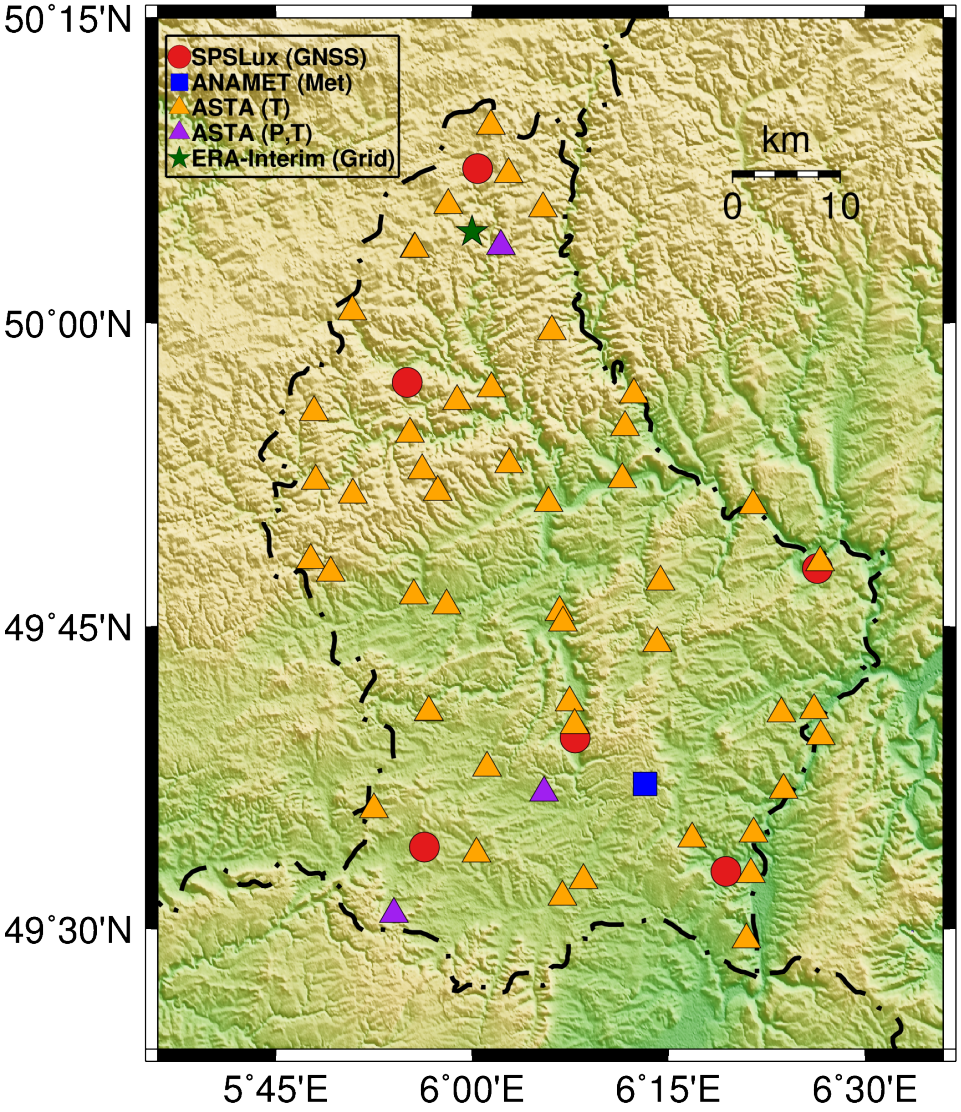

Figure 6.6: Ground-based GNSS and meteorological data sources available inside Luxembourg

6.8 Comparison to WMO IWV Accuracy Requirements

The requirements on the accuracy of the IWV, set by WMO, for applications in nowcasting, NWP and climate monitoring can be found at `https://www.wmo-sat.info/oscar/variables/view/162`. A comparison was performed between the achieved accuracy of IWV for Luxembourg using different processing modes and the WMO accuracy requirements. The real-time and near real-time retrieval of IWV is intended for nowcasting and NWP applications, whereas the IWV retrieval in post-processing mode is intended for use in climate monitoring. Table 6.7 summarizes the results of this comparison by mentioning if the IWV for Luxembourg obtained using the three processing modes meets the target and threshold requirements on accuracy for the various applications.

It can be seen from Table 6.7 that the IWV obtained in all the three modes (real-time, near real-time and post-processing) either meets the target or the threshold requirement on the accuracy.

Table 6.7: Summary of comparison between the achieved accuracy of GNSS-derived IWV with WMO accuracy requirements

	Nowcasting		**Numerical Weather Prediction**		**Climate Monitoring**	
Processing Mode	**Meets Target?**	**Meets Threshold?**	**Meets Target?**	**Meets Threshold?**	**Meets Target?**	**Meets Threshold?**
Real-Time (RT)	No	Yes	No	Yes	-	-
Near Real-Time (NRT)	Yes	-	Yes	-	-	-
Post-Processing (PP)	-	-	-	-	No	Yes

Chapter 7

Conclusions and Suggestions for Future Work

> *Thou seest not, in the creation of the All-merciful any imperfection, Return thy gaze, seest thou any fissure. Then Return thy gaze, again and again. Thy gaze, Comes back to thee dazzled, aweary.*
>
> Qur'an, 67:4-5

This chapter summarizes all the results and findings of the thesis in form of conclusions. After the conclusions, it provides the suggestions for the future work.

7.1 Conclusions

This thesis presents the results of the doctoral research project titled "The Potential of Precipitable Water Vapour Measurements from Global Navigation Satellite Systems in Luxembourg" (project acronym: PWVLUX). PWVLUX, as a major outcome, has established the infrastructure for the utilization of GNSS observations for meteorological and climatological applications in Luxembourg. Furthermore, it has put Luxembourg on a map with 18 other GNSS meteorology groups in Europe through establishing a participation in the EUMETNET EIG Water Vapour Programme (EGVAP).

The scientific conclusions of this thesis have been divided into seven parts in accordance to the order of the described experiments in Chapter 3.

RT ZTD for NWP Applications

The suitability of RT-PPP ZTD estimates from three different software packages for operational meteorology was assessed through a comparative analysis using the IGS final troposphere product and RS data as references. In terms of standard deviation, it was seen that the solutions from the G-Nut/Tefnut software library achieved the best agreement with these.

The solutions from BNC2.7 are the next closest to the reference. Among the BNC2.7 solutions, lower biases have been found for the solutions computed using the correction stream containing a Kalman Filter combination (IGS02) rather than the one computed using a single-epoch solution correction stream (IGS01). The ambiguity float solution from the PPP-Wizard has the largest bias to IGFT because of the fact that it currently does not apply receiver ARP eccentricity and PCO corrections during processing. However, the application of ARP eccentricity and PCO corrections on the coordinates prior to processing leads to a 66% reduction in this bias. Integer ambiguity resolution using the PPP-Wizard seems to have a millimeter-level effect on the RT-PPP ZTD estimates and is beneficial for the rapid re-convergence of PPP solutions. The RT-PPP ZTD solutions were compared with the established user requirements for NWP nowcasting by using the RMS bias to IGFT as a measure of relative accuracy. It was found that GN01, GN02, and BN02 fulfill the threshold requirements on ZTD accuracy, whereas BN01, and PWFL, PWFX (and PWFX2) exceed this threshold. The RT-PPP ZTD solutions were also compared with RS-based ZTD, and an agreement of 1-3 cm in terms of bias and 1-4 cm in terms of standard deviation was found between the two. Furthermore, the comparison with the user requirements was repeated by using the RMS bias between GNSS-derived ZTD and RS-based ZTD as a measure of relative accuracy, and it showed that only the two G-Nut/Tefnut solutions (GN01 and GN02) meet the threshold requirements, whereas the BNC2.7 and PPP-Wizard solutions, without the implementation of precise bias models in the software, exceed the threshold. However, the implementation of precise bias models such as receiver antenna PCV, ocean tide loading and higher-order ionospheric corrections in these software packages can enhance their suitability for NWP nowcasting (Ahmed et al., 2016).

NRT ZTD for NWP Applications

An impact assessment of the assimilation of GNSS-derived ZTD observations into the 3D-VAR system of the convective scale NWP model AROME developed at Météo-France for issuing operational mesoscale short-range forecasts over Western Europe was performed. Assimilation experiments were undertaken for a 1-month period in July-August 2013, corresponding to an upgrade of the model's operational forecasting suites with additional

observing systems at Météo-France. Even though many impact studies have been performed in the past to examine the interest of GNSS-derived ZTD on the forecast skill of NWP models, an original aspect concerns the design of the observing system where GNSS-derived ZTD data represents less than 2 percent of the total observations assimilated in AROME. This small fraction is a consequence of the capacity of 3D-VAR to ingest many other data types, in particular radar reflectivity and radial winds, that provide significant information on moisture and dynamical fields at mesoscale levels. However, contrary to other remote sensing observations that are only useful when it rains (weather radars) or in clear-sky or above clouds (satellite radiances), GNSS-derived ZTD data are available in all weather conditions with high temporal resolution and lower cost. Three assimilation experiments were conducted where in the first experiment (NOGPS), all other observations were assimilated except for the GNSS-derived ZTD. In the second experiment (EGVAP), the GNSS-derived ZTD from the operational EGVAP solutions were assimilated in addition to the observations assimilated in the NOGPS experiment. In the third experiment, GNSS-derived ZTD observations from UL01 solution were assimilated in addition to those assimilated in the NOGPS and EGVAP experiments. The NOGPS experiment served as a baseline to verify that the GNSS-derived ZTD still contributes in a positive manner to the model analyses and to the forecasts of AROME, in particular since a recent revision of the model's white list and data selection. The UL01 experiment in addition to the EGVAP experiment was conducted to examine the sensitivity of the forecasting system to additional GNSS-derived ZTD observations provided by the UL01 solution. It was found that for both the EGVAP and UL01 ZTD datasets, the static bias correction scheme allowed to remove most of the bias and that the data selection lead to unbiased and Gaussian statistics that are necessary conditions for an optimal assimilation. Among the stations present in the UL01 solution, the six stations in Luxembourg were found to have very large biases (around 30 mm) with the model equivalent ZTD and were therefore not selected to enter the 'white list'. The reason for this has been identified by the supervisor since the completion of the PhD research and is related to the handling of PCO corrections by the data provider. The quality of the remaining stations in the UL01 solution was found to be similar to that of the current operational stations provided through EGVAP. Therefore, after excluding the six stations in Luxembourg,

the UL01 solution was found to be fulfilling the criteria for the assimilation and its assimilation was successful in AROME. As a result of the assimilation of the GNSS-derived ZTD, the AROME short-range forecasts were found to be closer to the observations that are sensitive to humidity which implies that through the assimilation of GNSS-derived ZTD, the 3-hour prediction of the humidity field by AROME becomes closer to the truth. The investigation of the impact on objective forecast skill scores revealed a small positive impact on screen-level relative humidity and the 24-hour precipitation accumulations. The categorical scores were found to be systematically improved when the UL01 data were assimilated in addition to the operational EGVAP ZTD observations. Examination of three precipitation case studies confirmed that the GNSS-derived ZTD observations affect the predicted location and intensity of rain systems that generally improved the quality of the numerical forecasts. It was found that the additional ZTD data provided by UL01 significantly modified rainfall patterns with, most of the time, a better location and intensity of precipitating cells.

NRT IWV for Storm Tracking

Results from the hourly NRT GNSS data processing system for a warm front and its corresponding precipitation events crossing over Luxembourg and the Greater Region on 22-23 February 2012 were presented. The 2D maps of IWV obtained from the hourly NRT system are compared with cloud distribution and precipitation maps from satellite and weather radar data, respectively, and a good agreement in the location of the front system has been found. The evolution of the GNSS-derived IWV was observed during the passage of the front and it was found that the IWV increased by approximately 15 kg/m^2 as the front passed over Luxembourg. It was shown that by observing the IWV change over the ground-based GNSS stations in Luxembourg in NRT, it is possible to determine the speed and direction of passing fronts and hence storms can also be tracked.

Validation of ERA-Interim Climate Reanalysis Dataset

ZTD derived from the ERA-Interim climate reanalysis model (ZTD_{erai}) were validated for 25 climate zones by a comparison with GNSS-derived ZTD (ZTD_{gnss}) at the locations of over 400 globally distributed (in different

climate zones) ground-based GNSS stations. The correlation coefficient (r_{eg}) between ZTD_{erai} and ZTD_{gnss} was found to be between 0.87 and 1.00 for the various climate zones. The highest value of r_{eg} (1.00) was found for the three "Cold" climate zones namely Dsc (cold - dry summer - cold summer), Dwa (cold - dry winter - hot summer) and Dwc (cold- dry winter - cold summer), and the second-highest value (0.99) of r_{eg} was found for another "Cold" climate zone (Dwc or cold- dry winter - cold summer). The lowest value of r_{eg} (0.87) was found for the "Tropical" climate zone Af (tropical - rainforest) whereas the second-lowest value ($r_{eg} = 0.88$) has been found for the "Tropical" climate zones As (tropical - dry summer) and Aw (tropical - savannah). These values of the correlation coefficient suggested that the correlation between ZTD_{erai} and ZTD_{gnss} is high in the regions with low amount of atmospheric water vapor and is low in the regions with high amount of atmospheric water vapour.

It was also found that the highest mean, standard deviation and RMS of the differences correspond to the climate zones with high altitude, high topographic variation and high periodicity in the ZTD residuals. Furthermore, a generalization of the global statistics in terms of latitude suggested that the agreement between ZTD_{erai} and ZTD_{gnss} is relatively better towards the polar regions as compared to that in the regions around the equator. This fact reinforced the conclusion that ZTD_{erai} has higher accuracy in the regions with lower amount of atmospheric water vapour.

PP ZTD for Climate Variability Analysis

Monthly and seasonal means of GNSS-derived ZTD (ZTD_{gnss}) were computed using a global ZTD_{gnss} dataset consisting of 19-years of data from over 400 stations to study the climate variability in different climate zones.

It was found that for tropical climate zones (climate group A), the scatter of ZTD values lies within 40 mm. The ZTD in all the four zones of this type (Af, Am, As and Aw) was found to have one maximum around the month of May whereas that in the zones Am and Aw was found to have a second maximum around the month of October. The ZTD in the arid climate zones (climate group B) was found to have a scatter of 70 mm with one maximum in July for the zones BSh and BSk, two maxima for the zone

BWh in January and September, and two maxima for the zone BWk in January and December. The minima of ZTD in this climate group were found to be occurring in May for the zone BWh and in June for BWk. For the climate zones in the temperate climate group, it was found that the scatter of the ZTD lies within 160 mm. The climate zone Cwa was found to have one ZTD minimum in July (during Austral Winter) whereas all the other zones in climate group C were found to have a maximum of ZTD in the month of July (during Boreal Summer). It was found that the scatter of ZTD in the cold climate zones (climate group D) lies within 200 mm and all the climate zones in this group experience one ZTD maximum in the month of July. Whereas, in the polar climate zones (climate group E), the scatter of ZTD was found to be within 60 mm. In the climate zone ET (Polar - Tundra), one maximum of the ZTD was found in July whereas for the zone EF (Polar - Frost), one minimum in October and two maxima in January and December were found.

The values of the scatter of ZTD_{gnss}, as obtained using the monthly means, were confirmed when computed using the seasonal means. In terms of seasonal averages, it was found that the climate zones in the northern hemisphere have ZTD maxima in the Boreal Summer (JJA) whereas those in the southern hemisphere have ZTD maxima in the Austral Summer. In the polar climate zones, the ET (Polar - Tundra) zone was found to have maxima in the DJF and JJA seasons, and minima at the MAM and SON seasons.

Monthly and seasonal variability in ZTD_{gnss} were also studied for the locations of 6 ground-based GNSS (SPSLux) stations in Luxembourg. It was found that all the 6 SPSLux stations experience the same monthly and seasonal variability of ZTD_{gnss}. In terms of monthly variation, it was found that the maxima in ZTD_{gnss} occurs around the month of July for all the 6 SPSLux stations whereas in terms of seasonal variation, the location of maxima was found to be in Summer (JJA).

Comparison of PP-PPP and PP-DDP ZTD Estimates

In order to study the suitability of the PPP strategy for climate monitoring applications, a comparison of the ZTD estimates from PP-DDP

(ZTD_{ddp}) and PP-PPP (ZTD_{ppp}) solutions was conducted for 114 globally distributed stations and the year 2001. It was found that the mean difference between the ZTD_{ppp} and ZTD_{ddp} ranged from -3.35 to 2.37 mm over all the 25 analyzed climate zones. Furthermore, correlation coefficients ranging from 0.90 to 1.00, and RMS differences ranging from 1.19 to 5.55 mm were found between ZTD_{ppp} and ZTD_{ddp} for these climate zones. It was seen that for a station at very high altitude, the difference between ZTD_{ppp} and ZTD_{ddp} has very high instability (leading to a large standard deviation). In terms of IWV, the RMS differences were found to be ranging from 0.19 to 0.93 kg m^{-2}. As per two additional experiments, not shown in this thesis, it was found that for the Antarctic region, the RMS of the difference between ZTD_{ppp} and ZTD_{ddp} reduces and the correlation coefficient increases when a higher cutoff angle of 7^o was used, and that the agreement between ZTD_{ppp} and ZTD_{ddp} is degraded when the Global Mapping Function (GMF) is used during the processing (due to the fact that GMF is not based on NWP ray-tracing and does not properly account for the changes in atmospheric water vapour).

Assessment of Meteorological Data for IWV Estimation

For the locations of all the six ground-based GNSS stations located in Luxembourg, the ZTD and IWV derived from GNSS observations, and surface pressure and temperature values obtained from locally available data sources were evaluated by comparing them to their equivalent values derived using the ERA-Interim climate reanalysis dataset. It was found that the time series of GNSS-derived ZTD (ZTD_{gnss}) and ERA-Interim ZTD (ZTD_{erai}) follow the same pattern with mean biases ranging from -2.30 to 0.91 mm. The annual signal was found to be the most dominant periodic signal in the ZTD residuals. The correlation coefficients between ZTD_{gnss} and ZTD_{erai} were found to be between 0.94 and 0.96.

The surface pressure obtained from local meteorological data sources agrees to its ERA-Interim equivalent with mean differences between 0.49 and 1.17 hPa whereas a similar comparison for temperature values yields mean differences ranging from -0.63 to 0.10 K.

The mean difference between IWV of the three solutions (IWV_{asta}, IWV_{ukmo} and IWV_{anamet}) and the reference (IWV_{erai}) ranged from -1.79 to -1.44 kg m^{-2} with the lowest mean difference being computed for IWV_{asta}. However, the differences of IWV_{ukmo} and IWV_{anamet} are more stable (lower standard deviation than IWV_{asta}). It was also evident that all the IWV time series follow the same pattern. The RMS of the residuals of IWV_{asta}, IWV_{ukmo} and IWV_{anamet} were found to be agreeing to within 0.37 kg m^{-2}.

The results suggest that among the locally available sources of meteorological data, the UKMO dataset is the most suitable and should be the first preference for IWV estimation in Luxembourg. In case the UKMO data is not available, the second and third preferences should be given to the ANAMET and the ASTA datasets, respectively. This order of preference is valid for all real-time, near real-time and post-processing IWV solutions. Furthermore, it has been found that the IWV obtained in all the three modes (real-time, near real-time and post-processing) either met the target or the threshold accuracy requirements as set by WMO.

It is concluded that Luxembourg has the GNSS observations and meteorological data of adequate quality locally available which makes it possible to implement the application of GNSS meteorology and climatology operationally in the country. Furthermore, the spatial gap in the real-time, near real-time and post-processed observations of atmospheric water vapor over Luxembourg can be filled using the data presented and evaluated in this study.

7.2 Suggestions for Future Work

Based on the findings of this thesis, this section provides the suggestions for future work.

- The UL01 solution should be given the status of an 'operational' solution inside E-GVAP so that it could be operationally assimilated in the AROME model, the NWP model used by MeteoLux for their forecasts. This would enhance the quality of the weather forecasts for Luxembourg and the Greater Region.

- The processing engine of the UL01 system should be updated to BSW52 so that the more precise tropospheric mapping functions such as VMF1 could be implemented in the processing. This would also allow the expansion of the system to include GLONASS and other available GNSS observations.

- The processing engine of the RT system should be changed from BNC27 to the G-Nut/Tefnut as it produces more precise and stable RT-PPP ZTD estimates. The use of the PPP-Wizard would require a number of bias model updates before it could provide adequate results.

- The AROME assimilation experiments should be repeated by including the SPSLux ZTD estimates computed using the corrected real-time streams from the data provider.

- A grid of surface pressure and temperature values with a uniform spatial and temporal resolution should be defined by using the standardized meteorological data from all the available sources in Luxembourg. This could then be expanded to cover the Greater Region which would benefit the meteorological applications of GNSS discussed.

- This work highlights the scientific value of the archived GNSS data. For long-term studies in the future, it is of importance to follow the international recommendations for station operators and report any changes to the stations.

References

Ahmed F, Teferle FN, Bingley R, Laurichesse D (2014): The Status of GNSS Data Processing Systems to Estimate Integrated Water Vapour for Use in Numerical Weather Prediction models, International Association of Geodesy Symposia

Ahmed, F., Václavovic, P., Teferle, F. N., Douša, J., Bingley, R., Laurichesse, D., Comparative Analysis of Real-Time Precise Point Positioning Zenith Total Delay Estimates, GPS Solutions (2016) 20: 187, DOI: 10.1007/s10291-014-0427-z

Ahmed F, Hunegnaw A, Teferle FN, Bingley R (2014): An analysis of global climate variability from homogenously reprocessed GNSS measurements, Abstract A33A-3148 presented at 2014 Fall Meeting, AGU, San Francisco, Calif., 15-19 Dec

Ahmed F, Teferle FN, Bingley R, Bareiss J (2012): GNSS Meteorology in Luxembourg, Cahier Scientifique - Revue Technique Luxembourgeoise, 2012, Issue 1, Pages 16-22

Altamimi Z., Métivier L. and Collilieux X. (2012): ITRF2008 plate motion model, Journal of Geophysical Research: Solid Earth 117 (B7), DOI: 10.1029/2011JB008930

Arguez A and Vose, Russell S. (2011): The Definition of the Standard WMO Climate Normal: The Key to Deriving Alternative Climate Normals. Bull. Amer. Meteor. Soc., 92, 699-704

Askne J, Nordius H (1987) Estimation of tropospheric delay for microwaves from surface weather data. Radio Sci 22, 379-86

Bar-Sever YE, Kroger PM, Borjesson JA (1998): Estimating horizontal gradients of tropospheric path delay with a single GPS receiver. J. Geophys. Res. 103 (B3), 50195035

Bender M, Dick G, Ge M, Deng Z, Wickert J, Kahle HG, Raabe A, Tetzlaff G (2011): Development of a GNSS water vapour tomography system using algebraic reconstruction techniques, Advances in Space Research, Volume 47, Issue 10, 17 May 2011, Pages 1704-1720, ISSN 0273-1177

Benjamin, SG (2013): Data Assimilation and Model Updates in the 2013 Rapid Refresh (RAP) and High-Resolution Rapid Refresh (HRRR) Analysis and Forecast Systems, NCEP/EMC, MEG Meeting, June 6, 2013, NOAA/ESRL/GSD/AMB Stan Benjamin

Benjamin SG, Jamison BD, Moninger WR, Sahm SR, Schwartz BE, Schlatter TW (2010) Relative short-range forecast impact from aircraft, profiler, radiosonde, VAD, GPS-PW, METAR and mesonet observations via the RUC hourly assimilation cycle. Mon Weather Rev 138 (4): 1319-1343

Bevis, M., S. Businger, Chiswell S., T. A. Herring, R. A. Anthes, C. Rocken, R. H. Ware (1994) GPS Meteorology: Mapping Zenith Wet Delays onto Precipitable Water, Journal of Applied Meteorology, 33(3), 379-386

Bevis, M., S. Businger, T. A. Herring, C. Rocken, R. A. Anthes, and R. H. Ware (1992) GPS Meteorology: Remote Sensing of atmospheric water vapour using the Global Positioning System, Journal of Geophysical Research, 97(D14), 15 787-15 801

Byun, S H and Bar-Sever, Y E (2009) A new type of troposphere zenith path delay product of the international GNSS service. J Geodesy 83(3-4), 1–7

Bruyninx C., Legrand J., F. Roosbeek (2008) Status and Performance of the EUREF Permanent Tracking Network, June 18-21 2008, EUREF Publication, Mitteilungen des Bundesamtes fr Kartographie und Geodsie

Byram S, Hackman C, Slabinski V, Tracey J (2011) Computation of a high-precision GPS-based troposphere product by the USNO. In: Proceedings of the 24th International

Brousseau, P., Berre, L., Bouttier, F. and Desroziers, G. 2011. Background-error covariances for a convective-scale data-assimilation system: AROME-France 3D-Var. Q. J. Roy. Meteorol. Soc. 137, 409422

Bubnova, R., Hello, G., Bénard, P. and Geleyn, J.-F. 1995. Integration of the fully elastic equation cast in the hydrostatic pressure terrain-following in the framework of the ARPEGE/ALADIN NWP model. Mon. Weather Rev. 123, 515535

Boehm, J.; Schuh, H. Vienna Mapping Functions in VLBI analyses. Geophys. Res. Lett. 2004, 31

Boehm, J., B. Werl, and H. Schuh (2006), Troposphere mapping functions for GPS and very long baseline interferometry from European Centre for Medium-Range Weather Forecasts operational analysis data, J. Geophys. Res., 111, B02406, doi:10.1029/2005JB003629

Boehm J, Kouba J, Schuh H (2008) Forecast Vienna mapping functions 1 for realtime analysis of space geodetic observations. J Geodesy 83(5):397401

Bennitt G, Levick T (2011) The impact of assimilating zenith total delay measurements from ground-based GNSS receivers in the met office numerical weather prediction UK model. Geophys Res Abstr, Vol. 13, EGU2011-6705

Caissy M, Agrotis L, Weber G, Hernandez-Pajares M, Hugentobler U (2012) The International GNSS Real-Time Service. GPS World, 23 (6), p52

Courtier, P., Freydier, C., Geleyn, J.-F., Rabier, F. and Rochas, M. 1991. The ARPEGE project at Mto-France. In: Proceedings of 1991 ECMWF Seminar on Numerical Methods in Atmospheric Models, Shinfield Park, Reading, ECMWF, 193231

Dach, R and Brockmann, E and Schaer, S and Beutler, G and Meindl, M and Prange, L and Bock, H and Jäggi, A and Ostini, L (2009) GNSS processing at CODE: Status report. J Geodesy 83(3-4), 353–365

Dach R, Hugentobler U, Fridez P, Meindl M (2007) Bernese GPS Software Version 5.0. Astronomical Institute, University of Bern, Bern, Switzerland

Dach, R., S. Lutz, P. Walser, P. Fridez (Eds); 2015: Bernese GNSS Software Version 5.2. User manual, Astronomical Institute, University of Bern, Bern Open Publishing. DOI: 10.7892/boris.72297; ISBN: 978-3-906813-05-9

Dessler, A. E., Z. Zhang, and P. Yang (2008), Water-vapor climate feedback inferred from climate fluctuations, 20032008, Geophys. Res. Lett., 35, L20704, doi:10.1029/2008GL035333.

Douša J (2012) The impact of errors in predicted GPS orbits on zenith troposphere delay estimation. GPS Solut, 14 (3): 229-239

De Haan S (2011) Impact of GPS ZTD on rainfall estimates in an hourly update cycle of a numerical weather prediction model. Geophys Res Abstr Vol. 13, EGU2011-4222

Dow, John M and Neilan, R E and Rizos, C (2009) The International GNSS Service in a changing landscape of Global Navigation Satellite Systems. J Geodesy 83(3-4), 191–198

Dee, D. P. and Uppala, S. M. and Simmons, A. J. and Berrisford, P. and Poli, P. and Kobayashi, S. and Andrae, U. and Balmaseda, M. A. and Balsamo, G. and Bauer, P. and Bechtold, P. and Beljaars, A. C. M. and van de Berg, L. and Bidlot, J. and Bormann, N. and Delsol, C. and Dragani, R. and Fuentes, M. and Geer, A. J. and Haimberger, L. and Healy, S. B. and Hersbach, H. and Hólm, E. V. and Isaksen, L. and Kållberg, P. and Köhler, M. and Matricardi, M. and McNally, A. P. and Monge-Sanz, B. M. and Morcrette, J.-J. and Park, B.-K. and Peubey, C. and de Rosnay, P. and Tavolato, C. and Thépaut, J.-N. and Vitart, F. (2011): The ERA-Interim reanalysis: configuration and performance of the data assimilation system, Quarterly Journal of the Royal Meteorological Society 137 (656), p(553–597) DOI: 10.1002/qj.828

Douša, J, Václavovic, P, (2014) Real-time zenith tropospheric delays in support of numerical weather prediction applications, Advances in Space Research, 53(9), 1 May, 1347-1358

Drogue, G., Mestre, O., Hoffmann, L., Iffly, J.-F., Pfister, L. (2005): Recent warming in a small region with semi-oceanic climate, 1949-1998: What is the ground truth?, Theoretical and Applied Climatology, 81 (1-2), pp. 1-10

Elgered G (2001) An overview of COST Action 716: Exploitation of ground-based GPS for climate and numerical weather prediction applications, Phys Chem Earth Pt A, 26(6-8): 399-404

Fritsche M, Dietrich R, Knöfel C, Rülke A, Vey S (2005) Impact of higher-order ionospheric terms on GPS estimates. Geophys Res Lett, 32, L23311, doi:10.1029/2005GL024342

Geng J, Meng X, Dodson AH, Teferle FN (2010) Integer ambiguity resolution in precise point positioning: Method comparison. J Geodesy, 84(9): 569-581

Geng J, Teferle FN, Shi C, Meng X, Dodson AH, Liu J (2009) Ambiguity resolution in precise point positioning with hourly data. GPS Solut, 13 (4): 263-270

Groisman PY, Knight RW, Easterling DR, Karl TR, Hegerl GC, and Razuvaev VN (2005): Trends in Intense Precipitation in the Climate Record. J. Climate, 18, 13261350

Glowacki TJ, Penna NT, Bourke WP (2006) Validation of GPS-based estimates of integrated water vapour for the Australian region and identification of diurnal variability. Aust Met Mag 55, 131-148

Goergen, K., Beersma, J., Hoffmann, L., Junk, J. (2013): ENSEMBLES-based assessment of regional climate effects in Luxembourg and their impact on vegetation, Climatic Change, 119 (3-4), pp. 761-773

Guerova, G., Jones, J., Douša, J., Dick, G., de Haan, S., Pottiaux, E., Bock, O., Pacione, R., Elgered, G., Vedel, H., and Bender, M. (2016): Review of the state of the art and future prospects of the ground-based GNSS meteorology in Europe, Atmos. Meas. Tech., 9, 5385-5406, doi:10.5194/amt-9-5385-2016

Gutman S, Sahm S R, Benjamin S G, Schwartz B E, Holub K L, Stewart J Q, Smith T L (2004) Rapid retrieval and assimilation of ground based GPS precipitable water observations at the NOAA forecast systems laboratory: Impact on weather forecasts. J Meteorol Soc Jpn Ser II 82(1B), 351–360

Ha SY, Kuo YH, Guo YR, Rocken C, and Van Hove T (2002): Comparison of GPS slant wet delay measurements with model simulations during the passage of a squall line, Geophys. Res. Lett., 29(23), 2113, doi:10.1029/2002GL015891

Hofmann-Wellenhof B, Lichtenegger H, Wasle E. (2007). GNSS-global navigation satellite systems: GPS, GLONASS, Galileo, and more. Wien: Springer

H van der Marel, COST-716 demonstration project for the near real-time estimation of integrated water vapour from GPS, Physics and Chemistry of the Earth, Parts A/B/C, Volume 29, Issues 23, 2004, Pages 187-199, ISSN 1474-7065, http://dx.doi.org/10.1016/j.pce.2004.01.001

Hill EM, Davis JL, Elósegui P, Wernicke BP, Malikowski E, Niemi NA (2009) Characterization of site-specific GPS errors using a short-baseline network of braced monuments at Yucca Mountain, southern Nevada. J Geophys Res, 114, B11402, doi:10.1029/2008JB006027

Huang XY et al. (2003) TOUGH: Targeting optimal use of GPS humidity measurements in meteorology, Proc. International Workshop on GPS Meteorology, Tsukuba, Japan, 14-17 January 2003

Hartmann DL, Klein Tank AMG, Rusticucci M, Alexander LV, Brnnimann S, Charabi Y, Dentener FJ, Dlugokencky EJ, Easterling DR, Kaplan A, Soden BJ, Thorne PW, Wild M and Zhai PM (2013): Observations: Atmosphere and Surface. In: Climate Change 2013: The Physical Science Basis. Contribution of Working Group I to the Fifth Assessment Report of the Intergovernmental Panel on Climate Change [Stocker TF, Qin D, Plattner GK, Tignor M, Allen SK, Boschung J, Nauels A, Xia Y, Bex V, and Midgley PM (eds.)]. Cambridge University Press, Cambridge, United Kingdom and New York, NY, USA

Hagemann, S., L. Bengtsson, and G. Gendt (2003), On the determination of atmospheric water vapor from GPS measurements, J. Geophys. Res., 108, 4678, doi:10.1029/2002JD003235, D21

HernandezPajares M, Juan JM, Sanz J, Orús R (2007): Secondorder ionospheric term in GPS: Implementation and impact on geodetic estimates, Journal of Geophysical Research: Solid Earth 112 (B8)

Iwabuchi T, Naito I, Mannoji N (2000) A comparison of Global Positioning System retrieved precipitable water vapor with the numerical weather prediction analysis data over the Japanese Islands. J Geophys Res, 105, 4573-4585 C2000

Jones J, Guerova G, Dousa J, de Haan S, Bock O, Dick G, Pottiaux E, Pacione R (2014) COST Action ES1206 : Advanced Global Navigation Satel-

lite Systems Tropospheric Products for Monitoring Severe Weather Events and Climate (GNSS4SWEC). Geophys Res Abstr Vol. 16, EGU2014-14097

Junk, J., Matzarakis, A., Ferrone, A., Krein, A. (2014): Evidence of past and future changes in health-related meteorological variables across Luxembourg, Air Quality, Atmosphere and Health, 7 (1), pp. 71-81

Karl TR, Melillo JM, and Peterson TC (eds.) (2009): Global Climate Change Impacts in the United States. Cambridge University Press

Katz RW (2010): Statistics of extremes in climate change. Climate Change 100: 71-76

Kunkel KE, Karl TR, Brooks H, Kossin J, Lawrimore JH, Arndt D, Bosart L, Changnon D, Cutter SL, Doesken N, Emanuel K, Groisman PY, Katz RW, Knutson T, O'Brien J, Paciorek CJ, Peterson TC, Redmond K, Robinson D, Trapp J, Vose R, Weaver S, Wehner M, Wolter K, Wuebbles D (2013): Monitoring and Understanding Trends in Extreme Storms: State of Knowledge. Bull. Amer. Meteor. Soc., 94, 499514

Kalnay et al. (1996): The NCEP/NCAR 40-year reanalysis project, Bull. Amer. Meteor. Soc., 77, 437-470

Kalman RE (1960): A New Approach to Linear Filtering and Prediction Problems, Transactions of the ASME–Journal of Basic Engineering 82 (Series D), pp. 35–45

Lagler, K, M Schindelegger, J Boehm, H Krásná, and T Nilsson (2013), GPT2: Empirical slant delay model for radio space geodetic techniques, Geophys Res Lett, 40, 10691073, doi:10.1002/grl.50288 Technical Meeting of The Satellite Division of The Institute of Navigation 2011, 572–578

Laurichesse D (2011) The CNES real-time PPP with undifferenced integer ambiguity resolution demonstrator. In: Proceedings of the 24th International Technical Meeting of The Satellite Division of The Institute of Navigation 2011, 654–662

Li, X., G. Dick, M. Ge, S. Heise, J. Wickert, and M. Bender (2014) Real-time GPS sensing of atmospheric water vapor: Precise point positioning with orbit, clock, and phase delay corrections, Geophys. Res. Lett., 41, doi:10.1002/2013GL058721

Mahfouf, JF, Ahmed F, Moll, P (2015): Assimilation of zenith total delays in the AROME France convective scale model: a recent assessment. (accepted in Tellus A, In Press)

Ning T (2012) GPS meteorology: With focus on climate applications, PhD Thesis, Chalmers University of Technology, ISBN 978-91-7385-675-1

Niell, A.E. Global mapping functions for the atmosphere delay at radio wavelengths, Haystack Observatory, Massachusetts Institute of Technology, Westford, J.G.R. 101, b2, 3227-3246, 1996 corrected)

Niell, A.E., Preliminary Evaluation of Atmospheric Mapping Functions Based on Numerical Weather Models, Phys. Chem. Earth, 26 No.6-8, pp. 476-480, 2001

Nilsson T, Elgered G (2008) Long-term trends in the atmospheric water vapor content estimated from ground-based GPS data. J Geophys Res 113(D19), DOI 10.1029/2008JD010110

Nievinski FG, Santos M (2010) Ray-tracing options to mitigate the neutral atmosphere delay in GPS. Geomatica 64:191207

NERC Centres for Atmospheric Science-British Atmospheric Data Centre (2006) `http://badc.nerc.ac.uk/view/badc.nerc.ac.uk__ATOM__dataent_GLOBRADS`

Orliac EJ, Bingley RM, Dodson AH,, and Teferle FN (2005): Ground-based GPS near real-time zenith path delay estimation in the UK. Geophysical Research Abstracts, EGU05-A-09279

Orliac EJ (2009): Development of azimuth dependent tropospheric mapping functions, based on a high resolution mesoscale numerical weather model, for GNSS data processing. PhD thesis, University of Nottingham. Access from the University of Nottingham repository: `http://eprints.nottingham.ac.uk/10861/1/thesis_definitive_30_07_2009.pdf`

Pidwirny, M. (2013). Atmospheric composition. Retrieved from http://www.eoearth.org/view/article/51cbecfe7896bb431f68f01a

Park C-G, Roh K-M, Cho J (2012) Radiosonde Sensors Bias in Precipitable Water Vapor From Comparisons With Global Positioning System Measurements. J Astron Space Sci, 29(3): 295-303

Peel, M. C., Finlayson, B. L., and McMahon, T. A.: Updated world map of the Köppen-Geiger climate classification, Hydrol. Earth Syst. Sci., 11, 1633-1644, doi:10.5194/hess-11-1633-2007, 2007

Pfister, L., Drogue, G., El Idrissi, A., Iffly, J.-F., Matgen, P., Poirier, C., Hoffmann, L. (2004): Hydrological impacts of climate change at catchment scale: A case study in the Grand-Duchy of Luxembourg, Geologica Acta, 2 (2), pp. 135-145

Pfister, L., Drogue, G., Poirier, C., Hoffmann, L. (2005): Spatial variability of trends in hydrological extremes induced by orographically enhanced rainfall events due to westerly atmospheric circulations, Water Science and Technology, 51 (5), pp. 15-21

Pfister, L., Humbert, J., Hoffmann, L. (2000): Recent trends in rainfall-runoff characteristics in the Alzette River basin, Luxembourg, Climatic Change, 45 (2), pp. 323-337

Poli, P., Moll, P., Rabier, F., Desroziers, G., Chapnik, B. and co-authors. 2007. Forecast impact studies of zenith total delay from European near-real-time GPS stations in Mto-France 4D-Var. J. Geophys. Res. 112, D06114. DOI: 10.1029/2006JD007430

Rebischung P, Griffiths J, Ray J, Schmid R, Collilieux X, Garayt B (2012) IGS08: the IGS realization of ITRF2008. GPS Solut. 16(4):483494. doi:10.1007/s10291-011-0248-2

Saastamoinen, J. (1972) Atmospheric correction for the troposphere and stratosphere in radio ranging of satellites, in The Use of Artificial Satellites for Geodesy, Geophysics Monograph Series, 15, 247-251, AGU, Washington, D.C.

Seity, Y., Brousseau, P., Malardel, S., Hello, G., Bnard, P. and co-authors. 2011. The AROME-France convective-scale operational model. Mon. Weather Rev. 139, 976991

Shi J, Gao Y (2012) Improvement of PPP-inferred tropospheric estimates by integer ambiguity resolution. Adv Space Res, 50(10): 1374-1382

Smith TL, Benjamin SG, Gutman SI, Sahm SR (2007) Forecast impact from assimilation of GPS-IPW observations into the Rapid Update Cycle. Mon Wea Rev, 135(8): 29142930

Smith, W. H. F., Wessel, P. (1990) Gridding with a Continuous Curvature Surface in Tension, Geophysics, 55(3), 293-305

Stende M (2006) Monitoring climate variability and change by means of GNSS data. In: Foelsche U, Kirchengast G, Steiner A (eds) Atmosphere and Climate, Springer Berlin Heidelberg, 275–285,DOI 10.1007/3-540-34121-8_23

Taylor, F.W.(2005): Elementary climate physics, Oxford University Press, ISBN: 9780198567349

Teke, K and Böhm, J and Nilsson, T and Schuh, H and Steigenberger, P and Dach, R and Heinkelmann, R and Willis, P and Haas, R and Garcia-Espada, S and Hobiger, T and Ichikawa, R and Shimizu, S (2011) Multi-technique comparison of troposphere zenith delays and gradients during CONT08. J Geodesy 85(7), 395–413

Thayer, G. D. (1974) An improved equation for the radio refractive index of air, Radio Science, 9(10), 803807

Thomas ID, King MA, Clarke PJ, Penna NT (2011) Precipitable water vapor estimates from homogeneously reprocessed GPS data: An intertechnique comparison in Antarctica. J Geophys Res, 116, doi:10.1029/2010JD013889

Titchner, H. A., Thorne, P. W., McCarthy, M. P., Tett, S. F. B., Haimberger, L., and Parker, D. E.: Critically Reassessing Tropospheric Temperature Trends from Radiosondes Using Realistic Validation Experiments, J. Climate, 22, 465485, 2009

Tregoning P, Herring TA (2006) Impact of a priori zenith hydrostatic delay errors on GPS estimates of station heights and zenith total delays. Geophys Res Lett, 33, L23303, doi:10.1029/2006GL027706

Urquhart, L., Nievinski, F.G. and Santos, M.C. GPS Solut (2014) 18: 345. doi:10.1007/s10291-013-0334-8

Václavovic P, Douša J, Gyori G (2013) G-Nut software library - State of development and first results. Acta Geodyn Geomat, 10(172) (in print)

van Dam T., Altamimi Z., Collilieux X. and Ray J., 2010. Topographically induced height errors in predicted atmospheric loading effects. J. Geophys. Res., 115, B07415, DOI: 10.1029/2009JB006810

Vedel H, de Haan S, Jones J, Bennitt G, Offiler D (2013) E-GVAP third phase. Geophys Res Abstr Vol. 15, EGU2013-10919

Vey S, Dietrich R, Rülke A, Fritsche M, Steigenberger P, and Rothacher M, (2010): Validation of Precipitable Water Vapor within the NCEP/DOE Reanalysis Using Global GPS Observations from One Decade. J. Climate, 23, 16751695.doi: http://dx.doi.org/10.1175/2009JCLI2787.1

Wang J, and Zhang L (2009): Climate applications of a global, 2-hourly atmospheric precipitable water dataset from IGS ground-based GPS measurements. J. of Geodesy, 83, 209-217 (DOI: 10.1007/s00190-008-0238-5)

Weber G, Mervart L (2012) BKG Ntrip Client (BNC) Version 2.7 Manual. Federal Agency for Cartography and Geodesy, Frankfurt, Germany

Weber G, Dettmering D, Gebhard H (2006) Networked Transport of RTCM via Internet Protocol (NTRIP). IAG Symposia Series, vol. 128, 60-64

Wessel, P., and W. H. F. Smith, 1998, New, improved version of the Generic Mapping Tools Released, EOS Trans. AGU, 79, 579

Wübbena G, Schmitz M, Bagge A (2005) PPP-RTK: Precise Point Positioning using state-space representation in RTK networks. Proc. ION GNSS 2005, Institute of Navigation, Portland, OR, 2584-2594

Yan, X., Ducrocq, V., Jaubert, G., Brousseau, P., Poli, P. and co-authors. 2009a. The benefit of GPS zenith delay assimilation to high-resolution quantitative precipitation forecasts: a case-study from COPS IOP 9. J. Geophys. Res. 135, 17881800

Yan, X., Ducrocq, V., Poli, P., Hakam, M., Jaubert, G. and co-authors. 2009b. Impact of GPS zenith delay assimilation on convective-scale prediction of Mediterranean heavy rainfall. Q. J. Roy. Meteorol. Soc. 114, D03104. DOI: 10.1029/2008JD011036

Yuan, Y, K Zhang, W Rohm, S Choy, R Norman, and C-S Wang (2014), Real-time retrieval of precipitable water vapor from GPS precise point positioning, J Geophys Res Atmos, 119, doi:10.1002/2014JD021486

Zumberge, J F and Heflin, M B and Jefferson, D C and Watkins, M M and Webb, F H (1997) Precise point positioning for the efficient and robust analysis of GPS data from large networks. J Geophys Res 102(B3), 5005–5017, DOI 10.1029/96JB03860 Series, Springer, Vol. 143, DOI: 10.1007/1345_2015_178

Appendix A

Ground-based GNSS Stations

A.1 Stations Processed by RT System

ID	Name	Country	Lat. [deg]	Lon. [deg]	Hgt. [m]
AJAC	Ajaccio	France	41.55	8.45	99.00
ARLO	Arlon	Belgium	49.65	5.82	428.66
BASC	Bascharage	Luxembourg	49.57	5.94	375.76
BATT	Battice	Belgium	50.64	5.83	322.81
BERL	Berloz	Belgium	50.70	5.19	185.58
BOGI	Borowa Gora	Poland	52.28	21.02	139.90
BOR1	Borowiec	Poland	52.28	17.07	124.36
BORJ	Island of Borkum	Germany	53.58	6.67	48.30
BRST	Brest	France	48.22	-4.29	65.80
BRUX	Brussels	Belgium	50.47	4.21	158.30
BZRG	Bolzano - Bozen	Italy	46.29	11.20	328.80
CAGZ	Capoterra	Italy	39.09	8.58	238.00
CHAR	Charleroi	Belgium	50.41	4.45	164.72
DARE	Daresbury	United Kingdom	53.34	-2.64	88.44
DENT	Dentergem	Belgium	50.93	3.40	63.88
DRES	Dresden	Germany	51.03	13.73	203.05
EBRE	Roquetes	Spain	40.82	0.49	107.79
ECHT	Echternach	Luxembourg	49.80	6.44	304.54
ENTZ	Entzheim	France	48.55	7.64	204.26
ERPE	Erpeldange	Luxembourg	49.55	6.32	217.38
FLOR	Florenville	Belgium	49.76	5.14	447.98
FOVA	FOVA	Belgium	50.32	4.22	172.16
GANP	Ganovce	Slovakia	49.02	20.19	745.20
GHIS	St. Ghislain	Belgium	50.45	3.88	79.78
GOPE	Ondrejov	Czech Republic	49.91	14.79	592.58
GRAS	Caussols	France	43.45	6.55	1319.30
GRAZ	Graz	Austria	47.07	15.49	538.28

HERT	Hailsham	United Kingdom	50.87	0.33	83.33
HOE2	Hoernum / Island Sylt	Germany	54.76	8.29	62.40
HOFN	Hoefn	Iceland	64.27	-15.20	82.64
HUEG	Huegelheim	Germany	47.50	7.35	278.40
INVR	Inverness	United Kingdom	57.49	-4.22	66.16
JOZ2	Jozefoslaw	Poland	52.05	21.02	152.50
KAIN	Kain	Belgium	50.63	3.37	66.36
KARL	Karlsruhe	Germany	49.01	8.41	182.90
KURE	Kuressaare	Estonia	58.26	22.51	41.50
LAMA	Olsztyn	Poland	53.53	20.40	187.00
LEGL	Leglise	Belgium	49.86	5.51	544.51
LEIJ	Leipzig	Germany	51.33	12.37	178.40
LIL2	Lille-IUTA2	France	50.61	3.14	96.20
MABO	MABO	Belgium	50.07	5.74	493.85
MAFA	Marche-en-Famenne	Belgium	50.24	5.30	287.21
MAR6	Maartsbo	Sweden	60.60	17.26	75.40
MARI	Mariembourg	Belgium	50.09	4.51	210.31
MARS	Marseille	France	43.27	5.35	61.80
MATE	Matera	Italy	40.65	16.70	535.64
MEIX	Meix-devant-Virton	Belgium	49.62	5.44	369.49
MOHA	Moha	Belgium	50.54	5.19	180.89
NAMR	Namur	Belgium	50.47	4.86	159.35
NIVL	Nivelles	Belgium	50.59	4.30	186.22
OLLN	Ottignies-Louvain-la-Neuve	Belgium	50.68	4.63	189.24
ONHA	Onhaye	Belgium	50.25	4.85	293.04
ONSA	Onsala	Sweden	57.40	11.93	45.59
ORID	Ohrid	Macedonia	41.13	20.79	773.00
OSLS	Oslo	Norway	59.74	10.37	221.55
OSTI	Ostiches	Belgium	50.68	3.80	90.29
PADO	Padova	Italy	45.41	11.90	64.70
PENC	Penc	Hungary	47.79	19.27	291.70
POTS	Potsdam	Germany	52.38	13.07	144.41
REYK	Reykjavik	Iceland	64.14	-21.96	93.02
ROUL	Roullingen	Luxembourg	49.95	5.92	542.38
SASS	Sassnitz Island of Ruegen	Germany	54.51	13.64	68.22
STAS	Stavanger	Norway	59.02	5.60	104.91

TELL	Tellin	Belgium	50.05	5.21	451.66
TILM	Tilff	Belgium	50.58	5.57	302.41
TITZ	Titz	Germany	51.00	6.42	155.60
TLSE	Toulouse	France	43.56	1.48	207.20
TRDS	Trondheim	Norway	63.37	10.32	317.74
TROI	Troisvierges	Luxembourg	50.13	6.01	537.82
VFCH	Villefranche-sur-Cher	France	47.29	1.72	153.24
VISO	Visby	Sweden	57.39	18.22	79.80
VITH	St. Vith	Belgium	50.32	6.09	607.27
WALF	Walferdange	Luxembourg	49.66	6.13	292.40
WARE	Waremme	Belgium	50.69	5.25	187.86
WARN	Rostock-Warnemuende	Germany	54.17	12.10	50.74
WERB	Werbomont	Belgium	50.38	5.77	490.04
WROC	Wroclaw	Poland	51.11	17.06	180.80
WSRT	Westerbork	Netherlands	52.91	6.60	86.00
WTZR	Bad Koetzting	Germany	49.14	12.88	666.02
ZIM2	Zimmerwald	Switzerland	46.90	7.50	956.40

A.2 Stations Processed by NRT System

ID	Name	Country	Lat. [deg]	Lon. [deg]	Hgt. [m]
ABER	Aberdeen	United Kingdom	57.14	-2.08	53.44
ABYW	Aberystwyth	United Kingdom	52.42	-4.00	98.99
ACOR	A Coruna	Spain	43.36	-8.40	66.89
ADAR	Aberdaron	United Kingdom	52.79	-4.74	148.39
ALAC	Alicante	Spain	38.34	-0.48	60.32
ALBA	Albacete	Spain	38.98	-1.86	751.77
ALME	Almeria	Spain	36.85	-2.46	127.48
ANKR	Ankara	Turkey	39.89	32.76	976.03
AQUI	L'Aquila	Italy	42.37	13.35	713.00
ARDL	Ardleigh	United Kingdom	51.92	0.96	91.47
ARIS	Arisaig	United Kingdom	56.91	-5.85	61.31
ARLO	Arlon	Belgium	49.65	5.82	428.66
ARTU	Arti	Russia	56.43	58.56	247.57

AUCH	Auch	France	43.65	0.58	232.05
AUT1	Thessaloniki	Greece	40.57	23.00	150.08
AXPV	Aix En Provence	France	43.49	5.33	229.31
BACA	Bacau	Romania	46.56	26.91	219.12
BADH	Bad Homburg	Germany	50.23	8.61	261.25
BAIA	Baia Mare	Romania	47.65	23.56	270.84
BARY	Sauveterre de Comminges	France	43.04	0.67	633.52
BASC	Bascharage	Luxembourg	49.57	5.94	375.76
BATT	Battice	Belgium	50.64	5.83	322.81
BELL	Bellmunt de Segarra	Spain	41.60	1.40	853.40
BERL	Berloz	Belgium	50.70	5.19	185.58
BLFT	Belfort-Danjoutin	France	47.63	6.86	416.49
BMHG	Beaumont Hague	France	49.66	-1.83	231.24
BOGO	Borowa Gora	Poland	52.48	21.04	149.60
BOR1	Borowiec	Poland	52.28	17.07	124.36
BORR	Borriana	Spain	39.91	-0.08	72.90
BRAE	Braemar	United Kingdom	57.01	-3.40	400.85
BRET	Brtigny-sur-Orge	France	48.61	2.31	140.27
BUDP	Kobenhavn	Denmark	55.74	12.50	94.03
BUTE	Budapest	Hungary	47.48	19.06	180.77
CACE	Caceres	Spain	39.48	-6.34	436.49
CAEN	Aroport de Caen-Carpiquet	France	49.18	-0.46	113.55
CAMO	Camborne	United Kingdom	50.22	-5.33	140.98
CANT	Santander	Spain	43.47	-3.80	99.26
CASC	Cascais	Portugal	38.69	-9.42	76.02
CEU1	Ceuta	Spain	35.89	-5.31	52.47
CHAR	Charleroi	Belgium	50.41	4.45	164.72
CHAS	Chtillon-sur-Seine	France	47.86	4.56	299.40
CHIO	Chilbolton	United Kingdom	51.15	-1.44	128.30
COBA	Cordoba	Spain	37.92	-4.72	202.05
COMO	Como	Italy	45.80	9.10	292.28
COST	Constanta	Romania	44.16	28.66	46.19
CRAO	Simeiz	Ukraine	44.41	33.99	365.80
CREU	Cadaques	Spain	42.32	3.32	133.36
CUBX	Bordeaux	France	44.87	-0.57	59.04
DARE	Daresbury	United Kingdom	53.34	-2.64	88.44

DENT	Dentergem	Belgium	50.93	3.40	63.88
DGLG	Dunkerque G. L. Gomatique	France	50.99	2.34	56.76
DOUR	Dourbes	Belgium	50.09	4.59	282.69
DRES	Dresden	Germany	51.03	13.73	203.05
DRUS	Drusenheim	France	48.77	7.95	184.50
EBRE	Roquetes	Spain	40.82	0.49	107.79
ECHT	Echternach	Luxembourg	49.80	6.44	304.54
EDIN	Edinburgh	United Kingdom	55.92	-3.29	119.04
ENTZ	Entzheim	France	48.55	7.64	204.26
ERPE	Erpeldange	Luxembourg	49.55	6.32	217.38
ESKD	Eskdalemuir	United Kingdom	55.31	-3.21	297.43
EUSK	Euskirchen	Germany	50.67	6.76	245.31
FETA	Fre-en-Tardenois	France	49.20	3.51	168.39
FLOR	Florenville	Belgium	49.76	5.14	447.98
FOUC	Foucarmont	France	49.84	1.58	237.54
FOVA	FOVA	Belgium	50.32	4.22	172.16
GHIS	St. Ghislain	Belgium	50.45	3.88	79.78
GLAS	Glasgow	United Kingdom	55.85	-4.30	71.62
GLSV	Kiev	Ukraine	50.36	30.50	226.31
GOPE	Ondrejov	Czech Republic	49.91	14.79	592.58
GORN	Gorron	France	48.41	-0.81	225.18
GRAZ	Graz	Austria	47.07	15.49	538.28
GSR1	Ljubljana	Slovenija	46.05	14.54	351.65
GUIP	Guipavas	France	48.44	-4.41	154.69
HELG	Helgoland Island	Germany	54.17	7.89	48.39
HERO	Herstmonceux	United Kingdom	50.87	0.34	71.62
HERT	Hailsham	United Kingdom	50.87	0.33	83.33
HOBU	Hohenbuenstorf	Eschenberg	53.05	10.48	152.23
HOFN	Hoefn	Iceland	64.27	-15.20	82.64
HUEL	Huelva	Spain	37.20	-6.92	81.81
HUNG	Hungerford	United Kingdom	51.40	-1.51	183.09
INVR	Inverness	United Kingdom	57.49	-4.22	66.16
IZAN	Izana	Spain	28.31	-16.50	2417.43
JOEN	Joensuu	Finland	62.39	30.10	113.73
JOZE	Jozefoslaw	Poland	52.10	21.03	141.44
KAIN	Kain	Belgium	50.63	3.37	66.36

KARL	Karlsruhe	Germany	49.01	8.41	182.90
KING	Kings Lynn	United Kingdom	52.75	0.40	66.44
KINT	Kintore	United Kingdom	57.25	-2.33	141.20
KLOP	Kloppenheim / Frankfurt	Germany	50.22	8.73	222.45
KLRE	Kilrea	United Kingdom	54.96	-6.62	147.97
KRAW	Krakow	Poland	50.07	19.92	267.10
LCAU	Lacanau	France	44.98	-1.08	73.60
LEED	Leeds	United Kingdom	53.80	-1.66	215.62
LEEK	Leek	United Kingdom	53.13	-1.98	352.77
LEGL	Leglise	Belgium	49.86	5.51	544.51
LENE	Le Neubourg	France	49.15	0.91	188.84
LERI	Lerwick	United Kingdom	60.14	-1.18	132.01
LIL2	Lille-IUTA2	France	50.61	3.14	96.20
LINZ	Linz	Austria	48.31	14.28	335.03
LMCU	Lille M. Communaut Urbaine	France	50.64	3.08	111.09
LOCG	Lochgilphead	United Kingdom	56.01	-5.45	71.90
MABO	MABO	Belgium	50.07	5.74	493.85
MAFA	Marche-en-Famenne	Belgium	50.24	5.30	287.21
MALA	Malaga	Spain	36.73	-4.39	119.81
MALL	Palma de Mallorca	Spain	39.55	2.62	62.01
MARG	Marignier	France	46.08	6.51	524.19
MARI	Mariembourg	Belgium	50.09	4.51	210.31
MAT1	Matera	Italy	40.65	16.70	534.52
MATE	Matera	Italy	40.65	16.70	535.64
MEIX	Meix-devant-Virton	Belgium	49.62	5.44	369.49
MERY	Mery sur Seine	France	48.51	3.89	139.84
MIMZ	Mimizan	France	44.20	-1.23	71.66
MODA	Modane	France	45.21	6.71	1182.26
MOHA	Moha	Belgium	50.54	5.19	180.89
MORO	Morpeth	United Kingdom	55.21	-1.69	145.13
MORP	Morpeth	England	55.21	-1.69	144.44
MTMN	Montmorillon	France	46.43	0.88	179.62
NAMR	Namur	Belgium	50.47	4.86	159.35
NEWL	Newlyn TG	United Kingdom	50.10	-5.54	64.49
NICA	Nice	France	43.70	7.23	256.49
NICO	Nicosia	Cyprus	35.14	33.40	190.02

NIVL	Nivelles	Belgium	50.59	4.30	186.22
NOA1	Athens	Greece	38.05	23.86	537.81
NOT1	Noto	Italy	36.88	14.99	126.34
NRIL	Norilsk	Russia	69.36	88.36	47.89
NYA1	Ny-Alesund	Norway	78.93	11.87	84.16
NYAL	Ny-Alesund	Norway	78.93	11.87	84.16
OLLN	Ottignies-Louvain-la-Neuve	Belgium	50.68	4.63	189.24
OMGH	Omagh	United Kingdom	54.62	-7.26	217.42
ONHA	Onhaye	Belgium	50.25	4.85	293.04
ONSA	Onsala	Sweden	57.40	11.93	45.59
ORID	Ohrid	Macedonia	41.13	20.79	773.00
OROS	Oroshaza	Hungary	46.56	20.67	145.99
OSLS	Oslo	Norway	59.74	10.37	221.55
OSTI	Ostiches	Belgium	50.68	3.80	90.29
OXFR	Oxford	United Kingdom	51.82	-1.29	119.76
PANA	Paris	France	48.85	2.39	120.66
PERP	Perpignan	France	42.69	2.88	95.38
PLEM	Plemet	France	48.17	-2.60	197.29
POL2	Bishkek	Kyrgyzstan	42.68	74.69	1714.20
POTS	Potsdam	Germany	52.38	13.07	144.41
POUS	Poustka	Czech Republic	50.14	12.30	572.17
PRAT	Prato	Italy	43.89	11.10	119.96
PUYV	Le Puy en Velay	France	45.04	3.88	710.36
RENN	Rennes	France	48.11	-1.67	93.28
REYK	Reykjavik	Iceland	64.14	-21.96	93.02
ROUL	Roullingen	Luxembourg	49.95	5.92	542.38
ROVE	Rovereto	Italy	45.89	11.04	261.67
ROYA	Royan	France	45.64	-1.02	69.05
SALA	Salamanca	Spain	40.95	-5.50	855.39
SARZ	Sarzeau	France	47.52	-2.77	83.80
SASS	Sassnitz Island of Ruegen	Germany	54.51	13.64	68.22
SCDA	Saint Chely d Apcher	France	44.79	3.27	1115.29
SCIL	Scilly Isles	United Kingdom	49.91	-6.30	83.84
SEUR	Seurre	France	46.99	5.15	244.47
SGIL	Saint-Gilles	France	43.68	4.43	90.75
SMID	Smidstrup	Denmark	55.64	9.56	122.83

SMLE	St Martin de St Maixant	France	46.41	-0.22	170.46
SMNE	Saint-Mande	France	48.84	2.43	126.24
SNEO	St. Neots	United Kingdom	52.19	-0.11	120.02
SODA	Sodankyla	Finland	67.42	26.39	299.83
SONS	Sonseca	Spain	39.68	-3.96	808.94
STAS	Stavanger	Norway	59.02	5.60	104.91
STOR	Stornoway	United Kingdom	58.20	-6.38	63.83
STPS	Saint-Pourcain sur Sioule	France	46.31	3.29	299.34
STRN	Stranraer	United Kingdom	54.87	-4.71	164.15
SULD	Suldrup	Denmark	56.84	9.74	120.72
SWAN	Swanland	United Kingdom	53.74	-0.51	148.99
SWAS	Swansea	United Kingdom	51.57	-3.98	89.96
SWTG	Stornoway TG	United Kingdom	58.21	-6.39	60.07
TELL	Tellin	Belgium	50.05	5.21	451.66
TERS	West-Terschelling	Netherlands	53.36	5.22	56.10
THUS	Thurso2	United Kingdom	58.58	-3.73	94.25
TILM	Tilff	Belgium	50.58	5.57	302.41
TORI	Torino	Italy	45.06	7.66	310.73
TRDS	Trondheim	Norway	63.37	10.32	317.74
TREM	Trementines - TERIA	France	47.12	-0.79	166.43
TRO1	Tromsoe	Norway	69.66	18.94	138.07
TROI	Troisvierges	Luxembourg	50.13	6.01	537.82
TRYS	Troyes	France	48.29	4.01	168.35
TUBO	Brno	Czech Republic	49.21	16.59	324.26
TUC2	Chania	Greece	35.53	24.07	160.89
UNME	Pau	France	43.32	-0.33	278.73
UNPG	Perugia	Italy	43.12	12.36	351.06
VAAS	Vaasa	Finland	62.96	21.77	58.14
VARS	Vardoe	Norway	70.34	31.03	174.88
VFCH	Villefranche-sur-Cher	France	47.29	1.72	153.24
VIGO	Vigo	Spain	42.18	-8.81	87.76
VILO	Vilhelmina	Sweden	64.70	16.56	450.04
VILR	Villars de Lans	France	45.07	5.55	1076.70
VITH	St. Vith	Belgium	50.32	6.09	607.27
VNTE	Venette	France	49.43	2.78	137.44
WALF	Walferdange	Luxembourg	49.66	6.13	292.40

WARE	Waremme	Belgium	50.69	5.25	187.86
WARN	Rostock-Warnemuende	Germany	54.17	12.10	50.74
WEAR	Wear Head	United Kingdom	54.75	-2.23	408.43
WERB	Werbomont	Belgium	50.38	5.77	490.04
WEYB	Weybourne	United Kingdom	52.94	1.13	74.13
WROC	Wroclaw	Poland	51.11	17.06	180.80
WTZR	Bad Koetzting	Germany	49.14	12.88	666.02
YEBE	Yebes	Spain	40.52	-3.09	972.76
ZARA	Zaragoza	Spain	41.63	-0.88	298.22
ZIMM	Zimmerwald	Switzerland	46.88	7.47	956.33
ZOUF	Cercivento	Italy	46.56	12.97	1946.49

A.3 Stations Processed by PP System

ID	Lat.	Lon.	Hgt.	ID	Lat.	Lon.	Hgt.
AB07	55.35	-160.48	89.58	NTUS	1.35	103.68	75.39
AB11	64.56	-165.37	349.45	NVSK	54.84	83.24	123.09
AB44	59.53	-135.23	304.12	NYA1	78.93	11.87	84.19
AB50	58.42	-134.55	51.50	NYAC	78.93	11.87	79.06
ABER	57.14	-2.08	53.45	NYBP	40.70	-74.01	-15.75
AC67	57.79	-152.43	347.21	OHI2	-63.32	-57.90	32.44
ACOR	43.36	-8.40	66.94	OHI3	-63.32	-57.90	32.56
ADE1	-34.73	138.65	38.04	ONSA	57.40	11.93	45.54
AIS5	55.07	-131.60	32.35	OOST	51.23	2.92	70.36
ALAC	38.34	-0.48	60.34	OSLS	59.74	10.37	221.52
ALBH	48.39	-123.49	31.76	OSN1	37.08	127.02	48.81
ALGO	45.96	-78.07	200.89	OUAG	12.36	-1.51	331.05
ALME	36.85	-2.46	127.49	OUS2	-45.87	170.51	26.09
ALRT	82.49	-62.34	78.12	OUSD	-45.87	170.51	26.21
AMC2	38.80	-104.52	1911.39	P059	38.93	-123.73	-11.29
ANTC	-37.34	-71.53	745.38	P101	43.21	140.86	38.34
AREQ	-16.47	-71.49	2488.91	P102	42.08	139.49	42.27
ARGI	62.00	-6.78	110.24	P103	40.90	140.86	44.20
ARP7	27.84	-97.06	-16.42	P104	39.94	139.70	44.68

ARTU	56.43	58.56	247.58	P105	38.56	139.55	45.52
AUCK	-36.60	174.83	132.67	P107	35.13	140.25	39.44
AUKT	-36.84	174.77	40.07	P108	35.16	139.62	42.92
AUT1	40.57	23.00	150.08	P109	37.81	138.28	44.76
AUTF	-54.84	-68.30	71.87	P110	37.36	138.51	45.59
AV09	53.88	-166.54	105.68	P111	37.41	136.90	43.90
BAIE	49.19	-68.26	27.47	P112	36.25	136.15	42.05
BAKE	64.32	-96.00	4.41	P113	34.90	139.13	47.15
BAMF	48.84	-125.14	10.77	P114	34.81	138.76	47.45
BAN2	13.03	77.51	831.88	P115	34.87	138.33	46.53
BARH	44.40	-68.22	6.77	P116	34.90	136.82	47.00
BELE	-1.41	-48.46	9.09	P117	34.14	135.19	45.73
BJFS	39.61	115.89	87.43	P118	35.59	134.32	42.55
BLUF	-46.59	168.29	124.62	P119	34.63	131.60	39.36
BNDY	-24.91	152.32	80.01	P120	33.33	133.24	43.17
BOAV	2.85	-60.70	69.51	P121	33.47	129.85	39.07
BOGT	4.64	-74.08	2577.04	P122	32.43	131.67	36.53
BOMJ	-13.26	-43.42	419.38	P123	32.02	130.19	39.79
BOR1	52.28	17.07	124.37	P124	26.18	127.82	38.47
BORJ	53.58	6.67	53.04	P162	40.69	-124.24	-6.44
BRAZ	-15.95	-47.88	1106.15	P202	44.02	144.29	36.48
BREW	48.13	-119.68	238.60	P203	42.98	144.37	35.35
BRST	48.38	-4.50	65.84	P204	41.78	140.72	39.51
BRUS	50.80	4.36	149.66	P205	39.02	141.75	47.04
BRUX	50.80	4.36	158.13	P206	34.92	139.82	45.60
BSHM	32.78	35.02	225.11	P207	36.76	137.22	44.21
BUDP	55.74	12.50	94.01	P208	33.48	135.77	46.44
BUE2	-34.57	-58.52	48.66	P209	34.90	132.07	39.58
BUR2	-41.05	145.91	3.82	P210	32.74	129.87	38.60
BYSP	18.41	-66.16	49.22	P211	31.58	131.41	36.91
CABL	42.84	-124.56	37.81	P212	26.21	127.67	38.66
CACC	41.75	-124.18	-21.96	P213	27.09	142.19	56.20
CAGL	39.14	8.97	238.36	P231	36.62	-121.91	-26.34
CAGZ	39.14	8.97	238.00	P365	43.40	-124.25	27.10
CANT	43.47	-3.80	99.28	P435	48.06	-123.50	287.32
CCJM	27.10	142.18	208.73	PALM	-64.78	-64.05	31.02

CEDU	-31.87	133.81	144.74	PAPE	-17.53	-149.57	11.94
CEFE	-20.31	-40.32	14.28	PARC	-53.14	-70.88	22.30
CEU1	35.89	-5.31	52.47	PARK	-33.00	148.26	397.35
CFAG	-31.60	-68.23	702.55	PAT0	38.28	21.79	121.04
CHAC	-27.42	-58.96	77.95	PCLA	30.47	-87.19	1.94
CHAT	-43.96	-176.57	57.96	PDEL	37.75	-25.66	110.61
CHET	18.50	-88.30	2.96	PERT	-31.80	115.89	12.72
CHTI	-43.74	-176.62	75.69	PETP	53.07	158.61	210.32
CHUM	43.00	74.75	716.34	PETS	53.02	158.65	102.10
CHUR	58.76	-94.09	-19.45	PGC5	48.65	-123.45	3.55
CKIS	-21.20	-159.80	18.40	PIE1	34.30	-108.12	2347.73
CN12	18.00	-76.75	169.91	PIMO	14.64	121.08	95.52
CNMR	15.23	145.74	64.40	PLO5	32.67	-117.24	-22.54
CONZ	-36.84	-73.03	180.70	PLPK	66.90	-34.03	122.25
COYQ	-45.51	-71.89	476.17	PMTG	50.80	-1.11	56.55
CRAO	44.41	33.99	365.80	PNGM	-2.04	147.37	116.31
CTGR	41.34	-72.05	-19.57	POAL	-30.07	-51.12	76.74
CUCU	7.90	-72.49	311.17	POHN	6.96	158.21	90.68
CUIB	-15.56	-56.07	237.43	POL2	42.68	74.69	1714.20
CUPR	18.31	-65.28	-30.39	POLV	49.60	34.54	178.37
CUSV	13.74	100.53	74.28	PORE	45.23	13.60	66.20
DAEJ	36.40	127.37	116.82	PPTE	-22.12	-51.41	431.02
DARW	-12.84	131.13	125.12	PRE1	-25.75	28.22	1416.33
DGAR	-7.27	72.37	-64.93	PRMI	17.97	-67.05	-25.48
DGAV	-7.27	72.37	-64.93	PTKL	-34.48	150.91	34.44
DNRC	39.16	-75.52	-15.17	PTLD	-38.34	141.61	0.85
DRAG	31.59	35.39	31.80	PTRB	38.00	-123.02	145.71
DRAO	49.32	-119.62	541.86	PTSG	41.78	-124.26	-10.22
DSL1	70.33	-148.47	17.13	PTSV	-35.09	138.49	57.72
DUB2	42.65	18.11	457.92	QAQ1	60.72	-46.05	110.42
DUBO	50.26	-95.87	245.29	QUI2	-0.22	-78.49	2922.55
DUBR	42.65	18.11	454.29	QUIN	39.97	-120.94	1105.78
DUND	-45.88	170.60	386.92	RABT	34.00	-6.85	90.10
DUNT	-45.81	170.63	13.45	RAMO	30.60	34.76	886.82
EPRT	44.91	-66.99	30.38	RBAY	-28.80	32.08	31.75
ESBC	55.49	8.46	59.48	RECF	-8.05	-34.95	20.17

ESBH	55.46	8.44	50.09	RED5	39.56	-75.57	-26.90
ESCU	47.07	-64.80	-15.99	REUN	-21.21	55.57	1558.38
ESPA	-33.87	121.89	32.43	REYK	64.14	-21.96	93.05
EYAC	60.55	-145.75	146.02	RIGA	56.95	24.06	34.71
FAA1	-17.56	-149.61	12.04	RINK	71.85	-50.99	1337.81
FAIR	64.98	-147.50	319.00	RIO2	-53.79	-67.75	32.03
FALK	-51.69	-57.87	50.83	RIOB	-9.97	-67.80	172.62
FLRS	39.45	-31.13	80.18	ROAP	36.46	-6.21	73.67
FTS5	46.20	-123.96	-13.77	ROTG	48.72	-3.97	56.12
FUNC	32.65	-16.91	78.43	ROTH	-67.57	-68.13	39.69
GARI	44.68	12.25	47.74	RSBY	-23.16	150.79	58.13
GENO	44.42	8.92	155.54	SABL	46.53	-1.81	56.74
GIBR	36.15	-5.36	45.64	SAGA	-0.14	-67.06	94.89
GLSV	50.36	30.50	226.30	SAMA	11.23	-74.19	22.69
GMAS	27.76	-15.63	195.42	SANT	-33.15	-70.67	723.02
GODE	39.02	-76.83	14.52	SC02	48.55	-123.01	-15.03
GOLD	35.43	-116.89	986.75	SCCC	32.78	-79.94	-11.39
GOUG	-40.35	-9.88	81.25	SCH2	54.83	-66.83	498.17
GRAS	43.75	6.92	1319.32	SCOA	43.40	-1.68	59.47
GRIS	29.27	-89.96	-17.02	SCOR	70.49	-21.95	128.51
GUAM	13.59	144.87	201.90	SCRZ	-17.80	-63.16	442.09
GUAO	43.47	87.18	2028.70	SCUB	20.01	-75.76	20.91
GUAT	14.59	-90.52	1519.87	SEAT	47.65	-122.31	44.20
GUUG	13.43	144.80	134.73	SELD	59.45	-151.71	20.31
HARB	-25.89	27.71	1558.08	SELE	43.18	77.02	1342.00
HARV	34.47	-120.68	14.96	SETE	43.40	3.70	53.92
HEL2	66.40	-38.22	424.78	SEY1	-4.67	55.48	537.07
HIL1	-31.83	115.74	-27.25	SFER	36.46	-6.21	84.16
HIRS	57.59	9.97	50.14	SHAO	31.10	121.20	22.03
HJOR	63.42	-41.15	762.64	SHE2	46.22	-64.55	-15.30
HLFX	44.68	-63.61	3.10	SHK5	40.47	-74.01	-24.53
HNLC	21.30	-157.86	21.97	SIMO	-34.19	18.44	39.48
HNPT	38.59	-76.13	-27.96	SMST	33.58	135.94	97.52
HNUS	-34.42	19.22	63.03	SMTG	48.64	-2.03	57.74
HOB2	-42.80	147.44	41.06	SOLO	-9.43	159.95	122.95
HOE2	54.76	8.29	62.73	SPBY	-42.55	147.93	1.06

HOFN	64.27	-15.20	82.60	SSA1	-12.98	-38.52	-2.10
HOLB	50.64	-128.13	559.60	SSIA	13.70	-89.12	626.60
HOLM	70.74	-117.76	0.42	STAS	59.02	5.60	104.92
HOLP	33.92	-118.17	-6.71	STJO	47.60	-52.68	152.83
HRAO	-25.89	27.69	1414.16	STNY	-38.38	145.21	29.20
HUEL	37.20	-6.92	81.85	SUR4	59.46	24.38	84.41
HYDE	17.42	78.55	441.69	SUTH	-32.38	20.81	1799.74
ICAM	19.85	-90.53	2.58	SUTM	-32.38	20.81	1797.60
IGM1	-34.57	-58.44	50.69	SUWN	37.28	127.05	82.26
IISC	13.02	77.57	843.68	SYDN	-33.78	151.15	85.58
ILDX	46.01	-1.18	59.03	TAH1	-17.58	-149.61	97.72
IMBT	-28.23	-48.66	31.37	TAH2	-17.58	-149.61	99.81
IMPZ	-5.49	-47.50	104.99	TAMP	22.28	-97.86	21.04
INVK	68.31	-133.53	46.39	TCMS	24.80	120.99	77.24
IPAZ	24.15	-110.33	-14.85	TEHN	35.70	51.33	1194.57
IQUI	-3.77	-73.27	122.11	TELA	32.07	34.78	58.34
IRKJ	52.22	104.32	502.07	TERS	53.36	5.22	56.10
IRKT	52.22	104.32	502.34	TFNO	49.15	-125.91	-3.88
ISPA	-27.12	-109.34	112.50	THTI	-17.58	-149.61	98.03
JOZE	52.10	21.03	141.35	THU2	76.54	-68.83	36.08
JPLM	34.20	-118.17	424.03	TIBB	37.89	-122.45	-21.23
KARR	-20.98	117.10	109.12	TIDB	-35.40	148.98	665.36
KBUG	65.14	-41.16	290.61	TIMM	62.54	-42.29	313.24
KERG	-49.35	70.26	73.00	TNML	24.80	120.99	75.87
KGNI	35.71	139.49	123.52	TONG	-21.14	-175.18	56.30
KHAJ	48.52	135.05	130.49	TOPL	-10.17	-48.33	256.54
KIT3	39.13	66.89	622.51	TOW2	-19.27	147.06	88.18
KMOR	81.25	-63.53	203.25	TPW2	46.21	-123.77	-14.96
KOD5	57.62	-152.19	27.22	TRDS	63.37	10.32	317.73
KOKB	22.13	-159.66	1167.35	TREO	64.28	-41.38	121.89
KOSG	52.18	5.81	96.83	TRIE	45.71	13.76	323.41
KOUC	-20.56	164.29	84.14	TSEA	61.19	-149.89	42.94
KOUR	5.25	-52.81	-25.78	TSKB	36.11	140.09	67.24
KSNB	66.86	-35.58	1720.83	TWTF	24.95	121.16	201.53
KUNM	25.03	102.80	1986.20	UBA1	-23.50	-45.12	6.17
LAE1	-6.67	146.99	140.32	UCLU	48.93	-125.54	10.05

LAGO	37.10	-8.67	62.72	UFPR	-25.45	-49.23	925.78
LAMA	53.89	20.67	187.03	ULAB	47.87	107.05	1575.51
LAUT	-17.61	177.45	89.64	UNSA	-24.73	-65.41	1257.81
LHAZ	29.66	91.10	3624.58	USN3	38.92	-77.07	57.41
LHCL	-38.00	-65.60	404.52	USNO	38.92	-77.07	48.88
LMMF	14.59	-61.00	-27.10	VACS	-20.30	57.50	421.15
LPGS	-34.91	-57.93	29.82	VALE	39.48	-0.34	77.57
LROC	46.16	-1.22	57.86	VALP	-33.03	-71.63	31.40
LWTG	60.15	-1.14	51.61	VBCA	-38.70	-62.27	59.47
MAGO	59.58	150.77	361.82	VEN1	45.43	12.35	60.42
MAJU	7.12	171.36	33.70	VESL	-71.67	-2.84	862.35
MAL2	-3.00	40.19	-20.92	VIGO	42.18	-8.81	87.77
MALA	36.73	-4.39	119.83	VIKH	17.72	-64.80	-6.39
MALL	39.55	2.62	62.03	VILL	40.44	-3.95	647.36
MANA	12.15	-86.25	71.04	VIS0	57.65	18.37	79.80
MAPA	0.05	-51.10	-4.23	VITH	18.34	-64.97	4.42
MAR6	60.60	17.26	75.40	VNAD	-65.25	-64.25	20.99
MARG	77.19	-65.69	670.57	VNDP	34.56	-120.62	-11.47
MARN	-46.88	37.86	61.94	VTIS	33.71	-118.29	59.48
MARS	43.28	5.35	61.81	WES2	42.61	-71.49	85.02
MAS1	27.76	-15.63	197.17	WGTN	-41.32	174.81	26.06
MAT1	40.65	16.70	534.51	WHIT	60.75	-135.22	1427.36
MATE	40.65	16.70	535.63	WILL	52.24	-122.17	1095.67
MAUI	20.71	-156.26	3062.10	WIND	-22.57	17.09	1734.64
MBAR	-0.60	30.74	1337.54	WRHS	33.96	-118.43	7.86
MCM4	-77.84	166.67	97.99	WTZR	49.14	12.88	666.04
MDO1	30.68	-104.01	2004.50	WUHN	30.53	114.36	28.20
MDVJ	56.02	37.21	257.12	YAR2	-29.05	115.35	241.28
METS	60.22	24.40	94.56	YAR3	-29.05	115.35	242.44
MKEA	19.80	-155.46	3754.70	YARR	-29.05	115.35	241.35
MOBS	-37.83	144.98	40.59	YEBE	40.52	-3.09	972.76
MONP	32.89	-116.42	1842.57	YELL	62.48	-114.48	180.85
MORP	55.21	-1.69	144.51	YSSK	47.03	142.72	91.29
MPL2	-38.01	-57.57	53.57	ZADA	44.11	15.23	64.31
MQZG	-43.70	172.65	154.65	ZAMB	-15.43	28.31	1324.92
MTKA	35.68	139.56	108.93	ZEEB	51.34	3.21	60.26

NAIN	56.54	-61.69	32.77	ZHN1	21.31	-157.92	24.21
NANO	49.29	-124.09	6.55	ZIMM	46.88	7.47	956.31
NASO	25.05	-77.46	-21.24				
NAUS	-3.02	-60.06	93.89				
NCDU	36.18	-75.75	-26.15				
NEIA	-25.02	-47.92	6.04				
NICA	43.70	7.23	256.48				
NICO	35.14	33.40	190.00				
NIEB	-39.87	-73.40	57.56				
NKLG	0.35	9.67	31.51				
NLIB	41.77	-91.57	207.03				
NNOR	-31.05	116.19	234.83				
NNVN	61.63	-44.90	2134.57				
NOT1	36.88	14.99	126.35				
NOVM	55.03	82.91	149.95				
NPLY	-39.18	174.12	416.94				
NRC1	45.45	-75.62	82.46				
NRIL	69.36	88.36	47.92				
NRMD	-22.23	166.48	160.32				

Appendix B

Height Correction Formulas

B.1 Height Correction for Pressure

Let p_0 $[hPa]$ be the pressure value at height H_0 $[m]$. In order to correct p_0 to the pressure value p_H $[hPa]$ at height H $[m]$, the following formula is used:

$$p_H = p_0 \left[1 - \frac{\gamma(H - H_0)}{T_0}\right]^{\frac{g}{\gamma R_d}} \tag{B.1}$$

where γ $(= -0.0065\ K\ m^{-1})$ is the vertical temperature lapse rate, R_d $(= 287.058\ m^2\ s^{-2}\ K^{-1})$ is the specific gas constant for dry air, T_0 $[K]$ is the temperature at height H_0 and g $(= 9.80665\ m\ s^{-1})$ is the acceleration due to gravity.

B.2 Height Correction for Zenith Hydrostatic Delay (ZHD)

Let ZHD_0 $[m]$ be the ZHD value at height H_0 $[m]$. In order to correct ZHD_0 to the value ZHD_H $[m]$ at height H $[m]$, a correction term ΔZHD is first computed and then is added to ZHD_0. The following formula is used to compute ΔZHD:

$$\Delta ZHD = \frac{0.0022768(p_H - p_0)}{1 - 0.00266cos(2\varphi_0) - 0.00028H_0} \tag{B.2}$$

where p_H $[hPa]$ is the pressure at height H $[m]$, p_0 $[hPa]$ is the pressure at height H_0, and φ_0 $[rad]$ is the latitude of the site under consideration. ZHD_H is then computed as:

$$ZHD_H = ZHD_0 + \Delta ZHD \tag{B.3}$$

B.3 Height Correction for Zenith Wet Delay (ZWD)

Let ZWD_0 $[m]$ be the ZWD value at height H_0 $[m]$. In order to correct ZWD_0 to the value ZWD_H $[m]$ at height H $[m]$, the following relation is

used:

$$ZWD_H = ZWD_0 \left[1 - \frac{\gamma(H - H_0)}{T_0}\right]^{\frac{(\beta+1)g}{R_d\gamma}} \tag{B.4}$$

where γ ($= -0.0065\ K\ m^{-1}$) is the temperature lapse rate, T_0 $[K]$ is the temperature at height H_0, β is the ZWD decay rate, g ($= 9.80665\ m\ s^{-1}$) is acceleration due to gravity and R_d ($= 287.058\ m^2\ s^{-2}\ K^{-1}$) is the specific gas constant for dry air.

Appendix C

i-GNSS Modules and Scripts

The i-GNSS software consists of various Perl modules and scripts, and Python scripts which are contained in three directories namely i-GNSS, spsdownloader and walcorsdownloader. Table C.1 shows the type of content of each of these directories.

Table C.1: i-GNSS Directory Structure

Directory	**Sub-directory**	**Content Type**
i-GNSS/	callers/	Perl scripts to execute i-GNSS operations (data handling, product handling, data processing, archiving)
	mod/	Perl modules written for various functionalities of i-GNSS
	info/	XML files containing information about all the GNSS stations included in the processing
	conf/	XML file containing FTP addresses and credentials for data sources
spsdownloader/		Python script to fetch 15-minute SPSLux RINEX files created from RT streams and merge these into 1-hour RINEX file
walcorsdownloader/		Python script to fetch 15-minute WALCORS RINEX files created from RT streams and merge these into 1-hour RINEX file
tools/		Python scripts for making 2D ZTD and IWV maps, and E-GVAP upload

Table C.2: i-GNSS Hourly Scripts

Script	Purpose
In i-GNSS/callers/	
call_HD_maintain.pl	Update station-wise tables in the HD database to identify the RINEX files to be downloaded
call_MET_maintain.pl	Update the MET database and identify the meteorological files to be downloaded
call_download_EUREF_stations.pl	Download the required RINEX files for EUREF stations
call_download_IGS_stations.pl	Download the required RINEX files for IGS stations
call_download_RGP_stations.pl	Download the required RINEX files for RGP stations
call_download_OS_active_stations.pl	Download the required RINEX files for OSGB stations
call_download_Irish_stations.pl	Download the required RINEX files for OSi stations
call_download_scientific_stations.pl	Download the required RINEX files for scientific stations from BIGF
call_download_SPS_stations.pl	Copy the 1-hourly SPSLux RINEX files to i-GNSS hourly data directory
call_download_WALCORS_stations.pl	Copy the 1-hourly WALCORS RINEX files to i-GNSS hourly data directory
iGNSS_NRT.pl	Run the GNSS data processing using the Bernese GNSS Software
In spsdownloader/	
sps_dl.py	Create 1-hourly RINEX files from RT streams for SPSLux network
In walcorsdownloader/	
walcors_dl.py	Create 1-hourly RINEX files from RT streams for WALCORS network
In tools/	
nrt_plotter.py	Create 2D maps of IWV and ZTD
cost_to_egvap.py	Upload the UL01 solution files to the E-GVAP server

Table C.3: i-GNSS Daily Scripts

Script	**Purpose**
In i-GNSS/callers/	
genFilesDownloader.pm	Download latest general files (e.g. satellite antenna information)
iGNSS_NRT_COORD_IGS08.pl	Update a-priori coordinates for hourly NRT processing
iGNSS_ANT_I08.pl	Download the latest antenna PCV information
get_newnrt.sta	Download the latest station information file
iGNSS_PPP_EUREF_IGS08ALI.pl	Run PPP processing for EUREF stations
iGNSS_PPP_IGS08.pl	Run PPP processing for IGS stations
iGNSS_PPP_IRELAND_IGS08ALI.pl	Run PPP processing for OSi stations
iGNSS_PPP_RGP_IGS08ALI.pl	Run PPP processing for RGP stations
iGNSS_PPP_SPS_IGS08ALI.pl	Run PPP processing for SPSLux stations
iGNSS_PPP_UK_IGS08ALI.pl	Run PPP processing for OSGB and Scientific stations
iGNSS_PPP_WALCORS_IGS08ALI.pl	Run PPP processing for WALCORS stations

Appendix D

Comparison of $\mathbf{ZTD}_{erai}$ and $\mathbf{ZTD}_{gnss}$ - Full Results

The contents of this appendix can be found on the thesis DVD in the directory named "Appendix_D_CH5_Results". The results are stored as image files that are saved with the name format "[ZONE]_[STA]_ztd.png" where [ZONE] is the climate zone identifier and [STA] is the GNSS station name.

Appendix E

Pressure, Temperature, ZTD and IWV Time Series for SPSLux Stations

The contents of this appendix can be found on the thesis DVD in the directory named "Appendix_E_CH6_Results". The station-wise images are saved with the name format "[STA]_PT.png" for pressure and temperature time series, "[STA]_ZTD.png" for ZTD time series and "[STA]_IWV.png" for IWV time series where [STA] is the SPSLux GNSS station name.

Appendix F

Formulas Used to Obtain IWV

F.1 To Obtain IWV from ERA-Interim

The integrated water vapour (IWV) values from the ERA-Interim model have been obtained by the following procedure:

1. The zenith wet delay (ZWD $[mm]$) and mean atmospheric temperature (T_m $[^oK]$), interpolated to the six SPSLux GNSS station locations, were obtained directly using the GOP - TropDB - TropModel service (`http://www.pecny.cz/gop/index.php/gop-tropdb/tropo-model-service`) by specifying the SPSLux station coordinates.

2. The ZWD is converted to IWV $[kg\ m^{-2}]$ using the following equation:

$$IWV = \frac{ZWD}{R_w \left(\frac{k_3}{T_m} + k_2 - \frac{k_1 R_d}{R_w} \right)} 10^5 \tag{F.1}$$

   where $R_w (= 461.525\ [J\ kg^{-1}\ K^{-1}])$ is the specific gas constant for water vapour, $R_d (= 287.0586\ [J\ kg^{-1}\ K^{-1}])$ is the specific gas constant for dry air and $k_{1,2,3}$ are constants with values of 77.6 $[K\ hPa^{-1}]$, 70.4 $[K\ hPa^{-1}]$ and 373900 $[K^2\ hPa^{-1}]$, respectively (Bevis et al., 1992, 1994).

F.2 To Convert GNSS-derived ZTD into IWV

The GNSS-derived ZTD has been converted to IWV using the following procedure:

1. Surface pressure "P_s"$[hPa]$ values have been obtained using the meteorological sources ASTA, ANAMET (Findel) and UKMO (Details given in Chapters 4 and 6).

2. Surface temperature "T"$[^oK]$ values have been obtained using the meteorological sources ASTA, ANAMET (Findel) and UKMO (Details given in Chapters 4 and 6).

3. Zenith hydrostatic delay (ZHD $[mm]$) has been computed using P_s and the following relation (Saastamoinen, 1972):

$$ZHD = \frac{2.2779(P_s)}{1 - 0.00266cos(2\varphi_0) - 0.00028H_0} \tag{F.2}$$

where H_0 $[km]$ is the GNSS station's ellipsoidal height and φ_0 $[rad]$ is the latitude of the GNSS station.

4. Zenith wet delay (ZWD) is computed by subtracting the ZHD obtained in Step 3 from the GNSS-derived ZTD:

$$ZWD = ZTD - ZHD \tag{F.3}$$

5. Mean atmospheric temperature "T_m" $[^oK]$ has been obtained using T and the following relation (Bevis et al., 1992, 1994):

$$T_m = 70.2 + 0.72T \tag{F.4}$$

6. The ZWD is converted to IWV $[kg\ m^{-2}]$ using the following equation:

$$IWV = \frac{ZWD}{R_w\left(\frac{k_3}{T_m} + k_2 - \frac{k_1 R_d}{R_w}\right)}10^5 \tag{F.5}$$

where $R_w(= 461.525\ [J\ kg^{-1}\ K^{-1}])$ is the specific gas constant for water vapour, $R_d(= 287.0586\ [J\ kg^{-1}\ K^{-1}])$ is the specific gas constant for dry air and $k_{1,2,3}$ are constants with values of 77.6 $[K\ hPa^{-1}]$, 70.4 $[K\ hPa^{-1}]$ and 373900 $[K^2\ hPa^{-1}]$, respectively (Bevis et al., 1994).

7. Three IWV datasets (IWV_{asta},IWV_{anamet} and IWV_{ukmo}) have been obtained by repeating the Steps 1 to 6 using the P_s and T values obtained from ASTA, ANAMET (Findel) and UKMO.